PORTUGALIAE PHYSICA

VOLUME 10
FASCÍCULO 1-2
1979

SOCIEDADE PORTUGUESA DE FÍSICA

PORTUGALIAE PHYSICA

Fundada em 1943 por A. Cyrillo Soares, M. Telles Antunes, A. Marques da Silva e M. Valadares

Publicação subsidiada pelo INSTITUTO NACIONAL DE INVESTIGAÇÃO CIENTÍFICA

CDU 53 (469) (05)

PORTUGALIAE PHYSICA

VOLUME 10
FASCÍCULO 1-2
1979

GENERATOR COORDINATE METHOD AND QUANTUM FLUID DYNAMICS (*)

J. DA PROVIDÊNCIA

Departamento de Física, Universidade de Coimbra

We wish to discuss the equivalence between the Generator Coordinate Method [1] (GCM) and Quantum Fluid Dinamics (QFD).

We considerer the Hamiltonian

$$H = \sum_{i=1}^{n} \frac{p_i^2}{2m} + \frac{1}{2} \sum_{i \neq j} v(\vec{r}_i - \vec{r}_j)$$

and the Hartree-Fock state

$$| \Phi_o > = \prod_{\vec{p}\,(p \leq p_F)} c^+_{\vec{p}} \, | 0 >$$

where $c^+_{\vec{p}}$ is the creation operator for a fermion with momentum $\vec{p}$ and $| 0 >$ is the absolute vacuum. Let

$$b^+_{\vec{k}} = \sum_{\vec{p} \in D_{\vec{k}}} c^+_{\vec{p}+\vec{k}} \, c_{\vec{p}}$$

denote the generator for density deformations [2]. Here $D_{\vec{k}}$ is the domain defined by $p \leqslant p_F$, $| \vec{p} + \vec{k} | > p_F$. The time evolution of the deformed Slater determinant

$$| \Phi(z) > = \exp \left[\sum_{\vec{k}} z_{\vec{k}} \, b^+_{\vec{k}} \right] | \Phi_o >$$

(*) Results presented at the Conference of the Portuguese Physics Society (Lisbon, February, 1978).

is determined by the variational principle

$$\delta\left[<\Phi\,|\,H\,|\,\Phi>/<\Phi\,|\,\Phi>\right]-i\left[<\delta\Phi\,|\,\dot{\Phi}>-<\dot{\Phi}\,|\,\delta\Phi>\right]=0$$

which, to leading order in the small quantities z_k, z_k^*, may be written

$$\sum\Big\{i\,(\delta\, z_{\vec{k}}^{*}\,\dot{z}_{\vec{k}}-\dot{z}_{\vec{k}}^{*}\,\delta\, z_{\vec{k}})\,N_k$$

$$-\delta\Big[A_k\; z_{\vec{k}}^{*}\, z_{\vec{k}}+\frac{1}{2}B_k\,(z_{\vec{k}}\, z_{-\vec{k}}+z_{\vec{k}}^{*}\, z_{-\vec{k}}^{*})\Big]\Big\}=0\,,$$

where

$$A_k=<\Phi_o\,|\,b_{\vec{k}}\,(H-E_o)\;b_{\vec{k}}^{+}\,|\,\Phi_o>\,,$$

$$B_k=<\Phi_o\,|\,b_{\vec{k}}\;b_{-\vec{k}}\;H\,|\,\Phi_o>\,,$$

$$E_o=<\Phi_o\,|\,H\,|\,\Phi_o>\,,$$

$$N_k=<\Phi_o\,|\,b_{\vec{k}}\;b_{\vec{k}}^{+}\,|\,\Phi_o>\,.$$

We introduce now the quantities

$$\rho=\sum_{\vec{k}}N_k\,(z_{\vec{k}}+z_{-\vec{k}}^{*})\;e^{i\vec{k}\cdot\vec{r}}/\,V$$

$$\phi=\sum_{\vec{k}}(z_{\vec{k}}-z_{-\vec{k}}^{*})\;e^{i\vec{k}\cdot\vec{r}}\,/\,(2\,m\,i)\,.$$

The variational principle becomes

$$m\int(\delta\,\rho\,\dot{\phi}-\delta\,\phi\,\dot{\rho})\,a^3\,\vec{r}+\frac{m\,n}{2\,V}\,\delta\int\nabla\,\phi\;\cdot\;\nabla\,\phi\,d^3\,\vec{r}$$

$$+\,\delta\iint\rho\,(\vec{r})\,\rho\,(\vec{r'})\,u\,(\vec{r}-\vec{r'})\,d^3\,\vec{r}\,d^3\,\vec{r'}=0$$

where $$u\,(\vec{r})=\sum_{\vec{k}}(A_k-B_k)\;e^{i\vec{k}\cdot\vec{r}}/\,N_k^2$$

and n denotes the particle number.

This may be recognized as the variational principle of QFD [3], for small deviation from equilibrium. The conditions for validity of QFD and of GCM. in the version described here [2], are, therefore, essentially the same.

REFERENCES

[1] D. L. HILL and J. A. WHEELER, *Phys. Rev.* **89** (1953) 1102; D. M. BRINK and A. WEIGUNY, *Nucl. Phys.* **A120** (1968) 59.

[2] J. DA PROVIDÊNCIA, *Portgal. Phys.* **5** (1969) 125.

[3] M. J. GIANNONI, D. VAUTHERIN, M. VÉNÈRONI and D. M. BRINK, *Phys. Lett.* **63B** (1976) 8.

ISOSPIN SELECTION RULES IN ^{28}Si (*)

P. M. CORRÊA

Laboratório de Física e Engenharia Nucleares, Sacavém, Portugal

ABSTRACT — More than 300 electromagnetic transitions in ^{28}Si, concerning levels with well known J^{π} and T are classified according to their character and strength and examined from a statistical point of view. Reliable upper limits are obtained for the transition strengths, based upon a quantitative criterion and useful as spectroscopic tools. Isospin selection rules for dipole and electric quadrupole radiation in self-conjugate nuclei are studied in ^{28}Si. Preferential decay to highly excited energy states is found to be a characteristical feature of this nucleus.

1 — INTRODUCTION

The effect of isospin selection rules in ^{28}Si was studied by Lawergren [1]. Since then, however, a large amount of experimental data obtained with Ge(Li) detectors was published, namely more reliable spin and isospin assignments and decay schemes and lifetime measurements. Therefore, the check of isospin selection rules relevant to electromagnetic transitions in this nucleus can now be made with a much greater experimental support.

Usually, the electromagnetic transition matrix element is splitted into two parts [2]:

$$< J_b M_b ; T_b T_{3b} | H_0(L, M) + H_1(L, M) | J_a M_a ; T_a T_{3a} > \qquad (1)$$

H_0 and H_1 being the isoscalar and isovector interactions, respectively. It can easily be seen that [2]:

— both contributions vanish unless $\Delta T = 0, \pm 1$;

(*) Results presented at the Conference of the Portuguese Physics Society (Lisbon, February, 1978).

— the isoscalar part can only contribute to $\Delta T = 0$ transitions;
— the isovector part vanishes for $\Delta T = 0$ transitions in selfconjugate nuclei.

It can be shown that the isoscalar contribution to El transitions vanishes in all cases in the long-wavelength approximation [2]. This result can be considered as almost exact, because the effect of the higher order terms, neglected in this approximation, is indeed very small (for a 10 MeV transition in ^{28}Si, e. g., their contribution would be less than about 6.5×10^{-4} of the corresponding isovector transition strength):

$$B(E1;\ \text{isoscalar}) \approx 0 \tag{2}$$

Por electric quadrupole transitions, one expects [2] that E2, $\Delta T = 1$ are retarded relatively to E2, $\Delta T = 0$ transitions by an average factor equal to $(e_p + e_n)^2 / (e_p - e_n)^2$ e_p and e_n being the effective charges of the proton and the neutron, respectively. Therefore, the expected retardation factor is 4, for $e_p / e = 1.5$ and $e_n / e = 0.5$, and 9 for $e_p / e = 2$ and $e_n / e = 1$.

For magnetic transitions, on the other hand, an estimate of the average enhancement exhibited by isovector transitions when compared with isoscalar transitions can also be obtained [2]:

$$\frac{(\mu_p - \mu_n - 1/(L+1))^2}{(\mu_p + \mu_n - 1/(L+1))^2} \tag{3}$$

where μ_p and μ_n are the magnetic moments of the proton and the neutron, respectively, in nuclear magnetons, and L is the multipolarity of the transition. This expression gives enhancement factors of 122 and 64 for $L = 1$ and $L = 2$, respectively, but is not expected to be very accurate.

Shortly, the following isospin selection rules to the electromagnetic transitions in ^{28}Si can be derived:

A: E1, $\Delta T = 0$ transitions are forbidden.
B: E2, $\Delta T = 1$ transitions are retarded relatively to E2, $\Delta T = 0$ transitions by a factor of 5 to 10.
C: M1, $\Delta T = 0$ transitions are expected to be about 100 times weaker than the average M1, $\Delta T = 1$ transitions.

These rules are not expected to be obeyed rigidly in actual nuclei for several reasons [3], the most important of which is usually supposed to be the isotopic spin impurity in the initial or final states. Taking this impurity into account, a T-forbidden E1 transition between states $|a>$ and $|b>$ will have a non-zero matrix element of the form [2]:

$$\mathfrak{M}_{ab}(\mathrm{E1};\mathrm{T}_a - \mathrm{T}_b = 0) = \sum_i \frac{<a|\mathrm{V}_c|i>}{\mathrm{E}_a - \mathrm{E}_i} \mathfrak{M}_{ib}(\mathrm{E1};|\mathrm{T}_i - \mathrm{T}_b| = 1) \quad (4)$$

where V_c is the Coulomb interaction, responsible for the isospin admixture between states $|i>$ and $|a>$. The isospin impurity in the excited state will be proportional to

$$\sum_i \left[\frac{<a|\mathrm{V}_c|i>}{\mathrm{E}_a - \mathrm{E}_i}\right]^2 \quad (5)$$

In the past, isospin selection rules have been studied on statistical collections of electromagnetic transition intensities (ref. [1], [4], [5], [6] among others). The use of larger Ge(Li) detectors, associated with better electronics and sophisticated data handling systems, have been giving and will give information about many more weak transitions, therefore distorting the transition strength distributions and lowering their mean values. Although statistical studies can be delicate and although refined nuclear models can account for individual cases of electromagnetic transitions, it is nevertheless interesting to examine the experimental data from a statistical point of view, by considering the average behaviour of the transition rates. However, as can be seen from expressions (4) and (5), it will not be legitimate to obtain a mean value for the isospin impurity from the ratio of the average T-forbidden and T-allowed transition rates, as it has been done in some cases.

Even if the mean values of the transition strengths are rather delicate quantities, that must be regarded carefully, their upper limits, that can be extracted from the statistical collections, are quite reliable. The biggest difficulty connected with these is the choice of an appropriate probability acceptance criterion, since there is no established theoretical model for the shape of the distribution corresponding to a certain type of transitions. However, because of the usefulness of these upper limits in nuclear spectroscopy, it is worthwhile to make an effort to define them quantitatively.

2 — EXPERIMENTAL DATA SOURCES

Transition strengths were calculated by comparison with the Weisskopf single-particle strengths [4]:

$$|M|^2 = \frac{\Gamma \exp}{\Gamma \text{ Weisskopf}} \tag{6}$$

It must be emphasized that only transitions between states of well known and unique J^π and T values were accepted. Electric transitions up to $L=3$ and magnetic transitions of $L=1$ and $L=2$ were considered, both with $\Delta T=0$ and 1. Mixing-ratios were never taken into account, because there are not enough δ-measurements in ^{28}Si. Transitions of the $EL+M(L+1)$ type were supposed to be pure electric. Transitions of the $ML+E(L+1)$ type were supposed to be either pure magnetic (if the existence of an electric component with a strength equal to the corresponding upper limit would not introduce a carrection to the strength of the magnetic component greater than 54 % (*)) or mixed; in both cases they were simultaneously included in special ML and $E(L+1)$ collections, denoted by an asterisk. Transition strengths were only included in the statistical collections (fig. 1 and 2) when their relative error (combination of the errors in branching-ratio and lifetime or gamma-width of the initial state) was smaller than 54 %.

The radiative widths of the (p,γ) resonances were obtained from the resonance strength, assuming that $\Gamma_p >> \Gamma_\gamma$, i. e.:

$$\Gamma_\gamma \approx \frac{\omega \gamma}{2J+1} \tag{7}$$

At least three cases are known [7] where this assumption is not correct (resonances at $E_p = 1183$, 1365 and 1647 keV), but corrections for the known value of Γ_p / Γ_γ would not change the conclusions obtained from the statistical collections.

(*) The choice of this limit corresponds to the fact that an error of 54 % in the transition strength gives a maximum corrective factor of 2.15, that is, the extension of one class in the histograms of figs. 1 and 2. In the same way, an error of 79 % gives a maximum corrective factor of 4.65, that is, two classes in those histograms.

Most of the data used in this work (E_x, T, J^π, τ or $\omega\gamma$ and decay scheme) were taken from Meyer et al. [8]. A few exceptions are indicated below:

a) The energies of the bound states were taken from Endt and van der Leun [9], as well as the lifetimes of the bound states at 1.779, 4.979, 6.276, 6.879, 8.413, 10.901, and 11.445 MeV.

b) The lifetimes of the levels at 7.933 MeV (9 ± 6 fs), 8.543 MeV (13 ± 10 fs) and 9.316 MeV (10 ± 5 fs) were taken from Gonidec [10].

c) The decay schemes of the levels at 7.417 and 10.901 MeV were taken from Endt and van der Leun [9]. The decay scheme of the level at 9.702 MeV was taken from Lam et al. [11].

d) Data concerning the resonance at $E_p = 1439$ keV were obtained from Forsblom [12] and Lyons et al. [13].

e) The J^π value of the resonance at $E_p = 1724$ keV was taken from Tveter [7].

f) The strength and decay scheme of the upper member of the doublet at $E_p = 1363/1365$ keV were taken from Cunha et al. [14].

g) The strengths, J^π values and decay schemes of both members of the doublet at $E_p = 1575/1579$ keV were taken from Gonidec [10].

A list of all the calculated transition strengths is presented in table 8.

3 — EXPRESSIONS AND DEFINITIONS

The transition rates, calculated by means of expression (6), were classified according to their character and intensity. The resultant distributions are presented in figs. 1 and 2, as well as the mean transition strength, defined by:

$$\log \langle W \rangle = \frac{1}{N} \sum_i n_i \log W_i \qquad (8)$$

For each collection, the error in the mean transition strength (table 1) was calculated by the expression:

$$\varepsilon\{\log < W >\} = \frac{1}{N}\left[\sum_i n_i^2 (\varepsilon\{\log W_i\})^2\right]^{1/2}$$
$$\varepsilon\{\log W_i\} = 0.167 \text{ (half a class)} \qquad (9)$$

In these expressions, W_i and n_i are the central value and the number of transitions of each class of the distribution, and N is the total number of transitions of the distribution.

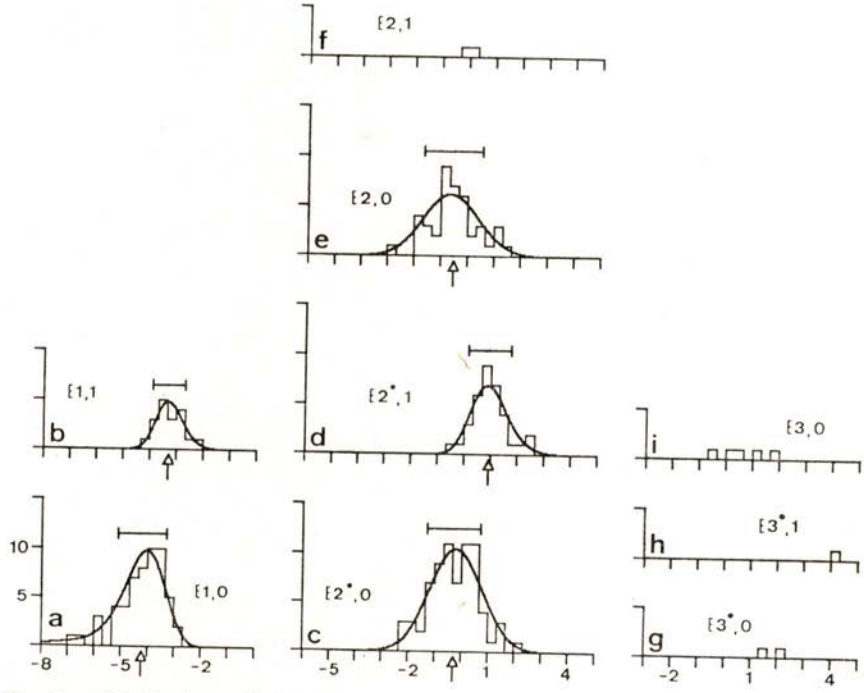

Fig. 1 — Distributions of electric transition strengths. The vertical arrows below the histograms indicate the mean strengths; the horizontal bars above the histograms indicate the intervals corresponding to 68.3 % of the total area, around the mean. The abcissas are log(W) and the ordinates are the number of transition strengths accepted inside each class. The amplitude of all classes is one third of an order of magnitude. The smooth curves are computer-made fits to the most significant distributions, as explained in section 3.

For the statistically significant distributions, the transition strength upper limits were calculated assuming that $x = \log W_i$ followed a function of the form:

$$f(x) = k \,.\, \exp[-(a + bx + cx^2 + dx^3)] \qquad (10)$$

smoothly connected at both sides by decreasing exponentials, at the central value of the first (last) class to the left (right) of which there were no observed transitions. Rightmost values of x were obtained, which defined 99.0, 99.5 and 99.9 % of the area under these curves; all adopted upper limits (table 2) define areas between 99.5 and 99.9 % of the total area. For these distributions, the intervals corresponding to 68.3 % of the total area (around the mean) were also obtained; they correspond to the horizontal bars in the histograms of figs. 1 and 2 and to the value of σ in table 1.

For the other collections, the upper limits are quite arbitrary and correspond only to values reasonably higher than the strongest

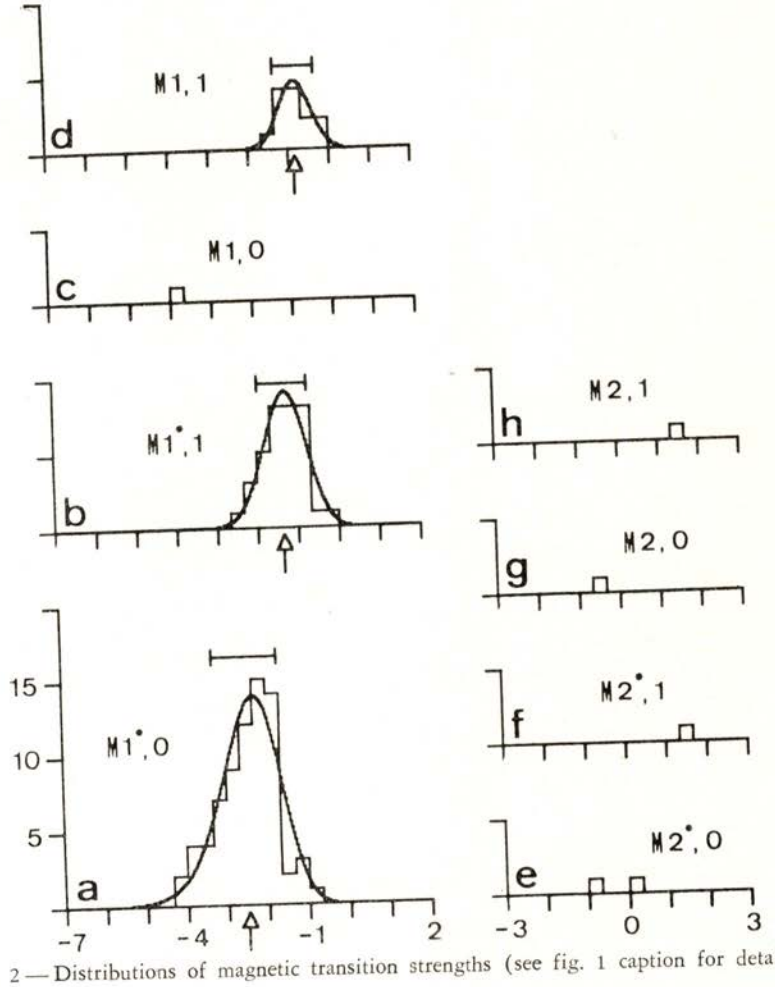

Fig. 2 — Distributions of magnetic transition strengths (see fig. 1 caption for details).

observed (and accepted) transition stength (values between brackets in table 2).

The data in the diagrams (figs. 1 and 2) corresponding to pure transitions can be directly interpreted, but those diagrams which correspond to (possibly) mixed transitions, denoted by an asterisk, must be regarded carefully, since mixing ratios were not considered. In the discussion of the data the following quantities will be considered:

a) Enhancement (or retardation) of (E, M) L, $\Delta T = 1$ radiation relatively to (E, M) L, $\Delta T = 0$ radiation:

$$k_{(E,\,M)\,L} = \frac{< \left| M_{(E,\,M)\,L,\,1} \right|^2 >}{< \left| M_{(E,\,M)\,L,\,0} \right|^2 >} \tag{11}$$

In particular:

$$k_{M\,1} = \frac{< \left| M_{M\,1,\,1} \right|^2 >}{< \left| M_{M\,1,\,0} \right|^2 >} = \frac{< \delta_0^2 >}{< \delta_1^2 >} \tag{11a}$$

b) Apparent enhancement (or retardation):

$$k^*_{(E,\,M)\,L} = \frac{< \left| M^*_{(E,\,M)\,L,\,1} \right|^2 >}{< \left| M^*_{(E,\,M)\,L,\,0} \right|^2 >} \tag{12}$$

c) Mixing-ratios of E2/M1 radiation, with $\Delta T = 0$ and 1:

$$< \delta_0^2 > = \frac{1}{\dfrac{< \left| M^*_{E\,2,\,0} \right|^2 >}{< \left| M_{E\,2,\,0} \right|^2 >} - 1} \tag{13}$$

$$< \delta_1^2 > = \frac{1}{\dfrac{< \left| M^*_{E\,2,\,1} \right|^2 >}{< \left| M_{E\,2,\,1} \right|^2 >} - 1} = \frac{1}{\dfrac{1}{k_{E\,2}} \dfrac{< \left| M^*_{E\,2,\,1} \right|^2 >}{< \left| M_{E\,2,\,0} \right|^2 >} - 1} \tag{14}$$

d) Relation between the mixing-ratios of E2/M1 radiation for $\Delta T = 0$ and 1:

$$< \delta_0^2 > = \frac{1}{\dfrac{k_{E\,2}}{k^*_{E\,2}} \left(1 + \dfrac{1}{< \delta_1^2 >} \right) - 1} \tag{15}$$

and the subsequent limit for $<|\delta_1|>$:

$$<|\delta_1|> \leqslant \left[\frac{k^*_{E2}}{k_{E2}} - 1\right]^{-1/2} \tag{16}$$

e) Statistical factor $G_{\Delta T}$ containing the angular and spin dependence of the M1 transition matrix element. Using the definition quoted by Lawergren [1]:

$$\frac{<|M_{M1,0}|^2>}{<|M_{M1,1}|^2>} = \left[-\frac{1.8 + <G_0>}{9.4 + <G_1>}\right]^2 \tag{17}$$

and simplifying it by assuming $<G_0> = <G_1> = <G>$, as done by that author, one obtains:

$$<G> = -\frac{9.4 + 1.8(k_{M1})^{1/2}}{1 + (k_{M1})^{1/2}} \tag{18}$$

4 — ISOSPIN SELECTION RULES

The values of the quantities defined in section 3 are presented in tables 1, 2 and 3. Relatively to table 3, it was assumed that E2 radiation is not affected by isospin selection rules ($k_{E2} = 1$; see discussion in subsection 4.2).

4.1 — *The dipole transitions*

Lawergren [1] has considered a number of E1 transitions (10 with $\Delta T = 0$ and 8 with $\Delta T = 1$) much smaller than that considered in this work (55 and 18, respectively). However, the value now obtained k_{E1} is in good agreement with the one given by that author. It can be seen from table 3 that there is also agreement with the values that can be obtained from the works by Skorka et al. [5] an Endt and van der Leun [6]. Since rule A should prevent any E1, $\Delta T = 0$ transitions, the value of k_{E1} is somehow related to the isospin admixture in ^{28}Si.

Figs. 2.a-d present data from 14 M1 transitions (1 with $\Delta T = 0$ and 13 with $\Delta T = 1$) and 108 M1* transitions (73 with $\Delta T = 0$ and 35 with $\Delta T = 1$), to compare with the 36 used by Lawergren [1]

TABLE 1

Type of radiation	$\langle \lvert M \rvert^2 \rangle$ (W. u.) Present	Ref. [5] *a*)	Ref. [1] *b*)	Ref. [6] *b,c*)	σ *d*) Present	Ref. [5]
E1, $\Delta T=0$	$(6.4 \pm 0.9) \times 10^{-5}$	1.8×10^{-4}	2×10^{-4}	3×10^{-5}	7.9	7.2
E1, $\Delta T=1$	$(5.5 \pm 1.0) \times 10^{-4}$	1.5×10^{-3}	10^{-3}	3×10^{-4}	4.0	6.6
E2, $\Delta T=0$	$(3.1 \pm 0.5) \times 10^{-1}$	1.5	--	3	12.6	10.0
E2, $\Delta T=1$	---	0.44	--	7×10^{-1}	-	12.0
M1, $\Delta T=0$	---	8.8×10^{-3}	7×10^{-3}	10^{-3}	-	3.4
M1, $\Delta T=1$	$(1.5 \pm 0.3) \times 10^{-1}$	2×10^{-1}	9×10^{-2}	5×10^{-2}	3.2	7.2
E2*, $\Delta T=0$	$(5.5 \pm 0.7) \times 10^{-1}$	--	--	--	10.0	-
E2*, $\Delta T=1$	9.1 ± 1.4	--	--	--	6.3	-
M1*, $\Delta T=0$	$(3.3 \pm 0.5) \times 10^{-3}$	--	--	--	6.3	-
M1*, $\Delta T=1$	$(4.6 \pm 0.8) \times 10^{-2}$	--	--	--	4.0	-

a) $20 \leqslant A \leqslant 40$.

b) Estimates obtained from the reported distributions of transition rates.

c) $A < 45$.

d) See text (section 3) for definition.

(25 and 11, respectively). On the other hand, this author does not refer any precautions taken into account for the effect of unknown mixing-ratios. As a matter of fact, if we calculate the apparent enhancement of M1 radiation, directly from the data of figs. 2.a, b, we obtain $k^{*}_{M1} = 14 \pm 4$, which is in much better agreement with the value given in ref. [1] than $k_{M1} = 45 \pm 30$, obtained through expression (11a). Table 3 shows that there is no serious disagreement between the present value for k_{M1} and those that can be obtained from refs. [5], [6]. Anyway, the enhancement of M1, $\Delta T = 1$ radiation relatively to M1, $\Delta T = 0$ radiation is found to be weaker than predicted by rule C, showing once more that isospin admixture is present in the ^{28}Si nucleus (see subsectian 4.2).

TABLE 2

Type of radiation	Upper limits (W. u.) *c*) Present	Ref. [6]
E1 , $\Delta T = 0$	5×10^{-3}	3×10^{-3}
E1 , $\Delta T = 1$	2×10^{-2}	10^{-1}
E2 , $\Delta T = 0$	10^{2}	10^{2}
E2 , $\Delta T = 1$	(10) *a*)	10
E3 , $\Delta T = 0$	(2×10^{2})	10^{2}
E3 , $\Delta T = 1$	(50) *b*)	--
M1 , $\Delta T = 0$	(5×10^{-1})	3×10^{-2}
M1 , $\Delta T = 1$	2	10
M2 , $\Delta T = 0$	(1)	10^{-1}
M2 , $\Delta T = 1$	(10^{2})	3
E2 * , $\Delta T = 0$	5×10^{2}	--
E2 * , $\Delta T = 1$	5×10^{3}	--
E3 * , $\Delta T = 0$	(5×10^{2})	--
E3 * , $\Delta T = 1$	(5×10^{4})	--
M1 *, $\Delta T = 0$	2×10^{-1}	--
M1 *, $\Delta T = 1$	2	--
M2 *, $\Delta T = 0$	(5)	--
M2 *, $\Delta T = 1$	(10^{2})	--

a) Several transitions with strengths between 2 and 5 W. u. can only be accepted on the basis of a 79 % error criterion.

b) Not illustrated. The suggested upper limit was found from two transitions that can only be considered on the basis of a 79 % error criterion.

c) See text (section 3) for definition.

The fact that rule A is much more seriously violated than rule C is not surprising. The effects of isospin impurities on M1 and E1 radiation differ greatly because the M1 transition operator has no radial dependence; thus, the only isospin impurities relevant to M1 transitions come from states with the same configuration but one unit different in isospin (if we write for M1 radiation an expression similar to (4), states $|i>$ will have the same configuration as $|a>$ but will be one unit different in isospin). It must be expected, then, that the E1 active isospin impurities present in a specific state have their origin in states much closer in energy to this one than in the case of M1 transitions; therefore, apart from the Coulomb matrix element, the violation of the E1 isospin selection rule must be easier than that of the M1 rule, as can be seen from expressions (4) and (5).

4.2 — *The electric quadrupole transitions*

Figs. 1.c, d show an apparent enhancement of the E2*, $\Delta T=1$ transitions (35 examples) relatively to the E2*, $\Delta T=0$ transitions (73 examples), which must be due to the assumption of «pure electric character» of the (possibly) mixed E2/M1 transitions. This indicates that the average mixing-ratios must depend on ΔT.

Unfortunately, the statistics of E2, $\Delta T=1$ transitions is not good enough to obtain a mean value. If we assume that E2 radiation is not affected by isospin selection rules ($<|M_{E2,1}|^2>\approx<|M_{E2,0}|>^2$;

TABLE 3

	Present	Ref. [1]	Ref. [5] *a*)	Ref [6] *b*)
k_{E1}	9 ± 2	7	8.3	10
k_{M1}	45 ± 30	10 *c*)	23	50
$<G>$	$-(2.8\pm0.9)$	-3.7	-3.1	-2.7
$<|\delta_0|>/<|\delta_1|>$	6 ± 2	-	-	-
Max. val. of $<|\delta_1|>$	0.3	-	-	-

a) Calculations made over the reported mean values for $20\leqslant A\leqslant 40$.
b) Calculations made over the estimates referred in table 1.
c) See subsection 4. 1

$e_p/c=1$ and $e_n/e=0$), the values obtained for $<|\delta_0|>/<|\delta_1|>$ and for the upper limit of $<|\delta_1|>$ (and, of course, the value for k_{M1}) are those shown in table 3. If, however, we assume $k_{E2}=0.29$ (Skorka et al. [5], $20\leqslant A\leqslant 40$), we obtain $<|\delta_0|>/<|\delta_1|>=$ $=11\pm 4$ and $<|\delta_1|>\leqslant 0.15$ (and $k_{M1}=130\pm 80$); assuming also that $k_{E2}\approx(e_p-e_n)^2/(e_p+e_n)^2$, this value for k_{E2} implies that the effective charges of the proton and the neutron are related as $e_p/e_n\approx 3$.

In either assumption, the absolute value of the mixing-ratio for the $\Delta T=1$, E2/M1 transitions is predicted to be usually very small, but the one of the $\Delta T=0$, E2/M1 transitions is predicted to be of the order of unit. It is interesting to remark that none of the 73 M1*, $\Delta T=0$ transitions considered could be supposed «pure», on the basis of the criterion expressed in section 2, whereas 9 of the 35 M1*, $\Delta T=1$ transitions were supposed to be «pure»

4.3 — *Transitions of higher multipolarity*

Figs. 1 and 2 include also some data on electric octupole and magnetic quadrupole transitions, but the statistics is too poor to draw any conclusions. A few transitions included in table 8 deserve, however, a special reference.

4.3.1 — The M3, $\Delta T=0$ transition: 12.240 MeV, $J^\pi=3^+$, $T=0\rightarrow 0$ $J^\pi=0^+$, $T=0$, with a strength of 6 W.u., resulting from a branching-ratio of 0.1%, and the M3/E4, $\Delta T=0$ transition 13.427 MeV, $J^\pi=5^+$, $T=0\rightarrow$ 11.780 MeV, $J^\pi=2^+$, $T=0$, with a strength of $|M^*_{M3}|^2=5.9\times 10^8$ (or $|M^*_{E4}|^2=2.5\times 10^{12}$) W u., resulting from a branching-ratio of 2.5%. Endt and van der Leun [6] present in their compilation only one isoscalar M3, with a strength of 0.55 ± 0.02 W.u., extracted from the mirror pair $^{24}Na/^{24}Al$ (0.47/0.44 MeV $\rightarrow$ 0).

4.3.2 — The M2/E3, $\Delta T=0$ transitions:

13.417 MeV, $J^\pi=1^-$, $T=0\rightarrow$ 8.589 MeV, $J^\pi=3^+$, $T=0$

B.r. = 1.8 % $\quad |M^*_{M2}|^2=5.5$ W.u.

$|M^*_{E3}|^2=1800$ W.u.

13.104 MeV, $J^\pi = 2^+$, $T = 0 \rightarrow$ 8.413 MeV, $J^\pi = 4^-$, $T = 0$

B.r. = 0.9 % $\quad |M^*_{M2}|^2 = 3.2$ W.u.

$|M^*_{E3}|^2 = 1100$ W.u.

13.034 MeV, $J^\pi = 2^+$, $T = 0 \rightarrow$ 8.413 MeV, $J^\pi = 4^-$, $T = 0$

B.r. = 1 % $\quad |M^*_{M2}|^2 = 4.4$ W.u.

$|M^*_{E3}|^2 = 1600$ W.u.

12.974 MeV, $J^\pi = 1^-$, $T = 0 \rightarrow$ 8.589 MeV, $J^\pi = 3^+$, $T = 0$

B.r. = 5 % $\quad |M^*_{M2}|^2 = 6$ W.u.

$|M^*_{E3}|^2 = 2400$ W.u.

4.3.3 — The E3, $\Delta T = 0$ transition: 13.108 MeV, $J^\pi = 3^-$, $T = 0 \rightarrow$ 8.543 MeV, $J^\pi = 6^+$, $T = 0$, with a strength of $|M_{E3}|^2 = 4600$ W.u., corresponding to a branching-ratio of 40 % [10]. The $E_x = 13.108$ MeV is the upper level of an overlapped doublet ($E_p = 1575/1579$ keV) in the $^{28}Al + p$ reaction, that was claimed to have been resolved by Gonidec [10]. Its (p,γ) strength is reported to be about ten times smaller than that of its partner. Due to the calculated E3 strength it is reasonable to suppose that some (non reported) troubles have occurred in the doublet resolution, either in the assignment of the transition (it would not be confortable to assign it to the lower member of the doublet, however, because in that case it would be a very strong E4, $\Delta T = 0$), or in the estimate of the branching-ratio or the resonance strength values. The J^π assignment can also be wrong.

4.3.4 — The M2/E3, $\Delta T = 0$ transition: 12.901 MeV, $J^\pi = 2^+$, $T = 0 \rightarrow$ 8.143 MeV, $J^\pi = 4^-$, $T = 0$, with a strength of $|M^*_{M2}|^2 = 16$ ($|M^*_{E3}|^2 = 6000$) W. u., corresponding to a branching-ratio of 1 % [14]. Once again such high, unreasonable, strengths can arise from uncertainties in the resolution of the doublet ($E_p = 1363/1365$ keV; $E_x = 12.901$ MeV corresponds to the upper member): the branching-ratio is too small to allow a reliable assignment about the origin of the gamma ray.

4.3.5 — The following transitions:

13.248 MeV, $J^\pi = 5^-$, $T = 1 \rightarrow 0$, $J^\pi = 0^+$, $T = 0$

B. r. $= 0.1\%$ $|M_{E5}|^2 = 3.5 \times 10^6$ W. u.

13.248 MeV, $J^\pi = 5^-$, $T = 1 \rightarrow 9.316$ MeV, $J^\pi = 3^+$, $T = 1$

B. r. $= 1.2\%$ $|M^*_{M2}|^2 = 76$ W. u.

$|M^*_{E3}|^2 = 3.8 \times 10^4$ W. u.

The branching-ratios observed by Meyer et al. [8] are very small, but any observable branch corresponding to these transitions (e. g., one tenth of the reported values) would still give too high strengths. The $E_x = 13.248$ MeV is the upper member of the doublet at $E_p = 1723/1724$ keV. The lower member, with $J^\pi = 3^-$, was reported to have no gamma-decay [15]. However, if this is not the case and if the transitions observed by Meyer et al. [8] can be ascribed to the lower member of the doublet, their characters and strengths will be, assuming $\Gamma\gamma = 10$ meV for both:

13.247 MeV $\rightarrow$ 0	E 3, $\Delta T = 0$	$\lvert M_{E3}\rvert^2 = 8$ W. u.
13.247 MeV $\rightarrow$ 9.316 MeV	E 1, $\Delta T = 1$	$\lvert M_{E1}\rvert^2 = 2.5 \times 10^{-2}$ W. u.

which seem to be much more reasonable. Evidence in this direction can be obtained from the work by Lam et al. [11]. These authors have exhaustively studied the 13.248 MeV level and did not report these transitions.

4.4 — *The statistical factor* $G_{\Delta T}$.

A rough estimate of the expected theoretical value of G can be obtained by averaging over all possible combinations of single-particle transitions in ^{28}Si. This average value, $\langle G \rangle = -2$ [1] is in better agreement with the figure obtained in the present work than with that reported by Lawergren. The arguments about the retardation of E2, $\Delta T = 1$ transitions relatively to E2, $\Delta T = 0$ transitions (subsection 4.2) do not change appreciably the value given in table 3 ($k_{E2} = 0.29$ would imply $\langle G \rangle = -(2.4 \pm 0.8)$).

5 — SPINS AND PARITIES

The upper limits for the transition strengths, presented in table 2, were used to restrict the possible spins and parities of levels with unknown J^{π}. Table 4 shows the relevant results, in comparison with those of ref. [8].

TABLE 4

E_x (MeV)	J^{π} assignments Present	Previous [8]
8.945	$(4+, 5^-, 6+)$	$\pi = (-)^J$
9.418	$(2+, 3^-)$	$(2+, 3^-, 4+)$
9.762	$(2, 3, 4^-)$	$(2-4)$
9.794	$(2, 3, 4+)$	$(1-4)$
10.210	$(2+, 3^-)$	$(2+, 3, 4+)$
10.312	$(2+, 3)$	$(4+)$
10.372	(2)	$(3+)$ *a)*
10.916	$(2+, 3^-, 4+)$	$\pi = (-)^J$
12.074	$(2^-, 3^-)$	$(2+)$ *b)*
12.715	(2)	$(1+, 2)$
13.205	$(2)+$	$(2, 3)+$
13.230	$(2+, 3^-)$	$(2,3^-)$ *c)*
13 984	$(3^-, 4)$	$(2+, 3^-)$

a) Ref. [9] quotes $J^{\pi} = (3)^+$. *b)* Ref. [9] quotes $J^{\pi} = 2^{(+)}$.
c) Ref. [9] quotes $J^{\pi} = (2,3)^+$

6 — PREFERENTIAL DECAY TO HIGHLY EXCITED STATES

A particular feature of the ^{28}Si nucleus is the occurrence of many strong gamma-transitions from (p,γ) resonances to highly excited energy states (see, e.g., ref. [16]). A picture of this can be seen in tables 5-7 (only transitions whose strengths have errors of less than 54 % are represented).

6.1 — *E1 transitions*

It can be seen from table 5 that about 50 % of the full E1 strength corresponds to transitions from the resonances to the levels at 9.316 and 9.381 MeV ($J^{\pi}=3^{+}$, $T=1$ and $J^{\pi}=2^{+}$, $T=1$, respectively), and that only about 15 % of the full strength corresponds to transitions to g.s. or to the first two excited states. On the other hand, the E1

TABLE 5

```
FINAL LEVELS   ( NUMBER: ENERGY(MEV) Jπ,T )

 1:  0.000 0+,0    2:  1.779 2+,0    3:  4.618 4+,0    4:  4.979 0+,0
 5:  6.276 3+,0    6:  6.691 0+,0    7:  6.879 3-,0    8:  6.889 4+,0
 9:  7.381 2+,0   10:  7.417 2+,0   11:  7.799 3+,0   12:  7.933 2+,0
13:  8.259 2+,0   14:  8.328 1+,0   15:  8.413 4-,0   16:  8.543 6+,0
17:  8.589 3+,0   18:  8.904 1-,0   19:  9.316 3+,1   20:  9.381 2+,1
21:  9.480 2+,0   22:  9.702 5-,0   23: 10.180 3-,0   24: 10.418 3+,0
25: 10.668 3+,0   26: 11.780 2+,0

     NORMALIZED STRENGTHS LESS THAN 0.00005 ARE REPRESENTED BY <;
     FROM 0.00005 TO 0.0005 BY .; FROM 0.0005 TO 0.005 BY :; FROM
     0.005 TO 0.05 BY *; AND FROM 0.05 TO 0.5 BY >.  THE SYMBOL T
           BEFORE THE STRENGTH IS FOR ISOVECTOR TRANSITIONS.

**********************

DECAY TABLE      E1 TRANSITIONS      ( 0.1000-01 W.U. <> 10 )

                1   3   5   7   9  11  13  15  17  19  21  23  25
                  2   4   6   8  10  12  14  16  18  20  22  24  26  SUM

 6.879 3-,0       : :                                                  0
 8.413 4-,0         :                                                  0
 8.904 1-,0     > >                                                    0
 9.702 5-,0       .       .                                            0
10.180 3-,0       * >                                                  0
10.195 3-,0       1 >     >       >       > >           T>T1           2
10.217 2-,0       >       >         >     >       >       T8           9
10.480 3-,0       > >     >           >                   T1           1
10.664 4-,1           T2      T>                  T3                   5
10.726 2+,0                     >                                      0
10.740 3-,1       T>      T1          T>T>T>        T>    1 1          4
10.800 3-,0       > >             >     >                              0
10.974 1-,0     *       *                                              0
10.991 3-,0       * *                   >             >   T2           2
11.034 2+,0                   >                                        0
11.251 2-,0       1                                                    1
11.304 2+,0                   >                                        0
11.373 3-,0       * *     *           * *                 T>           0
11.548 5-,1                   T>                                       0
11.572 2-,0       1                         >           T1             2
11.661 3-,0       * *     *       >     >               T1             1
11.717 1-,0     * *                                                  2   2

          SUM   0   1   3   2   0   0   0   2   3   5   0   0   0
                  4   0   0   1   0   1   0   0   0  11   0   0   2

                                                          FULL SUM   31
```

decay strength of the three represented T = 1 excited states (from the total of 22) is about 30 % of the full E1 strength, in accordance with isospin selection rules.

TABLE 6

DECAY TABLE M1 TRANSITIONS (0.100E+01 W.U. <> 10)

	1 2	3 4	5 6	7 8	9 10	11 12	13 14	15 16	17 18	19 20	21 22	23 24	25 26	SUM
8.328 1+,0	:													0
10.669 3+,0										T1				1
10.901 1+,1	T2													2
11.445 1+,1	T8													8
12.291 2+,0										T1T2				3
12.331 1+,1	T1		T>		T1									2
12.542 3+,1						T2T1								3
12.664 4-,1								T3						3
12.917 2+,1									T1					1
13.248 5-,1											T7			7
SUM	11	0	0	0	1	2	0	3	1	2	0	0	0	
	0	0	0	0	0	1	0	0	0	2	7	0	0	

FULL SUM 30

6.2 — *M1 transitions*

Most of the pure M1 transitions have $\Delta T = 1$ (see subsection 4.1). However, it is remarkable (table 6) that two of the T = 0 excited states (from a total of 10) contribute with about 15 % to the full M1 strength, corresponding once again to transitions to the levels at 9.316 and 9.381 MeV. Besides. 35 % of the full M1 strength correspond to transitions to g.s., in comparison with 65 % corresponding to levels with excitation energy higher than 7 MeV.

6.3 — *E2 transitions*

The E2 strength is mainly concentrated in the g.s. rotational band (0 — 1.779 MeV — 4.617 MeV): 40 % of the full E2 strength or even more if we consider also the decay of the fourth member of the band (8.543 MeV). There are, however, two strong E2 transitions to highly excited states (13.173 MeV → 9.702 MeV and 13.427 MeV → 10.418 MeV), which, by themselves, contribute with about

30 % to the full E2 strength. There has been an intense search (e.g., ref. [10] and references therein) for a second rotational band in ^{28}Si. As can be seen from table 7, there is no clear evidence of this.

TABLE 7

DECAY TABLE E2 TRANSITIONS (0.250E+02 W.U. <> 10)

	1	3	5	7	9	11	13	15	17	19	21	23	25	
	2	4	6	8	10	12	14	16	18	20	22	24	26	SUM
1.779 2+,0	5													5
4.618 4+,0		9												9
4.979 0+,0		4												4
6.691 0+,0		>												0
6.889 4+,0		>												0
7.381 2+,0	>													0
7.417 2+,0	>		2											2
8.259 2+,0	*	>	1											1
9.702 5-,0				*										0
12.072 2+,0	*	*			>									0
12.195 3-,0														1
12.291 2+,0				>										0
12.439 2+,0	*	*												0
12.475 4+,0		>												0
12.552 4+,0		*				>	>		>	>				0
12.726 2+,0	>		>											0
12.817 4+,0		:							>					0
12.855 4+,0		*												0
12.901 2+,0	*		>		>									0
12.917 2+,1		T	1											1
12.924 2+,1		T	>											0
13.034 2+,0			>		>									0
13.104 2+,0	*													0
13.173 3-,0											2			2
13.417 1-,0				>										0
13.427 5+,0									>			9		9
13.806 2+,0		>												0
13.973 2+,0		>												0
SUM	5	2	0	0	0	0	0	0	0	0	0	0	0	
	13	3	0	0	0	0	0	0	1	0	2	9	0	

FULL SUM 35

7 — CONCLUSIONS

The isospin selection rules for dipole transitions in self-conjugate nuclei seen well verified in ^{28}Si. However, the results obtained show a certain amount of isospin admixture. Hindrance factors of 9 ± 2 and (at least) 45 ± 30 were obtained for electric and magnetic radiation, respectively. The E2/M1 mixing-ratios are affected by the isospin selection rules, the average value for $\Delta T = 0$ transitions being about (at least) six times greater than the corresponding value for $\Delta T = 1$ transitions. On the other hand, an upper limit of 0.3 was obtained for the expected absolute value of this last quantity.

Reliable upper limits of transition strengths were obtained for several types of electromagnetic transitions in ^{28}Si, on the basis of a quantitative criterion, and qualitative estimates were suggested for other types. Possible spins and parities of some levels of ^{28}Si with unknown J^{π} could be restricted to a smaller number than previously by considering those upper limits.

It is a pleasure to thank Dr. C. M. da Silva for the stimulating discussions at the beginning of this work. It must be stressed that this work would not have been possible without the cooperation and friendship of J. D. Cunha.

REFERENCES

[1] B. T. LAWERGREN, *Nucl. Phys.* **A111** (1968) 652.

[2] E. K. WARBURTON and J. WENESER, in *Isospin* in *Nuclear Physic*, ed. by D. H. WILKINSON (Amsterdam: North Holland Publishing Company, 1969) ch. 5.

[3] W. M. MACDONALD, in *Nuclear Spectroscopy*, part B, ed. by F. Ajzenberg-Selove (New York: Academic Press, 1960) ch. V. H.

[4] D. H. WILKINSON, *ibid.* ch. V. F.

[5] S. J. SKORKA, J. HERTEL and T. W. RETZ-SCHMIDT, *Nucl. Data Section A*, Vol. 2 (1966) 347.

[6] P. M. ENDT and C. VAN DER LEUN, *Nucl. Phys.* **A235** (1974) 27; P. M. ENDT and C. VAN DER LEUN, *Atomic Data and Nucl. Data Tables* 13 (1974) 67.

[7] A. TVETER, *Nucl. Phys.* **A185** (1972) 433.

[8] M. A. MEYER, I. VENTER and D. REITMANN, *Nucl. Phys.* **A250** (1975) 235.

[9] P. M. ENDT and C. VAN DER LEUN, *Nucl. Phys.* **A214** (1973) 1.

[10] J. P. GONIDEC, *Thesis* (1972), Louis Pasteur University. Strasbourg.

[11] S. T. LAM, A. E. LITHERLAND and R. E. AZUMA, *Can. J. Phys.* **49** (1971) 685.

[12] I. FORSBLOM, *Comment. Phys. Math.* **40** (1970) 65.

[13] P. B. LYONS, J. W. TOEVS and D. G. SARGOOD, *Nucl. Phys.* **A130** (1969) 1.

[14] J. D. CUNHA, P. M. CORREA and C. M. DA SILVA, *Portgal. Phys.* **9** (1975) 85.

[15] A. HUCK, P. BAUMANN and G. WALTER, *J. de Phys.* **31** (1970) 869.

[16] C. M. DA SILVA and J. D. CUNHA, *Proc. of the Internat. Conf. on Nucl. Phys.* (Munich, 1973), Vol. 1, ed. by J. de Boer and H. J. Mang (Amsterdam: North Holland Publishing Company, 1973, pg. 575.

TABLE 8

ELECTROMAGNETIC TRANSITION RATES (WU)

NUCLEUS [28;14]SI

```
 1.779 2+,0     TO:
 0.000 0+,0 DT=0  E2 0.130E+02 +- 0.58E+00

 4.618 4+,0     TO:
 1.779 2+,0 DT=0  E2 0.214E+02 +- 0.37E+01  M3 0.191E+08 +- 0.34E+07

 4.979 0+,0     TO:
 1.779 2+,0 DT=0  E2 0.105E+02 +- 0.23E+01

 6.276 3+,0     TO:
 1.779 2+,0 DT=0  M1 0.266E-03 +- 0.27E-04  E2 0.662E-01 +- 0.66E-02
 4.618 4+,0 DT=0  M1 0.430E-03 +- 0.52E-04  E2 0.788E+00 +- 0.95E-01

 6.691 0+,0     TO:
 1.779 2+,0 DT=0  E2 0.552E+00 +- 0.14E+00

 6.879 3-,0     TO:
 0.000 0+,0 DT=0  E3 0.128E+02 +- 0.16E+01
 1.779 2+,0 DT=0  E1 0.104E-05 +- 0.14E-06  M2 0.182E+00 +- 0.25E-01
 4.618 4+,0 DT=0  E1 0.109E-05 +- 0.29E-06  M2 0.966E+00 +- 0.26E+00

 6.889 4+,0     TO:
 1.779 2+,0 DT=0  E2 0.101E+01 +- 0.20E+00  M3 0.278E+06 +- 0.56E+05

 7.381 2+,0     TO:
 0.000 0+,0 DT=0  E2 0.338E+00 +- 0.86E-01
 1.779 2+,0 DT=0  M1 0.139E-01 +- 0.35E-02  E2 0.224E+01 +- 0.56E+00

 7.417 2+,0     TO:
 0.000 0+,0 DT=0  E2 0.244E+00 +- 0.47E-01
 1.779 2+,0 DT=0  M1 0.202E-03 +- 0.14E-03  E2 0.320E-01 +- 0.23E-01
 4.979 0+,0 DT=0  E2 0.494E+01 +- 0.17E+01

 7.799 3+,0     TO:
 1.779 2+,0 DT=0  M1 0.503E-03 +- 0.88E-04  E2 0.699E-01 +- 0.12E-01
 4.618 4+,0 DT=0  M1 0.487E-04 +- 0.22E-04  E2 0.243E-01 +- 0.11E-01
 6.276 3+,0 DT=0  M1 0.129E-01 +- 0.23E-02  E2 0.280E+02 +- 0.50E+01

 7.933 2+,0     TO:
 0.000 0+,0 DT=0  E2 0.458E+00 +- 0.31E+00
 1.779 2+,0 DT=0  M1 0.672E-03 +- 0.57E-03  E2 0.895E-01 +- 0.76E-01
 4.618 4+,0 DT=0  E2 0.342E+01 +- 0.24E+01  M3 0.224E+07 +- 0.16E+07
 4.979 0+,0 DT=0  E2 0.445E+01 +- 0.33E+01

 8.259 2+,0     TO:
 0.000 0+,0 DT=0  E2 0.142E-01 +- 0.55E-02
 1.779 2+,0 DT=0  M1 0.310E-02 +- 0.11E-02  E2 0.372E+00 +- 0.13E+00
 4.618 4+,0 DT=0  E2 0.380E+00 +- 0.17E+00  M3 0.206E+06 +- 0.90E+05
 4.979 0+,0 DT=0  E2 0.272E+01 +- 0.96E+00

 8.328 1+,0     TO:
 0.000 0+,0 DT=0  M1 0.103E-03 +- 0.21E-04
 1.779 2+,0 DT=0  M1 0.822E-04 +- 0.20E-04  E2 0.966E-02 +- 0.24E-02
```

TABLE 8 *(continuation)*

```
 8.413 4-,0     TO:
 1.779 2+,0 DT=0   M2 0.204E+00 +- 0.54E-01   E3 0.355E+02 +- 0.95E+01
 4.618 4+,0 DT=0   E1 0.192E-05 +- 0.88E-06   M2 0.605E+00 +- 0.28E+00
 6.879 3-,0 DT=0   M1 0.161E-01 +- 0.40E-02   E2 0.344E+02 +- 0.87E+01

 8.543 6+,0     TO:
 4.618 4+,0 DT=0   E2 0.130E+02 +- 0.10E+02   M3 0.610E+07 +- 0.47E+07

 8.589 3+,0     TO:
 1.779 2+,0 DT=0   M1 0.186E-01 +- 0.75E-02   E2 0.202E+01 +- 0.81E+00
 6.276 3+,0 DT=0   M1 0.319E-01 +- 0.17E-01   E2 0.301E+02 +- 0.16E+02

 8.904 1-,0     TO:
 0.000 0+,0 DT=0   E1 0.635E-04 +- 0.18E-04
 1.779 2+,0 DT=0   E1 0.140E-03 +- 0.39E-04   M2 0.125E+02 +- 0.35E+01

 9.316 3+,1     TO:
 1.779 2+,0 DT=1   M1 0.532E-02 +- 0.27E-02   E2 0.472E+00 +- 0.24E+00
 6.276 3+,0 DT=1   M1 0.305E-01 +- 0.15E-01   E2 0.166E+02 +- 0.83E+01

 9.381 2+,1     TO:
 0.000 0+,0 DT=1   E2 0.870E-02 +- 0.73E-02
 1.779 2+,0 DT=1   M1 0.134E-01 +- 0.81E-02   E2 0.117E+01 +- 0.70E+00
 6.276 3+,0 DT=1   M1 0.838E-02 +- 0.56E-02   E2 0.438E+01 +- 0.29E+01

 9.702 5-,0     TO:
 1.779 2+,0 DT=0   E3 0.233E+00 +- 0.12E+00   M4 0.406E+05 +- 0.20E+05
 4.618 4+,0 DT=0   E1 0.150E-06 +- 0.75E-07   M2 0.263E-01 +- 0.13E-01
 6.879 3-,0 DT=0   E2 0.253E-01 +- 0.13E-01   M3 0.229E+05 +- 0.12E+05
 6.889 4+,0 DT=0   E1 0.413E-06 +- 0.21E-06   M2 0.236E+00 +- 0.12E+00
 8.413 4-,0 DT=0   M1 0.823E-03 +- 0.41E-03   E2 0.250E+01 +- 0.13E+01

10.180 3-,0     TO:
 1.779 2+,0 DT=0   E1 0.443E-04 +- 0.20E-04   M2 0.284E+01 +- 0.13E+01
 4.618 4+,0 DT=0   E1 0.458E-03 +- 0.19E-03   M2 0.671E+02 +- 0.27E+02

10.418 3+,0     TO:
 4.618 4+,0 DT=0   M1 0.892E-03 +- 0.41E-03   E2 0.134E+00 +- 0.61E-01
 6.276 3+,0 DT=0   M1 0.139E-01 +- 0.42E-02   E2 0.408E+01 +- 0.12E+01

10.669 3+,0     TO:
 1.779 2+,0 DT=0   M1 0.122E-03 +- 0.58E-04   E2 0.776E-02 +- 0.37E-02
 6.276 3+,0 DT=0   M1 0.387E-02 +- 0.15E-02   E2 0.101E+01 +- 0.40E+00
 7.933 2+,0 DT=0   M1 0.626E-02 +- 0.25E-02   E2 0.422E+01 +- 0.17E+01
 8.589 3+,0 DT=0   M1 0.111E-01 +- 0.48E-02   E2 0.129E+02 +- 0.56E+01
 9.316 3+,1 DT=1   M1 0.115E+00 +- 0.39E-01   E2 0.317E+03 +- 0.11E+03
 9.381 2+,1 DT=1   M1 0.333E-01 +- 0.18E-01   E2 0.101E+03 +- 0.53E+02

10.901 1+,1     TO:
 0.000 0+,0 DT=1   M1 0.229E+00 +- 0.30E-01
 1.779 2+,0 DT=1   M1 0.184E+00 +- 0.29E-01   E2 0.111E+02 +- 0.17E+01

11.445 1+,1     TO:
 0.000 0+,0 DT=1   M1 0.774E+00 +- 0.86E-01

12.072 2+,0     TO:
 0.000 0+,0 DT=0   E2 0.711E-01 +- 0.23E-01
 1.779 2+,0 DT=0   M1 0.844E-03 +- 0.27E-03   E2 0.401E-01 +- 0.13E-01
 4.618 4+,0 DT=0   E2 0.403E-01 +- 0.15E-01   M3 0.523E+04 +- 0.19E+04
 4.979 0+,0 DT=0   E2 0.148E-01 +- 0.89E-02
```

TABLE 8 *(continuation)*

6.276	3+,0	DT=0	M1	0.979E-03	+-	0.36E-03	E2	0.147E+00	+-	0.54E-01
6.889	4+,0	DT=0	E2	0.620E+00	+-	0.23E+00	M3	0.166E+06	+-	0.61E+05
7.381	2+,0	DT=0	M1	0.509E-03	+-	0.31E-03	E2	0.117E+00	+-	0.71E-01
7.417	2+,0	DT=0	M1	0.111E-02	+-	0.67E-03	E2	0.258E+00	+-	0.16E+00
7.799	3+,0	DT=0	M1	0.160E-02	+-	0.97E-03	E2	0.442E+00	+-	0.27E+00
7.933	2+,0	DT=0	M1	0.148E-02	+-	0.90E-03	E2	0.436E+00	+-	0.26E+00
8.259	2+,0	DT=0	M1	0.178E-02	+-	0.11E-02	E2	0.616E+00	+-	0.37E+00
8.589	3+,0	DT=0	M1	0.264E-02	+-	0.16E-02	E2	0.110E+01	+-	0.66E+00
9.316	3+,1	DT=1	M1	0.157E-02	+-	0.95E-03	E2	0.104E+01	+-	0.63E+00
9.381	2+,1	DT=1	M1	0.472E-02	+-	0.29E-02	E2	0.329E+01	+-	0.20E+01
12.195	3-,0	TO:								
0.000	0+,0	DT=0	E3	0.105E+01	+-	0.55E+00				
1.779	2+,0	DT=0	E1	0.780E-03	+-	0.14E-03	M2	0.326E+02	+-	0.59E+01
4.618	4+,0	DT=0	E1	0.416E-03	+-	0.76E-04	M2	0.329E+02	+-	0.60E+01
6.276	3+,0	DT=0	E1	0.873E-04	+-	0.46E-04	M2	0.113E+02	+-	0.60E+01
6.879	3-,0	DT=0	M1	0.840E-02	+-	0.21E-02	E2	0.150E+01	+-	0.38E+00
6.889	4+,0	DT=0	E1	0.113E-03	+-	0.60E-04	M2	0.182E+02	+-	0.96E+01
7.933	2+,0	DT=0	E1	0.780E-04	+-	0.41E-04	M2	0.195E+02	+-	0.10E+02
8.259	2+,0	DT=0	E1	0.139E-03	+-	0.73E-04	M2	0.406E+02	+-	0.21E+02
8.413	4-,0	DT=0	M1	0.800E-02	+-	0.42E-02	E2	0.282E+01	+-	0.15E+01
8.904	1-,0	DT=0	E2	0.282E+01	+-	0.15E+01	M3	0.188E+07	+-	0.99E+06
9.316	3+,1	DT=1	E1	0.152E-03	+-	0.80E-04	M2	0.830E+02	+-	0.44E+02
9.381	2+,1	DT=1	E1	0.119E-02	+-	0.30E-03	M2	0.683E+03	+-	0.17E+03
12.217	2-,0	TO:								
0.000	0+,0	DT=0	M2	0.234E+00	+-	0.85E-01				
1.779	2+,0	DT=0	E1	0.258E-03	+-	0.82E-04	M2	0.107E+02	+-	0.34E+01
6.276	3+,0	DT=0	E1	0.128E-03	+-	0.47E-04	M2	0.164E+02	+-	0.60E+01
6.879	3-,0	DT=0	M1	0.175E-02	+-	0.11E-02	E2	0.310E+00	+-	0.19E+00
7.417	2+,0	DT=0	E1	0.127E-03	+-	0.46E-04	M2	0.250E+02	+-	0.91E+01
7.933	2+,0	DT=0	E1	0.495E-03	+-	0.18E-03	M2	0.122E+03	+-	0.45E+02
8.259	2+,0	DT=0	E1	0.165E-03	+-	0.99E-04	M2	0.476E+02	+-	0.29E+02
8.328	1+,0	DT=0	E1	0.108E-03	+-	0.65E-04	M2	0.325E+02	+-	0.20E+02
8.413	4-,0	DT=0	E2	0.964E+00	+-	0.58E+00	M3	0.480E+06	+-	0.29E+06
8.589	3+,0	DT=0	E1	0.401E-03	+-	0.15E-03	M2	0.138E+03	+-	0.50E+02
8.904	1-,0	DT=0	M1	0.210E-02	+-	0.13E-02	E2	0.962E+00	+-	0.58E+00
9.316	3+,1	DT=1	E1	0.523E-03	+-	0.31E-03	M2	0.282E+03	+-	0.17E+03
9.381	2+,1	DT=1	E1	0.783E-02	+-	0.25E-02	M2	0.441E+04	+-	0.14E+04
12.240	3+,0	TO:								
0.000	0+,0	DT=0	M3	0.600E+01	+-	0.36E+01				
1.779	2+,0	DT=0	M1	0.256E-02	+-	0.81E-03	E2	0.118E+00	+-	0.37E-01
4.618	4+,0	DT=0	M1	0.399E-02	+-	0.13E-02	E2	0.347E+00	+-	0.11E+00
6.889	4+,0	DT=0	M1	0.622E-03	+-	0.37E-03	E2	0.109E+00	+-	0.66E-01
7.381	2+,0	DT=0	M1	0.474E-03	+-	0.29E-03	E2	0.101E+00	+-	0.61E-01
7.417	2+,0	DT=0	M1	0.127E-01	+-	0.40E-02	E2	0.276E+01	+-	0.88E+00
7.933	2+,0	DT=0	M1	0.511E-03	+-	0.31E-03	E2	0.139E+00	+-	0.84E-01
8.413	4-,0	DT=0	E1	0.366E-04	+-	0.22E-04	M2	0.113E+02	+-	0.68E+01
8.589	3+,0	DT=0	M1	0.419E-03	+-	0.25E-03	E2	0.159E+00	+-	0.95E-01
9.480	2+,0	DT=0	M1	0.971E-03	+-	0.58E-03	E2	0.642E+00	+-	0.39E+00
12.291	2+,0	TO:								
0.000	0+,0	DT=0	E2	0.145E-02	+-	0.87E-03				
1.779	2+,0	DT=0	M1	0.683E-02	+-	0.21E-02	E2	0.312E+00	+-	0.97E-01
4.618	4+,0	DT=0	E2	0.123E-01	+-	0.73E-02	M3	0.150E+04	+-	0.90E+03
4.979	0+,0	DT=0	E2	0.508E-01	+-	0.30E-01				
6.276	3+,0	DT=0	M1	0.231E-02	+-	0.83E-03	E2	0.321E+00	+-	0.12E+00
6.691	0+,0	DT=0	E2	0.356E+00	+-	0.13E+00				
7.933	2+,0	DT=0	M1	0.176E-02	+-	0.11E-02	E2	0.467E+00	+-	0.28E+00

TABLE 8 *(continuation)*

8.328	1+,0	DT=0	M1	0.156E-02	+-	0.93E-03	E2	0.501E+00	+-	0.30E+00
8.589	3+,0	DT=0	M1	0.223E-02	+-	0.13E-02	E2	0.822E+00	+-	0.49E+00
9.316	3+,1	DT=1	M1	0.603E-01	+-	0.22E-01	E2	0.343E+02	+-	0.12E+02
9.381	2+,1	DT=1	M1	0.204E+00	+-	0.64E-01	E2	0.121E+03	+-	0.38E+02
2.295	3+,0	TO:								
1.779	2+,0	DT=0	M1	0.120E-01	+-	0.40E-02	E2	0.545E+00	+-	0.18E+00
4.618	4+,0	DT=0	M1	0.758E-02	+-	0.26E-02	E2	0.648E+00	+-	0.22E+00
6.889	4+,0	DT=0	M1	0.723E-03	+-	0.45E-03	E2	0.125E+00	+-	0.77E-01
7.381	2+,0	DT=0	M1	0.369E-02	+-	0.14E-02	E2	0.771E+00	+-	0.30E+00
7.417	2+,0	DT=0	M1	0.377E-02	+-	0.14E-02	E2	0.800E+00	+-	0.31E+00
7.799	3+,0	DT=0	M1	0.147E-02	+-	0.90E-03	E2	0.366E+00	+-	0.23E+00
7.933	2+,0	DT=0	M1	0.689E-03	+-	0.42E-03	E2	0.182E+00	+-	0.11E+00
8.328	1+,0	DT=0	E2	0.293E+00	+-	0.18E+00	M3	0.134E+06	+-	0.83E+05
9.316	3+,1	DT=1	M1	0.144E-01	+-	0.89E-02	E2	0.818E+01	+-	0.50E+01
9.381	2+,1	DT=1	M1	0.385E-02	+-	0.24E-02	E2	0.228E+01	+-	0.14E+01
12.331	1+,1	TO:								
0.000	0+,0	DT=1	M1	0.603E-01	+-	0.19E-01				
1.779	2+,0	DT=1	M1	0.809E-02	+-	0.30E-02	E2	0.366E+00	+-	0.14E+00
6.691	0+,0	DT=1	M1	0.269E-01	+-	0.10E-01				
7.381	2+,0	DT=1	M1	0.118E+00	+-	0.44E-01	E2	0.243E+02	+-	0.93E+01
7.417	2+,0	DT=1	M1	0.127E-01	+-	0.77E-02	E2	0.265E+01	+-	0.16E+01
7.933	2+,0	DT=1	M1	0.496E-01	+-	0.18E-01	E2	0.129E+02	+-	0.48E+01
8.328	1+,0	DT=1	M1	0.353E-01	+-	0.21E-01	E2	0.111E+02	+-	0.67E+01
12.439	2+,0	TO:								
0.000	0+,0	DT=0	E2	0.345E-01	+-	0.12E-01				
1.779	2+,0	DT=0	M1	0.112E-03	+-	0.43E-04	E2	0.497E-02	+-	0.19E-02
4.618	4+,0	DT=0	E2	0.173E-01	+-	0.67E-02	M3	0.204E+04	+-	0.78E+03
6.276	3+,0	DT=0	M1	0.177E-03	+-	0.11E-03	E2	0.234E-01	+-	0.14E-01
6.889	4+,0	DT=0	E2	0.396E-01	+-	0.24E-01	M3	0.926E+04	+-	0.57E+04
7.417	2+,0	DT=0	M1	0.932E-04	+-	0.57E-04	E2	0.186E-01	+-	0.11E-01
7.799	3+,0	DT=0	M1	0.166E-02	+-	0.64E-03	E2	0.387E+00	+-	0.15E+00
7.933	2+,0	DT=0	M1	0.194E-03	+-	0.12E-03	E2	0.481E-01	+-	0.30E-01
8.328	1+,0	DT=0	M1	0.255E-03	+-	0.16E-03	E2	0.760E-01	+-	0.47E-01
9.316	3+,1	DT=1	M1	0.107E-01	+-	0.36E-02	E2	0.551E+01	+-	0.19E+01
9.381	2+,1	DT=1	M1	0.929E-03	+-	0.57E-03	E2	0.501E+00	+-	0.31E+00
12.475	4+,0	TO:								
1.779	2+,0	DT=0	E2	0.572E+00	+-	0.18E+00	M3	0.360E+05	+-	0.12E+05
4.618	4+,0	DT=0	M1	0.720E-03	+-	0.43E-03	E2	0.588E-01	+-	0.36E-01
6.276	3+,0	DT=0	M1	0.733E-03	+-	0.44E-03	E2	0.961E-01	+-	0.58E-01
7.381	2+,0	DT=0	E2	0.770E-01	+-	0.46E-01	M3	0.214E+05	+-	0.13E+05
7.417	2+,0	DT=0	E2	0.186E+00	+-	0.11E+00	M3	0.524E+05	+-	0.32E+05
7.799	3+,0	DT=0	M1	0.239E-02	+-	0.14E-02	E2	0.551E+00	+-	0.33E+00
7.933	2+,0	DT=0	E2	0.455E+00	+-	0.27E+00	M3	0.159E+06	+-	0.96E+05
8.259	2+,0	DT=0	E2	0.727E+00	+-	0.44E+00	M3	0.295E+06	+-	0.18E+06
8.589	3+,0	DT=0	M1	0.595E-03	+-	0.36E-03	E2	0.199E+00	+-	0.12E+00
9.316	3+,1	DT=1	M1	0.166E-02	+-	0.10E-02	E2	0.839E+00	+-	0.51E+00
12.489	3-,0	TO:								
0.000	0+,0	DT=0	E3	0.100E+01	+-	0.60E+00				
1.779	2+,0	DT=0	E1	0.267E-03	+-	0.85E-04	M2	0.106E+02	+-	0.34E+01
4.618	4+,0	DT=0	E1	0.266E-03	+-	0.85E-04	M2	0.195E+02	+-	0.62E+01
6.276	3+,0	DT=0	E1	0.200E-03	+-	0.73E-04	M2	0.234E+02	+-	0.86E+01
6.879	3-,0	DT=0	M1	0.185E-01	+-	0.59E-02	E2	0.296E+01	+-	0.94E+00
7.381	2+,0	DT=0	E1	0.154E-03	+-	0.56E-04	M2	0.267E+02	+-	0.98E+01
8.413	4-,0	DT=0	M1	0.723E-02	+-	0.26E-02	E2	0.219E+01	+-	0.80E+00
9.381	2+,1	DT=1	E1	0.797E-03	+-	0.29E-03	M2	0.374E+03	+-	0.14E+03

TABLE 8 *(continuation)*

(5)

12.542	3+,1		T0:								
1.779	2+,0	DT=1	M1	0.125E+00	+-	0.42E-01	E2	0.545E+01	+-	0.18E+01	
4.618	4+,0	DT=1	M1	0.208E-01	+-	0.80E-02	E2	0.167E+01	+-	0.64E+00	
6.276	3+,0	DT=1	M1	0.206E-01	+-	0.79E-02	E2	0.264E+01	+-	0.10E+01	
6.879	3-,0	DT=1	E1	0.233E-03	+-	0.14E-03	M2	0.330E+02	+-	0.20E+02	
6.889	4+,0	DT=1	M1	0.350E-02	+-	0.22E-02	E2	0.552E+00	+-	0.34E+00	
7.799	3+,0	DT=1	M1	0.192E+00	+-	0.74E-01	E2	0.430E+02	+-	0.17E+02	
7.933	2+,0	DT=1	M1	0.905E-01	+-	0.35E-01	E2	0.215E+02	+-	0.83E+01	
8.589	3+,0	DT=1	M1	0.102E-01	+-	0.63E-02	E2	0.330E+01	+-	0.20E+01	
9.480	2+,0	DT=1	M1	0.955E-01	+-	0.59E-01	E2	0.513E+02	+-	0.32E+02	
12.552	4+,0		T0:								
1.779	2+,0	DT=0	E2	0.612E-01	+-	0.20E-01	M3	0.380E+04	+-	0.12E+04	
4.618	4+,0	DT=0	M1	0.138E-03	+-	0.51E-04	E2	0.110E-01	+-	0.41E-02	
6.276	3+,0	DT=0	M1	0.534E-03	+-	0.20E-03	E2	0.684E-01	+-	0.25E-01	
6.889	4+,0	DT=0	M1	0.379E-03	+-	0.14E-03	E2	0.595E-01	+-	0.22E-01	
7.381	2+,0	DT=0	E2	0.150E+00	+-	0.56E-01	M3	0.404E+05	+-	0.15E+05	
7.417	2+,0	DT=0	E2	0.388E+00	+-	0.14E+00	M3	0.106E+06	+-	0.39E+05	
7.799	3+,0	DT=0	M1	0.102E-03	+-	0.62E-04	E2	0.229E-01	+-	0.14E-01	
7.933	2+,0	DT=0	E2	0.343E+00	+-	0.13E+00	M3	0.116E+06	+-	0.43E+05	
8.259	2+,0	DT=0	E2	0.304E+00	+-	0.11E+00	M3	0.119E+06	+-	0.44E+05	
9.316	3+,1	DT=1	M1	0.893E-03	+-	0.54E-03	E2	0.430E+00	+-	0.26E+00	
12.664	4-,1		T0:								
1.779	2+,0	DT=1	M2	0.936E-01	+-	0.57E-01	E3	0.606E+01	+-	0.37E+01	
4.618	4+,0	DT=1	E1	0.242E-04	+-	0.15E-04	M2	0.170E+01	+-	0.10E+01	
6.276	3+,0	DT=1	E1	0.175E-02	+-	0.56E-03	M2	0.195E+03	+-	0.63E+02	
6.879	3-,0	DT=1	M1	0.170E-02	+-	0.10E-02	E2	0.256E+00	+-	0.15E+00	
6.889	4+,0	DT=1	E1	0.409E-03	+-	0.15E-03	M2	0.557E+02	+-	0.21E+02	
8.413	4-,0	DT=1	M1	0.276E+00	+-	0.89E-01	E2	0.769E+02	+-	0.25E+02	
8.589	3+,0	DT=1	E1	0.326E-02	+-	0.10E-02	M2	0.891E+03	+-	0.29E+03	
9.702	5-,0	DT=1	M1	0.272E-01	+-	0.16E-01	E2	0.156E+02	+-	0.94E+01	
12.726	2+,0		T0:								
0.000	0+,0	DT=0	E2	0.127E+00	+-	0.39E-01					
1.779	2+,0	DT=0	M1	0.234E-02	+-	0.71E-03	E2	0.983E-01	+-	0.30E-01	
4.979	0+,0	DT=0	E2	0.145E+00	+-	0.51E-01					
6.276	3+,0	DT=0	M1	0.646E-03	+-	0.38E-03	E2	0.783E-01	+-	0.46E-01	
6.879	3-,0	DT=0	E1	0.536E-04	+-	0.19E-04	M2	0.711E+01	+-	0.25E+01	
7.381	2+,0	DT=0	M1	0.349E-03	+-	0.21E-03	E2	0.616E-01	+-	0.37E-01	
7.933	2+,0	DT=0	M1	0.727E-03	+-	0.43E-03	E2	0.159E+00	+-	0.95E-01	
8.259	2+,0	DT=0	M1	0.299E-03	+-	0.18E-03	E2	0.756E-01	+-	0.45E-01	
8.589	3+,0	DT=0	M1	0.942E-03	+-	0.56E-03	E2	0.277E+00	+-	0.16E+00	
9.316	3+,1	DT=1	M1	0.773E-02	+-	0.27E-02	E2	0.335E+01	+-	0.12E+01	
9.381	2+,1	DT=1	M1	0.107E-02	+-	0.63E-03	E2	0.481E+00	+-	0.29E+00	
12.742	3-,1		T0:								
0.000	0+,0	DT=1	E3	0.814E+00	+-	0.50E+00					
1.779	2+,0	DT=1	E1	0.968E-04	+-	0.33E-04	M2	0.365E+01	+-	0.12E+01	
6.276	3+,0	DT=1	E1	0.637E-03	+-	0.22E-03	M2	0.691E+02	+-	0.23E+02	
6.879	3-,0	DT=1	M1	0.217E-01	+-	0.74E-02	E2	0.319E+01	+-	0.11E+01	
7.417	2+,0	DT=1	E1	0.127E-03	+-	0.49E-04	M2	0.203E+02	+-	0.78E+01	
7.799	3+,0	DT=1	E1	0.169E-03	+-	0.65E-04	M2	0.314E+02	+-	0.12E+02	
7.933	2+,0	DT=1	E1	0.402E-03	+-	0.15E-03	M2	0.787E+02	+-	0.30E+02	
8.413	4-,0	DT=1	M1	0.258E-02	+-	0.16E-02	E2	0.695E+00	+-	0.43E+00	
8.589	3+,0	DT=1	E1	0.232E-03	+-	0.89E-04	M2	0.609E+02	+-	0.23E+02	
9.316	3+,1	DT=0	E1	0.571E-03	+-	0.22E-03	M2	0.221E+03	+-	0.85E+02	
9.381	2+,1	DT=0	E1	0.571E-03	+-	0.22E-03	M2	0.229E+03	+-	0.88E+02	
9.702	5-,0	DT=1	E2	0.370E+01	+-	0.23E+01	M3	0.288E+07	+-	0.18E+07	

TABLE 8 *(continuation)*

10.180	3-,0	DT=1	M1	0.453E-02	+-	0.28E-02	E2	0.348E+01	+-	0.21E+01	
12.802	3-,0	TO:									
0.000	0+,0	DT=0	E3	0.115E+01	+-	0.71E+00					
1.779	2+,0	DT=0	E1	0.286E-03	+-	0.96E-04	M2	0.107E+02	+-	0.36E+01	
4.618	4+,0	DT=0	E1	0.835E-04	+-	0.32E-04	M2	0.565E+01	+-	0.21E+01	
6.276	3+,0	DT=0	E1	0.403E-04	+-	0.25E-04	M2	0.429E+01	+-	0.26E+01	
6.879	3-,0	DT=0	M1	0.470E-01	+-	0.16E-01	E2	0.675E+01	+-	0.23E+01	
6.889	4+,0	DT=0	E1	0.122E-03	+-	0.46E-04	M2	0.158E+02	+-	0.60E+01	
7.417	2+,0	DT=0	E1	0.419E-03	+-	0.16E-03	M2	0.655E+02	+-	0.25E+02	
8.413	4-,0	DT=0	M1	0.825E-02	+-	0.31E-02	E2	0.216E+01	+-	0.82E+00	
9.316	3+,1	DT=1	E1	0.221E-03	+-	0.14E-03	M2	0.823E+02	+-	0.50E+02	
9.381	2+,1	DT=1	E1	0.303E-03	+-	0.19E-03	M2	0.117E+03	+-	0.72E+02	
12.817	4+,0	TO:									
1.779	2+,0	DT=0	E2	0.132E-02	+-	0.48E-03	M3	0.784E+02	+-	0.28E+02	
4.618	4+,0	DT=0	M1	0.817E-03	+-	0.26E-03	E2	0.613E-01	+-	0.19E-01	
6.276	3+,0	DT=0	M1	0.147E-03	+-	0.53E-04	E2	0.173E-01	+-	0.63E-02	
6.889	4+,0	DT=0	M1	0.197E-02	+-	0.62E-03	E2	0.283E+00	+-	0.89E-01	
8.543	6+,0	DT=0	E2	0.208E+00	+-	0.75E-01	M3	0.819E+05	+-	0.30E+05	
8.589	3+,0	DT=0	M1	0.570E-02	+-	0.18E-02	E2	0.161E+01	+-	0.51E+00	
12.855	4+,0	TO:									
1.779	2+,0	DT=0	E2	0.102E+00	+-	0.33E-01	M3	0.598E+04	+-	0.19E+04	
4.618	4+,0	DT=0	M1	0.602E-02	+-	0.19E-02	E2	0.447E+00	+-	0.14E+00	
6.276	3+,0	DT=0	M1	0.473E-01	+-	0.15E-01	E2	0.550E+01	+-	0.18E+01	
6.879	3-,0	DT=0	E1	0.660E-04	+-	0.40E-04	M2	0.838E+01	+-	0.51E+01	
6.889	4+,0	DT=0	M1	0.792E-02	+-	0.29E-02	E2	0.112E+01	+-	0.41E+00	
7.381	2+,0	DT=0	E2	0.144E+00	+-	0.87E-01	M3	0.346E+05	+-	0.21E+05	
7.417	2+,0	DT=0	E2	0.149E+00	+-	0.90E-01	M3	0.362E+05	+-	0.22E+05	
7.799	3+,0	DT=0	M1	0.117E-01	+-	0.43E-02	E2	0.231E+01	+-	0.85E+00	
8.589	3+,0	DT=0	M1	0.686E-02	+-	0.41E-02	E2	0.190E+01	+-	0.11E+01	
9.316	3+,1	DT=1	M1	0.392E-01	+-	0.14E-01	E2	0.158E+02	+-	0.58E+01	
10.418	3+,0	DT=0	M1	0.581E-02	+-	0.35E-02	E2	0.493E+01	+-	0.30E+01	
10.668	3+,0	DT=0	M1	0.107E+00	+-	0.39E-01	E2	0.113E+03	+-	0.41E+02	
12.901	2+,0	TO:									
0.000	0+,0	DT=0	E2	0.134E-01	+-	0.38E-02					
1.779	2+,0	DT=0	M1	0.443E-02	+-	0.99E-03	E2	0.181E+00	+-	0.41E-01	
4.618	4+,0	DT=0	E2	0.197E+00	+-	0.56E-01	M3	0.207E+05	+-	0.59E+04	
6.276	3+,0	DT=0	M1	0.151E-01	+-	0.34E-02	E2	0.173E+01	+-	0.39E+00	
6.889	4+,0	DT=0	E2	0.733E+00	+-	0.21E+00	M3	0.146E+06	+-	0.42E+05	
7.417	2+,0	DT=0	M1	0.231E-02	+-	0.13E-02	E2	0.387E+00	+-	0.21E+00	
7.799	3+,0	DT=0	M1	0.574E-02	+-	0.16E-02	E2	0.111E+01	+-	0.32E+00	
7.933	2+,0	DT=0	M1	0.155E-02	+-	0.85E-03	E2	0.317E+00	+-	0.17E+00	
8.413	4-,0	DT=0	M2	0.159E+02	+-	0.87E+01	E3	0.605E+04	+-	0.33E+04	
8.589	3+,0	DT=0	M1	0.475E-02	+-	0.26E-02	E2	0.129E+01	+-	0.71E+00	
9.316	3+,1	DT=1	M1	0.248E-01	+-	0.71E-02	E2	0.973E+01	+-	0.28E+01	
9.381	2+,1	DT=1	M1	0.437E-01	+-	0.12E-01	E2	0.178E+02	+-	0.51E+01	
12.917	2+,1	TO:									
1.779	2+,0	DT=1	M1	0.150E+00	+-	0.49E-01	E2	0.609E+01	+-	0.20E+01	
4.618	4+,0	DT=1	E2	0.212E+01	+-	0.79E+00	M3	0.222E+06	+-	0.83E+05	
6.276	3+,0	DT=1	M1	0.471E-01	+-	0.19E-01	E2	0.539E+01	+-	0.20E+01	
6.889	4+,0	DT=1	E2	0.175E+01	+-	0.11E+01	M3	0.347E+06	+-	0.21E+06	
7.381	2+,0	DT=1	M1	0.814E-02	+-	0.50E-02	E2	0.134E+01	+-	0.81E+00	
7.417	2+,0	DT=1	M1	0.531E-01	+-	0.20E-01	E2	0.885E+01	+-	0.33E+01	
7.799	3+,0	DT=1	M1	0.268E-01	+-	0.16E-01	E2	0.515E+01	+-	0.31E+01	
8.259	2+,0	DT=1	M1	0.246E-01	+-	0.15E-01	E2	0.571E+01	+-	0.35E+01	
8.589	3+,0	DT=1	M1	0.988E-01	+-	0.37E-01	E2	0.266E+02	+-	0.10E+02	

TABLE 8 *(continuation)*

9.480	2+,0	DT=1	M1	0.748E-01	+-	0.46E-01	E2	0.319E+02	+-	0.19E+02
10.668	3+,0	DT=1	M1	0.243E+00	+-	0.15E+00	E2	0.242E+03	+-	0.15E+03
12.924	2+,1	TO:								
0.000	0+,0	DT=1	E2	0.306E-02	+-	0.19E-02				
1.779	2+,0	DT=1	M1	0.125E+00	+-	0.40E-01	E2	0.507E+01	+-	0.16E+01
4.618	4+,0	DT=1	E2	0.587E+00	+-	0.22E+00	M3	0.613E+05	+-	0.23E+05
6.276	3+,0	DT=1	M1	0.373E-01	+-	0.14E-01	E2	0.425E+01	+-	0.16E+01
6.691	0+,0	DT=1	E2	0.235E+00	+-	0.14E+00				
6.879	3-,0	DT=1	E1	0.166E-03	+-	0.10E-03	M2	0.206E+02	+-	0.12E+02
6.889	4+,0	DT=1	E2	0.138E+01	+-	0.83E+00	M3	0.273E+06	+-	0.17E+06
7.381	2+,0	DT=1	M1	0.386E-01	+-	0.14E-01	E2	0.633E+01	+-	0.23E+01
7.417	2+,0	DT=1	M1	0.262E-02	+-	0.16E-02	E2	0.436E+00	+-	0.26E+00
7.799	3+,0	DT=1	M1	0.130E-01	+-	0.79E-02	E2	0.250E+01	+-	0.15E+01
7.933	2+,0	DT=1	M1	0.529E-01	+-	0.20E-01	E2	0.107E+02	+-	0.39E+01
8.259	2+,0	DT=1	M1	0.324E-01	+-	0.20E-01	E2	0.750E+01	+-	0.45E+01
8.328	1+,0	DT=1	M1	0.677E-02	+-	0.41E-02	E2	0.162E+01	+-	0.98E+00
8.589	3+,0	DT=1	M1	0.296E-01	+-	0.18E-01	E2	0.793E+01	+-	0.48E+01
10.668	3+,0	DT=1	M1	0.763E-01	+-	0.46E-01	E2	0.756E+02	+-	0.46E+02
12.974	1-,0	TO:								
0.000	0+,0	DT=0	E1	0.779E-05	+-	0.40E-05				
1.779	2+,0	DT=0	E1	0.152E-05	+-	0.83E-06	M2	0.548E-01	+-	0.30E-01
4.979	0+,0	DT=0	E1	0.125E-04	+-	0.64E-05				
6.879	3-,0	DT=0	E2	0.761E-01	+-	0.42E-01	M3	0.148E+05	+-	0.81E+04
7.417	2+,0	DT=0	E1	0.124E-04	+-	0.68E-05	M2	0.182E+01	+-	0.10E+01
8.589	3+,0	DT=0	M2	0.595E+01	+-	0.33E+01	E3	0.237E+04	+-	0.13E+04
9.316	3+,1	DT=1	M2	0.147E+02	+-	0.81E+01	E3	0.844E+04	+-	0.46E+04
12.991	3-,0	TO:								
0.000	0+,0	DT=0	E3	0.514E+00	+-	0.31E+00				
1.779	2+,0	DT=0	E1	0.602E-05	+-	0.22E-05	M2	0.217E+00	+-	0.81E-01
4.618	4+,0	DT=0	E1	0.314E-04	+-	0.12E-04	M2	0.203E+01	+-	0.76E+00
6.276	3+,0	DT=0	E1	0.110E-04	+-	0.67E-05	M2	0.110E+01	+-	0.67E+00
6.879	3-,0	DT=0	M1	0.224E-02	+-	0.84E-03	E2	0.303E+00	+-	0.11E+00
7.799	3+,0	DT=0	E1	0.107E-03	+-	0.40E-04	M2	0.180E+02	+-	0.67E+01
7.933	2+,0	DT=0	E1	0.713E-05	+-	0.43E-05	M2	0.126E+01	+-	0.77E+00
8.413	4-,0	DT=0	M1	0.253E-02	+-	0.94E-03	E2	0.608E+00	+-	0.23E+00
8.589	3+,0	DT=0	E1	0.169E-03	+-	0.63E-04	M2	0.395E+02	+-	0.15E+02
9.316	3+,1	DT=1	E1	0.193E-02	+-	0.63E-03	M2	0.649E+03	+-	0.21E+03
13.034	2+,0	TO:								
0.000	0+,0	DT=0	E2	0.572E-03	+-	0.34E-03				
1.779	2+,0	DT=0	M1	0.162E-02	+-	0.51E-03	E2	0.646E-01	+-	0.20E-01
4.618	4+,0	DT=0	E2	0.175E+00	+-	0.55E-01	M3	0.178E+05	+-	0.56E+04
6.276	3+,0	DT=0	M1	0.257E-03	+-	0.15E-03	E2	0.283E-01	+-	0.17E-01
6.879	3-,0	DT=0	E1	0.579E-04	+-	0.21E-04	M2	0.691E+01	+-	0.25E+01
6.889	4+,0	DT=0	E2	0.168E+00	+-	0.61E-01	M3	0.321E+05	+-	0.12E+05
7.381	2+,0	DT=0	M1	0.115E-02	+-	0.42E-03	E2	0.181E+00	+-	0.66E-01
7.417	2+,0	DT=0	M1	0.131E-02	+-	0.47E-03	E2	0.209E+00	+-	0.76E-01
7.799	3+,0	DT=0	M1	0.637E-03	+-	0.38E-03	E2	0.117E+00	+-	0.70E-01
7.933	2+,0	DT=0	M1	0.184E-02	+-	0.67E-03	E2	0.356E+00	+-	0.13E+00
8.259	2+,0	DT=0	M1	0.123E-02	+-	0.45E-03	E2	0.272E+00	+-	0.99E-01
8.413	4-,0	DT=0	M2	0.439E+01	+-	0.26E+01	E3	0.158E+04	+-	0.95E+03
9.316	3+,1	DT=1	M1	0.830E-03	+-	0.50E-03	E2	0.303E+00	+-	0.18E+00
9.381	2+,1	DT=1	M1	0.333E-02	+-	0.12E-02	E2	0.128E+01	+-	0.46E+00
9.480	2+,0	DT=0	M1	0.163E-02	+-	0.98E-03	E2	0.650E+00	+-	0.39E+00
13.051	2-,0	TO:								
0.000	0+,0	DT=0	M2	0.222E+00	+-	0.14E+00				

TABLE 8 *(continuation)*

1.779	2+,0	DT=0	E1	0.127E-02	+-	0.41E-03	M2	0.453E+02	+-	0.15E+02
6.276	3+,0	DT=0	E1	0.530E-04	+-	0.33E-04	M2	0.532E+01	+-	0.32E+01
6.879	3-,0	DT=0	M1	0.486E-01	+-	0.16E-01	E2	0.643E+01	+-	0.21E+01
7.381	2+,0	DT=0	E1	0.157E-03	+-	0.95E-04	M2	0.222E+02	+-	0.13E+02
7.799	3+,0	DT=0	E1	0.281E-03	+-	0.17E-03	M2	0.461E+02	+-	0.28E+02
7.933	2+,0	DT=0	E1	0.714E-04	+-	0.43E-04	M2	0.124E+02	+-	0.75E+01
8.328	1+,0	DT=0	E1	0.182E-03	+-	0.11E-03	M2	0.369E+02	+-	0.22E+02
13.104	2+,0	TO:								
0.000	0+,0	DT=0	E2	0.202E-01	+-	0.36E-02				
1.779	2+,0	DT=0	M1	0.367E-03	+-	0.76E-04	E2	0.144E-01	+-	0.30E-02
6.276	3+,0	DT=0	M1	0.151E-02	+-	0.51E-03	E2	0.163E+00	+-	0.55E-01
6.879	3-,0	DT=0	E1	0.741E-04	+-	0.23E-04	M2	0.866E+01	+-	0.26E+01
7.799	3+,0	DT=0	M1	0.393E-02	+-	0.75E-03	E2	0.704E+00	+-	0.13E+00
8.413	4-,0	DT=0	M2	0.321E+01	+-	0.25E+01	E3	0.112E+04	+-	0.87E+03
8.589	3+,0	DT=0	M1	0.869E-02	+-	0.18E-02	E2	0.215E+01	+-	0.45E+00
9.316	3+,1	DT=1	M1	0.157E-01	+-	0.31E-02	E2	0.552E+01	+-	0.11E+01
13.108	3-,0	TO:								
4.618	4+,0	DT=0	E1	0.402E-05	+-	0.25E-05	M2	0.253E+00	+-	0.16E+00
8.543	6+,0	DT=0	E3	0.460E+04	+-	0.25E+04	M4	0.242E+10	+-	0.13E+10
10.180	3-,0	DT=0	M1	0.683E-02	+-	0.36E-02	E2	0.402E+01	+-	0.21E+01
13.173	3-,0	TO:								
0.000	0+,0	DT=0	E3	0.684E+00	+-	0.41E+00				
1.779	2+,0	DT=0	E1	0.107E-04	+-	0.34E-05	M2	0.373E+00	+-	0.12E+00
4.618	4+,0	DT=0	E1	0.516E-05	+-	0.19E-05	M2	0.320E+00	+-	0.12E+00
6.276	3+,0	DT=0	E1	0.298E-04	+-	0.95E-05	M2	0.284E+01	+-	0.91E+00
7.381	2+,0	DT=0	E1	0.697E-05	+-	0.42E-05	M2	0.941E+00	+-	0.57E+00
7.417	2+,0	DT=0	E1	0.986E-05	+-	0.36E-05	M2	0.135E+01	+-	0.50E+00
7.799	3+,0	DT=0	E1	0.344E-04	+-	0.13E-04	M2	0.540E+01	+-	0.20E+01
9.316	3+,1	DT=1	E1	0.301E-03	+-	0.97E-04	M2	0.918E+02	+-	0.29E+02
9.702	5-,0	DT=0	E2	0.427E+01	+-	0.14E+01	M3	0.255E+07	+-	0.82E+06
13.188	2+,1	TO:								
0.000	0+,0	DT=1	E2	0.722E-02	+-	0.45E-02				
1.779	2+,0	DT=1	M1	0.779E-01	+-	0.27E-01	E2	0.302E+01	+-	0.11E+01
6.276	3+,0	DT=1	M1	0.117E-01	+-	0.46E-02	E2	0.123E+01	+-	0.49E+00
7.381	2+,0	DT=1	M1	0.263E-01	+-	0.10E-01	E2	0.393E+01	+-	0.15E+01
7.799	3+,0	DT=1	M1	0.173E-01	+-	0.11E-01	E2	0.301E+01	+-	0.19E+01
7.933	2+,0	DT=1	M1	0.177E-01	+-	0.11E-01	E2	0.323E+01	+-	0.20E+01
8.259	2+,0	DT=1	M1	0.155E-01	+-	0.97E-02	E2	0.322E+01	+-	0.20E+01
10.668	3+,0	DT=1	M1	0.625E-01	+-	0.39E-01	E2	0.496E+02	+-	0.31E+02
13.248	5-,1	TO:								
0.000	0+,0	DT=1	E5	0.348E+07	+-	0.21E+07				
1.779	2+,0	DT=1	E3	0.174E+02	+-	0.10E+02	M4	0.145E+07	+-	0.87E+06
4.618	4+,0	DT=1	E1	0.325E-04	+-	0.23E-04	M2	0.198E+01	+-	0.12E+01
6.276	3+,0	DT=1	M2	0.646E+01	+-	0.39E+01	E3	0.102E+04	+-	0.61E+03
6.889	4+,0	DT=1	E1	0.436E-03	+-	0.16E-03	M2	0.489E+02	+-	0.18E+02
8.413	4-,0	DT=1	M1	0.241E-02	+-	0.15E-02	E2	0.520E+00	+-	0.31E+00
9.316	3+,1	DT=0	M2	0.755E+02	+-	0.45E+02	E3	0.375E+05	+-	0.23E+05
9.702	5-,0	DT=1	M1	0.743E+00	+-	0.24E+00	E2	0.298E+03	+-	0.95E+02
13.272	2-,0	TO:								
0.000	0+,0	DT=0	M2	0.169E+00	+-	0.10E+00				
1.779	2+,0	DT=0	E1	0.558E-03	+-	0.18E-03	M2	0.192E+02	+-	0.63E+01
7.933	2+,0	DT=0	E1	0.389E-03	+-	0.15E-03	M2	0.619E+02	+-	0.23E+02
9.316	3+,1	DT=1	E1	0.135E-02	+-	0.51E-03	M2	0.392E+03	+-	0.15E+03
9.381	2+,1	DT=1	E1	0.260E-03	+-	0.16E-03	M2	0.778E+02	+-	0.47E+02

TABLE 8 *(conclusion)*

13.361	3-,0		TO:								
0.000	0+,0	DT=0	E3	0.285E+01	+-	0.11E+01					
1.779	2+,0	DT=0	E1	0.305E-04	+-	0.99E-05	M2	0.103E+01	+-	0.34E+00	
4.618	4+,0	DT=0	E1	0.111E-04	+-	0.41E-05	M2	0.657E+00	+-	0.24E+00	
6.276	3+,0	DT=0	E1	0.425E-04	+-	0.16E-04	M2	0.364E+01	+-	0.14E+01	
6.889	4+,0	DT=0	E1	0.645E-04	+-	0.24E-04	M2	0.698E+01	+-	0.26E+01	
7.381	2+,0	DT=0	E1	0.152E-04	+-	0.92E-05	M2	0.193E+01	+-	0.12E+01	
7.417	2+,0	DT=0	E1	0.206E-03	+-	0.73E-04	M2	0.290E+02	+-	0.94E+01	
7.799	3+,0	DT=0	E1	0.275E-04	+-	0.17E-04	M2	0.404E+01	+-	0.24E+01	
7.933	2+,0	DT=0	E1	0.333E-04	+-	0.20E-04	M2	0.513E+01	+-	0.31E+01	
8.589	3+,0	DT=0	E1	0.518E-04	+-	0.31E-04	M2	0.103E+02	+-	0.63E+01	
9.316	3+,1	DT=1	E1	0.940E-03	+-	0.31E-03	M2	0.260E+03	+-	0.85E+02	
13.417	1-,0		TO:								
0.000	0+,0	DT=0	E1	0.174E-04	+-	0.56E-05					
1.779	2+,0	DT=0	E1	0.245E-04	+-	0.78E-05	M2	0.820E+00	+-	0.26E+00	
4.618	4+,0	DT=0	E3	0.568E+02	+-	0.21E+02	M4	0.803E+07	+-	0.30E+07	
6.276	3+,0	DT=0	M2	0.137E+01	+-	0.50E+00	E3	0.206E+03	+-	0.76E+02	
6.879	3-,0	DT=0	E2	0.199E+00	+-	0.73E-01	M3	0.335E+05	+-	0.12E+05	
7.417	2+,0	DT=0	E1	0.146E-04	+-	0.88E-05	M2	0.184E+01	+-	0.11E+01	
8.589	3+,0	DT=0	M2	0.546E+01	+-	0.33E+01	E3	0.180E+04	+-	0.11E+04	
9.316	3+,1	DT=1	M2	0.261E+02	+-	0.96E+01	E3	0.119E+05	+-	0.44E+04	
11.780	2+,0	DT=0	E1	0.152E-02	+-	0.56E-03	M2	0.257E+04	+-	0.95E+03	
13.427	5+,0		TO:								
4.618	4+,0	DT=0	M1	0.189E-01	+-	0.61E-02	E2	0.123E+01	+-	0.40E+00	
6.889	4+,0	DT=0	M1	0.144E-01	+-	0.47E-02	E2	0.170E+01	+-	0.55E+00	
8.543	6+,0	DT=0	M1	0.364E-02	+-	0.22E-02	E2	0.770E+00	+-	0.47E+00	
8.589	3+,0	DT=0	E2	0.121E+01	+-	0.45E+00	M3	0.373E+06	+-	0.14E+06	
10.418	3+,0	DT=0	E2	0.217E+02	+-	0.80E+01	M3	0.172E+08	+-	0.64E+07	
11.780	2+,0	DT=0	M3	0.586E+09	+-	0.22E+09	E4	0.254E+13	+-	0.94E+12	
13.806	2+,0		TO:								
0.000	0+,0	DT=0	E2	0.322E-02	+-	0.20E-02					
1.779	2+,0	DT=0	M1	0.552E-02	+-	0.19E-02	E2	0.192E+00	+-	0.67E-01	
4.618	4+,0	DT=0	E2	0.600E+00	+-	0.21E+00	M3	0.513E+05	+-	0.18E+05	
6.276	3+,0	DT=0	M1	0.178E-02	+-	0.70E-03	E2	0.158E+00	+-	0.62E-01	
9.480	2+,0	DT=0	M1	0.371E-02	+-	0.23E-02	E2	0.998E+00	+-	0.62E+00	
13.973	2+,0		TO:								
0.000	0+,0	DT=0	E2	0.721E-02	+-	0.54E-02					
1.779	2+,0	DT=0	M1	0.651E-02	+-	0.33E-02	E2	0.221E+00	+-	0.11E+00	
4.618	4+,0	DT=0	E2	0.724E+00	+-	0.37E+00	M3	0.596E+05	+-	0.31E+05	
6.276	3+,0	DT=0	M1	0.125E-01	+-	0.64E-02	E2	0.107E+01	+-	0.55E+00	
7.381	2+,0	DT=0	M1	0.306E-02	+-	0.17E-02	E2	0.355E+00	+-	0.19E+00	
8.328	1+,0	DT=0	M1	0.508E-02	+-	0.28E-02	E2	0.804E+00	+-	0.44E+00	
8.589	3+,0	DT=0	M1	0.439E-01	+-	0.23E-01	E2	0.764E+01	+-	0.39E+01	
9.316	3+,1	DT=1	M1	0.868E-02	+-	0.48E-02	E2	0.202E+01	+-	0.11E+01	

DSAM LIFETIMES AND NUCLEAR STOPPING (*)

P. M. CORRÊA and J. M. G. CARAÇA

Laboratório de Física e Engenharia Nucleares, Sacavém, Portugal

ABSTRACT — The use of the Doppler Shift Attenuation Method (D.S.A.M.) in nuclear lifetime measurements is briefly described for the typical L.F.E.N. experimental conditions.

The method was used in the measurement of two well known lifetimes in ^{28}Si ($\sim$ 60 and $\sim$ 700 fs, for the levels at $E_x = 4.62$ and 1.78 MeV, respectively) by means of the ^{27}Al (p, γ) ^{28}Si reaction, as a test to experimental conditions and data analysis.

From these results, at low recoil energy ($v/c \sim 0.2\,\%$), conclusions are drawn about the validity of the Thomas-Fermi potential describing the ion-atom interaction. An empiric scale factor for the calculated nuclear stopping, $f_n = 0.7$, is extracted in this case.

1 — INTRODUCTION

Lifetimes are amongst the most important quantities to be measured in experiments. They provide prime information about the structure of nuclei.

The Doppler Shift Attenuation Method (DSAM) is a nuclear lifetime measurement technique based upon the apparent energy variation of a γ-ray emitted by a nucleus in motion with respect to an observer. If Θ_1 is the angle between the velocity of the emitting nucleus and the axis of the detector, the energy of the observed γ-ray is:

$$E_1 = E_0 \left(1 + \frac{v}{c} \cos \Theta_1\right), \qquad (1)$$

E_0 being the unshifted γ-ray energy, v the speed of the emitting nucleus and c the speed of light. If the experiment is conducted in

(*) Results presented at the Conference of the Portuguese Physics Society (Lisbon, February, 1978).

such a way that γ-rays are detected at two different angles, namely Θ_1 and Θ_2, the observed energy shift between the two peaks will be:

$$\Delta E = E_0 \frac{v}{c} (\cos \Theta_1 - \cos \Theta_2). \tag{2}$$

If the emitting nucleus is moving inside matter, instead of recoiling freely in vacuum, it will be slowed down by the collisions that take place and its velocity is a function of time. The mean value of the energy shift then corresponds to an integration over all decay times:

$$\overline{\Delta E} = \frac{E_0}{c} (\cos \Theta_1 - \cos \Theta_2) \int_0^\infty v(t) \frac{e^{-t/\tau}}{\tau} dt, \tag{3}$$

τ being the lifetime of the nuclear excited state.

Defining:

$$F(\tau) = \frac{1}{v_0 \tau} \int_0^\infty v(t) e^{-t/\tau} dt \tag{4}$$

we obtain:

$$\overline{\Delta E} = E_0 \frac{v_0}{c} F(\tau) [\cos \Theta_1 - \cos \Theta_2], \tag{5}$$

v_0 being the initial speed of the nucleus. In practice an experimental value is obtained,

$$F = \frac{E_1 - E_2}{\Delta E_{max}} \tag{6}$$

ΔE_{max} corresponding to the vacuum shift, and the lifetime is extracted from a calculated F (τ) curve [1]

The calculation of an F (τ) curve is a complex task in physical terms. In the slowing down process two types of collisions are usually considered. The collisions of the recoiling ion with the electrons of the medium are supposed inelastic, slowing down the ion basically without changing its direction of motion. The collisions with the atoms of the medium are assumed to be elastic and therefore associated with considerable deviation from the initial trajectory. The description of this process is usually made in terms of a screened Coulomb field, such as the Thomas-Fermi potential, which was treated in detail by Lindhard, Scharff and Schiøtt [2].

Assuming this description of the slowin down process, a method was devised by Blaugrund [3] to obtain the F (τ) curves relating the mean energy shifts with the lifetime of the nuclear states. For that, one considers both electronic and nuclear stopping mechanisms in the medium. Thus, the total stopping power can be written:

$$\frac{dE}{dx} = f_e \left(\frac{dE}{dx}\right)_e + f_n \left(\frac{dE}{dx}\right)_n \qquad (7)$$

f_e and f_n being empiric correction factors. Each term is dominant at characteristic ranges of the ion energy, depending on the recoiling ion and the stopping material. Broadly, the nuclear term is important at low ion energies, decreasing rapidly as the energy increases; on the contrary, the electronic term dominates at higher recoil energies.

Alternatively, calculations may also be made to obtain the theoretical spectrum of the emitted γ-rays, for an assumed value of τ, and then one compares this spectrum with the experimental one. This process is usually carried out by means of Monte-Carlo techniques [4].

However, the theoretical description of the slowing down process is far from perfect, and it is necessary to test it experimentally [5]. A direct way of doing it, is, of course, the measurement of the stopping power itself. This measurement is however difficult and, besides, it must be stressed that the decomposition of the stopping power in nuclear and electronic parts is somewhat artificial.

An elegant test, though indirect in nature, is the measurement of a well known nuclear lifetime, which has already been the object of much experimental concern. In brief, this test may be used to obtain estimates of the empiric scale factors of equation (7). It can also be used to draw conclusions about the ion-atom interaction potential and to enable us to distinguish between different theoretical descriptions.

2 — EXPERIMENTAL METHOD

The lifetimes of the levels at $E_x = 1.78$ and 4.62 MeV in ^{28}Si have been selected to test the slowing down theory. The adopted values of these lifetimes are 680 ± 30 and 59 ± 6 fs, respectively [6]. Both lifetimes have been measured several times by many authors, with different experimental conditions and even (the first one) by several independent techniques.

The proton resonance capture in ^{27}Al was chosen to populate the levels in question, for many reasons. Namely, it is very easy to use this reaction with the L. F. E. N. 2 MV Van de Graaff accelerator, it has been widely studied and it originates a beam of ^{28}Si ions with a very well and uniquely defined velocity. Two different resonances were used (and therefore ions with two different initial energies were obtained) to populate each of the excited levels in a very simple way. The chosen resonances were those at $E_p = 923$ and 1800 keV for the level at $E_x = 1.78$ MeV and $E_p = 767$ and 1588 keV for the level at $E_x = 4.62$ MeV.

Fig. 1 shows the curves for the electronic and nuclear stopping powers, assuming that the Thomas-Fermi potential describes the ion-atom interaction, for ^{28}Si ions recoiling in ^{27}Al. Also depicted are the ion energies during the recoil, up to a time corresponding to three lifetimes (for each case).

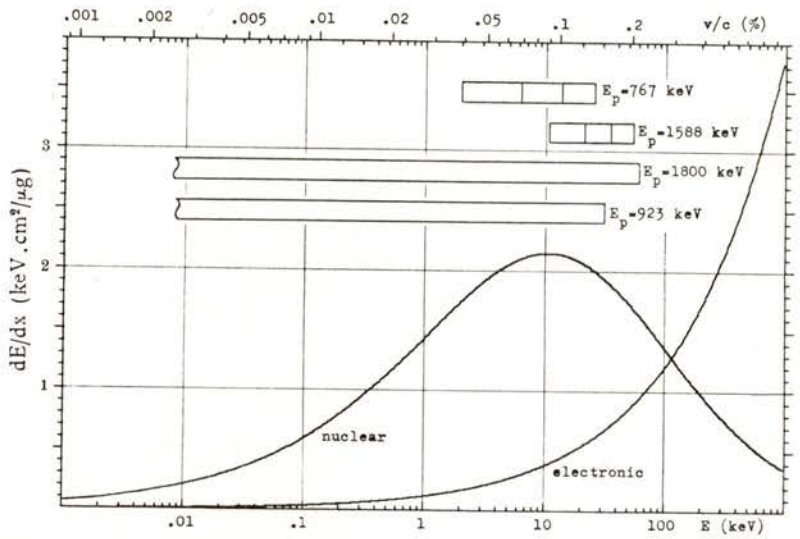

Fig. 1 — The electronic and nuclear stopping powers in the Thomas-Fermi case for ^{28}Si ions recoilling in ^{27}Al. Also depicted are the ion energies during the recoil, up to a time corresponding to three lifetimes.

The beam energy stability was improved to maximum possible (about 500 eV) and the spectrum stability warranted by a digital stabilization unit. Spectra calibrations were of 400–500 eV/channel. The Ge(Li) detector resolution was 2.5 keV at $E_\gamma = 1.33$ MeV.

Targets were of pure aluminium, deposited onto gold or tantalum thick backings. Targets with different thicknesses were used for the resonance at $E_p = 1588$ keV. For the other resonances, the targets were thick enough to guarantee that the recoiling ion was brought into rest inside them.

3 — RESULTS AND DISCUSSION

Fig. 2 presents the experimental spectra obtained (after background extraction) for the 2.84 MeV γ-ray ($E_x = 4.62 \rightarrow 1.78$ MeV transition) at the $E_p = 767$ keV resonance, and for the three measured angles.

Table 1 displays the experimental results. The $F(\tau)$ values presented are already corrected for the finite size of the detector and for the internal side-feeding due to the $E_p = 1588$ keV resonance decay scheme.

From the $F(\tau)$ analysis it is quite clear that the Thomas-Fermi potential does not describe correctly the slowing down mechanism. Assuming as correct the theoretical value for the electronic stopping power ($f_e = 1.0$), f_n was varied down to 0.6. The best set of values was found to be that corresponding to an empiric factor $f_n = 0.7$.

On the other hand the Monte-Carlo analysis of the $E_p = 767$ keV resonance ($v_0/c = 0.140\,\%$) quite corroborates this fact. Again, the value $f_n = 0.7$ appears to be the correct on. The analysis of the $E_p = 1588$ keV resonance ($v_0/c = 0.202\,\%$) was not attempted, as it is much more difficult to interpret than in the 767 keV case, due to the internal side feeding of the $E_x = 4.62$ MeV level. Also, the lifetime of the first excited state in ^{28}Si does not seem amenable to a Monte-Claro analysis, as its value is considerably higher than characteristic slowing down time (of the order of 120 fs), resulting in an appreciable fraction of γ-emissions proceeding with the excited nuclei at rest.

We can thus conclude that the commonly accepted theory, which is based upon the Thomas Fermi statistical model of the atom, seriously overestimates nuclear stopping at low recoil energies. For the ion-stopper combination and initial recoil velocity used in this experiment, the theoretical estimates must be corrected by an empiric factor $f_n = 0.7$. This indicates that the interaction potential actually gives rise to cross-sections that are correpondingly smaller than the

Thomas-Fermi ones, for this energy range, therefore encouraging the consideration of other theoretical descriptions conducing to lower stopping power values.

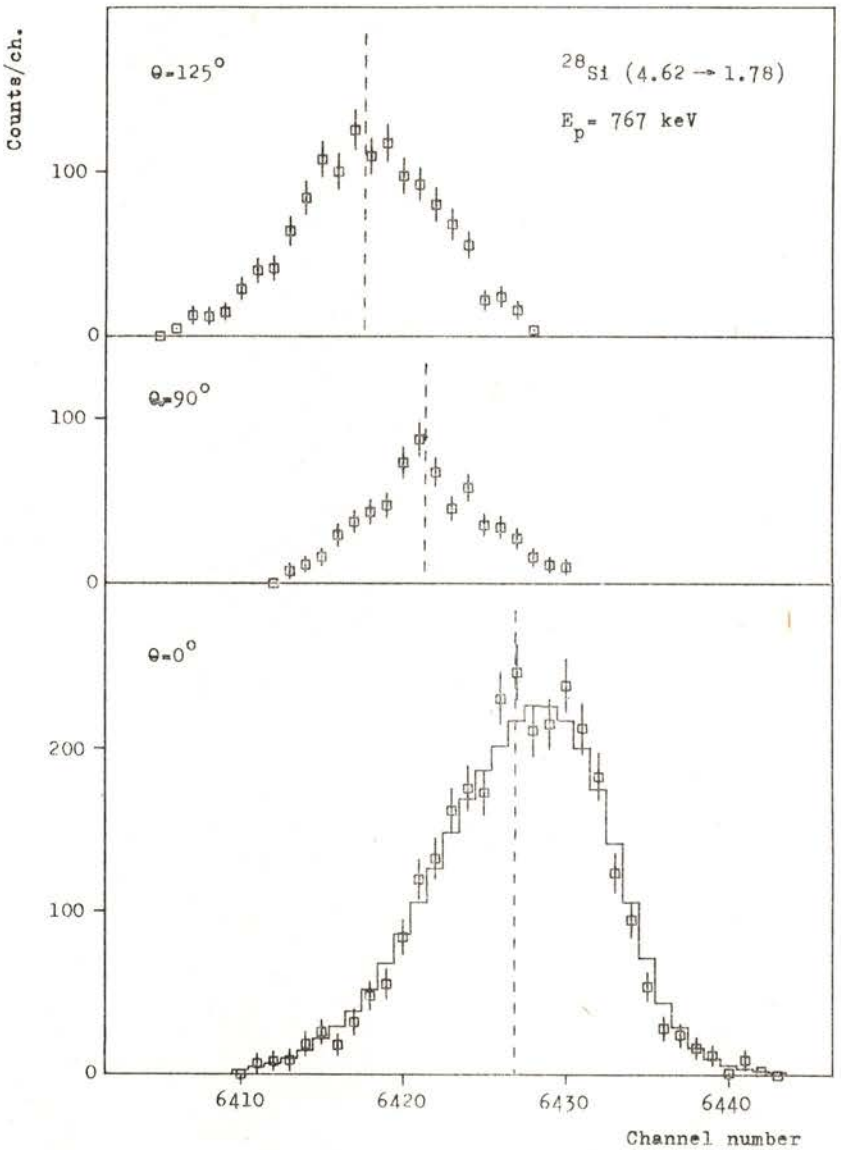

Fig. 2 — Experimental spectra obtained (after backgroud extraction) for the 2.84 MeV γ-ray ($E_x = 4.62 \rightarrow 1.78$ MeV transition) at the $E_p = 767$ keV resonance, for the three measured angles. Superimposed on the 0° peak is the calculated Monte-Carlo lineshape.

TABLE 1

Lifetime values (fs)

v_0/c (%)		0.155	0.216	0.140	0.202	
Target ($\mu g/cm^2$)		100	100	50	50	10 *a*)
F (τ) analysis	F (τ)	0.13 ± 0.01	0.17 ± 0.01	0.65 ± 0.02	0.74 ± 0.02	0.67 ± 0.01
	$f_n = 1.0$	490 ± 50	500 ± 30	41 ± 3	43 ± 4	48 ± 2
	$f_n = 0.7$	660 ± 70	670 ± 40	56 ± 4	57 ± 6	58 ± 2
Monte-Carlo analysis	$f_n = 1.0$			46 ± 3		
	$f_n = 0.7$			61 ± 4		
adopted value ref. [6]		680 ± 30		59 ± 6		

a) The recoiling ions travelled about 8 $\mu g/cm^2$ in aluminium before entering the tantalum backing.

Further elucidation of these questions shall be conducted in two main directions: (i) a systematic study of different ion-stopper combinations, and (ii) a wider choice of inital recoil velocities, covering the whole range of possible (and interesting) measurements.

The active collaboration of J. D. Cunha during experiments and in the early part of this work is gratefully ackowledged.

REFERENCES

[1] J. M. G. CARAÇA, «Vidas Médias Nucleares», LFEN-B N.º 6 (1976),

[2] J. LINDHARD, M. SCHARFF and H. E. SCHIØTT, «Range concepts and heavy ion ranges», *Mat. Fys. Medd. Dan. Vid. Selsk.* **33**, n.º 14 (1963).

[3] A. E. BLAUGRUND, «Notes on Doppler shift lifetime measurements», *Nucl. Phys.* **88** (1966) 501.

[4] W. M. CURRIE, «A Monte-Carlo programme for Doppler shift analysis», *Nucl. Instr. and Meth.* **73** (1969) 173.

[5] Many references exist in the literature on this subject. See, for instance, *Nucl. Instr. and Meth.* **132** (1976) *and* M. TOULEMONDE and F. HAAS, *Phys. Rev.* **C15** (1977) 49 and further references therein.

[6] P. M. ENDT and C. VAN DER LEUN, *Nucl. Phys.* **A214** (1973) 1.

Na AND K IONIZATION ON POLYCRYSTALLINE Ir (*)

M. A. C. ASSUNÇÃO (**) and A. M. C. MOUTINHO
Centro de Física Molecular das Universidades de Lisboa

ABSTRACT — The results of experiments on the ionization of thermal beams of Sodium and Potassium atoms by polycrystalline Iridium are presented. From the experiments we determine the work function of Iridium to be 5.34 ± 0.07 eV. The thermal electron emission method gives the value 5.25 ± 0.05 eV. These two methods and their results are discussed with reference to the «patch model» of ionization on heterogeneous surfaces.

INTRODUCTION

Surface ionization phenomena are important because of their vast area of application. Some of the important applications are in the fast neutral atom sources, ion sources, ionic motors. leak detectors for vacuum systems and semiconductor doping.

In surface ionization an electron in the valence band of an atom passes to the conduction band of a metal by tunnelling [1] and the resulting adsorbed ion remains on the surface for a certain time. This average residential time depends upon the heat of desorption of the ion at the surface. However, it is the probability of electron exchange between the atoms and the metal that dominates the phenomenon and this probability depends essentially upon the energy balance between the ionization potential of the atom and the work function of the metal (so positive surface ionization is more probable when the work function of the metal is higher).

(*) Results presented at the Conference of the Portuguese Physics Society (Lisbon, February 1978).

(**) Now at Department of Physics of the University of Aveiro.

Despite its high work function, Iridium, until now, has not been used widely in surface ionization applications. This may be partly due to the fact that its thermionic properties have not been studied systematically. In fact the number of materials which have been used so far as ionizers is small. Essentially the following have been commonly used: W, Pt, Re and 8% Pt-W and, in some applications, Ta, Mo, Ni, Sn, Ir, Os. Alloys of W-Re and W-Th have also been used.

In the following we present the result of our study on the ionization characteristics of thermal beams of Sodium and Potassium by polycrystalline Iridium.

EXPERIMENTAL

The experiment essentially consisted in generating a thermal beam of Sodium (or Potassium) and sending it onto a polycrystalline sample of Iridium placed in high vacuum ($\simeq 10^{-7}$ torr). The current due to ionization of the incident atomic beam was studied as function of the temperature of the surface of Iridium, the temperature being measured by an optical pyrometer. The effect on the ionization current due to the adsorption of foreign gases on the surface of Iridium was also analysed.

The experimental set up is schematically shown in Fig. 1. The atomic beam is produced in a charge-exchange type source; its intensity was controlled by measuring the ions which were not neutralised in the source. The beam, after collimation, hits the sample surface arranged in the form of a Langmuir-Taylor detector. A mechanical chopper and associated lock-in circuitry was used to measure the ionization current.

In the measurement of surface ionization, the incident beam particles themselves may contribute towards lowering the work function. In order to minimise this error the temperature of the filament was raised above 2000 K between each reading of the ionization current.

From the data obtained we can calculate the work function of Iridium and also the coefficient of ionization of Sodium or Potassium at thermal energies in the surface of Iridium. The work function was also measured by the thermal-electron emission method. The value obtained can be compared with the one obtained by the surface ionization method.

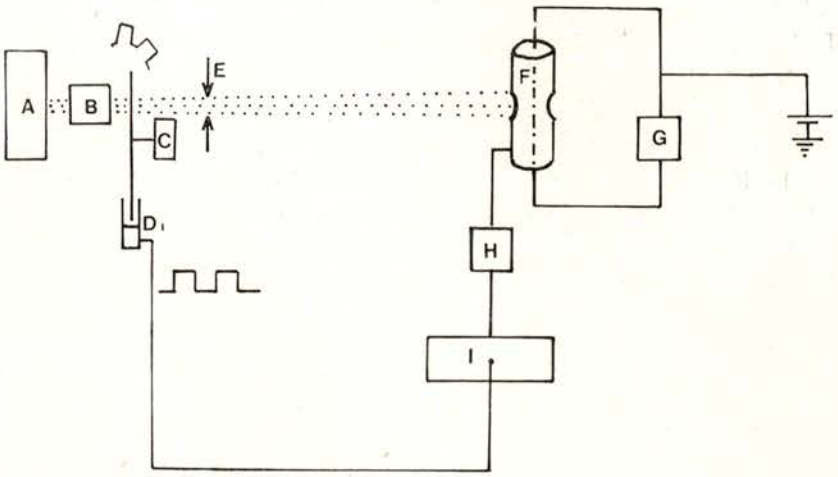

Fig. 1 — Schematic diagram of the apparatus

A — Charge-exchange source
B — Deflection plates
C — Chopper and rotor
D — Photodetector
E — Slit
F — Langmuir Taylor detector with Iridium surface
G — Direct current generator
H — Preamplifier
I — Lock-in amplifier.

DISCUSSION OF THE RESULTS

1 — *Thermal emission of electrons*

The electron current is given by the well-known Richardson--Dushman equation.

$$i = AT^2 \exp(-\phi_e / kT)$$

where ϕ_e is the work function and T the temperature. It follows that the graph $ln\ i/T^2$ vs. $1/T$ is a straight line (Richardson line) and the slope gives the value of ϕ_e; in our case we obtained the value 5.25 ± 0.05 eV. This value is close to the one obtained by other

authors using this method: Alekseev and Kaminskii [2] (5.3 eV), Hushman [3] (5.4 eV), and Zandberg and Tontegode [4] (5 30 eV).

The intluence of adsorption of oxygen and methane on the surface results in an increase of the work function in one case (oxygen) and a decrease in the other (methane).

In Fig. 2 are shown Richardson lines for the three cases: clean Iridium, Iridium in oxygen, and Iridium in methane atmosphere. In the case of oxygen the work function increased to 5.4 ± 0.11 eV. This value is, however, less than that obtained by Hurkmans et al [5]

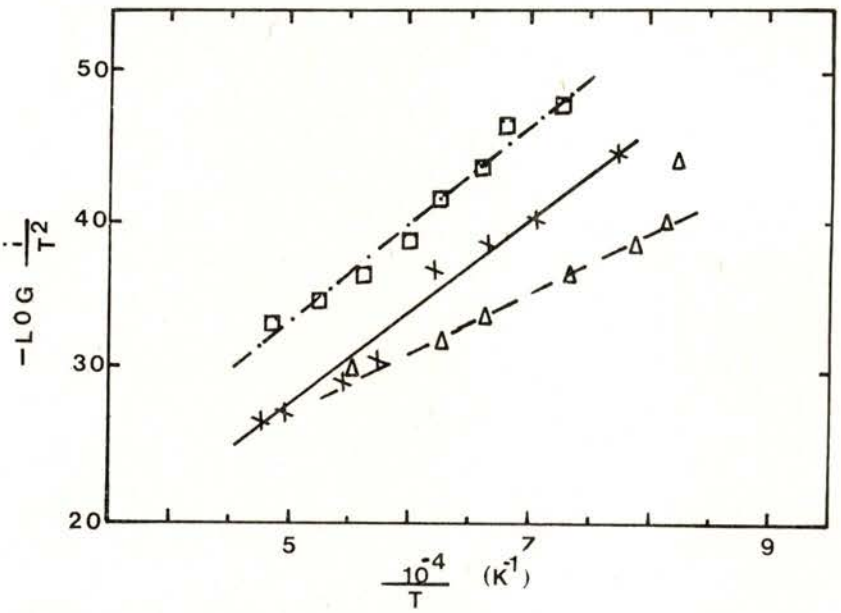

Fig. 2 — Richardson lines for: a cleaned Iridium surface (X), and Iridium in oxygen (□) or methane (Δ) atmospheres.

(5.6 eV). Probably the difference is due to the lower oxygen pressure employed by us; the pressure was low enough to ensure that only a monolayer was adsorbed on the surface. The pressure dependence of the work function has already been pointed out by other authors [6]. The difference between the value obtained with and without oxygen is explained, in general, by assuming the formation of a homopolar bond between the adsorbed atom and the sample surface. Using this model Slachter derived the expression for this difference [7] which, in our case, turns out to be 0.25 eV.

In the case of methane the work function is strongly dependent upon the temperature (see Fig. 2). The lowering of the work function in the region of 1250 K to 1700 K to approximately 4.4 eV should be noted.

2 — *Ionization of Sodium and Potassium on Iridium*

The typical data for the ionization current vs. temperature for Sodium and Potassium are shown in Fig. 3. The data indicates that the ionization starts at about 1050 K. Comparison between the two

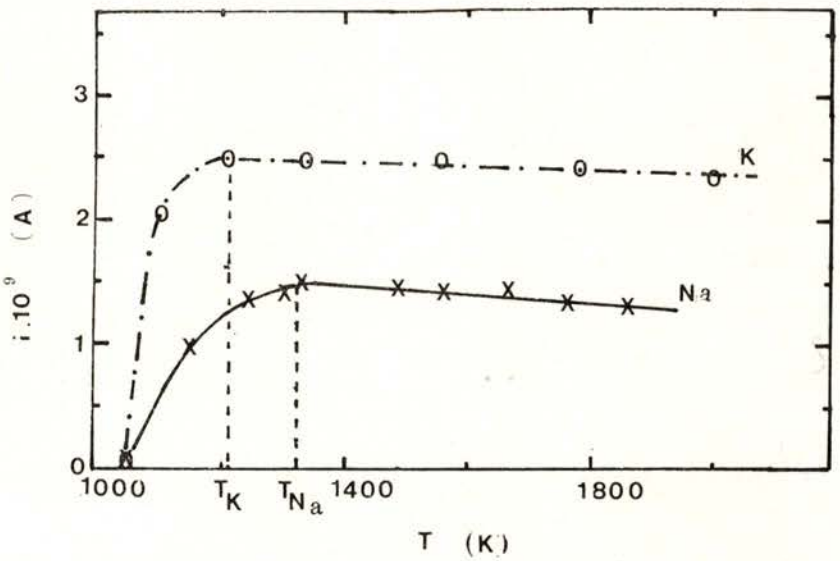

Fig. 3 — Ionization currents for a Sodium (X) and Potassium (O) atomic beams from a cleaned Iridium surface.

curves (Sodium and Potassium) shows that the surface ionization of Sodium is a little more strongly temperature dependent than that of Potassium. This is consistent with Saha-Langmuir equation

$$\beta = \left[1 + 2 \exp\left(\frac{I - \phi_i}{k\ T}\right)\right]^{-1},$$

where β is the coefficient of ionization and I the ionization potential of the incident atoms. From the same Fig. (and from other runs),

the temperatures at which maximum ionization takes place for the two atom beams are $T_K = 1200$ K and $T_{Na} = 1320$ K.

The work function of the polycrystalline Iridium for positive surface ionization was calculated by fitting experimental values

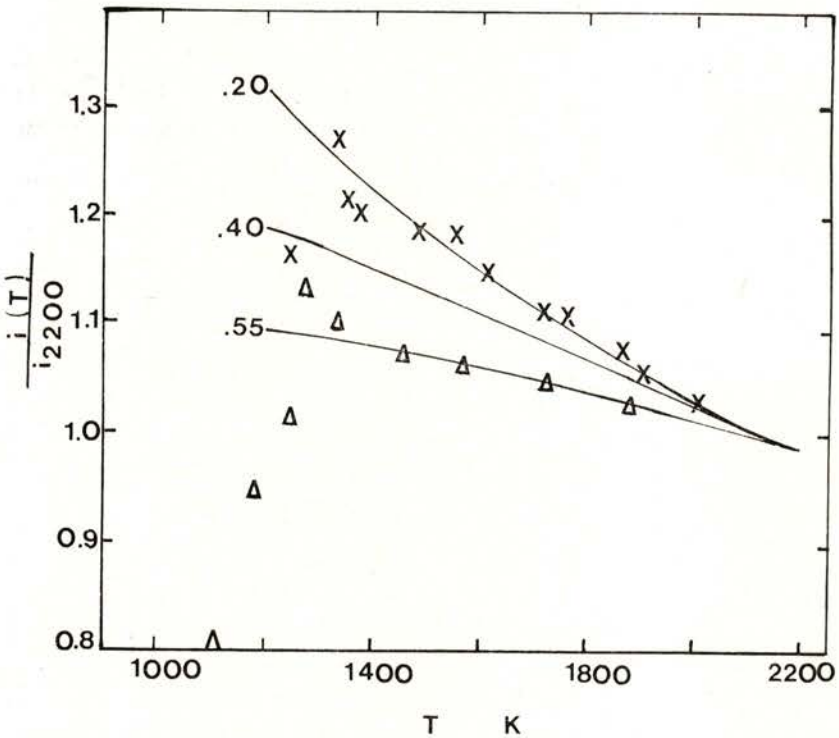

Fig. 4 — Data for Sodium ionization on cleaned Iridium surface (X) and on Iridium with adsorbed oxygen (Δ). Lines represent the theoretical behaviour of i(T)/i(2200 K) for several values of $\phi_i - I$

of $i(T)/i(2200\ K)$ to the Saha-Langmuir equation. As shown in Fig. 4 we obtain a value of $\phi_i = 5.34 \pm 0.07$ eV for Sodium using this method. For Potassium the method is less accurate and permits only to conclude that $(\phi_i - I) > 0.85$ eV and $\phi_i > 5.25$ eV. These values are qualitatively in agreement with the «patch model» of the positive ionization from a nonhomogeneous surface. In this model the surface is composed of patches each one with its own value of

work function. The effective work function of the whole surface is then the weighted average of the contributions from the individual patches. The patches can be divided into two types: some having work function ϕ_{min} and some ϕ_{max}. In the thermal emission of electrons the patches with ϕ_{min} contribute predominantly, therefore $\phi_e \simeq \phi_{min}$. It follows then that the effective work function for surface

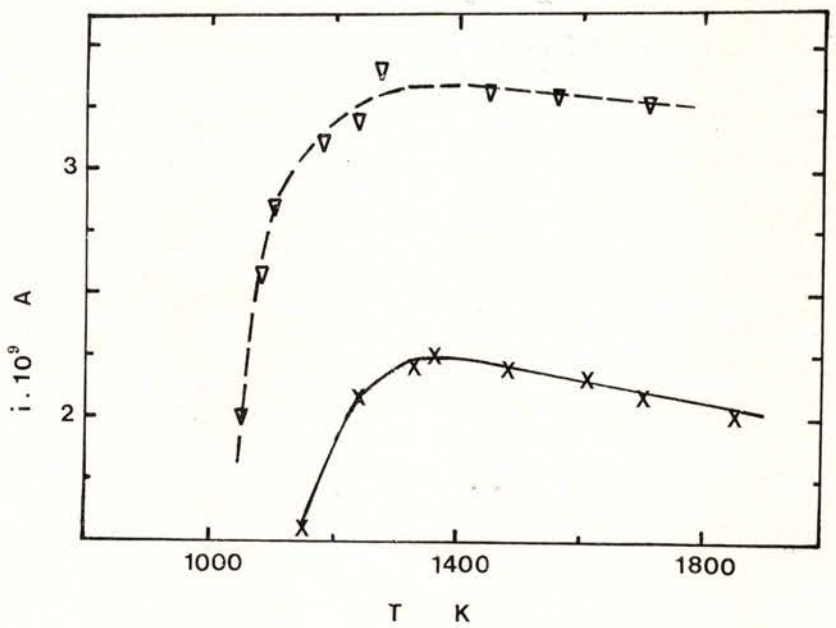

Fig. 5 — Ionization currents for Na: cleaned Iridium surface (X), Iridium in the presence of oxygen (▽).

ionization ϕ_i lies between ϕ_e, and ϕ_{max}, that is, $\phi_e < \phi_i < \phi_{max}$. From the thermal emission experiment we obtain $\phi_e \simeq \phi_{min} = 5.25$ eV and we verify from surface ionization experiments that ϕ_i lies between this value and $\phi_{max} = 5.8$ eV measured for the (1,1,1) surface [8] and confirmed by others [9], [10].

From the knowledge of the effective work function we can estimate that the coefficient of ionization β maximises (100 %) for Potassium in the region of 1200 to 1500 K, and takes the value of about 80 % for Sodium at 1300 K.

3 — *Effect of oxygen and methane adsorption*

Adsorption of oxygen raises the ionization coefficient in the case of Sodium to approximately 100% (see Fig. 5), while results on Potassium are unaffected. The method described before gives the value of the work function as $\simeq 5.7$ eV for Iridium in oxygen atmosphere.

Methane has the effect of lowering the coefficient of ionization. For example, at 1250 K, the ionization of potassium decreases to 55%, and the ionization of Sodium is negligible. From the calculations

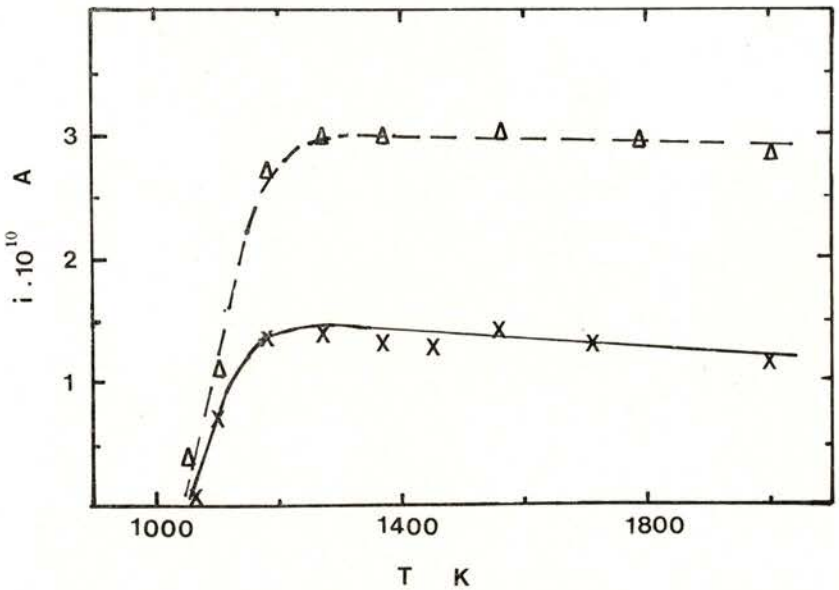

Fig. 6 — Ionization currents for K: cleaned Iridium surface (Δ), Iridium in the presence of methane (X).

on the work function in the case of Potassium, in the presence of methane, it was not possible to obtain an accurate value but only to ascertain that it lies between 4.5 and 4.7 eV.

The values of the work function in the presence of oxygen and methane are higher than those obtained from the thermal emission of electrons in identical conditions. This agrees with the patch model.

CONCLUDING REMARKS

From our experiments we observe that the work function is extremely sensitive to the presence of oxygen and methane. This points towards a good adsorption of these gases on the Iridium surface.

Globally, from the results obtained we can conclude that Iridium wire or Iridium wire covered with oxygen may be used as 100% eficiency detectors for Potassium and Sodium atomic beams respectively.

The financial support of INIC is gratefully acknowledged. The authors would like to thank Dr. M. Maneira and Eng. Isidro Pedro for cooperation in measurements; their help is gratefully recognised.

REFERENCES

[1] R. K. JANEV — *J. Phys. B: Atm. Mol. Phys.*, **7**, 1506 (1974).

[2] N. ALEKSEEV and D. KAMINSKY — *Sov. Phys. Techn. Phys.*, **9**, 1177 (1965).

[3] O. HUSMANN — *J. Applied Physics*, **37**, 4662 (1966).

[4] E. ZANDBERG and A. TONTEGODE — *Sov. Phys. Techn. Phys.*, **12**, 1548 (1968).

[5] A. HURKMANS, E. OVERBOSCH, K. KODERA and J. LOS — *Nuclear Instruments and Methods* **132**, 453 (1976).

[6] B. CHAO and F. WHITE — *International Journal of Mass Spectrometry and Ion Physics*, **12**, 423 (1973).

[7] M. KAMINSKY — *Atomic and Ionic impact phenomena on metal surfaces*, Springer Verlag. Berlin, 1965.

[8] E. ZANDBERG and N. IONOV — *Surface Ionization*, Jerusalem, 1971.

[9] R. THOMAS — *J. Applied Physics*, **41**, 5330 (1970).

[10] R. WILSON — *J. Applied Physics*, **44**, 2130 (1973).

INVESTIGATIONS ON THE EXISTENCE OF WELL DEFINED METALLIC CATION HYDRATES IN ELECTROLYTICAL SOLUTIONS (*)

M. ALVES MARQUES
Centro de Física da Matéria Condensada

Raman bands assigned to internal vibrations of cation hydrates in concentrated aqueous solutions of aluminium chloride [1] were investigated. The author considered, in the bulk of a concentrated aqueous solution, cation hydrates with a (defined) structure independent of the anion in order to calculate the isotopic shift of these bands when the ordinary water, in the solution, is replaced by deuterium oxide. No coupling of the internal vibration of the water molecule with the oscillations of the hydration complex was noticed in liquid solutions. The approach that H_2O and D_2O molecules are rigid ones was admitted. In the cation hydrate, assumed as octahedral, the interactions of each water molecule with the surrounding particles were considered cilindrically symmetric around the axis of its valence angle. Besides the vibration modes, already investigated, in which the six bonds from the cation to the six water molecules stretch or shorten, four triply degenerate oscillation modes, Raman active, are possible [1] — fig. 1. Three different non zero values for these frequencies are in general obtained for assumed values of the force constants of the oscillations of the water molecules about their equilibrium positions.

The simplified potential of the aggregate used here was:

$$V = \frac{1}{2} k \left\{ (\phi_1 - \theta_1)^2 + (\phi_2 - \theta_2)^2 \right\} + \frac{1}{2} k' (\theta_1 + \theta_2)^2$$

(*) Results presented at the Conference of the Portuguese Physics Society (Lisbon, February, 1978).

For low values of the ratio k'/k, up to $k'/k \sim 7$, the isotopic ratio of the lowest (non-zero) value of the frequencies of the above normal modes was calculated (*).

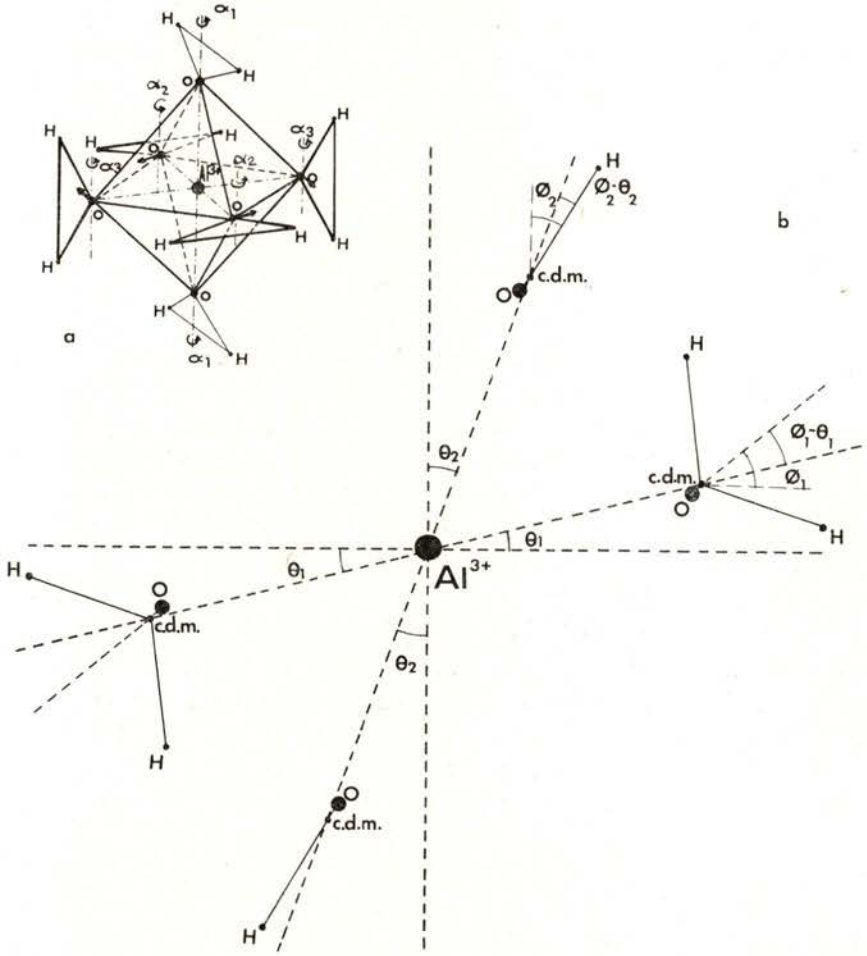

Fig. 1a. — Triply degenerate Raman active normal vibrations are different combinations of the indicated oscillations. 1b. — Bending and librational angles of the octahedral hydrate; ϕ_i are measured about the center of mass of the water molecule. Only the four water molecules drawn with a heavy line in the upper picture (1a) are represented here.

(*) The upper limit was obtained by considering only the interaction of the electrostatic field with the dipole moment of each coordinated water molecule, the short-range intermolecular forces being ignored.

Comparing the calculated ratio with the observed isotopic shift of the band that lies about 340 cm^{-1}, in the Raman spectra of the concentrated aqueous solutions of aluminium chloride, a reasonable agreement is obtained (fig. 2). As the isotopic shift was calculated without considering the anion interactions, the hypothesis about the

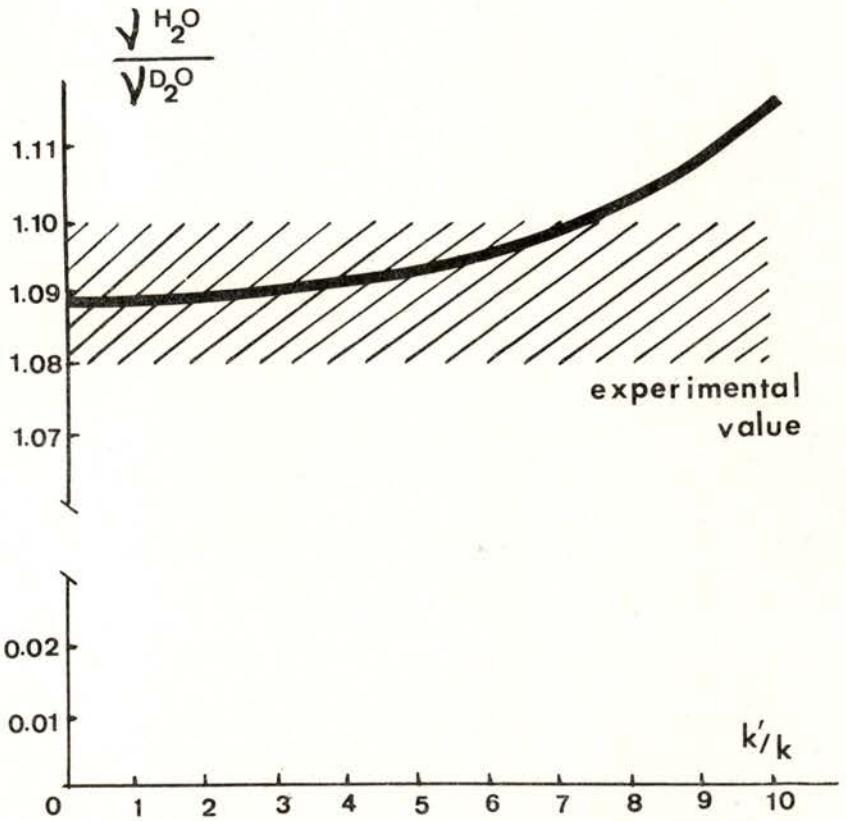

Fig. 2 — Isotopic ratio ν^{H_2O} / ν^{D_2O} of the frequency of the lowest wavenumber Raman band corresponding to the normal vibrations indicated (Fig. 1).

existence of a *well-defined* coordinated hydration shell of Al^{3+} in aqueous solutions of aluminium salts [1] seems plausible. For indium chloride solutions, at the moment of the experiments, the results were not yet sufficient for elaborate conclusions [2]. Positional correlations between the electrons of the In^{3+} and the electrons

of the neighbour water molecules, obtained from X-ray diffraction investigations [3] point out the presence of six water molecules in the first hydration shell.

The author wishes to thank Prof. Dr. N. Macias Marques and Dr. J. Resina Rodrigues for stimulating discussions. M. C. Carreiro da Costa did the necessary calculations.

REFERENCES

[1] M. ALVES MARQUES, thesis, Univ. T. Lisboa, 1962; A. DA SILVEIRA, M. A. MARQUES and N. M. MARQUES, *Mol. Phys,* **9**, 271 (1965). In this article only the investigations on the Raman active vibration modes of the octahedral hydrate where the water molecules are considered as punctual are reported.

[2] M. A. MARQUES, *Proc. 6th Int. Conf. on Raman Spectroscopy,* Bangalore Sept. 1978.

[3] M. A. MARQUES and M. I. B. MARQUES, *Proc. K. Ned. Akad. Wet.* **B77**, 286 (1974). M. A. SOUSA OLIVEIRA, M. I. CABAÇO e M. A. MARQUES, following research note.

X-RAY DIFFRACTION INVESTIGATION OF THE STRUCTURE OF CONCENTRATED IONIC SOLUTIONS (*)

M. A. SOUSA OLIVEIRA, M. I. CABAÇO, M. ALVES MARQUES
Centro de Física da Matéria Condensada

The existence of correlations of positions taken up by heavy ions in aqueous solutions was demonstrated using X-ray diffraction [1]. The existence of a (local) arrangement of hydrated light ions in concentrated electrolytic solutions was suggested [2] [3] for interpreting similar X-ray diffraction experiments; some of those cation hydrates have a defined structure.

Cations that have not shown well-defined coordination hydration shells in aqueous solutions were investigated. Correlations of positions taken up by hydrated cations in concentrated aqueous solutions of indium nitrate and sulphate and of calcium nitrate are reported. The X-ray diffraction pattern of each solution shows (fig. 1), among others, one interference maximum at $q \sim 1$ Å^{-1} (q, momentum transfer divided by $\hbar$). The value of q corresponding to this interference maximum varies with the cation concentration C according to the law $q \propto C^{1/3}$, (fig. 2 and table).

Results obtained with concentrated aqueous solutions of other inorganic salts of metallic cations and the influence of the atomic number of the anions on the intensity of the interference maxima will be discussed in a forthcoming publication.

The X-ray diffraction patterns were obtained with two different wavelengths: Cu K_α and Mo K_α.

(*) Results presented at the Conference of the Portuguese Physics Society (Lisbon, February 1978).

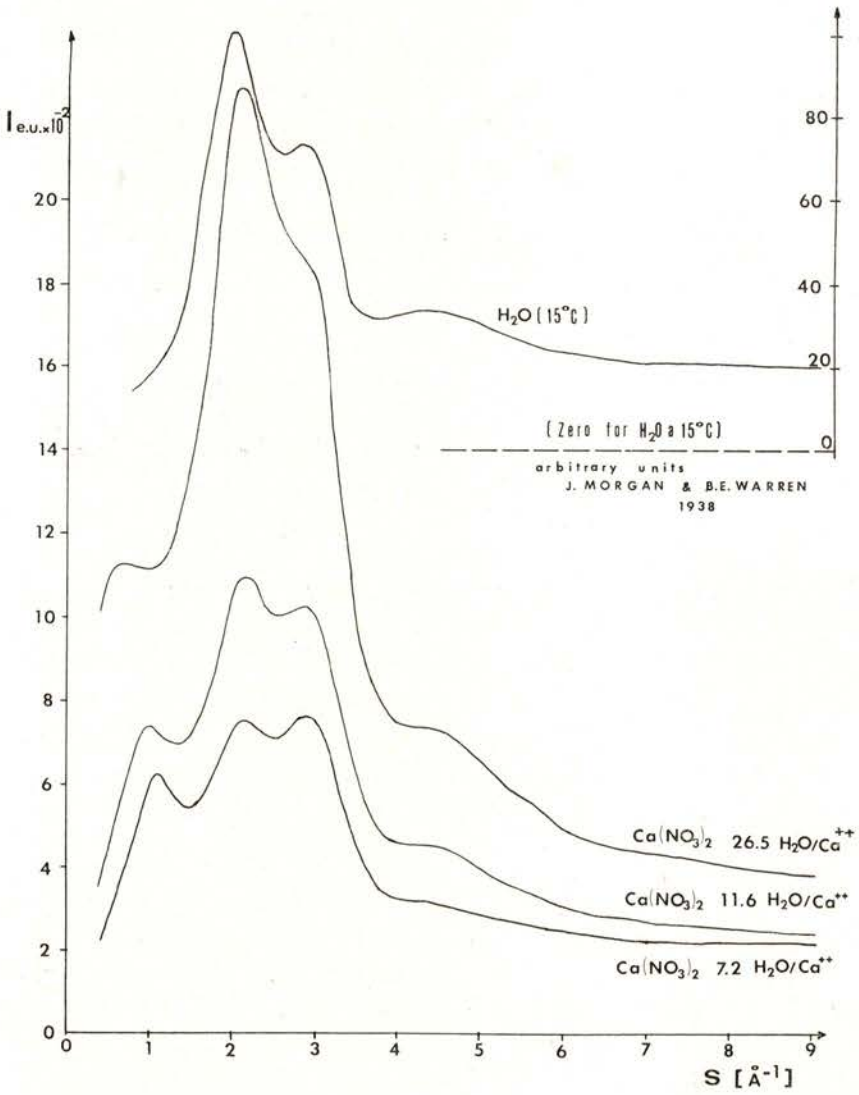

Fig. 1 — X-ray diffraction intensities, corrected for absorption and polarization, of concentrad aqueous solutions of calcium nitrate. H_2O diffraction intensities are given (in arbitrary units) for comparison. Here S has the same meaning as q.

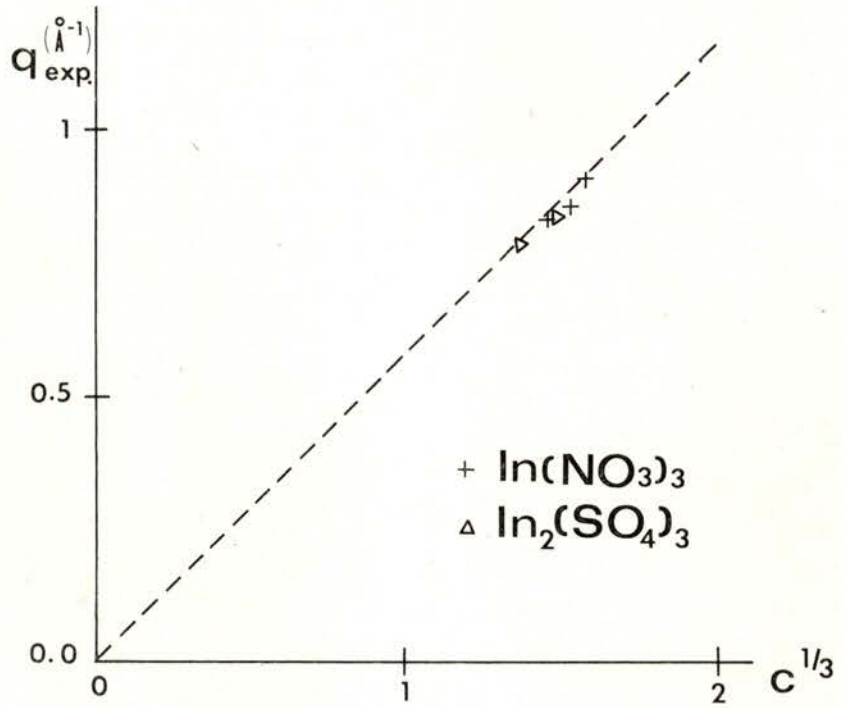

Fig. 2—Momentum transfer, $q_{exp.}$, corresponding to the inner diffraction ring, versus $C^{1/3}$.

TABLE

Solute salt	Molarity g.mol. 1^{-1}	Density (*)	Mol. H_2O per cation	Moving Diffraction Maximum	
				$q_{exp.}$ ($Å^{-1}$)	q_{theor} (**) ($Å^{-1}$)
$Ca(NO_3)_2$	5.3	1.55	7.2	1.01	1.01
	3.8	1.41	11.6	0.89	0.90
	2.8	1.31	16.8	0.80	0.82
	1.88	1.21	26.5	0.72	0.72
$In(NO_3)_3$	3.9	1.88	10.0	0.90(?)	0.91
	3.6	1.80	11.2	0.84	0.89
	3.1	1.71	13.6	0.81	0.85
$In_2(SO_4)_3$	1.59	1.68	15.0	0.82	0.85
	1.26	1.55	19.7	0.78	0.79

(*) Densities were measured at 20°C.

(**) q_{theor} corresponds to an assumed quasi-close packing of hydrated cations.

REFERENCES

[1] J. A. Prins and R. Fonteyne, *Physica,* **2**, 1016 (1935).

[2] M. Alves Marques and M. I. Barros Marques, *Proc. K. Ned. Akad. Wet,* **B77**, 286 (1974).

[3] M. I. de Barros Marques and M. Alves Marques, *VIII Hungarium Diffraction Conference* (April 1976).

THERMOELECTRIC POWER (S, dS/dT) IN ANTIFERROMAGNETIC Cr-Al ALLOYS (*) (**)

R. P. PINTO, J. B. SOUSA, J. M. MOREIRA,
M. M. AMADO, M. E. BRAGA
Centro de Física da Universidade do Porto, Porto, Portugal

G. GARTON
Clarendon Laboratory, Univ. Oxford, Parks Road, Oxford, England

ABSTRACT — Accurate measurements of the thermoelectric power (S) of antiferromagnetic Cr-Al dilute alloys are presented over a wide range of temperature (80-350 K).

Particular attention is given to the critical behaviour of the temperature derivative dS/dT near the Néel temperature (T_N). The anomalous concentration dependence of T_N in Cr-Al is also considered.

1 — INTRODUCTION

The antiferromagnetic b.c.c. Cr-Al dilute alloys constitute a very complex system, as revealed by the pronounced changes which occur in the electronic density of states [1], the Debye temperature [1] and the peculiarities in the magetic behaviour for Al compositions in the range $0 < c < 6$ at. %. Further difficulties arise in this range of compositions due to the exceptionally small magnetic anomalies found in most physical properties, even in those sensitive properties as the magnetic susceptibility [2] or the electrical resistivity [3, 4]. This occurs in spite of the steady increase in the magnetic moment

---

(*) Results presented at the Conference of the Portuguese Physics Society (Lisbon, February, 1978).

(**) Work fiancially supported by INIC (Portugal) and NATO Research Grant no. 1481.

per atom caused by the addition of Al, as shown by neutron diffraction studies [5, 6]. These studies revealed an abrupt transition from an incommensurate antiferromagnetic structure to a commensurate one when Al content exceeds about 1 at. %. This has been corroborated by recent latent heat measurements [7]. The information available on the Néel temperature also suggests a very complex and anomalous behaviour of T_N in the concentration range $0<c<6$ at. % Al [8].

The anomalous behaviour in T_N and the excepcionally small magnetic anomalies which occur in Cr-Al, were good reasons to start a detailed and systematic study of transport properties in this system. To our knowledge, the available information on transport properties in Cr-Al is rather scarce, and essentially restricted to the *general* features of the electrical resistivity (ρ). The first experimental account has been given by Chakrabarti [3] (including the Hall effect), but a more precise study of ρ for low Al content has been done subsequently by Arajs et al [4] ($0.3<c<6.2$ at % Al). For one particular case (1.2 at % Al) general information was also given for the thermoelectric power over a restricted range ot temperature [4].

In this preliminary report we present very accurate data on the thermoelectric power (S) of Cr-Al dilute alloys over a wide range of temperatures (~80-320K) and, for the first time, detailed and precise information is published on the behaviour of the temperature derivative of the thermoelectric power (dS/dT) for this system.

The importance of the thermal treatments on the behaviour of the thermoelectric power is also investigated.

A detailed analysis of the critical behaviour of dS/dT, its intimate connection with the critical behaviour of $d\rho/dT$, and the peculiar concentration dependence of the Néel temperature will be object of a forthcoming publication, when the present investigations (ρ, $d\rho/dT$, S, dS/dT) have been extended to the *whole* set of available Cr-Al samples in the range $0<c<6$ at % Al.

2 — EXPERIMENTAL TECHNIQUE

The thermoelectric power was measured by a static method [9]. The temperature difference across the sample ($\Delta T \simeq 0.5$ K), produced by Joule heating (H_1), was measured with a differential copper/constantan thermocouple, in good contact with, but electrically

insulated from the sample. Another similar thermocouple (T) allowed the determination of the sample mean temperature. The thermoelectric voltage (ΔV) was measured using Cu leads spotwelded to the sample. Both thermocouple and thermoelectric voltages were measured directly on sensitive digital voltmeters, with 10^{-2} and 10^{-3} μV resolution respectively.

The sample, attached at one end to a copper «basis» (thermocouple T), was surrounded by a radiation shield with a heater (H_3), and the assembly suspended inside a metallic vaccuum chamber ($\sim 10^{-6}$ torr) by a thin tube of stainless steel.

The electrical leads were carefully twisted, thermal anchored, and with reasonable lengths between sample and basis to minimize heat losses. The heating power delivered at the free end of the sample (H_1) could be transferred to an equal heater (H_2) on the basis.

The measuring technique was as follows: (*i*) with the power switched to H_2 in the basis (current stability $\pm 1/10^4$) a set of readings was taken (T_0, ΔV_0, ΔT_0) to define a zero reference for all circuits. (*ii*) Then the power was transferred abruptally to H_1 and a difference of temperature gradually established across the sample. A period of 15 min was adopted before taking the new readings (T_1, ΔV_1, ΔT_1). In general $T_1 \simeq T_0$, since the transfer of the same power from H_2 to H_1 practically does not affect the temperature at the basis when heat losses are small. (*iii*) Power is transferred again to H_2, and the whole process repeated as before. Obviously, the mean temperature of the sample can be adjusted with the heater H_3 in the radiation shield. In general we adopted very low rates of change of temperature, of the order of 15 mK/minute.

Since the differences of temperature between consecutive points were reasonably small ($\delta T/T_c \sim 10^{-3}$), we used the «sliding rule» process to obtain our final (smooth) dS/dT values. Therefore, groups of five consecutive points were slid along the whole set of initial dS/dT values, but without mixing dS/dT values on both sides of T_c.

The typical scatter in our S curves is generally fairly small ($\sim 1/10^3$) and of the order of a few per cent for dS/dT curves. Reproducibility of S values in different runs is of the order of 10^{-3}. This indicates that under the careful experimental conditions adopted, and by taking readings always at the same time intervals, the parasitic thermal emfs do not interfere in any significant way in our results.

3 — SAMPLES

The samples used in this work contain 0.06, 0.8, 1.93 and 4.8 at % Al. Except for 0.06 at % Al, all the other samples were prepared at the Clarendon Laboratory, Oxford, by melting the constituent elements (Johnsson Mathey spectrographically pure Cr and Al) in alumina crucibles using radiofrequency heating under argon atmosphere. Several melting operations were performed in order to improve the homogeneity of the samples. The final compositions were determined by the atomic absorption method. Metallographic analysis and hardness tests, made at the Faculty of Engineering in Porto, revealed a fairly homogeneous and single-phase system for these low Al compositions. The samples were cut from the melted ingots using a spark machine and a slab geometry ($cm \times mm \times 10^{-1}$ mm) obtained at the end.

The 0.06 at % Al sample was prepared at Imperial College of London, by the arc discharge method under argon atmosphere. Several melting operations were made in order to improve the homogeneity of the alloy. A cylindric-shaped sample was finally obtained by the suction method, through a cold copper mould. For this sample, the exact Al content is difficult to measure by the usual methods of analysis, including electron scanning microscopy. Therefore, its actual composition had to be inferred from residual resistivity measurements, assuming $\Delta\rho = 12\,\mu\Omega$. cm per 1 at % Al, which is an average figure obtained from a linear plot of ρ_0 vs Al composition, for a series of dilute alloys (< 4 at % Al) prepared under the *same* conditions. Annealing at about 1050 °C for 5 days was done for the 0.06, 1.93 and 4.8 at % Al samples, under argon atmosphere. In order to study the importance of heat treatments, we did not anneal the 0.8 at % sample, neither a second sample with the same nominal composition as 0.06 at % Al.

4 — EXPERIMENTAL RESULTS

Let us consider first the case of the annealed samples. All these measurements have been performed at the University of Porto.

Fig. 1 shows the temperature dependence of the thermoelectric power for the sample with 0.06 at % Al over a wide range of tempe-

ratures (120–340 K), and a direct comparison is made with the corresponding behaviour of the electrical resistivity measured in the *same* sample.

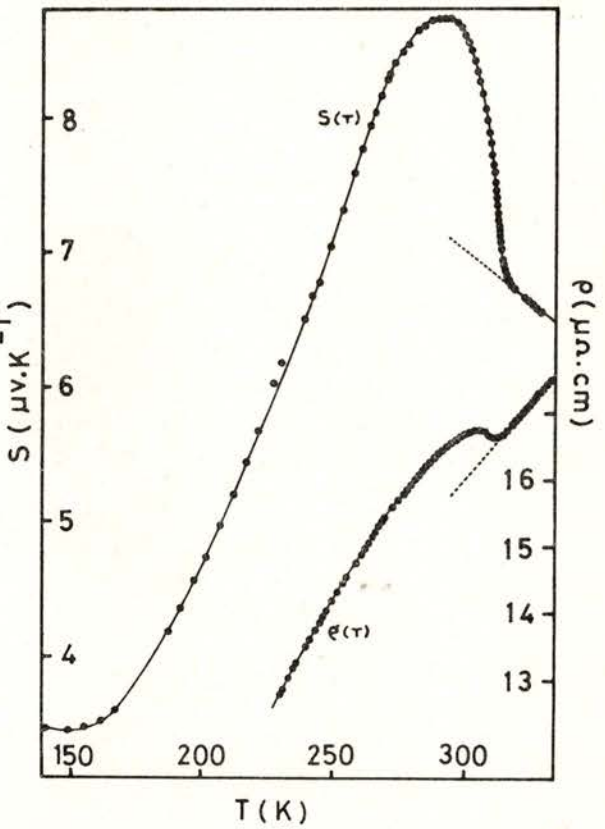

Fig. 1 — S and ρ for Cr-$Al_{0.06}$

The thermoelectric power for this sample closely resembles the behaviour of S in pure Cr. The antiferro-paramagnetic transition is also clearly marked by the sharp reduction in S at $T_N = 309.8$ K, a value which agrees well with the one obtained from the minimum in $d\rho/dT$, and is still close to the Néel temperature of Cr ($\simeq 311$K). This reduction in S is essentially due to the sharp increase in the effective number of conduction electrons as the antiferromagnetic

gap in the electron spectrum goes to zero at T_N. Similar effects have been observed in the thermoelectric power of Cr-Si [10], Cr-V, Cr-Mn [11] and Cr-Ni [12] alloys.

The temperature derivatives dS/dT and $d\rho/dT$ for $Cr_{99.94}Al_{0.06}$ are shown in Fig. 2, as a function of temperature. In both cases the antiferro-paramagnetic transition is clearly marked by a pro-

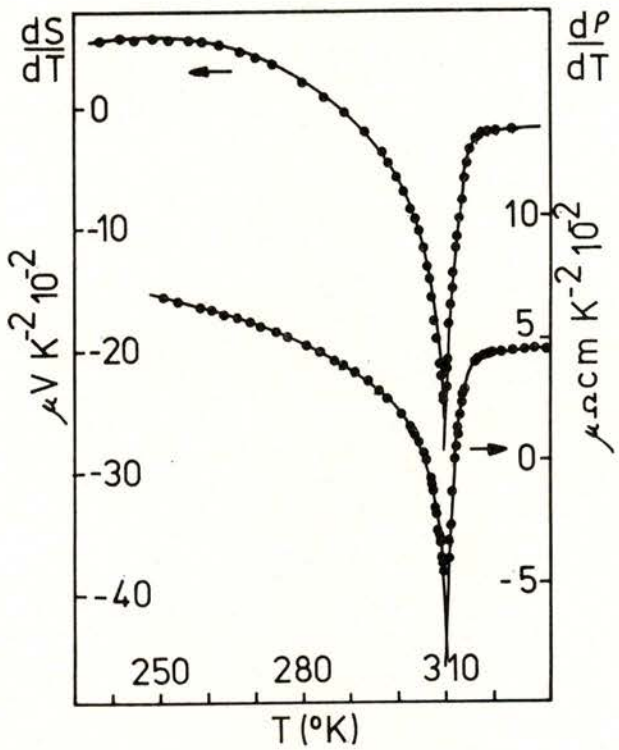

Fig. 2 — dS/dT and dρ/T for $Cr\text{-}Al_{0.06}$

nounced and very narrow dip of both derivatives at T_N. The general trend of both curves is remarkably similar, which suggests the possible existence of a close relationship between dS/dT and $d\rho/dT$ in the vicinity of the Néel temperature. The analysis of this important question and its possible theoretical implications for critical phenomena studies will be object of a forthcoming paper (with M. Ausloos).

Fig. 3 shows the temperature dependence of S for the sample with 1.93 at% Al. This curve is similar to that of $Cr_{99.94}Al_{0.06}$. However, the transition is not as sharp, probably due to the attenuation

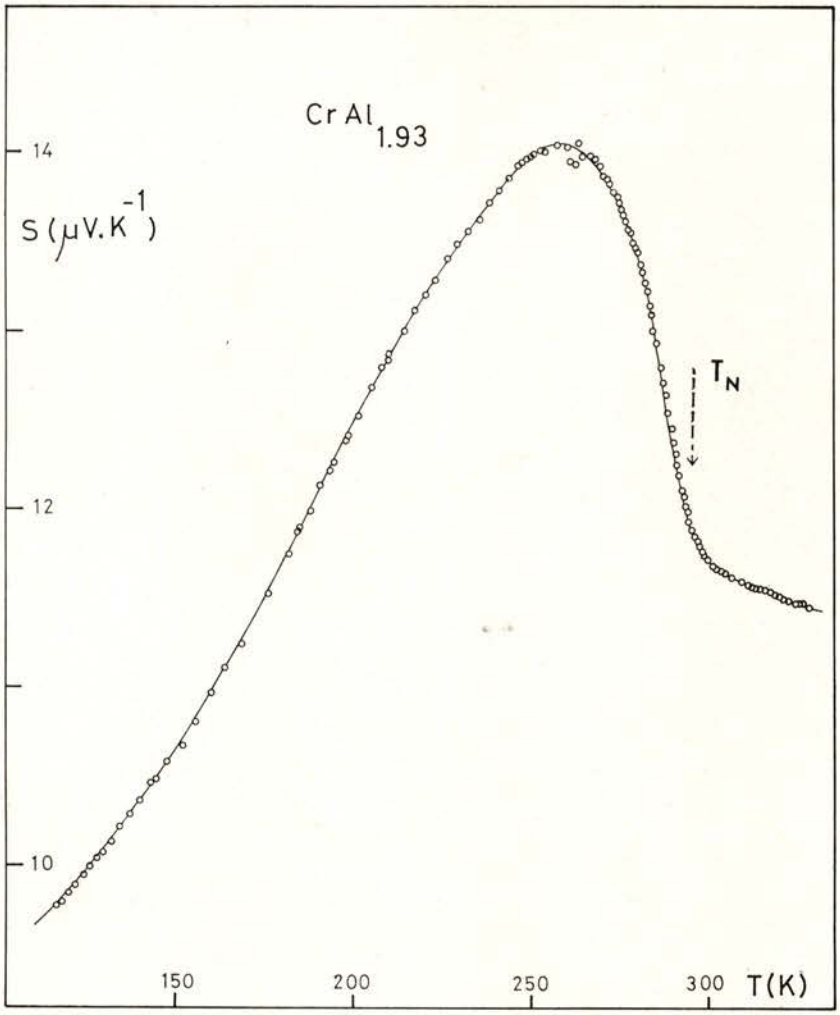

Fig. 3 — S for $Cr\text{-}Al_{1.93}$

of the first-order character of the antiferromagnetic transition, as impurities are added to Cr [13]. Again, the Néel temperature as given by $d\rho/dT$ studies ($T_N = 290$) agrees well with the inflexion

point in the S(T) curve, as shown in the figure by the dotted arrow.

The temperature derivative of the thermoelectric power for $Cr_{98.07}Al_{1.93}$ (Fig. 4) still exhibits a marked «critical» behaviour, with a sharp dip at T_N, in the same manner as for $d\rho/dT$.

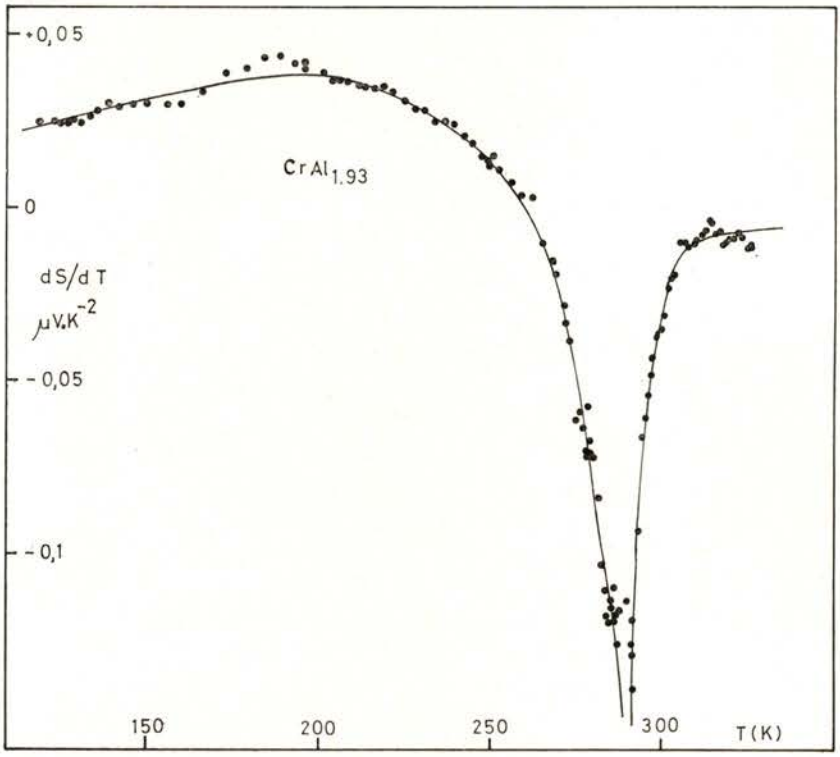

Fig. 4 — dS/dT for Cr-$Al_{1.93}$

The behaviour of S(T) for $Cr_{98.2}Al_{4.8}$ is shown in Fig. 5. The anomaly in the transition region is now much attenuated, and dS/dT (Fig. 6) shows a considerable broadening in the dip around T_N ($\simeq$ 288K). It is possible that this behaviour might be associated with a complex mixing of magnetic phases in the transition regime between incommensurate and commensurate antiferromagnetism [5], [14].

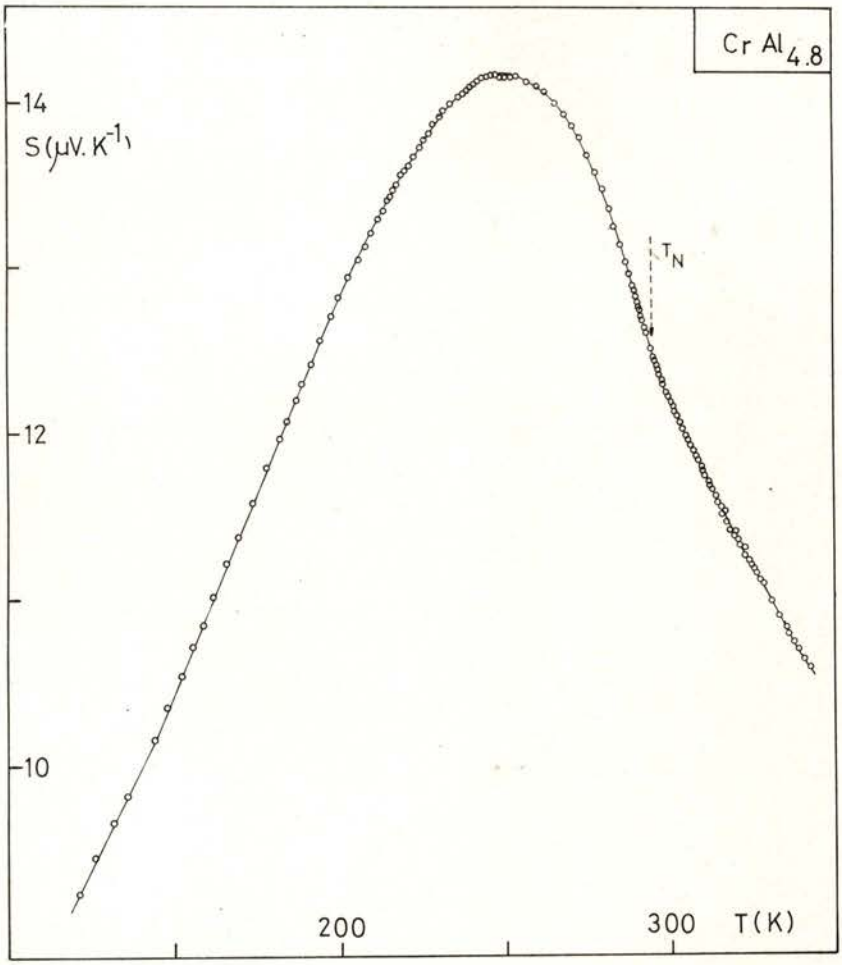

Fig. 5 — S for $Cr\text{-}Al_{4.8}$

Finally, we discuss the importance of heat treatments for the behaviour of the thermoelectric power in Cr-Al.

Fig. 7 shows the thermoelectric power S for *annealed* $Cr_{99.94}Al_{0.06}$ sample (I), compared with S measured in non-annealed sample (II) with the *same* nominal composition. Several points deserve mention here. First, the considerable reduction in the critical temperature (309.8 → 280K), the general broadening of the transition, and the greater dispersion of fhe experimental points for sample II. Second,

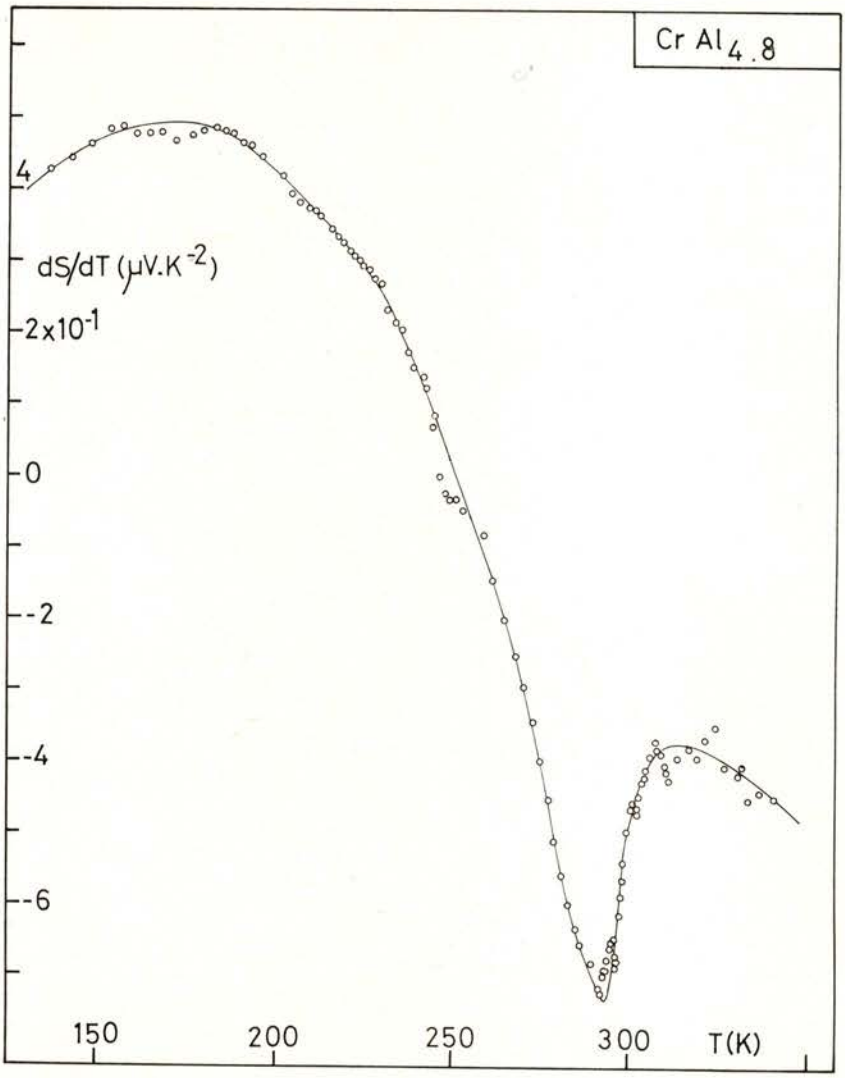

Fig. 6 — dS/dT for Cr-$Al_{4.8}$

two opposite effects appear in S: whereas for sample II (not annealed) S has much higher values in the cooperative phase, the reverse happens in the paramagnetic phase. However, the general shape and the pronounced reduction in S(T) near T_N are still present in the non-annealed sample.

We have also measured S in a sample with higher Al content (0.8 at %, nominal) in the non-annealed condition. As can be seen in Fig. 8, there is a dramatic enhancement in the magnitude of S in the antiferromagnetic state. On the other hand, in the paramagnetic phase there is again a marked reduction with respect to sample I.

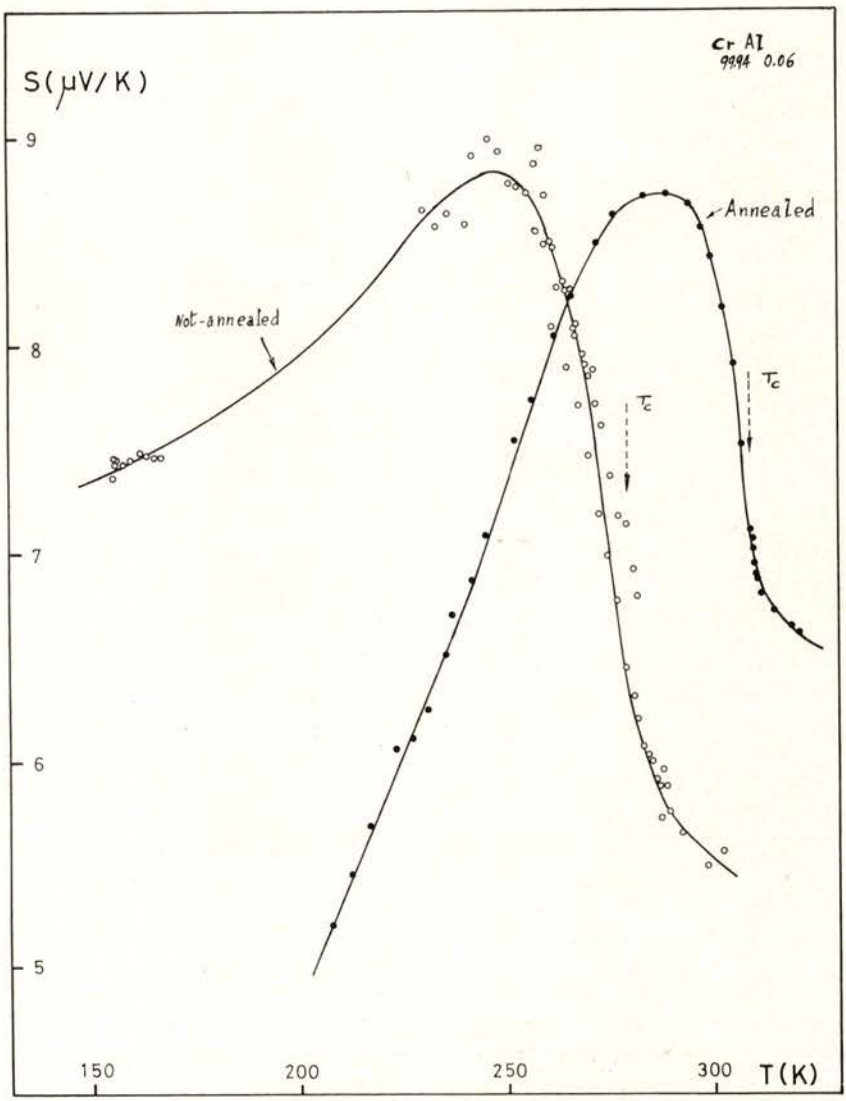

Fig. 7 — S for annealed (and non-annealed) $Cr\text{-}Al_{0.06}$

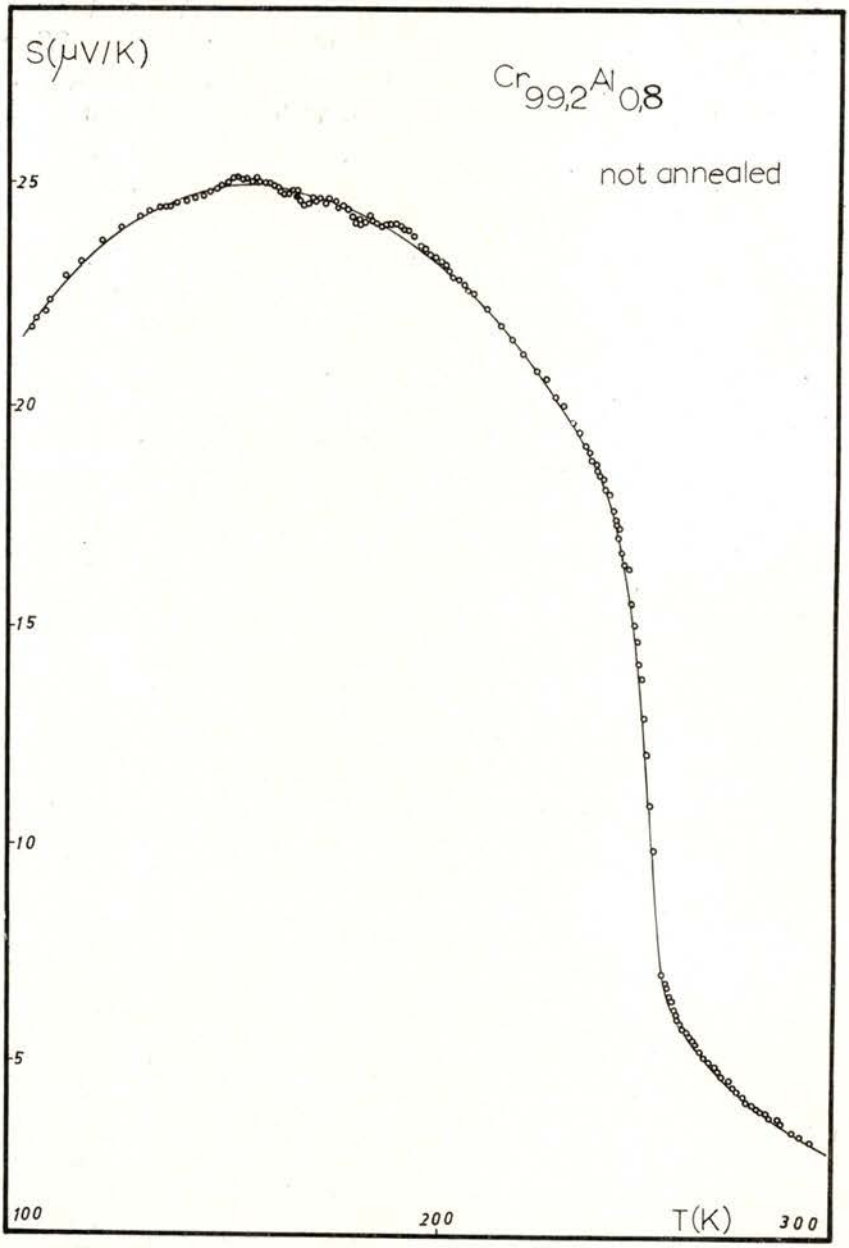

Fig. 8 — S for $Cr\text{-}Al_{0.8}$ (non-annealed)

5 — DISCUSSION

Taking the S curve for the sample with lowest Al content (Fig. 1), let us sumarize the main features in the thermoelectric power:

(i) S has fairly high values in the paramagnetic phase. In this region S is approximately linear in T, with a negative slope ($-dS/dT \sim 10^{-2}$ μV/K²), *but* not extrapolating through the origin.
(ii) S is always positive (hotter junction negative).
(iii) The transition to the antiferromagnetic state enhances S (*positive* contribution).
(iv) A slight minimum is observed at low temperatures.

In order to discuss these features let us review briefly some relevant theory of the thermoelectric power, starting from Mott formulae [15]:

$$S = +\frac{\pi^2 k^2}{3e} . T . \left(\frac{\partial \ln \rho}{\partial \varepsilon}\right)_{\varepsilon_F} \qquad \rho = \left(\frac{m^*}{e^2}\right) \cdot \frac{1}{n} \cdot \frac{1}{\tau} \qquad (1)$$

where e, m^*, n have the usual meanings and τ is the electron relaxation time due to the scattering mechanisms. Combining these two expressions we obtain:

$$S = -\frac{\pi^2 k^2}{3e} . T . \left[\left(\frac{\partial \ln n}{\partial \varepsilon}\right) + \left(\frac{\partial \ln \tau}{\partial \varepsilon}\right)\right]_{\varepsilon = \varepsilon_F} \qquad (2)$$

Assuming a one-band normal metal, several scattering mechanisms for the s-electrons and isotropic relaxation times $\tau_i \propto \varepsilon^{r_i}$ (r_i = small number), one can show that:

$$S = -\frac{\pi^2 k^2}{3e\,\varepsilon_F} . T . \left[\left(\frac{\partial \ln n}{\partial \ln \varepsilon}\right)_{\varepsilon_F} + \sum_i r_i \frac{\rho_i}{\rho}\right] \qquad (3)$$

where $\rho = \sum_i \rho_i$.

The first contribution in the second member depends directly on the band structure of the *carriers*. Assuming these to be s-electrons (as usually happens in normal and transition metals), and a free

electron model with $n \propto \varepsilon^{3/2}$, we get a negative contribution to S, linearly dependent on T:

$$S = -\frac{\pi^2}{2} \cdot \frac{k}{e} \cdot \left(\frac{kT}{\varepsilon_F}\right) \tag{4}$$

Its magnitude is fairly small at ordinary temperatures, since $k/e \sim 86$ μV/Kelvin, $kT \sim 10^{-2}$ *e*V, $\varepsilon_F \sim 5$ *e*V, and $S \simeq$ μV/Kelvin.

The remaining contributions in (3) do not generally give, for the usual scattering mechanisms (impurities, phonons, spin-disorder in the paramagnetic phase) much different results. For example, assuming the predominance of *one* single scattering mechanism we get simply:

$$S = -\frac{\pi^2}{3} \cdot \frac{k}{e} \cdot \left(\frac{kT}{\varepsilon_F}\right) \cdot r_1 \quad \simeq \mu V/\text{Kelvin} \tag{5}$$

Therefore, in order to obtain much higher values for S, as is experimentally observed in most transition metals ($\sim 10-20$ μV/Kelvin), one must seek alternative explanations.

There is no doubt that contributions from *n* in (3) are essentially due to *s*-electrons, since the *d*-electrons in transition metals have very low mobility (narrow *d*-bands, high effective mass). The successful explanation was given by Mott [15], who noticed hat in metals with an incomplete *d*-band the conduction *s*-like electrons can be effectively scattered (e.g. by phonons) *into* vacant states in the *d*-band. Since the transition probability is proportional to the density of states in the *d*-band, $N_d(\varepsilon)$, and this is very high for a narrow *d*-band, the *s-d* interaction dominates the scattering process so that approximately

$$\frac{1}{\tau} \propto N_d(\varepsilon) \tag{6}$$

Therefore, for transition metals we have from (2):

$$S \simeq -\frac{\pi^2}{3} \cdot \frac{k}{e} . kT . \left[\left(\frac{\partial \ln n}{\partial \varepsilon}\right)_{\varepsilon_F} - \left(\frac{\partial \ln N_d}{\partial \varepsilon}\right)_{\varepsilon_F}\right] \tag{7}$$

In transition metals, $N_d(\varepsilon)$ is a very irregular function of ε with very sharp peaks, where $|\partial N_d / \partial \varepsilon|$ is very high. If ε_F, for a particular

element, occurs near such a peak, $|S|$ will be very large. The sign of S can be (+) or (−), depending on whether ε_F is to the right or left of such a peak, respectively. Similar reasonings can be made near a sharp minimum in N_d.

A simple physical explanation of this effect has been given by Kolomoets et al [16]. Electrons in the interval kT around ε_F are subjected to selective scattering due to pronounced variation of N_d over this interval. In the case of an almost filled *d*-band, the electrons which are diffused from the cold junction of the specimen to the hot one are subjected to the more intense scattering. This facilitates a still greater accumulation of electrons at the cold end of the specimen, which means $S < 0$ in *this* case ($dN_d/d\varepsilon < 0$).

We may now understand the high values of S for Cr in the paramagnetic region and from $S > 0$ we conclude that ε_F sits in a point where $(\partial N_d/\partial \varepsilon) > 0$. Due to the irregular shape of $N_d(\varepsilon)$, a slight shift in ε_F within the *d*-band, produced e. g. by an increase in temperature or slight changes in the lattice parameters [17], may produce dramatic changes in $\partial N_d/\partial \varepsilon$. This may be the cause for the reversal in the sign of S which occurs in Cr at fairly high temperatures (~ 1500 K) [17].

Since $(\partial N_d/\partial \varepsilon)_{\varepsilon F}$ will thus generally depend on T, we may understand why the paramagnetic thermoelectric power does not extrapolate through the origin. However, the small linear contribution to S in the paramagnetic state, with a negative slope of $\sim 10^{-2}$ μV/K is probably due to the *n*-term in (7). The negative sign indicates $(\partial n/\partial \varepsilon)_{\varepsilon F} > 0$, i. e., the Fermi level occurs in the first part of the *s*-band.

Let us examine now the pronounced enhancement of S in the antiferromagnetic state, certainly associated with the severe reduction in the electronic concentration *n*, as confirmed from electrical resistivity measurements. Such reduction is caused by the new gaps which appear in the system, due to the extra periodicity introduced by the antiferromagnetic structure [18, 19]. These gaps appear in the conduction *s*-band, affecting therefore the first term in equation (2). Obviously, one such gap (Δ) must occur in the vicinity of the Fermi level in order to affect drastically the transport properties.

This gap increases with the enhancement of the magnetic periodic structure, i. e., with the sub-lattice magnetization; a BCS — like theory describes well the temperature dependence of Δ [20]. By

coincidence, this function is fairly close to the Brillouin function $B_{1/2}$ (T/T_N). At absolute zero we have

$$\Delta\,(0) \simeq 1.76\ kT_N$$

so that larger gaps are expected for the antiferromagnets with higher Néel temperatures.

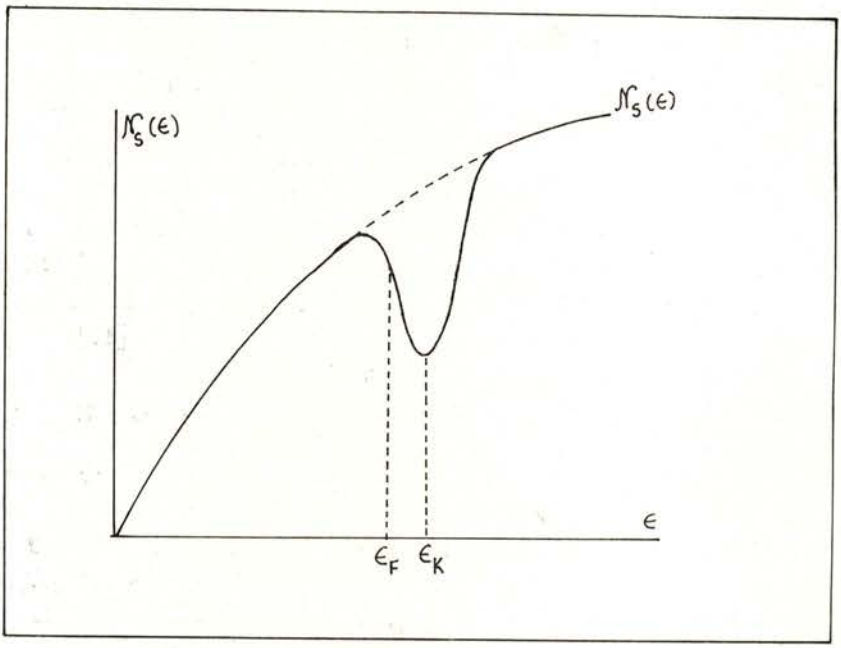

Fig. 9 — Expected effect of antiferromagnetic gap in density of states

The appearance of a gap in the *s*-band will apparently reduce the density of states to zero within the gap-width. However, one must keep in mind the unidimensional character of the antiferromagnetic structure, so that the gap appears only along certain directions in k-space. Therefore, the integrated density of states over all directions, N_s (ε), will simply present a dip in the gap region around a particular energy ε_K [21], as shown in Fig. 9.

Two different cases may appear, whether ε_F occurs below or above ε_K [22]. In the first case, as shown in Fig. 9, the appearance of the magnetic gap produces negative $(\partial n/\partial \varepsilon)\varepsilon_F$ values, which means positive S-values, as occurs in our Cr-Al alloys. The sharp

increase in S is certainly due to the dramatic rise in Δ as T is slightly lowered below T_N. However, this increase soon gets fairly slow, and for $T/T_N \approx 0.7$ almost 85% of the gap full value $\Delta(0)$ has been attained. This means that $(\partial n/\partial \varepsilon)_{\varepsilon_F}$ has reached now an almost constant negative value, and the kT factor in eq. (2) will dominate the physics, making S decrease towards fairly low values. We see therefore the origin of the well marked maximum in S which occurs at intermediate temperatures in our alloys.

Some difficulty arises with the ($Cr_{99.94}Al_{0.06}$) sample at the lowest temperatures reached, where a minimum occurs in S, certainly preceeding a maximum at still lower temperatures, since S must ultimately vanish as $T \to 0K$ (3rd. principle). This maximum has in fact been observed in pure Cr between 50 and 100K, and has been atributted to a phonon-dragg efect [23]. It is known that the addition of impurities always decreases the magnitude of these effects. This may explain why we do not observe such a minima in our curves for the other (more impure) Cr-Al samples in the range of temperatures investigated.

Finally, let us examine the efects of alloying [23], assuming the validity of Mathiessen's rule

$$\rho = \rho_i + \rho_j \tag{8}$$

where ρ is the total resistivity (Cr-Al), ρ_i is the ideal resistivity of the pure solvent metal (Cr), and ρ_j is the resistivity attributable to scattering of conduction electrons by impurities of type j. Substitution of (8) into (1) gives

$$S = + \frac{\pi^2 k^2 T}{3 e} \left[\frac{\partial \ln (\rho_i + \rho_j)}{\partial \varepsilon} \right]_{\varepsilon_F} \tag{9}$$

and a bit of algebra leads to the Gorter-Nordheim relation

$$S = S^{Al} + \frac{\rho^{Cr}}{\rho} (S^{Cr} - S^{Al}) \tag{10}$$

Here S^{Cr} is the diffusion thermopower of pure Cr, and

$$S^{Al} = \frac{\pi^2 k^2 T}{3 e} \left[\frac{\partial \ln \rho^{Al}}{\partial \varepsilon} \right]_{\varepsilon_F} , \tag{11}$$

where ρ^{Al} is the part of the resistivity attributable to scattering of conduction electrons by Al impurities.

In the paramagnetic region, and at a definite temperature, a plot of S vs $1/\rho$ should be a straight line

$$S = a + b(1/\rho) \tag{12}$$

Since ρ increases monotonically with the addition of Al (and most likely $S^{Cr} >> S^{Al}$), we should expect a corresponding monotonic decrease of S in the paramagnetic phase. Although a pronounced decrease occurs in all our samples with respect to Cr, it is by no means monotonic.

This discrepancy is probably due to the violation of the basic assumptions of the theory, *i.e.*, the validity of Matthiessen's rule and the presumption that alloying does not alter the Fermi surface and thereby change S^{Cr}. We think that this last assumption is not justified in Cr-Al, in view of the pronounced alterations in such basic parameters as the electronic specific heat constant (γ) and the Debye temperature (Θ), which are known to occur in this system for low Al concentrations. Thus, thermopower measurements give another indirect confirmation of the great complexity of the Cr-Al system.

Further work is now in progress, in order to obtain a better understanding of the very peculiar physical properties of Cr-Al alloys with low Al content.

The authors wish to thank Dr. M. Ausloos from Univ. Liège, for the very iluminating discussions and his permanent interest and encouragement. Thanks are due also to: Dr. Margarida Costa, from Univ. Coimbra, for providing the inital samples which made possible to start this work; Dr. H. Stone, from Imp. College of London, for preparing the $Cr_{99.94}Al_{0.06}$ sample; Prof. J. M. Araújo, for useful comments and help during the correction of proofs; Eng. Jaime Bessa for the valuable technical assistance; and to Prof. Maia e Costa for the metalographic studies. Finally, the financial support given by the Instituto Nacional de Investigação Científica (INIC, Portugal) and by the NATO Organization (Research Grant no. 1481) is gratefully acknowledged.

REFERENCES

[1] PESSAL N., GUPTA K. P., CHENG C. H., BECK P. A., *J. Phys. Chem. Solids*, **25**, 993 (1964).

[2] KOSTER W., WACHTEL E., GRUBE K., *Z. Metallkde*, **54**, 393 (1963).

[3] CHAKRABARTI D. J., BECK P. A., *J. Phys. Chem. Solids,* **32**, 1609 (1971).

[4] ARAJS S., REEVES N. L., ANDERSON E. E., *J. Appl. Phys.,* **42**, 1961 (1971)

[5] KALLEL A., DE BERGEVIN F., *Solid St. Commun.* **5**, 955 (1967).

[6] COSTA M. M. R., BROWN P. J., *J. Phys. F: Metal Phys.* **7**, 493 (1977).

[7] BENEDIKTSSON G., ASTRÖM H. U., RAO K. V., *J. Phys. F: Metal Phys.* **5**, 1966 (1975).

[8] ARAJS S., RAO K. V., ASTRÖM H. U., DE YOUNG T. F., *Physica Scripta,* **8**, 109 (1973).

[9] See for exemple, POWELL R. F., *Contemp. Phys.* **13**, 159 (1972). Details of our method given at I Encontro de Física da Matéria Condensada, Porto 1976 (to be published).

[10] ARAJS S., ANDERSON E. E., EBERT E. E., *Il Nuovo Cimento* **4B**, 40 (1971).

[11] GIANNUZZI A., TOMASCHKE H., SCHRÖDER K., *Phil. Mag.* **21**, 479 (1970).

[12] SCHRODER K., BAUM N. P., *Phys. Stat. Sol.* **29**, 107 (1968).

[13] ISHIKAWA Y., HOSHING S., ENDOH Y., *J. Phys. Soc. Japan* **22**, 1221 (1967).

[14] KOTANI A., *J. Phys. Soc. Japan,* **36**, 103 (1974).

[15] MOTT N. F., JONES H., *The Theory of the Properties of Metals and alloys,* Dover Publications, p. 305 (1958 edition).

[16] KOLOMOETS, N. V., VEDERNIKOV M. V., *Soviet Phys. Solid State* **3**, 1996 (1962).

[17] STEWART A. D., ANDERSON J. M., *Phys. Stat. Sol.* (b) **45**, K89 (1971).

[18] ELLIOTT R. J., WEDGWOOD F. A., *Proc. Phys. Soc. London* **81**, 846 (1963).

[19] MIWA H., *Progr. Theor. Phys.* **29**, 477 (1963).

[20] OVERHAUSER A. W., *Phys. Rev.* **128**, 1437 (1962).

[21] AUSLOOS M., *J. Phys. F: Metal Phys.* **6**, 1723 (1976).

[22] ABEL'SKII Sh. Sh., IRKHIN Yu. P., *Soviet Phys. Solid State* **13**, 2035 (1972).

[23] BLATT J. J., SCHROEDER P. A., FOILES C. L., GREIG D., *Thermoelectric power of metals,* Plenum Press, p. 38 and p. 174 (1976).

A SELF-CONSISTENT METHOD IN THE STUDY OF THE MAGNETIC PROPERTIES OF RARE-EARTH INTERMETALLIC COMPOUNDS (*)

J. M. MACHADO DA SILVA

Laboratório de Física e Centro de Física da Universidade do Porto

ABSTRACT — The magnetic properties of many Rare Earth compounds can be understood in terms of a crystal field and an exchange interaction. We give an account of the calculation of the direction of magnetization and crystalline electric field in $NdAl_2$. The exchange interaction in this compound is expressed by means of an isotropic molecular field proportional to the magnetization.

The magnetic properties of Rare-Earth metals, salts and alloys have been studied by many investigators, both experimentally and theoretically, in the last few years.

These works have been reviewed by Taylor [1] and by Buschow [2]. The magnetic properties of the Rare-Earths are due to the 4 f electronic shell, shielded by the $5s^2\ 5p^6$ conduction electrons. The spin-orbit coupling in the Rare Earth group is sufficiently strong to give rise to a total angular momentum J whose magnitude is not altered by the crystalline electric field.

The exchange interaction between the Rare-Earth spins is an indirect one via the conduction electrons. It is the competition between the crystalline electric field and the exchange interaction which gives rise to many interesting properties in the Rare-Earth metals, salts and alloys. In the metals, mainly in the heavy Rare-Earths, the exchange interaction is at least one order of magnitude stronger than the crystalline electric field, which is responsible for the complex orientations of the magnetic moments without altering their values; the magnetic moment at 0 K will have the value $g\mu_B J$/ion, where g is the Landé factor and μ_B the Bohr

(*) Results presented at the Conference of the Portuguese Physics Society (Lisbon, February 1978).

magneton. In the salts, the crystalline electric field dominates over the exchange interaction; the crystalline electric field lifts the degeneracy of the ground state leaving a new ground state with lower degeneracy. The exchange interaction does not change, in a first order approximation, the new ground state.

In the Rare-Earth alloys the crystalline electric field and the exchange interaction are comparable. The exchange interaction mixes the different crystalline states, originating a new ground state whose magnetic moment is usually bigger than that of the crystalline ground state. Among Rare-Earth alloys many present a crystalline field with cubic symmetry. The magnetic properties of these alloys are not very difficult to analyse if we can assume an exchange interaction represented by a molecular field proportional to the magnetization.

We assume, very generally, that the magnetization may have one of the three possible directions [1, 0, 0] , [1, 1, 0] , [1, 1, 1] and therefore write the exchange hamiltonian as $\mathscr{H}_{ex} = -g\mu_B \mathbf{H}_{ex} \cdot \mathbf{J}$, where $\mathbf{H}_{ex} = \lambda \mathbf{M}$. We use this term to calculate the saturation moment at 0 K and therefore replace $\mathbf{M}$ by its maximum value $\mathbf{M}_o$. The entire hamiltonian will have the form

$$\mathscr{H} = W \left(x \frac{O_4^0 + 5 O_4^4}{F(4)} + (1 - |x|) \frac{O_6^0 - 21 O_6^4}{F(6)} - c \sum_{k=1}^{3} a_k J_k \right),$$

where

$$Wc\, a_k = g \mu_B \lambda M_{ok}$$

$$M_{ok} = Ng \mu_B < i \mid J_k \mid i > ,$$

$| i >$ being the ground state of the Hamiltonian $\mathscr{H}$. In this expression O_4^0, O_4^4, O_6^0 and O_6^4 are angular momentum operators, and F(4) and F(6) are known coefficients [3]. The parameter x reflects the relative importance of the fourth and sixth order terms, while W is a scale factor which determines the magnitude of the crystal field splittings. Both x and W can be calculated from a point charge model, but reliable results are hardly expected. We have therefore treated both W and x as unknown quantities.

At 0 K the free energy $F = U - TS$ is simply U and therefore the minimum of F is achieved for $\mathbf{H}_{ex}$ parallel to $\mathbf{J}$, i.e. for $\mathbf{M}_o$ parallel to $\mathbf{J}$. In the Hamiltonian, W can be obtained for each value of x, making use of the paramagnetic susceptibility. In the

molecular field model the paramagnetic susceptibility χ is related to the susceptibility χ_o which would be obtained if there was no exchange interaction, by the relations

$$M = \chi H_{ext} = \chi_o (H_{ext} + \lambda M)$$

which gives $$\chi^{-1} = \chi_o^{-1} - \lambda.$$

The inverse of the actual susceptibility χ^{-1} (T) is therefore parallel to χ_o^{-1} (T), since λ is assumed to be independent of temperature; χ_o^{-1} can be computed for any choice of W and x, using only the crystal field hamiltonian. For each value of x a certain value of W results, which makes χ^{-1} parallel to χ_o^{-1}; this same choice of W determines λ, since at T_c, $\chi^{-1} = 0$ and $\lambda \chi_o = 1$.

The magnetic moments for each of the directions [1, 0, 0], [1, 1, 0], [1, 1, 1] and for each value of x are only a function of c. We can therefore determine the value of c which gives the right magnetic moment at 0 K. Finally, using W and c we can calculate $W.c$, which for the correct values of W, x and the direction of the magnetic moment should be the same as $Ng^2\mu_B^2 \lambda \sqrt{<i|J_x|i>^2 + <i|J_y|i>^2 + <i|J_z|i>^2}$, where $|i>$ is the linear combination of the basis vectors $|m>$ which gives the right value of c. We have carried out the calculation as discussed above for the compound $NdAl_2$, for which J=9/2, g=8/11 and the crystal field has cubic symmetry [4]. We have found just one possible solution, where the direction of magnetization is along [1,0,0], and the unperturbed crystalline ground state is a Γ_6 doublet whose parameters are $x \simeq -0.9$, $W \simeq 6$ K. The molecular field coefficient determined in this way was $Ng^2\mu_B^2\lambda \simeq 9$ K.

These compare quite well (see table) with the values $W \simeq 6$ K, $Ng^2\mu_B^2 \lambda \simeq 9$ K, $x = -0.6$ quoted by Houmann et al [5] and used in the interpretation of their inelastic neutron experiments.

TABLE

	Unperturbed crystalline ground state	Direction of easy magnetization	Molecular parameter $Ng^2\mu_B^2\lambda$	Crystal Field Parameters	
				W	x
Experimental	Γ_6	[1,0,0]	$\simeq 9$ K	$\simeq 6$ K	$\simeq -0.6$
Theoretical	Γ_6	[1,0,0]	$\simeq 9$ K	$\simeq 6$ K	$\simeq -0.9$

We have therefore shown that a self-consistent method can be used in the interpretation of the magnetic properties of Rare-Earth alloys; the crystalline electric field and exchange interaction were treated on equal terms and the analyses were carried out for the three directions [1,0,0] , [1,1,0] and [1,1,1] , one of which is the direction of easy magnetization.

REFERENCES

[1] TAYLOR, K. N. R., *Adv. Phys.* **20**, 551 (1971).

[2] BUSCHOW, K. H. J., *Rep. Progr. Phys.* **40**, 1179 (1977).

[3] LEA, K. R., LEASK, M. J. M., and WOLF. W. P., *J. Phys. Chem. Solids,* **23**, 1381 (1962).

[4] BLEANEY, B., *Proc. R. Soc.* **A276**, 19 (1963).

[5] HOUMANN, J. G., BAK, P., PURWINS, H-G and WALKER, E., *J. Phys.* C, **7**, 2961 (1974).

TRANSPORT PROPERTIES IN FERROMAGNETIC RARE EARHT ALLOYS (Tb-Gd) AND TbZn COMPOUND (*) (**)

J. B. SOUSA, R. S. PINTO, M. M. AMADO
J. M. MOREIRA, M. E. BRAGA
Centro de Física da Universidade do Porto, Porto, Portugal
M. AUSLOOS
Int. Centre Theor. Sol. St. Phys. ESIS, Univ. Liège B5, Liège, Belgium
D. HUKIN
Clarendon Laboratory, Univ. Oxford, Parks Road, Oxford, England

ABSTRACT — Very accurate data on the thermoelectric power (S) and the temperature derivative dS/dT have been obtained for a set of poly-and mono-crystalline ferromagnetic Tb-Gd alloys (80–340 K). The critical behaviour of S and dS/dT in the vicinity of the Curie point is analysed in detail; direct comparison is made with the critical behaviour of the electrical resistivity (ρ, $d\rho/dT$).

The critical behaviour of the thermal conductivity (k) near a magnetic phase transition (T_c) is also considered, and a new method to obtain very accurate data near T_c is discussed ($1:10^4$ resolution). Preliminary results are presented for a single crystal of ferromagnetic TbZn.

1 — INTRODUCTION

The theory of the variation of $d\rho/dT$ near the Curie temperature of magnetic metals has been presented by several authors and refined recently [1]. In particular, the qualitative features of $d\rho/dT$ close to T_c are essentially determined by the magnitude of the parameter $k_F d$, where d is the relevant lattice parameter [2]. For low $k_F d$ values, the usual maximum in $d\rho/dT$ at T_c should be immediately

(*) Results presented at the Conference of the Portuguese Physics Society, (Lisbon, February 1978).

(**) Work financially supported by INIC (Portugal), ESIS (Belgium) and NATO Research Grant no. 1481.

followed by a sharp negative minimum, just above T_c. For high $k_F d$ values, the predicted minimum is much attenuated and should occur only at $T \gg T_c$, where the high phonon background in $d\rho/dT$ probably overshadows that feature (Ni-like behaviour).

Our knowledge on transport properties such as the thermoelectric power (S, dS/dT) and the thermal conductivity (K, dK/dT) is rather limited. This comes mainly from the greater complexities inherent in the theoretical treatments of both properties, and from the well known experimental difficulties involved in the *accurate* determination of S and K, as is required for critical phenomena studies. Some relevant literature is given here for the thermoelectric power [3–23] and the thermal conductivity [3, 24–29].

By using a very anisotropic rare-earth binary system (Tb–Gd, hexagonal structure), and by measuring $d\rho/dT$ along a and c axes ($k_{F_c} c \ll k_{F_a} a$) we have made recently the experimental confirmation of the theoretical predictions on the effect of the $k_F d$ parameter in $d\rho/dT$ [30]. In this preliminary report we extend the information on this system to the case of the thermoelectric power (S) and its temperature derivative (dS/dT).

As for the thermal conductivity, we present here a new experimental approach to obtain direct information on the *changes* of the thermal conductivity near a magnetic critical point. A preliminary set of results is given for the case of the thermal conductivity of a monocrystalline ferromagnetic sample of TbZn near its critical point.

2 — EXPERIMENTAL TECHNIQUES

2.1 — *Thermoelectric power*

The thermoelectric power was obtained with a static method. The temperature difference across the sample ($\Delta T \simeq 0.5$ K) was measured with a differential copper/constantan thermocouple, in good contact with (but electrically insulated from) the sample. Another similar thermocouple (T) allowed the determination of the sample mean temperature. The thermoelectric voltage (ΔV) was measured using Cu leads spotwelded to the sample. Both thermocouple and thermoelectric voltages were measured directly on sensitive digital voltmeters, with 10^{-2} μV resolution. Further details of the method can be found elsewhere [33].

2.2 — *Thermal conductivity*

It is well known that the accurate measurement of the thermal conductivity puts serious experimental difficulties. Standard accuracy is of the order of 1 %, but in some exceptional cases accuracies of ~ 0.1 % have been achieved. In this context, it is instructive to compare the intrinsic difficulties inherent to thermal conductivity, thermoelectric power and electrical resistivity measurements.

By far electrical resistivity measurements are the easiest and the most accurate, enabling relative resolutions in ρ as high as 1 part in 10^7. The reason is that, apart from a geometrical factor, the resistivity measurements essentially involve only the accurate measurement of electrical voltages (V). Assuming as typical $V \sim 10^3\,\mu V$, and a nanovolt detection level, we achieve easily $1/10^6$ in resolution.

In a thermoelectric power measurement ($S = \Delta V / \Delta T$), besides an electrial voltage ΔV ($= S.\Delta T$), we must also measure the small difference of temperature ΔT. Assuming the use of a differential thermocouple to measure ΔT, this is equivalent to a voltage measurement ΔV_o ($= S_o . \Delta T$), where S_o stands for the sensitivity of the thermocouple. Since one always aims at the highest possible value for S_o, we generally have $S_o >> S$, $\Delta V_o >> \Delta V$. Therefore, problems in voltage measurements tend to arise first in ΔV. Assuming $S \sim 4\,\mu V\,K^{-1}$, $\Delta T \simeq 0.5\,K$, we are faced with the accurate measurement of a small voltage $\Delta V \simeq 2\,\mu V$. Even with nanovolt resolution, and neglecting all other causes of error, we could not expect better than $5/10^4$ resolution when a difference $\Delta T \simeq 0.5\,K$ is used.

In a thermal conductivity measurement ($K = f\dot{Q}/\Delta T$), apart from a geometrical factor f, we must measure ΔT (equivalent to an electric voltage) *and* the heat flow $\dot{Q}$ *inside* the sample. This last measurement involves the accurate estimate of all the heat losses from the sample, which are far from negligible in every case. This explains the difficulties in achieving even 0.1 % resolution in thermal conductivity measurements.

Let us consider now the special case of critical phenomena, for which very accurate and detailed data are usually required down to 10^{-4} (or better) of the critical point. In spite of these severe demands, nature is sometimes generous to those properties which cannot be measured with the highest accuracy. For example, the relative chan-

ges produced by a magnetic phase transition in the thermoelectric power are usually much bigger than the corresponding ones for the electrical resistivity. For instance, in TbZn near T_c we have $(1/\rho)\,(d\rho/dT) \sim 5.10^{-3}$, whereas $(1/S)\,(dS/dT) \sim 10^{-1}$. Unfortunately, the same does not happen with the thermal conductivity.

Still, some progress can be made here if we remember that the important features in critical phenomena do occur in a very restricted range of temperature, within which the non-critical contributions can hardly change significantly.

Even not being able to measure accurately the crucial quantity $\dot{Q}$, it might be possible to maintain it practically *constant* over a very restricted range of temperature, if one uses a relatively short period of time to bridge it. Then $K \simeq \text{const.}\,(\Delta T)^{-1}$, and the relative changes in K are simply equal to the relative changes in ΔT:

$$\frac{1}{K}\,\frac{dK}{dT} \simeq \frac{1}{\Delta T}\,\frac{d(\Delta T)}{dT}$$

Let us examine in more detail the validity of this approximation, starting from $\dot{Q}$. This is simply given by the difference between the power dissipated in the sample heater ($\dot{Q}_o$) and the heat losses ($\dot{q}$). Using a very stable current and heater winding, it will not be difficult to maintain $\dot{Q}_o$ practically constant over a limited range of temperature.

As to the heat losses $\dot{q}$, which are usually a small (although non-negligible) fraction of $\dot{Q}$, the important point is that they essentially depend on the difference of temperature between sample and surroundings. Assuming, in first approximation, that $\dot{q}$ is proportional to some small power α of ΔT, and taking f and $\dot{Q}_o$ as constants, we can easily show that :

$$\frac{1}{K}\,\frac{dK}{dT} = \frac{1}{\Delta T}\,\frac{d(\Delta T)}{dT}\left[1 + \alpha\,\frac{\dot{q}}{\dot{Q}_o}\right]$$

Therefore, if we keep $\dot{q} \ll \dot{Q}_o$, the relative changes in the thermal conductivity are approximately equal to the corresponding changes in ΔT. This procedure, which only requires the accurate measurement of ΔT, has been used here to investigate the relative changes in the thermal conductivity of TbZn through its magnetic-structural phase transition in the vicinity of 200 K.

3 — THERMOPOWER IN Tb-Gd ALLOYS

3.1 — *Experimental results*

Fig. 1 shows the thermoelectric power S of a polycrystalline ferromagnetic sample of Tb_{75}-Gd_{25}, measured in increasing temperatures from 80 to 340 K. The critical temperature ($T_c \simeq 244$ K), as obtained from electrical resistivity measurements ($d\rho/dT$) [30] is also marked on the graph.

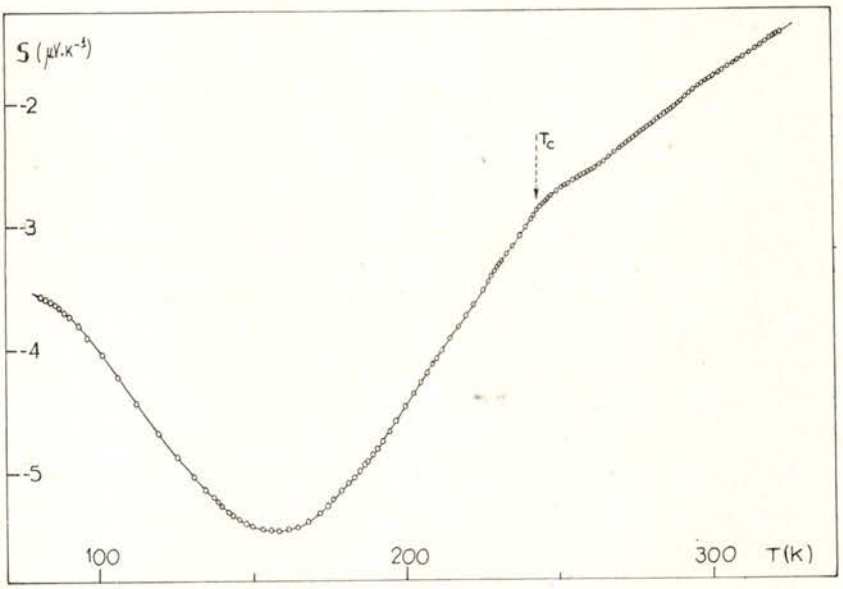

Fig. 1 – Temperature dependence of thermoelectric power (S) in polycrystalline Tb_{75}-Gd_{25}; T_c is the Curie temperature.

The *general* features of S (T), including its magnitude and sign, closely resemble those found in the basal thermoelectric power of pure monocrystalline Terbium [7]. The pronounced minimum in S is still present around 160 K, and the ferro-paramagnetic transition is also accompanied by a pronounced decrease in the slope of the curve when the sample enters the paramagnetic state.

The same qualitative features at the magnetic transition are also found in the electrical resistivity, as shown in fig. 2. The resemblance

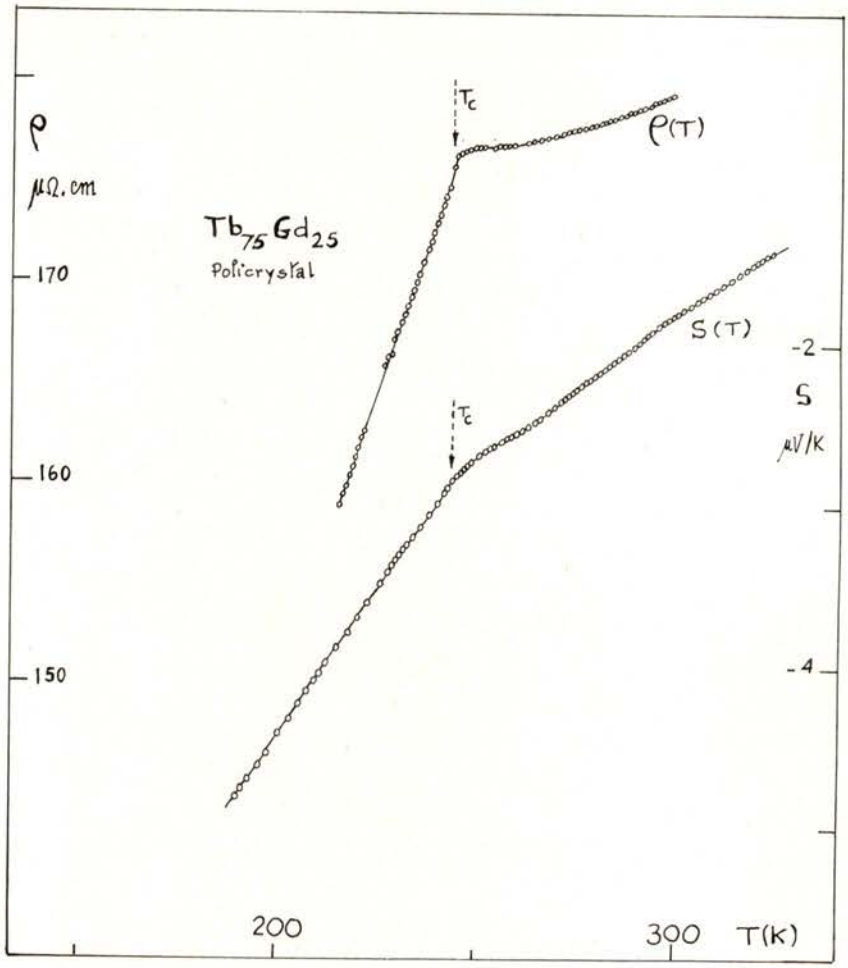

Fig. 2 – Thermoelectric power (S) and electrical resistivity (ρ) for Tb_{75}-Gd_{25} polycrystalline sample.

between the behaviour of the thermoelectric power and the electrical resistivity becomes more evident when we compare the temperature derivatives $d\rho/dT$ and dS/dT (fig. 3).

We alve also measured the thermoelectric power in a *monocrystalline* sample of Tb_{75}-Gd_{25}, with the temperature gradient applied along the c-axis. The behaviour is now very different from that found in the polycrystalline sample, S exhibiting a pronounced hump below T_c and an absolute maximum around T=145 K, as shown in

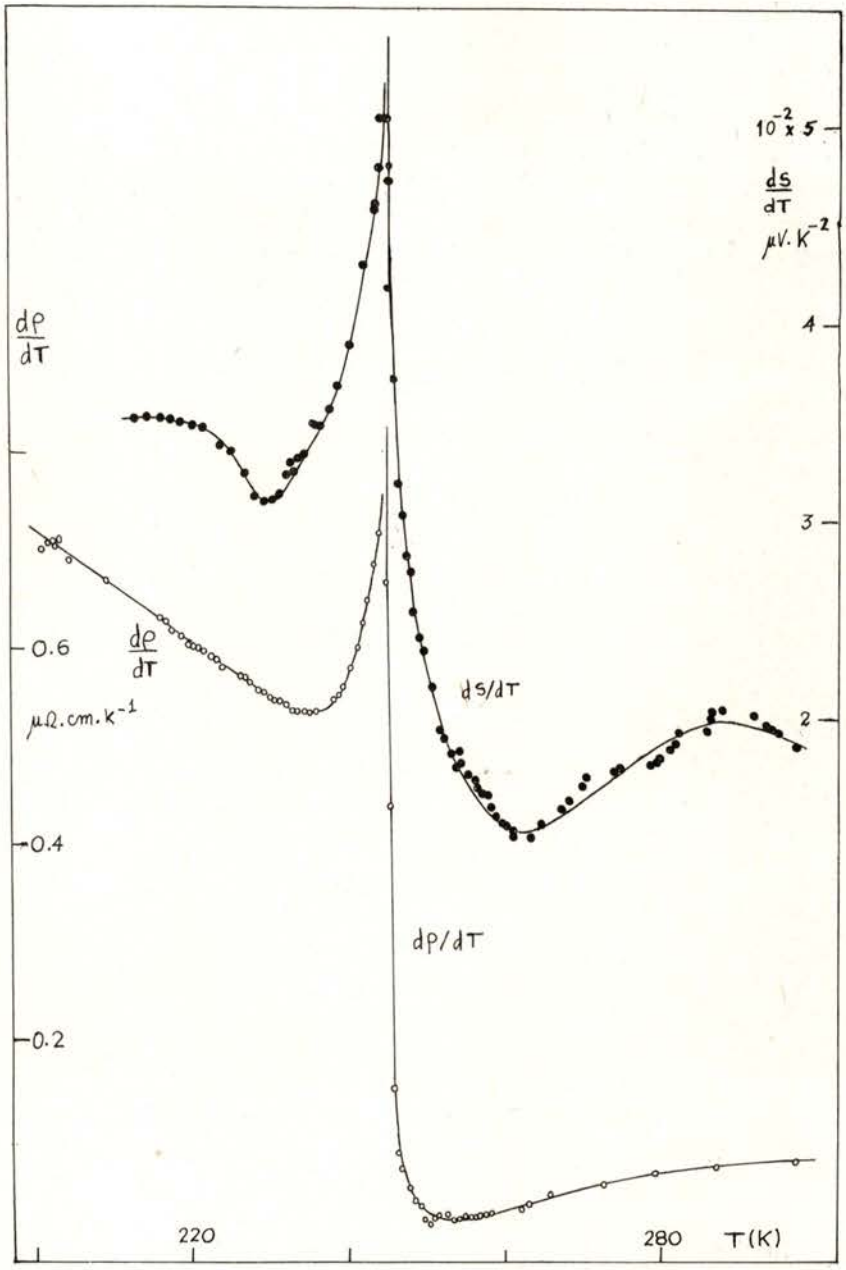

Fig. 3 – Critical behaviour of the temperature derivatives dS/dT and $d\rho/dT$ for polycrystalline Tb_{75}-Gd_{25} sample.

Fig. 4. A similar hump below T_c has been found in the c-axis thermoelectric power of other ferromagnetic heavy rare earth metals like Gd and Tb [6].

The ferro-paramagnetic transition for this monocrystalline sample of Tb-Gd is again associated with a change in the slope of the $S(T)$ curve in the vicinity of $T_c = 244$ K. However, due to the steepness of the $S(T)$ curve in this region, it is difficult to extract further information on the dS/dT details within the critical region.

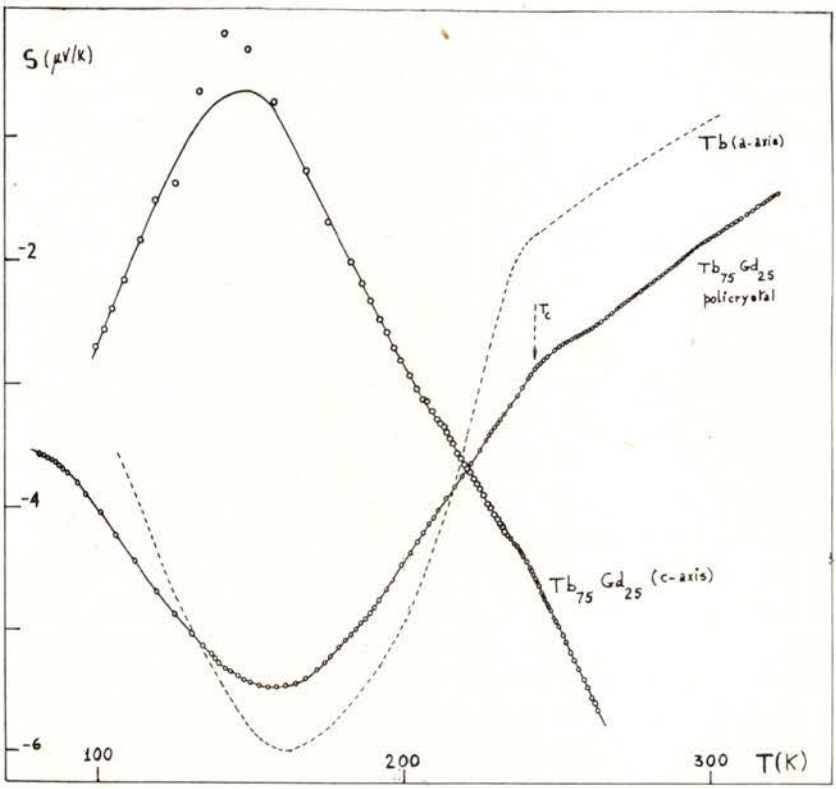

Fig. 4 – S(T) : Tb_{75}-Gd_{25} single crystal along *c*-axis; Tb (*a*-axis); Tb_{75}-Gd_{25} (polycrystal).

In the same figure, a direct comparison is made between our S results for poly- and monocrystalline (*c*-axis) Tb_{75}-Gd_{25} samples *and* those for the basal (*a*-axis) thermoelectric power of pure Tb. The radical differences between the *a*- and *c*-axis behaviour should be appre-

ciated. This pronounced anisotropy in $S(T)$ is in contrast with the relatively small anisotropy of the electrical resistivity curves $\rho(T)$ in the ferromagnetic region [25]. We should also stress the large *negative* slope of S in the paramagnetic region for the c-axis Tb_{75}-Gd_{25} sample, as compared with the *positive* slopes found in the polycrystalline sample, and in the a-axis thermoelectric power of pure Tb.

3.2 — *Discussion*

As pointed above, the thermoelectric power for the polycrystalline Tb_{75}-Gd_{25} sample exhibits a behaviour which closely resembles the one found for the electrical resistivity in the vicinity of the critical point. These similarities have also been found in other ferromagnetic systems, e.g. in Ni and Gd [5] and $GdNi_2$ [8]. For antiferromagnets, the same intimate connection between $d\rho/dT$ and dS/dT has been observed by Fote et al [4] in their detailed and very accurate thermopower measurements in pure chromium. Recently we have shown [31] for an antiferromagnetic $Cr_{99.94}Al_{0.06}$ alloy that $d\rho/dT$ and dS/dT accurately obey a linear relation, both above and *below* T_N. This strongly suggests that both properties are governed by the same critical exponents in the transition region. However, further experiments are still needed, particularly in the range of reduced temperatures down to $\varepsilon \approx 10^{-4} - 10^{-5}$, in order to see if these findings still hold in the *very vicinity* of T_N.

The general features of S below T_c are qualitatively consistent with Kasuya's predictions for the ferromagnetic region [3]. The pronounced rise in S with increasing temperature in the ferromagnetic region is due to the increasing magnetic-spin disorder in the system. However, the rate of increase of S with T slows down as we approach T_c, giving a shallow minimum in dS/dT, as we see in Fig. 3. A similar decrease of dS/dT has also been observed in the basal thermoelectric power of pure Gd [5].

In the paramagnetic region there is a minimum in dS/dT at temperatures slightly above T_c, in the same manner as for $d\rho/dT$ in the same sample. As shown elsewhere [30], this minimum is reminiscent of that found along the c-axis, and such c-axis effects are always present (in some degree) in a polycrystalline sample.

We have not yet measured the thermoelectric power of Tb_{75}-Gd_{25} along a basal axis. Let us then consider the case of the thermoelectric

power along the *c*-axis in the Tb_{75}-Gd_{25} monocrystal. For this direction the general behaviour of S is very anomalous, showing a pronounced hump below T_c, as also happens in other ferromagnetic rare earth metals like Gd [7]. Apparently similar humps below the critical temperature are also present in antiferromagnetic metals, where they can be explained in terms of the appearance of an energy gap in the electron spectrum due to the extra periodicity caused by the spatially modulated antiferromagnetic structure. Obviously, no such explanation can be advanced for a ferromagnetic system.

Legvold [7] relates the humps below T_c in ferromagnetic rare earth metals to the effect of the internal field, which shifts the conduction band into spin-up and spin-down bands. This means that there will be Fermi surface effects which should show up in the thermoelectric power. On the other hand, Tang et al [5] argue that it is possible to reconcile the *a*- and *c*-axis thermoelectric power of Gd by ascribing the humpback anomaly to the effect of anomalous negative lattice expansion along the *c*-axis of Gd.

For this monocrystalline *c*-axis Tb_{75}-Gd_{25} sample, we were not able to extract accurate data on dS/dT to enable a relevant comparison with $d\rho/dT$. We observe, however, that dS/dT gets more negative with the transition to the paramagnetic phase, as also happens with $d\rho/dT$, for which a sharp negative minimum is observed just above T_c.

Work is in progress for the measurement of the thermoelectric power and its temperature derivative in the vicinity of the critical point in other monocrystalline Tb-Gd samples.

4 — THERMAL CONDUCTIVITY IN TbZn

4.1 — *Experimental results*

When using the method described in 2. over a restricted range of temperatures and with $\dot{q}_o$ approximately constant and fairly small, the thermal conductivity is approximately proportional to the inverse of the temperature difference (ΔT) across the sample.

Vacuum conditions in the experimental chamber were 10^{-6} torr, and a temperature rate of 20 mK/minute was used during the measurements. As a compromise between accuracy and detail we adopted $\Delta T \simeq 1$ K.

Fig. 5 shows, apart from a constant factor, the inverse of ΔT as a function of temperature for a ferromagnetic monocrystalline sample of TbZn, which is a compound with CsCl structure and a critical temperature $T_c \simeq 200\,K$ [32]. Our results span the temperature interval from 180 to 210 K. In contrast to the case of the thermoelectric power of TbZn, the K-variation is rather weak over the range

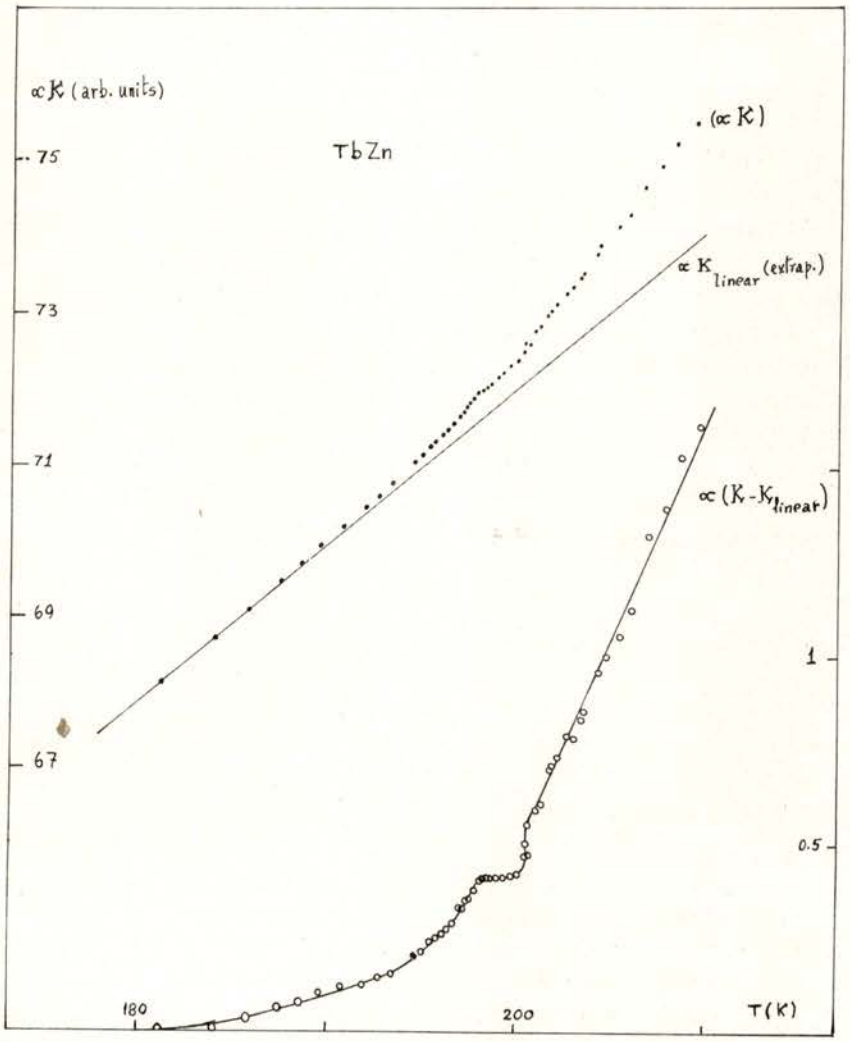

Fig. 5 — Upper curve: Thermal conductivity for single crystal of ferromagnetic TbZn (k_{lin} = linear extrapolation from low temperature data).
Lower curve: (k-k_{lin}) shows clearly the anomaly near the Curie temperature.

of temperatures investigated ($K^{-1}\,dK/dT \sim 10^{-3}$ as compared to $S^{-1}\,dS/dT \sim 10^{-1}$ Kelvin^{-1}).

Away from the transition region, K shows an almost linear dependence on T, but with a different magnitude in the (positive) slopes below and above T_c. In particular, the thermal conductivity increases with T at a much bigger rate in the paramagnetic region. This is in contrast with the monotonic decrease of the thermal conductivity in the case of ordinary metals, towards an approximately constant value at high temperatures. We observe however that positive dK/dT values in the paramagnetic phase have also been observed in pure Tb, Ho and Gd, both along a- and c-axes [25].

In order to get further insight into the details of the thermal conductivity in the transition region, we subtracted from $K(T)$ a linear background, as also shown in Fig. 5. We see that K increases very rapidly with T as we approach the critical region from below, showing a well marked kink between ~ 198 and 199 K.

In the critical region K has a very complex behaviour, and we cannot exclude the possiblity of an almost discontinuous step in K at a temperature fairly close to 200 K. On the whole, it generally looks as if the critical fluctuations cause a depression on the thermal conductivity below its general trend in the neighbourhood of the critical region. In the paramagnetic region, the marked increase in dK/dT should be emphasized again.

4.2 — *Discussion*

The scarce experimental information generally available on the thermal conductivity, and the fairly small changes which occur near T_c, preclude at the present stage of our knowledge, any discussions on such matters as the values for the critical exponents of dK/dT within the critical region. Therefore, only the general features of the thermal conductivity will be considered here.

The sharp increase of the slope dK/dT in the paramagnetic state can be easily understood in terms of an enhancement in the electron scattering, due to the spin-disorder in the paramagnetic phase. Qualitatively, we can describe this effect in terms of a modified Wiedemann-Franz law, since previous measurements in Tb [25] show that $K\rho/T$ keeps a fairly constant value ($L \neq L_o$, Lorentz number) in the first part of the paramagnetic region, with a particular

(constant) value for each crystal orientation. Assuming this, we should have for the thermal conductivity,

$$K = L.T.\frac{1}{\rho_o + \alpha T + \rho_s}$$

where ρ_o is the (constant) impurity resistivity, αT is the phonon contribution to the electrical resistivity, and ρ_s is the spin-disorder resistivity, which is constant in the paramagnetic phase. In magnetic metals at ordinary temperatures, the spin-disorder dominates the phonon-term, and we should have

$$K \simeq \frac{L}{\rho_o + \rho_s}.T$$

i.e. a linear increase of K with T, in good agreement with experiment. In the ferromagnetic phase, magnetic order increases, which decreases the electron-spin scattering, lowering therefore ρ_s. In particular ρ_s can get smaller than αT, and for reasonably pure materials we should then have

$$K \simeq L/\alpha$$

which gives a zero slope for the thermal conductivity curve.

Finally, let us consider the behaviour of K near $T_c \simeq 200\,K$. Here, we can say that the thermal conductivity appears depressed with respect to the extrapolated behaviour from both sides of the critical region. It therefore suggests the existence of extra scattering mechanisms for the heat carriers in the system (electrons, magnons *and* phonons). We think that phonons might play a relevant role, since the magnetic transition in TbZn at 200 K is accompanied by a structural transition, from a tetragonal ($T < T_c$) to a cubic lattice structure ($T > T_c$).

Since the phonon spectrum is directly affected by any alteration in the atomic spacing, and above all by a change in symmetry, we should not rule out the possibility of such an explanation for the almost discontinuous increase in K at temperatures slightly above 200 K.

Further work is still needed to clarify this interesting behaviour of K near a magnetic-and-structural phase transition. We are certainly

aware of the great experimental difficulties ahead, and also that we are almost in the limit of potentialities in our present techniques.

The authors wish to thank Dr. P. Morin from Univ. Grenoble, for providing the TbZn sample which made possible our thermal conductivity measurements. The technical assistance of Eng. Jaime Bessa is also gratefully acknowledged.

Finally, the financial support given by the Instituto Nacional de Investigação Científica (INIC, Portugal) and by the NATO organization (Research Grant no. 1481) is gratefully acknowledged.

REFERENCES

[1] ALEXANDER, S., HELMAN, J. S., BALBERG, I., *Phys. Rev.* **B13**, 304 (1976).

[2] GELDART, D. J. W., RICHARD, T. G., *Phys. Rev.* **B12**, 5175 (1975).

[3] KASUYA, T., *Prog. Theor. Phys.* **22**, 227 (1959).

[4] FOTE, A., AXLER, R., SHÜRMANN, H., MIHALISIN, J., *Phys. Rev.* **B8**, 2099 (1973).

[5] TANG, S. H., KITCHENS, T. A., CADIEN, F. J., CRAIG, P. P., *Proc. Int. Low Temp. Phys. Conf.* **LT13**, p. 385 (1972).

[6] SILL, L. R., LEGVOLD, S., *Phys. Rev.* **137**, A1139 (1965).

[7] LEGVOLD, S., in *Magnetic Properties of Rare Earth Metals*, ed. R. J. Elliott, *Plenum Publ. Co.*, p. 365 (1972).

[8] ZORIC', I., THOMAS, G. A., PARKS, R. D., *Phys. Rev. Lett.* **30**, 22 (1973).

[9] AUSLOOS, M., *Sol. St. Comm.* **21**, 373 (1977).

[10] KOLOMOETS, N. V., VEDERNIKOV, M. V., *Sov. Phys. Sol. St.* **3**, 1996 (1962).

[11] ABEL'SKII, Sh. Sh., IRKHIN, YU P., *Sov. Phys. Sol. St.* **13**, 2035 (1972).

[12] ORA ENTIN-WOHLMAN, DEUTSCHER, G., *Phys. Rev.* **B14**, 4015 (1976).

[13] TANG, S. H., CRAIG, P. P., KITCHENS, T. A., *Phys. Rev. Lett.* **27**, 593 (1971.)

[14] KITCHENS, T. A., CRAIG, P. P., TANG, C. H., *Phys Rev.* **7**, 1198 (1973).

[15] THOMAS, G. A., LEVIN, K., PARKS, R. D., *Phys. Rev. Lett.* **29**, 1321 (1972).

[16] SOUMURA, T., MAEDA, T., *J. Phys. Soc. Japan* **41**, 1544 (1976).

[17] TAYLOR, P. L., *Phys. Rev.* **7**, 1197 (1973).

[18] ARAJS, S., ANDERSON, E. E., EBERT, E., *Il Nuovo Cimento* **4B**, 40 (1971).

[19] MEADEN, G. T., SZE, N. H., *J. Low Temp. Phys.* **1**, 567 (1969).

[20] MAC INNES, W. M., HUGUENIN, R., *Phys. Lett.* **44A**, 51 (1973).

[21] TANG, S. H., PH. D. THESIS, *SUNY at Stony Brook,* New York (1972).

[22] TANG, S. H., CADIEN, J. J., KITCHENS, T. A., CRAIG, P. P., *Magnetism and Magnetic Materials,* AIP Conf. Proc. n.º 5, American Inst. Phys. New York, 1265 (1971).

[23] PAPP, E., MAPOTHER, D. E., (to be published).

[24] MEADEN, G. T., RAO, K. V., TEE, K. T., *Journal de Physique, Supplément, Tome* **32**, C1-342 (1971).

[25] NELLIS, W. J., LEGVOLD, S., *Phys. Rev.* **180**, 582 (1969).

[26] BAYS, D. W., LEGVOLD, S., *Phys. Rev.* **174**, 377 (1968).

[27] STERN, H., *J. Phys. Chem. Solids* **26**, 153 (1964).

[28] SUEZAKI, Y., MORI, H., *Prog. Theor. Phys.* **41**, 1177 (1969).

[29] ARAJS, S., COLVIN, R. V., *Phys. Rev.* **136,** A439 (1961).

[30] SOUSA, J. B., AMADO, M. M., BRAGA, M. E., PINTO, R. S., MOREIRA, J. M., HUKIN, D., *Comm. on Phys.* **2**, 95 (1977).

[31] SOUSA, J. B., PINTO, R. S., AMADO, M. M., MOREIRA, J. M., BRAGA, M. E. (to be published).

[32] MORIN, P., *Champ Cristallin et Couplage Magnétoélastique dans les Composés de Terres Rares de Structure Type Cs Cl,* Univ. Crenoble, CNRS, A. O. 9223 (1975).

[33] PINTO, R. P., SOUSA, J. B., MOREIRA, J. M., AMADO, M. M., BRAGA, M. E., GARTON, G., *Portgal Phys.* **10**, 61 (1979).

THE APPLICATION OF NEUTRON ACTIVATION ANALYSIS AND NUMERICAL TAXONOMIC METHODS TO THE STUDY OF ANCIENT FINE GREY POTTERY (*)

J. M. P. CABRAL and M. A. GOUVEIA
Laboratório de Física e Engenharia Nucleares, Sacavém, Portugal

ABSTRACT — The concentrations of three major elements and fourteen trace elements in selected sherds of Iron Age and first century A.D. fine grey ceramics, found at five different archaeological sites in Portugal, were determined by instrumental neutron activation analysis. These concentrations were used to calculate distance matrices which where then subjected to cluster analysis employing SAHN methods, k-means cluster analysis and principal components analysis, to group the sherds according to the overall similarity of their compositional features. The results showed that roughly equivalent groupings appeared regardless of the numerical method used. Three major clusters were recognized corresponding to three different sites, namely Conímbriga, Santa Olaia and Lisbon, suggesting that the ceramics from these sites were made locally. Some of the sherds studied showed patterns suggesting trade relationships between sites.

1 — INTRODUCTION

At Conímbriga, as well as at other archaeological sites in continental Portugal, large quantities of sherds of dark-grey pottery have been recovered, which possess the common feature of being very carefully made. Although mineralogical analysis has been unsuccessful to discriminate between those sherds, archaeologists were able to define two classes based on traditional archaeological attributes (shape, finishing and presence in a particular stratigraphic level), namely: (i) Iron Age fine grey pottery and (ii) Roman fine grey pottery dating from the first century A. D. [1].

(*) Results presented at the Conference of the Portuguese Physics Society (Lisbon, February 1978).

Important archaeological questions concerned with the study of this pottery are, on the one hand, whether it is possible to define local centers of manufacture and, on the other, whether one is able to establish for each burial deposit any relationships between the Iron Age grey ware and the Roman grey ceramics.

To answer this type of question, activation analysis has been frequently used and the analytical data processed by methods of numerical taxonomy [2].

In the present paper we report the results of the application of instrumental neutron activation analysis and of some numerical taxonomic methods to a group of sherds of this fine grey pottery, which were made available by Drs. A. Alarcão and J. Alarcão of the *Museu Monográfico de Conímbriga*. This contribution is the first part of a study aimed at answering the questions referred to above.

2 — EXPERIMENTAL

Analysed sherds. The provenances and identifications of the sherds studied are presented in table 1.

TABLE 1 — Provenances and identifications of sherds

Sherd	Provenance	Class according to archaeological evidence
C 16 – C 24 C 26 C 28 – C 32	Conímbriga	Iron Age
C 25, C 27 C 33 – C 36	Conímbriga	Roman (first century A. D.)
F 37	Fiães (Feira)	»
SO 1 – SO 9	Santa Olaia (Montemor-o-Velho)	Iron Age
TA 10	Tavarede (Figueira da Foz)	»
L 11 – L 15	Lisbon	»

Sample preparation. The sherds were sampled by using the procedure employed by Abascal, Harbottle and Sayre [3]. A fraction of about 1 g was usually removed from each sherd. Each of those fractions was then carefully homogenized by mixing, and oven-dried at 110°C before use. Samples of about 100 mg of each homogenized powder were finally weighed out and sealed into ultrahigh purity containers. The samples for short irradiations were introduced into small polyethylene cans. Those for long irradiations into fused quartz ampoules.

Standards. Six U. S. Geological Survey standard rocks, namely G-2, BCR-1, GSP-1, AGV-1, PCC-1 and DTS-1, were used as standards. Weighed amounts of the first four, dried and packaged in the same fashion as the ceramic samples, were included with each set of 16–20 cans in the short irradiations. Weighed amounts of all six, prepared in the same manner, were included with each set of 30–35 ampoules in the long irradiations.

Irradiations. All irradiations were done in the core grid of the RPI reactor (Sacavém) at a neutron flux of $\sim 3.5 \times 10^{12}$ n.cm^{-2}.s^{-1}. For each sample two irradiations were made: a 10 minutes one and a 70 hours one (14 hours periods on 5 successive days). Flux monitors were irradiated together in order to measure differences in neutron fluxes at the positions where samples and standards stood.

Counting. The equipment used for measurements was a gamma-ray spectrometer consisting of a 54 cm^3 Ge(Li) coaxial detector (Ortec) connected through an Ortec model 120-4 F preamplifier and an Ortec 452 amplifier to an Intertechnique Didac 4000 multichannel analyser. This system had a FWHM resolution of 2.5 keV at 1.33 MeV energy. The spectrometric data were collected on punched paper tape for further processing. Since the polyethylene cans and silica tubes contribute no significant blank, samples and standards were left in their irradiation containers for radioassay. Measurements of the gamma spectra were made at four decay times: 2 hours after the short irradiation, for counting ^{56}Mn; 20 hours after the same irradiation, for counting ^{24}Na and ^{42}K; 7–10 days after the long irradiation, for counting ^{140}La and ^{177}Lu; and 28–35 days after this

irradiation, for counting ^{141}Ce, ^{233}Pa, ^{51}Cr, ^{181}Hf, ^{131}Ba, ^{134}Cs, ^{46}Sc, ^{86}Rb, ^{182}Ta, ^{59}Fe, ^{60}Co and ^{152}Eu. The gamma-ray energies used in the determination of each element are given in table 2.

TABLE 2 — Radionuclides and energies of gamma-rays used in the determination of element concentrations

Element	Radionuclide	Energy of gamma-rays used (keV)
Sodium	^{24}Na	1368
Potassium	^{42}K	1525
Rubidium	^{86}Rb	1077
Cesium	^{134}Cs	796
Barium	^{131}Ba	496
Scandium	^{46}Sc	889
Lanthanum	^{140}La	1596
Cerium	^{141}Ce	145
Europium	^{152}Eu	1408
Lutetium	^{177}Lu	208
Hafnium	^{181}Hf	482
Thorium	^{233}Pa	312
Tantalum	^{182}Ta	1221
Chromium	^{51}Cr	320
Manganese	^{56}Mn	847
Iron	^{59}Fe	1099
Cobalt	^{60}Co	1332

Spectrum analysis. All spectra were processed in a PDP 15 computer using computer programs which are adaptations of the GELIAN and OLIVE programs [4], [5]. The values of each element in each standard rock used for calculating element concentrations in samples were taken from data tabulated by Abascal, Harbottle and Sayre [3].

3 — METHODS OF DATA ANALYSIS

Data matrix. The data used in this study are the results obtained by applying the instrumental neutron activation analysis method described above, which are shown in table 3. Thus our original data matrix has 37 columns representing the 37 sherds (OTU's) to be grouped, and 17 rows representing the concentrations of the 17 elements (attributes) which have been analysed in those sherds.

Scaling. Standardization oi attributes was applied to the raw data in order to equalize the size of each attribute. In this method one computes the mean and standard deviation of the states of each attribute and expresses each state as a deviation from the mean in standard deviation units. Logarithmic transformation was also applied for the purpose of seeing how the final classification would be affected by the scaling method.

Measures of similarity. Two dissimilarity coefficients were calculated, namely the mean Euclidean distance, d_{jk}, and the mean character difference, $(\mathrm{MCD})_{jk}$, defined as follows:

$$d_{jk} = \left[\frac{1}{n} \sum_{i=1}^{n} (X_{ij} - X_{ik})^2 \right]^{1/2}$$

$$(\mathrm{MCD})_{jk} = \frac{1}{n} \sum_{i=1}^{n} | X_{ij} - X_{ik} |$$

where n is the number of attributes, X_{ij} is the transformed value of OTU j for attibute i and X_{ik} is the transformed value of OTU k for the same attribute.

Cluster analysis. This analysis was carried out by various methods: some SAHN methods (complete linkage, UPGMA and size-of-cluster methods) and a nonhierarchic method (k-means). The results of SAHN methods were represented by phenograms. Cophenetic correlation coefficients between the dissimilarity values implied by the phenograms and those of the original dissimilarity

TABLE 3 — Oxide concentrations for specimens of Iron Age and early-Roman sherds from Conímbriga, Santa Olaia, Fiães (Feira), Tavarede and Lisbon

	C16	C17	C18	C19	C20	C21	C22	C23	C24	C25	C26	C27
Na_2O %	0,240	0,164	0,198	0,324	0,712	0,259	0,303	0,204	0,192	0,205	0,195	0,193
K_2O %	3,95	4,04	3,73	4,32	3,73	4,28	4,64	3,99	4,11	3,70	4,48	4,34
Rb_2O	295	356	331	324	248	335	320	330	349	328	354	388
Cs_2O	24	33	26	25	22	26	24	29	31	24	31	30
BaO	456	512	564	490	997	417	582	683	602	475	568	518
Sc_2O_3	20	18	18	25	30	14	14	17	18	16	16	17
La_2O_3	87	70	68	84	65	81	65	72	76	67	73	97
CeO_2	156	114	130	145	128	194	135	125	145	110	130	224
Eu_2O_3	1,7	1,5	1,6	2,3	2,3	1,4	1,4	1,6	1,8	1,1	1,6	2,5
Lu_2O_3	0,99	0,84	0,91	0,99	1,27	0,99	0,86	0,86	0,99	0,81	0,88	1,02
HfO_2	10,1	9,2	9,3	10,0	7,0	14,5	9,8	9,4	9,6	9,5	10,5	12,4
ThO_2	33,7	34,8	34,8	33,4	20,4	47,7	34,2	35,0	36,3	39,6	38,8	52,5
Ta_2O_5	3,9	5,5	6,0	4,3	2,9	6,9	6,1	5,7	6,3	5,7	5,7	5,8
Cr_2O_3	84,0	66,5	68,4	110	132	45,6	48,8	61,7	59,5	49,3	47,1	51,5
MnO	169	217	274	358	261	403	184	240	279	156	202	371
Fe_2O_3%	4,42	4,53	5,00	6,22	3,81	5,50	3,92	4,71	4,60	3,87	4,83	6,69
CoO	9	7	7	17	20	17	11	17	24	14	6	9

TABLE 3 — Oxide concentrations for specimens of Iron Age and early-Roman sherds from Conímbriga, Santa Olaia, Fiães (Feira), Tavarede and Lisbon

	C28	C29	C30	C31	C32	C33	C34	C35	C36	F37	S01	S02
Na_2O%	0,411	0,219	0,208	0,231	0,210	0,212	0,260	0,190	0,178	0,150	0,349	0,603
K_2O %	4,05	3,78	3,71	4,39	4,29	4,67	3,89	4,07	4,18	3,58	3,44	3,90
Rb_2O	286	325	312	318	351	379	783	352	355	297	267	230
Cs_2O	23	30	25	26	32	30	54	30	30	25	24	21
BaO	670	502	588	478	497	552	1520	396	521	406	496	690
Sc_2O_3	16	16	16	16	18	17	37	19	18	18	27	25
La_2O_3	61	77	65	61	65	92	63	91	76	77	60	64
CeO_2	130	152	131	135	130	164	282	214	149	110	129	109
Eu_2O_3	1,4	1,7	1,5	1,4	1,6	2,2	2,9	2,1	1,5	1,5	2,2	2,0
Lu_2O_3	0,77	0,95	0,79	0,76	0,87	1,04	0,73	1,05	0,79	0,77	0,81	1,03
HfO_2	7,5	12,1	9,1	9,8	9,6	11,5	21,5	11,7	9,7	10,4	7,3	8,0
ThO_2	30,9	42,8	32,7	36,5	36,7	44,3	85,5	46,4	43,8	47,0	20,6	21,3
Ta_2O_5	4,8	5,9	6,1	5,1	6,0	5,8	11,4	6,9	6,1	6,2	2,9	2,9
Cr_2O_3	59,1	55,4	70,7	61,5	70,5	57,2	139	75,3	54,7	60,6	116	105
MnO	252	195	231	297	214	251	245	359	273	148	199	201
Fe_2O_3%	4,19	6,07	4,55	4,59	5,21	5,12	11,7	5,56	6,21	6,23	4,58	3,73
CoO	13	14	30	9	6	10	15	11	10	7	13	13

TABLE 3 — Oxide concentrations for specimens of Iron Age and early-Roman sherds from Conímbriga, Santa Olaia, Fiães (Feira), Tavarede and Lisbon

	S03	S04	S05	S06	S07	S08	S09	TA10	L11	L12	L13	L14	L15
Na_2O %	0,623	0,728	0,435	0,427	0,335	0,595	0,591	0,158	0,259	0,851	1,10	0,819	1,06
K_2O %	3,54	4,15	2,98	3,36	4,85	3,81	4,42	3,25	4,02	4,04	3,43	4,02	4,81
Rb_2O	242	241	215	249	377	255	285	205	301	243	198	242	248
Cs_2O	20	22	14	22	25	22	32	25	39	14	11	13	15
BaO	746	888	788	563	669	872	554	566	577	740	467	736	779
Sc_2O_3	22	27	18	24	15	28	23	26	26	31	24	31	31
La_2O_3	67	70	50	64	67	61	51	47	56	40	38	40	49
CeO_2	139	118	96,4	104	160	121	112	82,9	116	83,5	86,2	79,0	117
Eu_2O_3	2,0	2,3	1,7	2,1	1,6	2,2	1,6	1,8	2,3	1,7	1,6	1,6	2,3
Lu_2O_3	0,96	1,06	0,77	0,95	0,81	0,99	0,62	0,74	0,90	0,67	0,64	0,68	0,76
HfO_2	9,1	7,6	8,2	8,9	11,4	8,2	6,9	6,3	6,4	5,6	5,7	5,7	6,0
ThO_2	23,3	22,9	16,6	21,8	37,9	22,0	23,1	20,8	23,1	15,1	13,8	15,5	16,6
Ta_2O_5	3,1	2,9	2,4	2,9	5,3	3,1	3,2	3,6	3,5	2,0	2,4	2,0	2,4
Cr_2O_3	90,0	116	73,9	101	45,3	124	88,0	106	104	148	123	146	151
MnO	209	283	709	191	202	166	332	162	194	192	328	169	241
Fe_2O_3 %	3,68	3,55	3,52	4,21	4,32	4,07	3,50	5,67	4,92	5,33	5,43	5,31	5,85
CoO	15	14	12	14	8	12	11	35	29	16	21	14	26

matrices were calculated. The k-means method was applied repeated times for partitions into k clusters from $k = 2$ to $k = 7$.

Ordination methods. Ordination of samples in A-space was carried out by employing principal components analysis. The variation accounted for by a given number of principal components as well as the cophenetic correlation between distances in the three first principal components space and the fully dimensional one were calculated.

Computations. They were carried out by employing the MINT computer programs system [6] as well as the following programs: NADIST [7], AGCLUS [8] and BUILD [9]. These programs were run either at the computer center of the *Instituto Gulbenkian de Ciências, Oeiras,* or at the computer center of the Universities of Lisbon.

4 — RESULTS AND DISCUSSION

Fig. 1 shows the results of the UPGMA clustering obtained with the standardized data and using the mean Euclidean distance as a measure of dissimilarity. The cophenetic correlation coefficient was 0.91 indicating a good agreement of the phenogram with the original dissimilarity matrix. A very good agreement was also found between the phenogram illustrated in fig. 1 and the result of the UPGMA clustering based on log transformed data and the same distance measure. This observation confirms an earlier conclusion [10] that change of scaling method does not seem to affect significantly the clustering of archaeological ceramics.

The results of the other mentioned hierarchic methods obtained with the identically transformed data and the same dissimilarity measure did not reveal any important disagreement with the result presented in fig. 1. Moreover, it was found that change of the distance coefficient did not produce any significant effect on the classification. It appears therefore that the phenogram of fig. 1 can be considered as a good representation of the taxonomic structure no matter which scaling method, distance measure and SAHN method of clustering has been employed.

This phenogram suggests that the Conímbriga samples, Santa Olaia samples and Lisbon samples may be compositionally distingui-

shable. In fact four clusters are discerned, two composed of practically all Conímbriga sherds, another composed primarily of Santa Olaia sherds and the fourth composed of nearly all Lisbon sherds. Most of Iron Age Conímbriga sherds (twelve out of fourteen) are in one cluster.

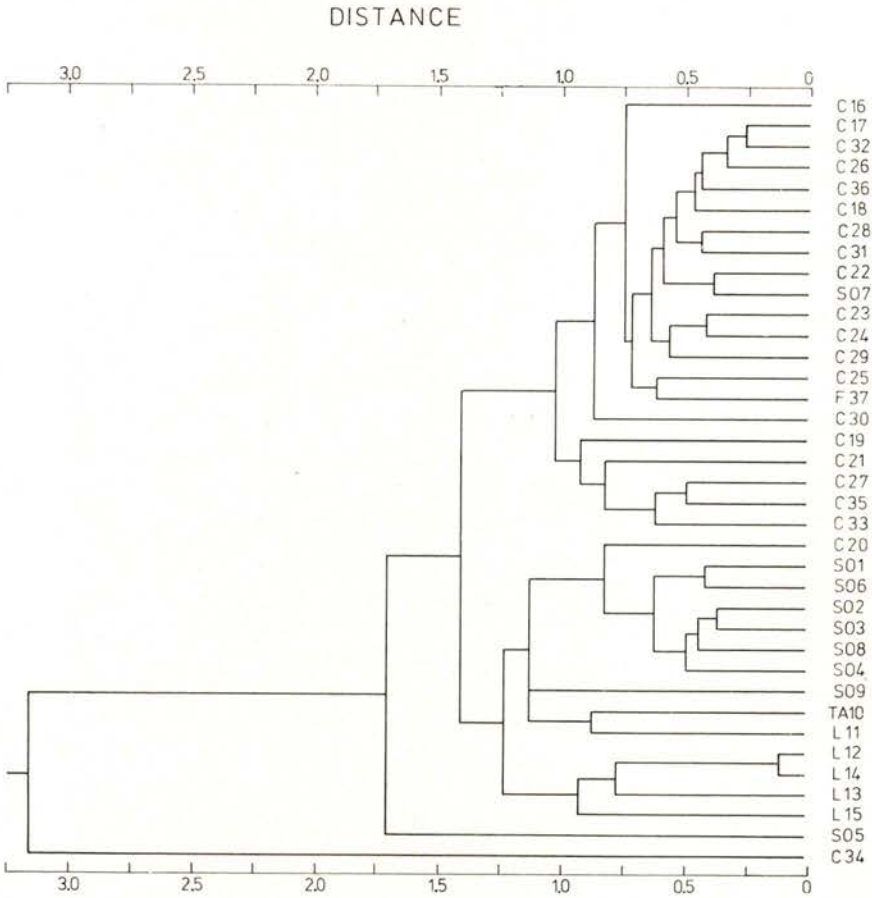

Fig. 1 — Phenogram of 37 sherds of fine grey ceramics based ou UPGMA cluster analysis of mean Euclidean distances. The cophenetic correlation coefficient was 0.91

Three of the six first century A.D. Conímbriga sherds are in the other. It is also shown that one of these sherds (C 34) is an outlier, another (C 20) belongs to the Santa Olaia cluster and that, inversely, a Santa Olaia sherd (SO 7) pertains to one of the Conímbriga clusters.

In addition, the phenogram indicates that the only sherd from Fiães is included in this Conímbriga cluster and that the only sherd from Tavarede, as well as one of the Lisbon samples (L 11), may be members of the Santa Olaia cluster.

The results of the k-means analysis are presented in table 4. Since C 34 sample was previously identified as an outlier, it was not considered in this analysis. These results confirm most of the conclusions from SAHN methods of cluster analysis. As a matter of fact the set of sherds was first split into two basic groups with all Conímbriga sherds (except C 20), the SO 7 and F 37 samples in one, and the residue in the other. It should be pointed out that the group of Conímbriga sherds always remained separated in all further subdivisions. This result suggests that probably the two clusters of Conímbriga sherds found by using SAHN methods of clustering are not significantly different. At the three-cluster partition the residue was split into two groups, one composed mainly of Santa Olaia samples (except SO 5, SO 7 and SO 9), the C 20 and L11 samples, and the other of the residual ones. The four-cluster partition divided the second residue into two groups, one consisting of three Lisbon samples and the other of the SO 5, TA 10 and L 13 samples. At the five-cluster partition there was no split and only a very slight rearrangement of samples was observed, which consisted in the attachment of L 13 sample to the group of Lisbon sherds and of the TA 10 sample to the group of Santa Olaia sherds, so that the SO 5 sample remained alone in one group. The six-cluster and seven-cluster partitions divided the group of Santa Olaia sherds into subgroups, leaving the Conímbriga cluster, the Lisbon cluster and the SO 5 sample as they were at the five-cluster level.

In order to know how many clusters should be considered the values of the reduction of within-cluster variance for each attribute between the k-cluster and $(k+1)$-cluster partitions, measured by means of the appropriate «F-ratio», as well as the values of the overall mean square ratio, were compared [9]. Those values indicate that partitions with $k > 5$ are not justifiable.

The results of ordination by principal components analysis are presented in fig. 2. The relative contribution of the original attributes to the first three principal components, as well as the percentages of the total variance accounted for by them, are shown in table 5. It should be pointed out that, as in the case of the application of k-means algorithm, the C 34 sample was not considered in this ana-

TABLE 4 — Results from application of the k-means algorithm

Number of clusters	Error of partition	Denotation and composition of clusters			
k = 5	271.2	CC — *Conimbriga cluster* All Conimbriga sherds (except C 20) + SO 7 + + F 37	SOC — *Santa Olaia cluster* All Santa Olaia sherds (except SO 5 and SO 7) + + C 20 + TA 10 + L 11	SO 5	LC — *Lisbon cluster* All Lisbon sherds (except L 11)
k = 4	281.1	C C	SOC — TA 10	SO 5 + TA 10 + L 13	LC — L 13
k = 3	311.7	C C	SOC — (TA 10 + SO 9)	SO 5 + SO 9 + TA 10 + LC	
k = 2	361.6	C C	SOC + SO 5 + LC		
k = 1	612.0	CC + SOC + SO 5 + LC			

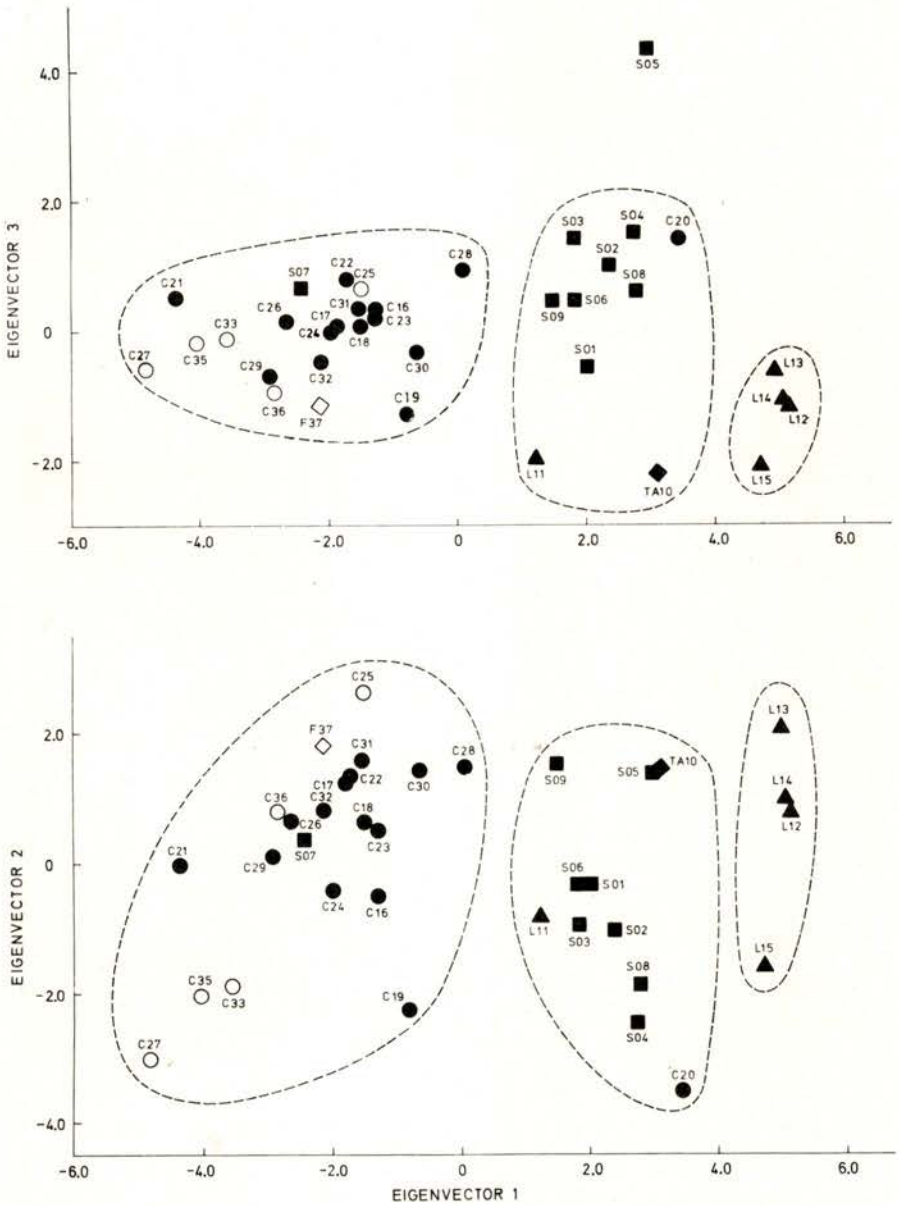

Fig. 2 — Ordination plots of 36 sherds of fine grey ceramics from principal components analysis. Signs and letters denote findspots: ● C (Conímbriga); ■ SO (Santa Olaia); ◆ TA (Tavarede) and F (Fiães); ▲ L (Lisbon). Closed signs denote Iron Age ceramics, open ones represent first century A. D. ceramics.

TABLE 5 — Relative contribution of attributes to first principal components and relative importance of these components

Attributes	Principal components		
	1	2	3
1 Na_2O %	0.827	-0.166	0.028
2 K_2O %	-0.391	-0.216	-0.223
3 Rb_2O ppm	-0.913	-0.050	-0.124
4 Cs_2O »	-0.719	-0.094	-0.202
5 BaO »	0.623	-0.377	0.374
6 Sc_2O_3 »	0.839	-0.387	-0.294
7 La_2O_3 »	-0.840	-0.451	0.054
8 CeO_2 »	-0.777	-0.476	0.031
9 Eu_2O_3 »	0.249	-0.890	-0.128
10 Lu_2O_3 »	-0.298	-0.807	0.254
11 HfO_2 »	-0.908	-0.139	0.151
12 ThO_2 »	-0.972	-0.019	-0.082
13 Ta_2O_5 »	-0.934	0.152	-0.072
14 Cr_2O_3 »	0.884	-0.316	-0.254
15 MnO »	-0.057	-0.086	0.510
16 Fe_2O_3 %	-0.313	-0.083	-0.739
17 CoO ppm	0.427	-0.055	-0.386
Relative importance of components indicated by			
eigenvalue	8.446	2.410	1.471
% variance	49.7	14.2	8.65
cumulative % variance	49.7	63.9	72.5

lysis. These results are a most useful complement to the former's. On the one hand, they provide a very satisfactory overall view of relationships between samples in three dimensions (the cophenetic correlation coefficient between the distances implied in the three-dimensional ordination and the original distance matrix is equal to 0.966 and the proportion of the variation accounted for by the three dimensions is equal to 72.5%). On the other, they provide very

useful information by themselves, particularly as far as the attribute weights on principal components are concerned. In this study the first component, accounting for 49.7 % of the variance, may be seen from table 5 to be appreciably related to several attributes, but most markedly to sodium, rubidium, scandium, lanthanum, hafnium, thorium, tantalum and chromium concentrations. The second component, accounting for 14.2 % of the variance, is heavily influenced by two attributes: europium and lutecium concentrations. The third component, accounting for 8.7 % of the variance, is mainly influenced by the iron concentration.

As seen in fig. 2 the results of ordination by principal components analysis also confirm most of the conclusions from SAHN methods of cluster analysis.

5 — CONCLUSIONS

Activation analysis and numerical taxonomy were applied to study 37 sherds of dark-grey pottery, 30 of the Iron Age, found at Conímbriga, Santa Olaia, Tavarede and Lisbon, and seven of the first century A.D., found at Conímbriga and Fiães. The study of this pottery has posed some questions to archaeologists, in particular whether one centre of manufacture supplied those and other sites or they were made at the sites, and whether it is possible to establish any relationships between ceramics of both periods.

The results obtained show that roughly equivalent groups are produced regardless of the numerical taxonomic method used. Three major clusters are recognized corresponding to three different sites, namely Conímbriga, Santa Olaia and Lisbon. The answer to the first question is then clear, that the sherds from these three sites were very likely made at the sites. However, doubts still subsist as far as Tavarede and Fiães sherds are concerned, since only one specimen from each site was analysed. Moreover, the results indicate that Conímbriga and Santa Olaia clusters include at least one sherd found at Santa Olaia and Conímbriga, respectively, suggesting trade relationships between sites. The results show in addition that, with the exception of one sherd (C 34), there are probably no significant differences in compositional patterns between Iron Age and first century A. D. Conímbriga sherds.

We are deeply grateful to Drs. A. Alarcão and J. Alarcão, who requested our help in solving some problems in their study of fine grey ceramics, for their enthusiastic support. Grateful acknowledgment is made to the LFEN Reactor Department, to the *Centro de Cálculo Científico* of the *Instituto Gulbenkian de Ciência, Oeiras,* and to the *Centro de Cálculo* of the Universities of Lisbon, for providing special assistance. We thank the International Atomic Energy Agency and the *Secretaria de Estado da Cultura* for financial support. We are also grateful to Dr. M. B. Lima and Prof. R. R. Sokal for their comments on the first draft of the manuscript.

REFERENCES

[1] ALARCÃO, J. (1975). La céramique commune locale et régionale, *Fouilles de Conimbriga,* V. Paris: E. de Boccard.

[2] HARBOTTLE, G. (1976). Activation analysis in archaeology. *A Specialist Periodical Report, Radiochemistry,* Vol. 3, 33-72. London: The Chemical Society, 141 pp.

[3] ABASCAL-M., R., HARBOTTLE, G. and SAYRE, E. V. (1974). Correlation between terra cotta figurines and pottery from the valley of Mexico and source clays by activation analysis. In C. W. Beck (ed.), *Archaeological Chemistry,* 81-99. Washington, D. C.: American Chemical Society, 254 pp.

[4] OP DE BEECK, J. (1972) *GELIAN program.* Institute for Nuclear Sciences, University of Ghent.

[5] OP DE BEECK, J. (1974) *OLIVE program.* Institute for Nuclear Sciences, University of Ghent.

[6] ROHLF, F. J. (1971). *MINT, User's manual.* Dept. of Ecology and Evolution, State University of New York, Stony Brook, New York.

[7] BIEBER, JR., A. M. (1973). *NADIST program.* Brookhaven National Laboratory, Upton, New York.

[8] OLIVER, D. C. (1973). *AGCLUS, an aggregative hierarchical clustering program.* Dept. of Psychology and Social Relations, Harvard University, Cambridge, Massachusetts.

[9] HARTIGAN, J. A. (1975). *Clustering algorithms.* New York: John Wiley & Sons, 351 pp.

[10] CABRAL, J. M. P. Effect of the scaling method on the classification of archaeological ceramics by numerical taxonomy. (To be published).

HIGH RESOLUTION γ- AND X-RAY SPECTROMETRY OF RADIOACTIVE MINERALS (*)

F. BRAGANÇA GIL and J. C. SOARES

Centro de Física Nuclear da Universidade de Lisboa,
Faculdade de Ciências, Lisboa, Portugal

ABSTRACT — Gamma ray-spectrometry has been used in qualitative and quantitative analysis of uranium ores. However till recently only NaI(Tl) detectors were used and due to the complexity of the spectra this was a great limitation. In this work we used Ge(Li) an Ge (hyperpure) detectors and so it was possible to show that the method was applicable to the measurement of uranium concentration as low as 0,02 %. On the other hand it was possible to detect the presence of other non radioactive elements through the analysis of their characteristic X-rays produced by autofluorescence.

1 — INTRODUCTION

In recent years the search for minerals of uranium and thorium has been pursued with great effort and even the detection of these radioactive elements in mineral ores with low concentration is assuming special relevance. It is then obvious that the use of the most advanced techniques of nuclear spectrometry will play an important role in this field.

Some years ago [1 – 6] the use of γ-spectrometry with NaI(Tl) detectors made possible the identification of certain groups of elements of the radioactive families. However the measurement of the concentration of several of these elements was dependent on proving the existence of radioactive equilibrium. In fact the low resolution of the

(*) Results presented at the Conference of the Portuguese Physics Society (Lisbon, February 1978).

NaI(Tl) detectors did not enable the unambiguous identification of uranium and thorium γ-rays.

Nowadays the introduction of the Ge(Li) detectors in this field [7] has changed the situation since it became easier to verify whether or not the radioactive equilibrium is present. Nevertheless the great complexity of the γ-ray spectrum in the range of energy below 120 keV calls for the use of Ge (hyperpure) detectors. These have the advantage of a high resolution in the range 10 to 120 keV together with a good efficiency and an almost transparency for γ-rays of higher energies. On the other hand the presence of these high energy γ-rays will induce the production of X-rays by autofluorescence. The detection of the X-rays can then be used as another technique to identify the elements present in the mineral ore. Furthermore this last technique makes possible the search for the other non radioactive elements. This by itself can be of great help to establish the chemical composition of the mineral ore.

2 — γ-RAY SPECTROMETRY

In figure 1 we show a γ-ray spectrum of a sample of an uranium ore from the mine of Cunha Baixa, Nelas (Portugal), obtained with a coaxial Ge(Li) detector with 25 cm^3 of active volume. It is possible to see several peaks corresponding to transitions with energies between about 150 keV and 2200 keV. The resolution (2 keV for the 662 keV peak) enabled us to separate several transitions corresponding to the decays of ^{226}Ra, ^{214}Po and ^{214}Bi. The first of these elements belongs to the group III of Rosholt [8] and the last two to the group IV.

As it is well known these groups were defined in such a way that each one started with a long lived element except the group IV which contains the ^{222}Rn. On the other hand all the elements in the same group of Rosholt are in radioactive equilibrium and have radiochemical and geochemical affinities. So group I contains the elements of the uranium-radium series from ^{238}U till ^{234}U; groups II and III contain only one element each, ^{230}Th and ^{226}Ra respectively; group IV contains the elements from ^{222}Rn till ^{210}Tl and finally to group V belong the elements from ^{210}Pb till ^{206}Pb.

The study of the decay scheme of all the nuclei of the uranium family shows that for the group I the γ-rays have energies equal to

or less than 93.5 keV. In groups II and V we only observe one γ-ray in each namely the 67.8 keV corresponding to the decay of ^{230}Th and the 46.5 keV from the decay of ^{210}Pb. These low energy γ-rays can all be seen with a Ge(Li) detector but the measurements made from the spectrum are spoilt by the presence of X-rays.

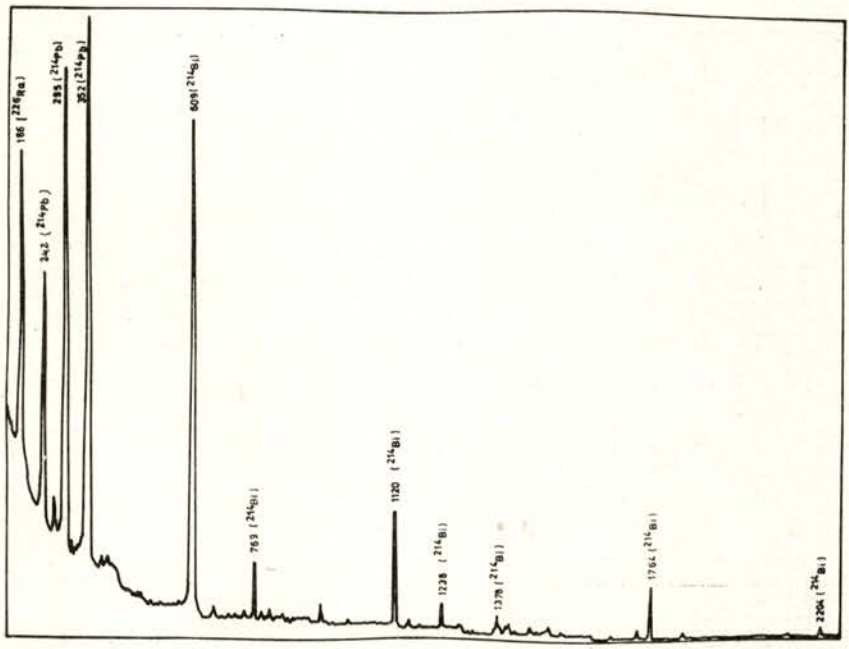

Fig. 1 — γ-ray spectrum of a sample of an uranium ore, obtained with a coaxial Ge(Li) detector (25 cm^3 of active volume), for transitions with energies between about 150 keV and 2200 keV.

In figure 2, we show a spectrum of a sample of uranium where it is possible to see transitions from 40 keV to 600 keV. Besides the peaks already present in the previous figure it is now possible to identify the 46.5 keV, 67.8 keV and 93.5 keV transitions mentioned above. We will see below the advantage of using a Ge (hyperpure) detector in these measurements.

Recently Mubarakmand et al. [9] used the direct γ-ray spectrometry in the measurement of absolute concentrations in uranium

ores. They have claimed that this method is accurate for uranium concentrations above 0.1%. However their measurements were based on the study of the 93.5 keV transitions and as we have shown in figures 1 and 2 a large contribution to the 93.5 keV peak is due to X-rays and Compton background. Furthermore if in the sample there is ^{232}Th and its daugther nuclei the 84.4 keV transition from

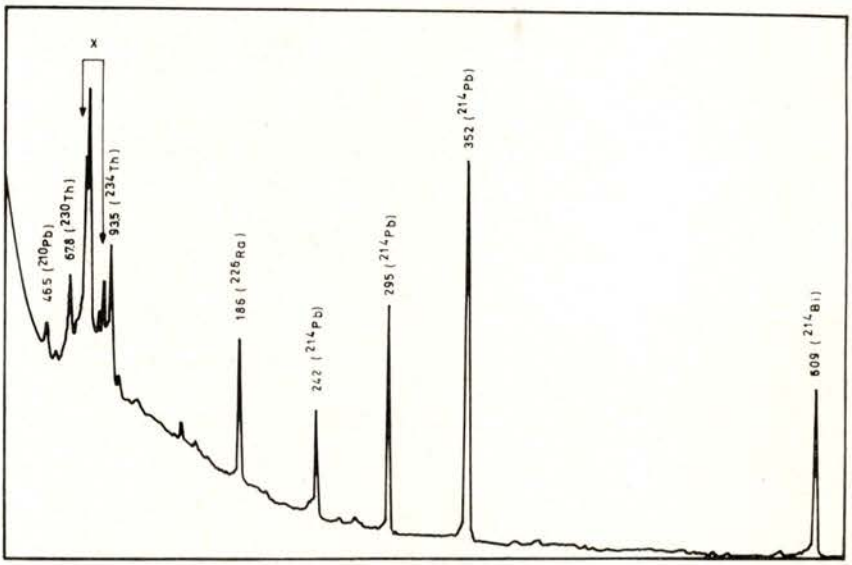

Fig. 2 — γ-ray spectrum of a sample of an uranium ore, obtained with a coaxial Ge(Li) detector (25 cm^3 of active volume), for transitions with energies between about 40 keV and 600 keV.

the decay of ^{228}Th and the 99 keV transition from the decay of ^{228}Ac are sufficiently near the 93.5 keV peak to mask the measurements. These problems led us to review the study of the γ-spectrum of radioactive minerals. Our aim is twofold:

i) to judge the possibilities of γ-ray spectrometry to measure concentration of uranium below 0.1%;
ii) to apply a similar technique to mineral ores containing a mixture of uranium and thorium.

As far as point i) is concerned we have obtained the γ-ray spectrum of samples containing 0.02 %, 0.04 % and 0.1 % of uranium. The corresponding activities were calculated from the counting rate of the

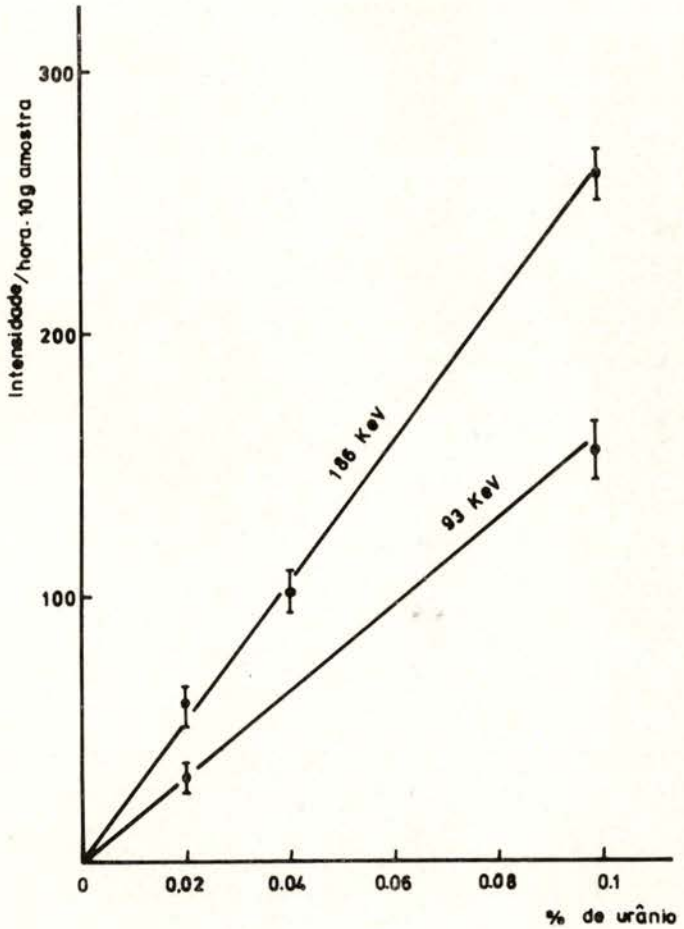

Fig. 3 — Activities of uranium ore standards measured from 93.5 keV and 186 keV transitions.

following peaks: 93.5 keV (group I), 186 keV (group III) and 352 keV and 609 keV (group IV). The linearity for the first two transitions is very good as can be seen in figure 3 but the points corresponding to the last sample and the last two transitions deviate clearly from

the straight line (fig. 4). This shows that in this sample the nuclei of group IV are not in radioactive equilibrium. In fact the ratios between the intensites calculated from fig. 4 and those actually measured gave a constant value equal to 1.6 .

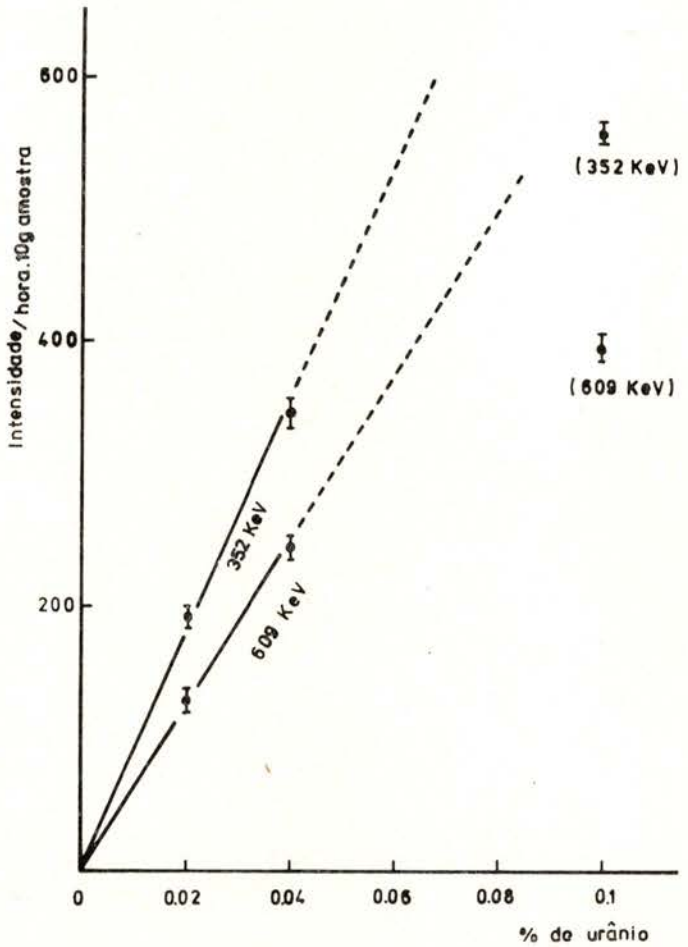

Fig. 4 — Activities of uranium ore standards measured from 352 keV and 609 keV transitions.

As far as point ii) is concerned we decided to study a specially unfavourable sample for this kind of measurements since it contained 0.04 % of uranium and 1 % of thorium. We show in figure 5 that although the measurements are practically impossible using the

93.5 keV or 242 keV transitions, they are still possible with the 186 keV, 352 keV and 609 keV transitions. These latter transitions are completely separated from the ones corresponding to the decay of thorium and its daughter nuclei.

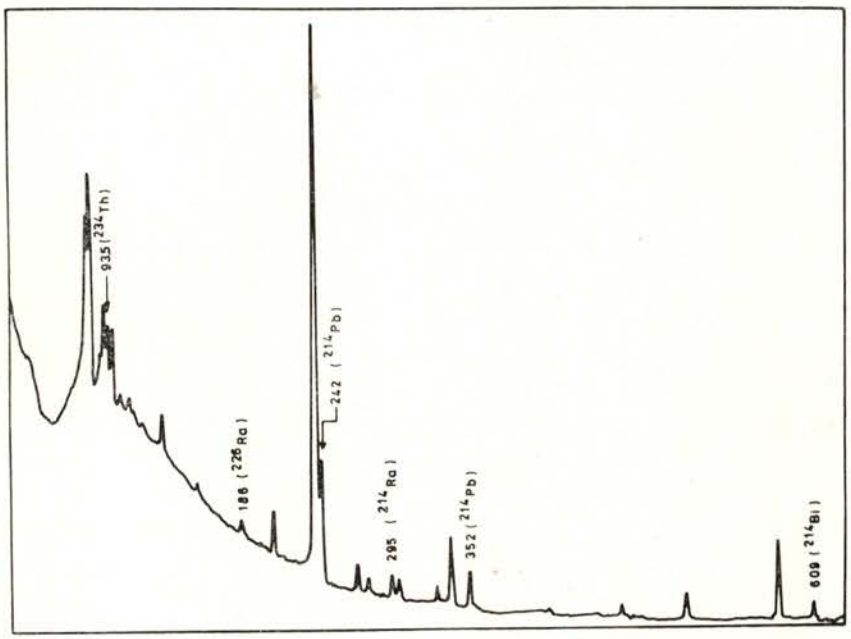

Fig. 5 — Spectrum of a ore sample with 0.04 % of uranium and 1 % of thorium, obtained with a coaxial Ge(Li) detector (25 cm^3 of active volume).

3 — X-RAY SPECTROMETRY

Figure 6 shows a spectrum of a monazite crystal obtained with a Ge (hyperpure) detector. One can notice the thorium X-rays produced by autofluorescence and also a small percentage of uranium. The concentration of uranium is obviously greater in the spectrum displayed in figure 7 which corresponds to thorianite. Actually the presence of uranium revealed by X-ray spectrometry is probably the best way to distinguish this mineral from another – thorite – which is very similar. Figure 8 shows another spectrum obtained with the same

detector but now the concentration of uranium is even greater since it corresponds to a sample of pitchblende. It is also worth noting the existence in this spectrum of the X-rays characteristic of lead which is not present in the mineral ores containing thorium. To be more precise one must say that lead is always present in all radioactive

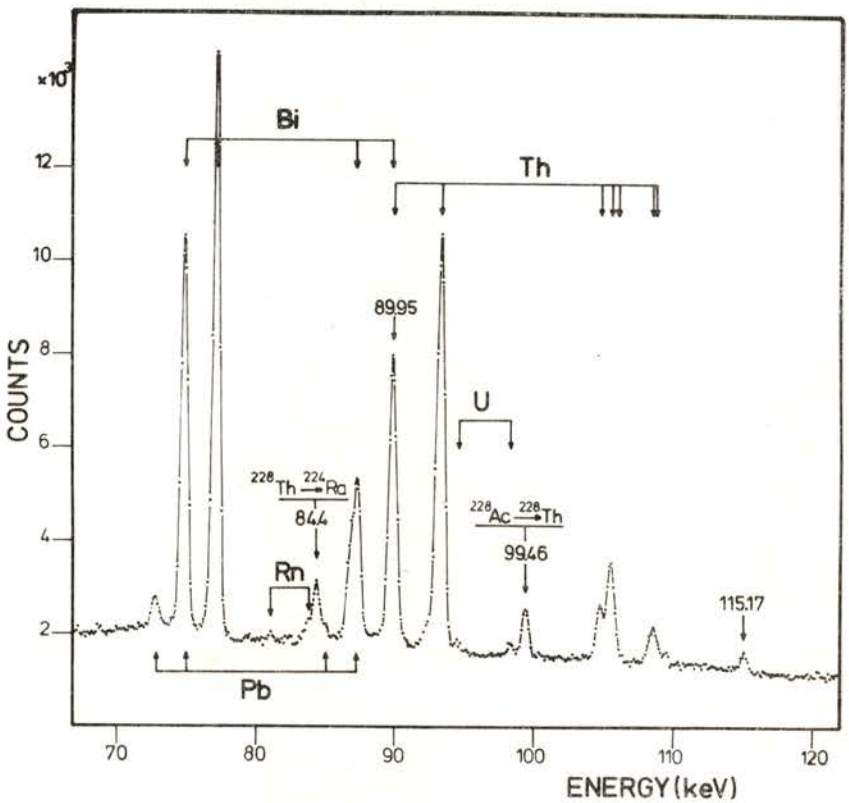

Fig. 6 — Spectrum of a ore sample of monazite obtained with a Ge (hyperpure) detector (presence of thorium and absence of uranium).

minerals but in some cases, like the one we have mentioned above, its concentration is so small that it can not be detected by X-ray analysis.

Another information that one can extract from this spectrum is the existence of tungsten which as far as we know is the first time that has been detected in association with uranium.

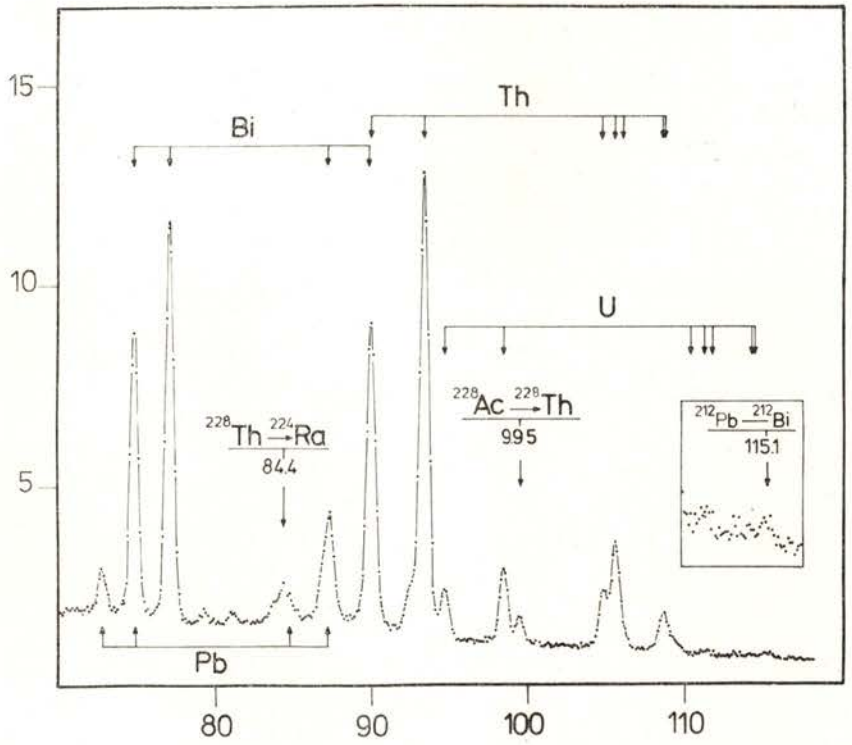

Fig. 7 — Spectrum of a sample of thorianite obtained with a Ge (hyperpure) detector (presence of thorium and uranium).

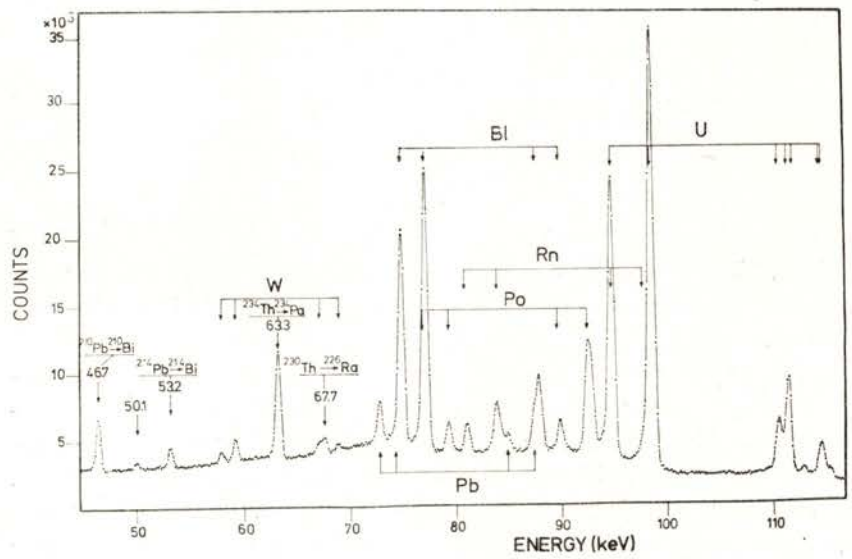

Fig. 8 — Spectrum of a sample of pitchblende obtained with a Ge (hyperpure) detector (presence of uranium, absence of thorium and presence of tungsten revealed by autofluorescence).

Since a large part of the world reserves of uranium, including the Portuguese, consists of minerals with low concentration we decided to apply this techique to one of them — saléeite (fig. 9).

As an example of a secondary mineral of uranium we show in figure 10 a spectrum of uranocircite. In it one cannot detect the

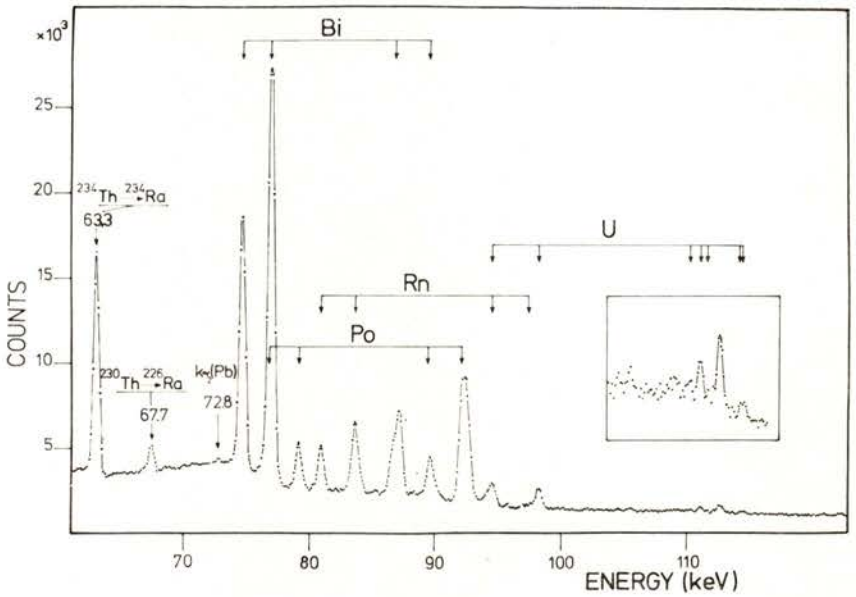

Fig. 9 — Spectrum of a sample of a radioactive ore very poor in uranium, obtained with a Ge (hyperpure) detector.

presence of lead and on the other hand one can see the existence of barium. The presence of barium is extremely useful to identify this mineral since its classification by conventional methods is very difficult.

Finnally figure 11 shows another piece of the spectrum of monazite already displayed in figure 6. It is now possible to see the different rare earth elements present in this mineral. The good resolution of this spectrum enables us to measure their relative concentrations. As far as we can judge from the analysis of two monazite crystals from different mines (Madagascar and Norway) the relative concentrations of rare earth elements do not vary significantly.

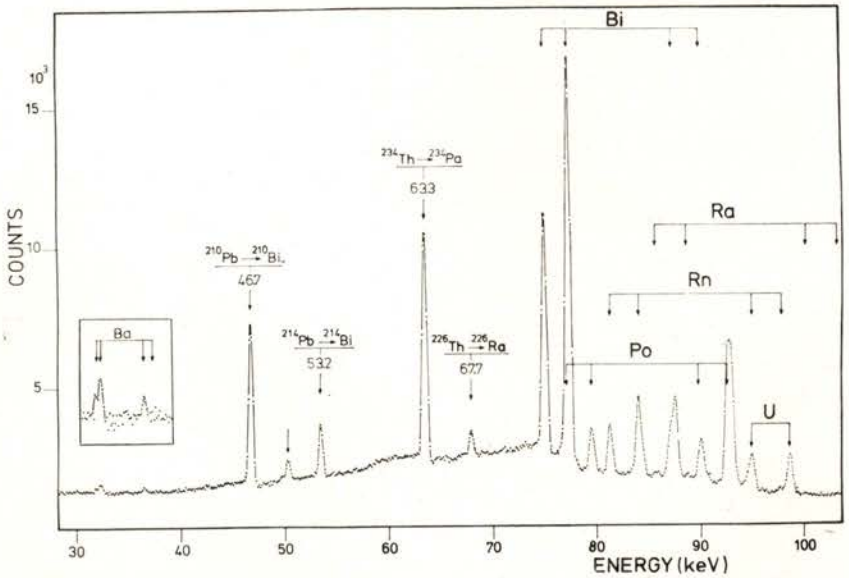

Fig. 10 — Spectrum of a sample of uranocircite obtained with a Ge (hyperpure) detector (absence of lead and presence of barium revealed by autofluorescence).

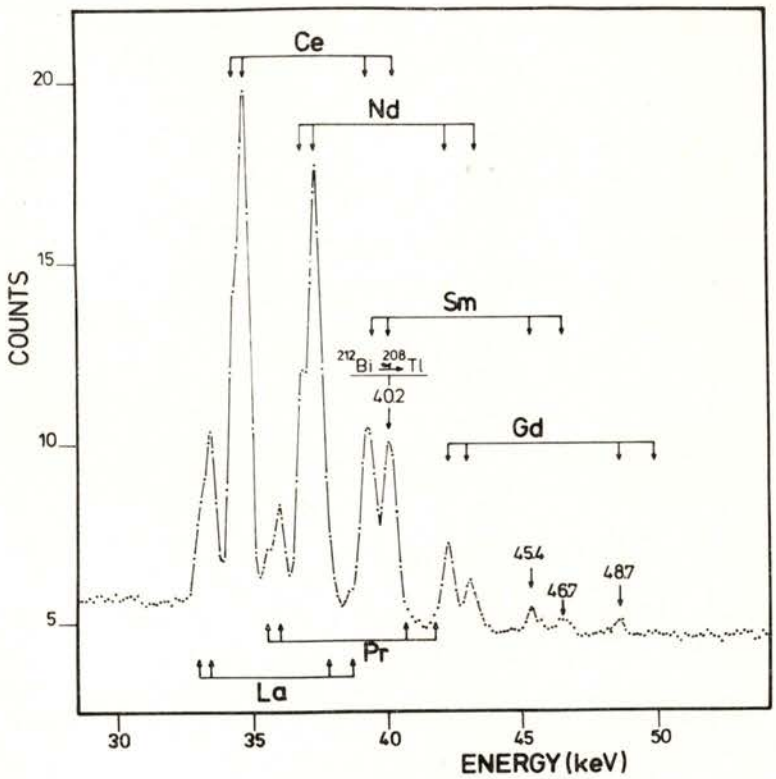

Fig. 11 — X-ray spectrum of rare earth elements present in a sample of monazite revealed by autofluorescence.

4 — CONCLUSION

In this paper we have shown how to use Ge(Li) and Ge (hyperpure) spectrometers in the qualitative and semi-quantitative analysis of radioactive minerals. This method reveals with high accuracy even the presence of non radioactive elements due to a process of X-ray emission by autofluorescence. Further work and specially more precise quantitative measurements are presently in progress and will be published elsewhere.

We woul like to thank the « Departamento de Física da Universidade de Coimbra » and specially Miss Maria Alice Alves for lending us the standard radioactive samples used in this work. Thanks are also due do Mrs. Maria da Graça Canelhas from « Museu e Laboratório Mineralógico e Geológico da Universidade de Lisboa », Mr. Lencastre from « Junta de Energia Nuclear » and the private collector Mr. Costa e Silva for lending us the samples that were analysed.

REFERENCES

[1] P. KELLER — *J. Phys. Rad.*, **19**, 289 (1958).

[2] G. JURAIN and J. MAILLOT — *J. Phys. Rad.*, **19**, 357 (1958).

[3] J. ADAMS, K. RICHARDSON and C. TEMPLETON — *Geochim. Cosmochim. Acta*, **13**, 270 (1958).

[4] M. A. ALVES, J. V. SIMÃO, C. CONDE and A. POLICARPO — *Rev. Fac. Cienc. Coimbra*, **28**, 23 (1959).

[5] P. HURLEY — *Bull. Geol. Soc. Am.*, **67**, 395 (1965).

[6] J. DOMINGOS and A. MELO — *Nucl. Inst. Meth.*, **48**, 28 (1967).

[7] G. MATHEVON — *Application des detecteurs Ge(Li) à l'étude de la radioactivité naturelle des roches et des mineraux radioactifs par spectrométrie* γ — Thèse de Docteur Ingénieur, Université de Strasburg, 1970.

[8] J. N. ROSHOLT — *Analytical Chemistry*, **29**, 1398 (1957).

[9] S. MUBARAKMAND, P. CHAUDHRY e F. NAGI — *Nucl. Inst. Meth.*, **140**, 133 (1977).

Imprensa Portuguesa • Rua Formosa, 108-116 • 4000 Porto

SOCIEDADE PORTUGUESA DE FÍSICA
AV. REPÚBLICA 37-4.°, 1000 LISBOA, PORTUGAL

PORTUGALIAE PHYSICA publishes articles or research notes with original results in theoretical, experimental or applied physics; invited review articles may also be included.

Manuscripts, with an abstract, may be written in English or French; they should be typewritten with two spaces and in duplicate. Figures or photographs must be presented in separate sheets and be suitable for reproduction with eventual reduction in size; captions should make the figures intelligible without reference to the text. Authors are requested to comply with the accepted codes concerning references.

There is no page charge. Author(s) will get 50 free reprints (without covers); these are to be shared among all the authors of the article. Authors interested in more reprints should say so when sending their manuscripts; quotations shall be sent with the proofs.

Subscription rates for volume 10:

1,000 Escudos (US$20) — individuals
2,500 Escudos (US$50) — libraries

PORTUGALIAE PHYSICA may also be sent on an exchange basis; we wellcome all suggestions to such effect.

All mail to be addressed to

PORTUGALIAE PHYSICA

C/O LABORATÓRIO DE FÍSICA, FACULDADE DE CIÊNCIAS
PRAÇA GOMES TEIXEIRA
4000 PORTO PORTUGAL

CONTENTS

PORTUGALIAE PHYSICA

VOLUME 10
FASCÍCULO 3-4
1979

SOCIEDADE PORTUGUESA DE FÍSICA

PORTUGALIAE PHYSICA

Fundada em 1943 por A. Cyrillo Soares, M. Telles Antunes, A. Marques da Silva e M. Valadares

Publicação subsidiada pelo INSTITUTO NACIONAL DE INVESTIGAÇÃO CIENTÍFICA

CDU 53 (469) (05)

PORTUGALIAE PHYSICA

VOLUME 10
FASCÍCULO 3-4
1979

TRANSFER REACTIONS WITH HEAVY-IONS (*)

A. M. GONÇALVES and F. D. SANTOS
Laboratório de Física, Faculdade de Ciências, Universidade de Lisboa

ABSTRACT – An extension of the Buttle and Goldfarb formalism for heavy ion transfer reactions is presented where recoil effects are considered using the local momentum approximation and the transition amplitude retains the structure of the zero range approximation. The reliability of the method was tested with numerical calculations which take a very small computing time compared with full finite range calculations.

It is well known that transfer reactions induced by heavy ions are a valuable tool in nuclear spectroscopy, in particular to study high spin nuclear states. The distorted wave Born approximation (DWBA), which is the basic theory for a quantitative quantal treatment of the reaction mechanism, is frequently used assuming the no-recoil approximation since a full finite range calculation requires large computer times. A DWBA code was developed where the corrections due to the recoil of the heavy ion cores are introduced in an approximate way performing a Taylor expansion of the distorted waves. The non-normal parity orbital angular momentum transfer is then automatically included and the terms in the expansion of the reduced amplitude can be characterized by the recoil orbital angular momentum transfer l_r. Due to the strong localization of the transfer it is usually a good approximation to represent the bound state wave function by the asymptotic Hankel function. With this description the transition amplitude can be calculated exactly using a local momentum approximation.

In the DWBA transition amplitude for the transfer reaction A (a, b) B, where $a = b + x$, and x is the transferred particle, a Taylor

(*) Sponsored in part by Centro de Física Nucler (INIC); communication delivered at the Conference of the Portuguese Physics Society (Lisbon, February 1978).

expansion of the distorted waves is performed at the displacement vector of the two ion cores. Using an irreducible tensor expansion of the translation operator, we obtain for each value of the transferred angular momentum l, a series of terms, characterized by an orbital angular momentum l_r that satisfies the vector relation

$$\vec{l}_r = \vec{l} - \vec{l}', \tag{1}$$

where $\vec{l}'$ is the angular momentum transferred from the relative motion of the ion cores in the entrance channel to the relative motion of the ion cores in the exit channel. We shall call $\vec{l}_r$ the recoil angular momentum. This variable is associated with linear recoil momentum

$$\vec{p} = -\left(\frac{M_x}{M_B} \vec{q}_b + \frac{M_x}{M_a} \vec{q}_a \right) \tag{2}$$

where M_i is the mass of the particle i, and $\vec{q}_a$ ($\vec{q}_b$) is the relative momentum in the entrance (exit) channel [1].

The above angular momentum quantum numbers satisfy the parity rule [2]

$$l' + l_r + L + L' = \text{even} \tag{3}$$

where L (L′) is the orbital angular momentum of x in the projectile (residual nucleus). The no-recoil approximation is obtained when we take into account only the no-recoil term of the series expansion of the transition amplitude corresponding to $l_r = 0$, which implies $l = l'$. In this approximation the non-normal parity values of l (without the parity of $L + L'$) do not contribute to the cross section.

Following Braun-Munzinger and Harney [3], we assume that in the asymptotic region where the transfer is more probable, the following approximation in the recoil terms can be made

$$\left(\frac{M_x}{M_A} \nabla_b - \frac{M_x}{M_a} \nabla_a \right) \chi^{(-)*}_{\vec{k}_b}(\gamma\vec{R})\, \chi^{(+)}_{\vec{k}_a}(\vec{R}) =$$

$$i\,\vec{p}\,\chi^{(-)*}_{\vec{k}_b}(\gamma\vec{R})\,\chi^{(+)}_{\vec{k}_a}(\vec{R}) \tag{4}$$

where $\gamma = M_A / M_B$, $\vec{R}$ is the displacement vector between the ion cores, $\chi^{(+)}_{\vec{k}_a}$ and $\chi^{(-)}_{\vec{k}_b}$ are the elastic scattering wave functions which describe, respectively, the relative motion of the pair A, a before the transfer, and the pair B, b after the transfer, and ∇_b (∇_a) is the gradient operator with respect to $\vec{R}$ and acts only on $\chi^{(-)}_{\vec{k}_b}$ ($\chi^{(+)}_{\vec{k}_a}$). In eq. (2) $\vec{q}_b$ and $\vec{q}_a$ are the local relative momenta in the exit and entrance channels. The modulus of $\vec{q}$ is determined by the relation

$$q(r_o) = \left[\frac{2\mu}{\hbar^2}\left(E - U_{opt}(r_o)\right)\right]^{1/2} \tag{5}$$

where μ is the reduced mass, E is the energy in the CM system, r_o is the interaction radius and U_{opt} is the optical potential that generates χ. The direction of $\vec{q}$ is assumed to be perpendicular to $\vec{R}$. This means that as regards the treatment of the recoil terms we assume that the transfer is more probable in the direction of $\vec{R}$.

The grazing collision character of heavy-ion reactions suggests that at least below the Coulomb barrier, where the no-recoil approximation is reasonable, the bound state wave functions may be approximated by the spherical Hankel function which describes their asymptotic behaviour [4].

With these assumptions, the reduced amplitude has the very simple form

$$\beta^{LL'l\lambda}_{sj} = \frac{4\pi}{\sqrt{2l+1}} {}_{l}\Sigma_{r\,l'} \int d\vec{R}\; {}_{\lambda}\Sigma_{r\,\lambda'} (l_r\, \lambda_r\, l'\, \lambda' \mid l\, \lambda)\, Y^{\lambda' *}_{l'}(\vec{R})$$

$$\times\; \mathcal{Y}^{\lambda_r *}_{l_r}(i\vec{p})\, F_{l l_r l'}(R)\, \chi^{(-)*}_{\vec{k}_b}(\gamma \vec{R})\, \chi^{(+)}_{\vec{k}_a}(\vec{R}) \tag{6}$$

where $F_{l l_r l'}(R)$ is the form factor containing the nuclear structure information and $\mathcal{Y}^{\lambda}_{l_r}$ is the solid spherical harmonic of order l_r.

In this asymptotic approximation the form factor $F_{l l_r l'}$, takes a very simple form. The term in eq. (6) corresponding to $l_r = 0$ is then the well known Buttle and Goldfarb approximation. The other terms in eq. (6) contain the effects of recoil and their form factors are given in ref. [1].

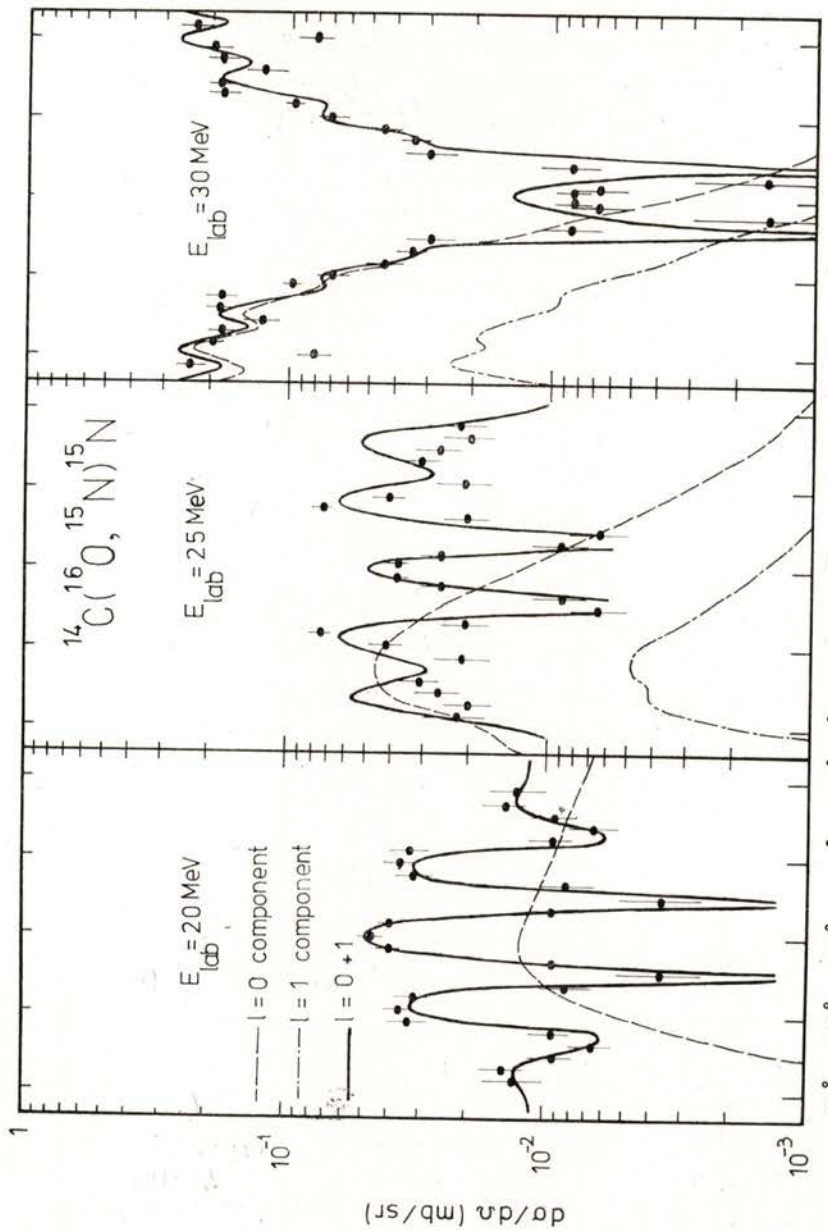

Fig. 1 — DWBA calculations for the $^{14}C(^{16}O,^{15}N)^{15}N$ ground state transition for three laboratory incident energies of 20, 25 and 30 MeV including recoil effects and showing the contributions from the allowed values of the total angular momentum transfer $l = 0$ and 1. The broken curves correspond to the direct transition amplitudes and the full curves result from antisymmetrization. The data are from ref. [7].

We have performed DWBA finite range calculations shown in Fig. 1 for the ^{14}C (^{16}O, ^{15}N) ^{15}N reaction at $E_{lab} = 20$, 25 and 30 MeV where the recoil effects were taken into account using the asymptotic approximation. The optical model potentials are from ref. [5, 6].

We find that the resulting spectroscopic factors are very close to those derived from a full finite range calculation using the DWBA code LOLA [7].

The approximation where the bound state wave functions are represented by the asymptotic Hankel functions is not essential for the application of the formalism which has been developed. It is possible to give a more realistic description of the bound states as a sum of Hankel functions [8] and still retain the simplicity of the above DWBA calculation.

REFERENCES

[1] F. D. SANTOS, *Nucl. Phys.* **A212** (1973) 341.

[2] F. D. SANTOS, *Phys. Lett.* **48B** (1974) 193.

[3] P. BRAUN-MUNZINGER and H. HARNEY, *Nucl. Phys.* **A223** (1974) 381.

[4] P. J. A. BUTTLE and L. J. B. GOLDFARB, *Nucl. Phys.* **78** (1966) 409; *Nucl. Phys.* **A115** (1968) 461; *Nucl. Phys.* **A176** (1971) 299.

[5] U. C. SCHLOTTHAUER-VOOS, H. G. BOHLEN, W. von OERTZEN and R. BOCK, *Nucl. Phys.* **A180** (1972) 385.

[6] W. F. W. SCHNEIDER, B. KOHLMEYER, F. PUHLHOFER and R. BOCK, *Nucl. Phys.* **A251** (1975) 331.

[7] W. F. W. SCHNEIDER, B. KOHLMEYER and F. PUHLHOFER, *Z. Physik* **A275** (1975) 249.

[8] A. M. GONÇALVES and F. D. SANTOS, *Proceedings of the International Conference on Nuclear Structure,* Tokyo (*International Academic Printing,* Japan) 1977, pag. 597.

RELATIVISTIC EQUATIONS AND THE STRUCTURE OF MESONS (*)

A. B. HENRIQUES
Centro de Física da Matéria Condensada (INIC), Lisboa

ABSTRACT — We present some preliminary results concerning the application of a relativistic model to the psi-family. This model differs from a previous one, based on the Bethe-Salpeter equation in instantaneous ladder approximation, in that it includes an anomalous magnetic moment at the quark-gluon vertex. With this improvement we get good numerical results for the hyperfine splitting between the Ψ (Ψ') and the η_c (η'_c).

Numerical estimates are also made for the light mesons. The aim is to fit the whole meson family with a single type of potential. We are still far from solving this problem, but we put forward some arguments showing that our expectations seem to be reasonable.

1 — INTRODUCTION

The charmed quark-antiquark ($c\bar{c}$) interpretation of Ψ (3.1) and Ψ' (3.7) has received considerable support after the observation of monoenergetic γ-ray transitions from Ψ and Ψ' to states easily interpreted as P-wave states of the $c\bar{c}$ system and as $^1S_0$ partners of the $^3S_1$ states (the Ψ and Ψ').

While some quark models have been able to accomodate the details of the P-wave spectrum [1], the large ground-state hyperfine splitting $E(\Psi)-E(\eta_c) \sim 270$ MeV still remains unexplained. To solve this problem, Schnitzer [2] proposed an effective quark-gluon anomalous moment, within the context of the linear potential model. Unfortunately, although in this model the $\Psi-\eta_c$ splitting comes with the right order of magnitude, the ratio $R=\{E(2^{++})-E(1^{++})\}\ \{E(1^{++})-$

(*) Communication delivered at the Conference of the Portuguese Physics Society (Lisbon, February 1978).

$-E(0^{++})\}\simeq 0.89$, too large when compared with the experimental value $R\simeq 0.40$.

In this paper we show how, in the context of a certain relativistic model, previously developed by Kellet, Moorhouse and the author [1], a quark-gluon anomalous magnetic moment may help us in solving the hyperfine splitting puzzle without destroying the very good results obtained, in that model, for the P-wave states.

In the remaining of this section we describe the main ingredients of our model and quickly summarize some of the results obtained for charmonium. Then, in the next section, we introduce the quark-gluon anomalous moment into the model and perform some rough numerical estimates, both for charmonium and for the light-mesons. Our ultimate goal is to fit the whole meson family with one single type of potential. Having found that such a goal seems reasonable, in section 3 we solve our relativistic equations, using the accurate numerical methods described in ref. [1].

Our general framework is provided by the Bethe-Salpeter equation, in ladder approximation with a static potential. The equation takes the form

$$(E-H_a+H_b)\,\phi(\vec{q})=(\Lambda_+^a\,\Lambda_-^b-\Lambda_-^a\,\Lambda_+^b)\,\beta^a\,\beta^b\int V(\vec{q}-\vec{q}')\,\phi(\vec{q}')\,d^3\vec{q}' \qquad (1)$$

where $$H_a=\vec{\alpha}_a\cdot\vec{q}_a+\beta_a m_a, \quad \Lambda_{\pm}^a=(W_a\pm H_a)/2W_a$$

and $$W_a=\sqrt{\vec{q}_a^{\,2}+m_a^2} \quad (\vec{q}_a=-\vec{q}_b\equiv\vec{q}).$$

In the following applications, and for simplicity, we shall supress the pair creation term, $\Lambda_-^a\,\Lambda_+^b$. [1] From the remaining equation the Fermi-Breit hamiltonian can be recovered, using the Foldy-Wouthuysen transformation.

The second ingredient of our model is an expansion of the amplitudes $\phi(\vec{q})$ in terms of the sixteen Dirac matrices. It is possible to do this and to select, among the terms of such an expansion, those appropriate to the state being studied [3].

Finally, we have to choose our potential. Following the general practice, we use a superposition of a 4−vector Coulomb potential (as suggested by asymptotic freedom, in the one-gluon exchange

approximation), with a linear 4−scalar potential, responsible for the confinement of quarks. The precise form of our potential is given by

$$V(r) = [\lambda(r-a) - \gamma^{\mu\, a}\gamma_{\mu_b}(3/4\ \alpha_s)\,1/r]\exp(-\mu r) + C \qquad (2)$$

with a, μ and C constants. The factor exp (-μr) acts as the screening effect described by Kogut and Susskind [4]. Without it we would need special limiting procedures to solve the equations for energy levels above 2m (m=quark mass) as discrete bound states.

The strong coupling constant α_s is assumed to vary with the relative momentum of the two quarks as again suggested by asymptotic freedom. The formula for α_s has not been deduced for the case of two momenta, $\vec{q}$ and $\vec{q}'$, and our application is only approximate. We took

$$\alpha_s'(\sqrt{q'q}) = \alpha_s(\bar{q})\,(1-(50/12\pi)\,\alpha_s\,L_n(\bar{q}/\sqrt{q\,q'}))^{-1}\ , \qquad (3)$$

where $\bar{q} \sim 1$ GeV.

With the model just described, we were able to find the correct positions for the P-Wave states, as well as good values for the $\Psi' \to {}^3P_J + \gamma$ decays. We also predicted the Ψ''_D at its correct position, 3.77 GeV. However, we were not able to get the correct positions for the pseudoscalars, η_c and η'_c.

Applying our equations to the light-mesons (quark masses of the order of 300 MeV), and putting δ, A_1 and A_2 at their approximate positions, we found that the ρ-π splitting was 3 times smaller than the experimental value. Although we are dealing here with light quarks, the situation at first sight appears to be much the same as with charmonium, suggesting that the same improvement in the model might simultaneously solve the hyperfine splitting problem in both families of mesons. The improvement is described in the next section.

2 — THE QUARK – GLUON ANOMALOUS MOMENT

It has been shown by Schnitzer [2] that the consideration of an effective quark-gluon anomalous vertex would lead to a qualitative explanation of the large Ψ-η_c hyperfine splitting. It is assumed that in the ladder approximation of the Bethe-Salpeter equation, with a

static potential, to lowest order in v/c the effective quark-gluon vertex is given by

$$\Gamma^{\mu} = \gamma^{\mu} - (k/2m)\,\sigma^{\mu\nu} q_{\nu}\,, \tag{4}$$

where k is the effective quark-gluon anomalous magnetic moment, and $\sigma^{\mu\nu} = 1/2\,[\gamma^{\mu}\,\gamma^{\nu}]$. It was further assumed that k was dependent on the quark-antiquark separation, being of O (α_s) at short distances and of O (1) at large distances.

Without questioning this argument, we just want to show that a simple phenomenological alternative is possible, within our model, if we assume that k comes from the short-distance part of the potential; that is, we take

$$V_{\text{Coulomb}} \sim \Gamma^{\mu a}\, 1/r\, \Gamma_{\mu_b}\,, \tag{5}$$

Γ^{μ} given by (4).

The introduction of Γ^{μ} makes a lot of difference in our equations, and it is reflected in the form of the Fermi-Breit terms, in the following way:

(a) Spin Orbit term : $\dfrac{(3+4k)}{2m^2}\,\dfrac{1}{r}\,\dfrac{dV}{dr}\,\mathrm{L.S}$

(b) Spin-Spin term : $\dfrac{(1+k)^2}{2m^2}\,\sigma_1.\sigma_2\,\nabla^2\,\mathrm{V}\,(r)$

(c) Tensor term : $\dfrac{(1+k)^2}{2m^2}\left(\dfrac{d^2V}{dr^2} - \dfrac{1}{r}\,\dfrac{dV}{dr}\right)\mathrm{S}_{12}$

Taking $k \sim 1$ the strenght of (b) and (c) increases faster than (a), and this is the important point for our purpose (remember the P-wave splittings are mainly controled by the spin-orbit term, while (b) is dominant for the Φ-η_c and ρ-π hyperfine splittings).

The introduction of k will not affect the possibility of getting the right value for R. We can see this with the help of the approximate treatment introduced in ref. [2].

Define the following matrix elements for the P-wave states, where by H_s we mean the spin dependent part of the Fermi-Breit

hamiltonian, and where for the 4-scalar linear part of the potential $(1 \otimes 1)$ only the L.S term is included (with $k=0$):

$\Gamma^{\mu} \otimes \Gamma_{\mu}$

$$<J=2 \mid H_s \mid J=2> = \alpha_s <r^{-3}> m\,[(3+4k)/2 - (1+k)^2/10]$$

$$<J=1 \mid H_s \mid J=1> = \alpha_s <r^{-3}> m\,[-(3+4k)/2 + (1+k)^2/2]$$

$$<J=0 \mid H_s \mid J=0> = \alpha_s <r^{-3}> m\,[-(3+4k) - (1+k)^2] \quad (6a)$$

$1 \otimes 1$

$$<J=2 \mid H_s \mid J=2> = -1/2\ \lambda <r^{-1}> m^{-2}$$

$$<J=1 \mid H_s \mid J=1> = +1/2\ \lambda <r^{-1}> m^{-2}$$

$$<J=0 \mid H_s \mid J=0> = +1\ \lambda <r^{-1}> m^{-2} \quad (6b)$$

Then, it is easily seen that

$$R = \frac{E(2^{++}) - E(1^{++})}{E(1^{++}) - E(0^{++})} =$$

$$= \frac{\alpha_s <r^{-3}> [(3+4k) - 3/5\,(1+k)^2] - \lambda <r^{-1}>}{\alpha_s <r^{-3}> [1/2\,(3+4k) + 3/2\,(1+k)^2] - 1/2\,\lambda <r^{-1}>} \quad (6c)$$

Using for $<r^{-1}>$ and $<r^{-3}>$ the expressions developed in ref. [2], with the help of a variational method, and with the parameters

$$\lambda = 0.132\ \text{GeV}^2,\ m = 2\ \text{GeV},\ \alpha_s = 0.54,\ k=1, \quad (7a)$$

we find $R=0.4$; as in ref. [1], this depends on our use of a 4-scalar confining potential.

We can go a little further and compute the absolute values of the P-wave and Ψ-η_c splittings. With the parameters $(7a)$ and with the help of expressions $(6a)$ and $(6b)$ we get

$$E(1^{++}) - E(0^{++}) = 100\ \text{MeV} \quad \text{and} \quad E(2^{++}) - E(1^{++}) = 40\ \text{MeV} \quad (7b)$$

To determine Ψ-η_c we apply

$$E(1^{--})-E(0^{-+})=8\pi/3\,(1+\kappa)^2\,\alpha_s\,|\phi(0)|^2 m^{-2}\,, \qquad (7c)$$

$|\phi(0)|^2$ being calculated from $\Gamma(\Psi\to e^+e^-)$ with the help of the Weisskopf–Van Royen formula.

Taking $\Gamma(\Psi\to e^+e^-)=5$ KeV, we have $|\phi(0)|^2=3.78\times10^{-2}$ GeV^{-3}, giving

$$E(1^{--})-E(0^{-+})=230 \text{ MeV}, \qquad (7d)$$

in approximate agreement with the experimental value.

Let us now see what we can say for the light–mesons. Here we have an additional difficulty due to the uncertainty in the position of the A_1 meson.

With the choice

$$\lambda=0.100 \text{ GeV}^2,\ m=0.34 \text{ GeV},\ \alpha_s=1\ 0\ ,\ \kappa=0.5 \qquad (8a)$$

we have $R=(A_2-A_1)/(A_1-\delta)=0.4$. Taking $\delta(0^{++})$ at 0.970 GeV we get 1.15 GeV for the position of the A_1 (1^{++}) meson, and 1.190 GeV for the A_2 (2^{++}), which seems a bit low, its experimental position being at 1.31 GeV.

If for $|\phi(0)|^2$ we take the value quoted in ref. [6], $|\phi(0)|^2=2.9\times10^{-3}$ GeV^{-3}, we get the correct value for the $\rho-\pi$ splitting:

$$E(\rho)-E(\pi)=630 \text{ MeV}. \qquad (8b)$$

The value of α_s in $(8a)$ seems high but is in agreement with deep inelastic scattering data [5].

As for λ, its value is smaller than the value quoted in $(7a)$, but rememember these are only rough numerical estimates, intended as a guide to help us in carrying on the program defined in the introduction.

3—RESULTS FOR CHARMONIUM

We now present the results for charmonium obtained by numerically integrating equation (1) with the potential described by expressions (2) and (3). (Due in part to computing difficulties we cannot yet present results for the light–mesons and for the Ψ''_D, in the spectrum of charmonium).

With the following typical set of parameters

$$\lambda = 0.194 \text{ GeV}^2, \ \alpha_s(1.0) = 0.30, \ m_c = 1.6 \text{ GeV}, \ k = 0.73 \quad (9a)$$

($a = 1.8$ Fermi, $C = 0.9$ GeV), we got for the $\Psi - \eta_c$ splitting the value 280 MeV, and for the $\Psi' - \eta'_c$ splitting 240 MeV. This last result is very interesting, because the η'_c comes close to 3.45 GeV, suggesting its identification with the state discovered at this energy.

The P-wave states come at

$$\chi(0^{++}) = 3.40 \text{ GeV}, \ \chi(1^{++}) = 3.49 \text{ GeV}, \ \chi(2^{++}) = 3.53 \text{ GeV}, \quad (9b)$$

giving $R \simeq 0.45$.

It is important to notice that the value for $\alpha_s(1.0)$ used here is very small in apparent disagreement with the deep inelastic scatering data [5], but is in agreement with the initial asymptotic freedom expectations.

4 — CONCLUSIONS

In the preceding sections we saw how the large ground-state hyperfine splitting in the charmonium spectrum could be explained by an effective quark-gluon anomalous magnetic moment, in the context of a relativistic quark model previously developed. We assumed the anomalous moment to come from the short distance part of our potential (2), while keeping the long range confining potential as a 4-scalar; this was essential to get the correct value for the ratio

$$R = \{E(2^{++}) - E(1^{++})\} / \{E(1^{++}) - E(0^{++})\}.$$

Simple numerical estimates suggest that the same improvement in our model will also enable us to explain the spectrum of the light--mesons, especially the large ρ-π splitting.

However, and going back to charmonium, we must remember that the large hyperfine splitting is only half the problem, the other half being the fact that the magnetic dipole transition rate $\Gamma(\Psi \to \eta_c + \gamma) \leq 1$ KeV; any real solution will have to solve both the problem posed by the large Ψ-η_c splitting and by the small decay rate for $\Psi \to \eta_c + \gamma$.

REFERENCES

[1] A. B. HENRIQUES, B. KELLET, R. G. MOORHOUSE, *Phys. Lett.* **64B**, (1976) 85.
R. G. MOORHOUSE, *Quarks and Hadron Structure* (Ed. C. Morpurgo, Plenum Press, New York 1977), p. 225.

[2] H. J. SCHNITZER, *Phys. Rev. Lett.* **35**, (1975) 1540.

[3] C. LLEWELLYN-SMITH, *Ann. of Physics* (N. Y.) **53**, (1956) 521.

[4] J. KOGUT, L. SUSSKIND, *Phys. Rev. Lett.* **34**, (1975) 767.

[5] H. D. POLITZER, *Nucl. Phys.* **B117**, (1976) 407.

[6] H. J. SCHNITZER, *Phys. Lett.* **69B**, (1977) 477.

E0-DECAY OF THE 1592 keV LEVEL IN ^{102}Pd

K. FARZINE, J. LANGE, M. L. NARASIMHA RAJU (*), D. CAEMMERER, J. NEUBER, K. UEBELGÜNN and H. v. BUTTLAR

Experimentalphysik III, Buhr-Universität Bochum, Germany

(*Received 11 July 1979*)

ABSTRACT — By means of a (p, p'e$^-$) coincidence experiment a previously reported E0 decay can be assigned to a level at 1592 keV in ^{102}Pd. The lifetime of this state is determined as 21 (1) ns.

INTRODUCTION

van Klinken et al. [1] have reported on the observation of an E0 transition in ^{102}Pd which they attribute to the ground state decay of a 1592 keV 0^+ level in this nucleus. In our (p, p'γ) experiment [2] we found no evidence for a γ-decay of a state at this excitation energy. Instead, we observed a level at 1658 keV to which, according to the isotropy of the pγ-angular correlations involving this level and the non-observation of this state in the radioactive decay, we have tentatively assigned an angular momentum of 0^+.

These findings give rise to the puzzling situation of the possible existence of two close lying 0^+ levels in this nucleus. In order to establish the assignment of the reported [1] E0 transition in the level scheme of ^{102}Pd and possibly to determine the lifetime of that state we have performed the experiment presented here [3].

EXPERIMENTAL DETAILS AND RESULTS

A schematic view of the experimental arrangement for the measurement of (p, p'e$^-$) coicidences is given in fig. 1. The target consisted of a metalic foil of isotopically enriched ^{102}Pd (76%)

(*) Present address: Department of Nuclear Physics, Andhra University, Waltair, India.

and had an aereal thickness of about 1 mg/cm^2. The scattered protons were registered by an annular surface barrier detector positioned at 180 degrees with respect to the beam direction. The incident beam energy was 6.9 MeV in order to separate the proton line originating from the excitation of the 1592 keV level in ^{102}Pd from the elastic peaks of the target contaminants ^{12}C and ^{16}O.

The electrons were detected at 135 degrees by a mini-orange device [1] which consists of a set of $SmCo_5$ permanent magnets, arranged to form a low dispersion spectrometer, and a cooled Si(Li)-diode. A central Au-absorber serves to prevent δ-electrons,

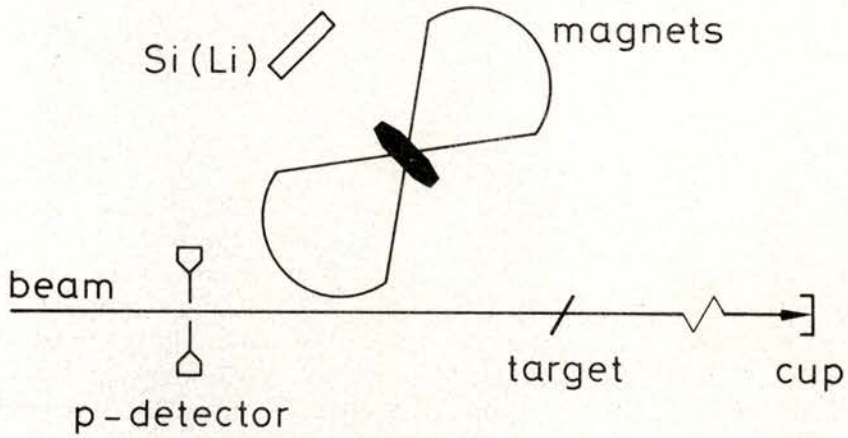

Fig. 1 — Schematic view of the experimental arrangement for (p,p'e$^-$) measurements

X- and γ-rays and also scattered particles from entering the detector, while the electrons of interest are deflected around this absorber in the appropriately dimensioned magnetic fields. The magnets are wedge-shaped and arranged such as to produce a toroidal field with focusing properties. Hence the effective solid angle for electron detection can be increased, in this case by a factor of 17, as compared to the diode alone. The magnetic field was chosen such that the transmission curve is centered at the energy of interest (see fig. 2). The energy calibration was carried out with ^{207}Bi and ^{60}Co radioactive sources. The energy resolution of the Si(Li)-detector amounts to 2.2 keV at 1 MeV. The coincidence data were taken in list-mode as triple information on the energy of proton and electron and the time

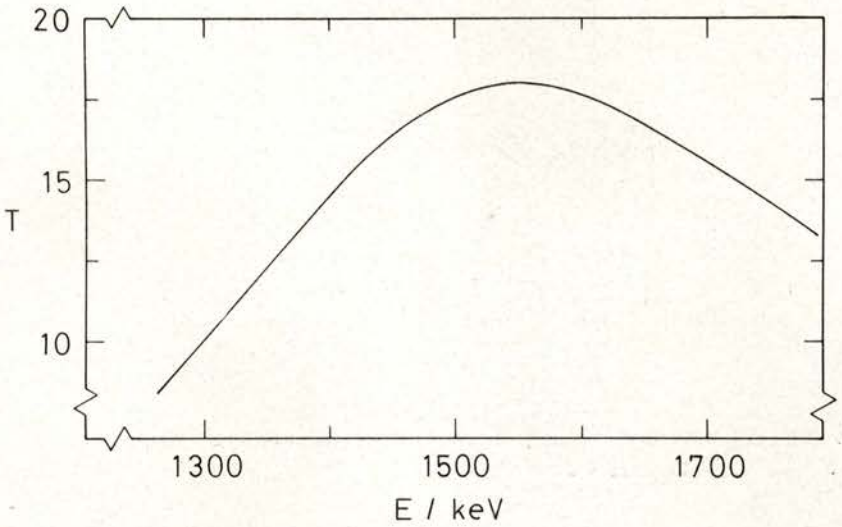

Fig. 2 — Relative transmission of the mini-orange device as obtained from the ratio of count rates with and without magnets.

difference between both events. Using constant fraction discriminators the time resolution was about 4 ns FWHM. Fig. 3 shows a chance and background corrected [4] electron spectrum in coinci dence with the proton line corresponding to the excitation of the 1593 (5) keV state. The energy of the K-conversion line was determined to be 1568.0 (5) keV which results in a level energy of 1592.4 keV. Our result verifies the assumption made in ref. [1] concerning the position of this E0 decay in the level scheme of ^{102}Pd. After correction for the energy dependence of the detection efficiency we find, from the intensities of K- and L-lines, a K/L ratio of 8.2(6) which is compatible with E0-conversion. The background corrected time spectrum of the (p, e^-) coincidence is shown in fig. 4. A fit to the data using an exponential function plus a constant (allowing for the chance events) yields a lifetime of 21 (1) ns. The same result has recently been obtained in a (p, 2n) experiment [5].

The long lifetime of the 1592 keV level indicates a strong hindrance of its γ-decay to the 2^+ first excited state. If the branching ratio I(E2, 1592-556 keV) / I(E0, 1592-0 keV) $\simeq 6$ as estimated by van Klinken et al. [1] is used, an E0 transition matrix element ρ (E0) $\simeq 0.03$ is obtained, a value about ten times smaller than the

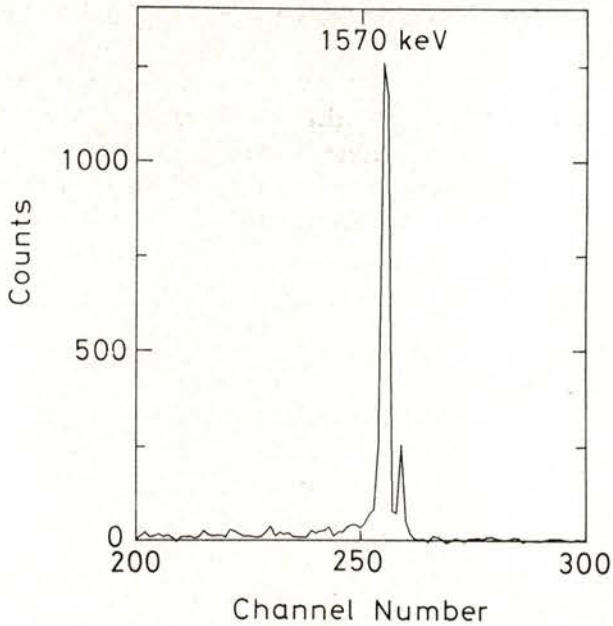

Fig. 3 — Part of the chance and background corrected electron spectrum in coincidence with the proton line populating the 1592 keV level.

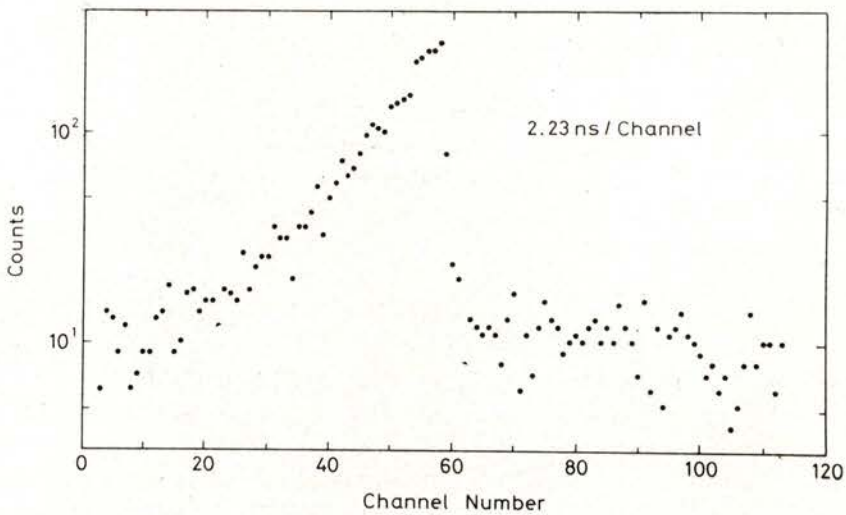

Fig. 4 — Time spectrum of the (p,e⁻) coincidences involving the 1592 keV state.

vibrational estimate. The γ-hindrance then turns out to be 4 orders of magnitude.

In order to reveal the nature of the 1592 keV level, experiments are in progress to secure the I(E2)/I(E0) estimate of ref. [1] and to establish relationships to other states in ^{102}Pd. Furthermore, a γγ-angular correlation measurement on the 1658 keV level is planned to ascertain the tentative spin assignment [2] for that state.

REFERENCES

[1] J. VAN KLINKEN, S. J. FEENSTRA, K. WISSHAK and H. FAUST, *Nucl. Instr. Meth.* **130** (1975) 427; S. J. FEENSTRA, J. M. GALEMA and J. VAN KLINKEN, *Annual Report K. V. I. Groningen,* 1976.

[2] J. LANGE, A. T. KANDIL, J. NEUBER, C. D. UHLHORN, H. v. BUTTLAR and A. BOCKISCH, *Nucl. Phys.* **A292** (1977) 301.

[3] K. FARZINE, J. LANGE, M. L. NARASIMHA RAJU and H. v. BUTTLAR, Contribution to the International Conference on the Structure of Medium-Heavy Nuclei, Rhodos, Greece, 1979, p. 82.

[4] B. W. HUBER and K. KRÄMER, *Nucl. Instr. Meth.* **114** (1974) 509.

[5] J. KANTELE, private communication.

NONRADIATIVE ENERGY TRANSFER. I - ENERGY MIGRATION AS A DIFFUSION PROCESS (*)

J. M. G. MARTINHO, A. GONÇALVES DA SILVA e J. C. CONTE
Centro de Química Física Molecular da Universidade Técnica de Lisboa,
Instituto Superior Técnico, Lisboa

ABSTRACT — The nonradiative energy transfer efficiency from pyrene to 9,10 diphenyl anthracene dissolved in benzene is shown to depend on pyrene concentration assuming that the transfer takes place only from the excited pyrene monomer. This result is attributed to an energy migration process taking place among pyrene molecules. A discussion of nonradiative energy transfer process is presented and the results are interpreted in terms of the available models.

1 — INTRODUCTION

It has been known for a long time [1] [2] that nonradiative energy transfer between an excited atom or molecule which is initially excited by absorption of u.v. radiation and another fluorescent species can occur, leading to fluorescence emission from the energy acceptor. It was FORSTER that first proposed a theory [3] [4] to describe this process. Although for some cases good agreement between the theoretical predictions for the transfer rate constants [5] and the experimental results was found it was soon verified that mainly when the energy donor was present at high concentrations and in liquid form the experimental values exceeded the «theoretical» ones. This led KALLMANN and FURST to propose [6] that material diffusion and/or energy migration among energy donor molecules could contribute to increase the magnitude of the energy transfer rate constant.

(*) Results presented at the Conference of the Portuguese Physics Society (Lisbon, February 1978).

As matter of fact, since the rate constant depends, according to FORSTER's theory, on the inverse sixth power of the distance between the energy donor and the energy acceptor, any process which decreases this distance would increase the energy transfer efficiency. The observed discrepancies between calculated and experimental values were interpreted in a qualitative way following FURST and KALLMANN's suggestion, although some authors tended to favour energy migration [7] while others thought that the important additional process was material diffusion [8]. In most cases, radiative energy transfer, consisting in reabsorption of the energy donor emission by the energy acceptor was considered unimportant [9] or at least accounted for [10]. However, the lack of a complete theoretical description or difficulties related with the verification of its predictions has shown the need of more experimental determinations in order to get more indications on the correct model to be used [11] [12].

The use of pyrene (Py) as an energy donor and 9,10 diphenylanthracene (DPA) as an energy acceptor has been proposed in this Laboratory [13] in the hope that by varying pyrene concentration evidence could be found for an energy migration effect. Furthermore, the fact that although pyrene is an excimer forming molecule the energy of the emissive excimer state is lower than the energy of the first excited singlet state of DPA could be invoked to assume that only pyrene monomer could transfer its energy to DPA. Obviously, this simplifies the equations used to analyse the experimental results [14].

The present work and the next one follow this line and are part of an extended study on the energy transfer processes which occur in a liquid system at room temperature containing fluorescent molecules which are excited with u.v. radiation. Experimental details have been described in previous publications [13] [14].

2 — EXPERIMENTAL RESULTS

If we consider excimer forming molecules Y which can transfer their energy to molecules Z which we assume not to form excimers, if we assume also that only excited monomers of the energy donor Y can transfer to Z, it is possible to derive the following expressions for the intensities of Y monomer emission (I_{MY}), Y excimer emission

(I_{DY}), Z emission (I_Z), when the samples are excited with u.v. radiation absorbed only by the energy donor [14].

$$I_{MY} = \frac{c_{hY}}{(1+\sigma^m_{ZY} c_Z) c_{hY} + c_Y} q_{MY} I_o \tag{1}$$

$$I_{DY} = \frac{c_Y}{(1+\sigma^m_{ZY} c_Z) c_{hY} + c_Y} q_{DY} I_o \tag{2}$$

$$I_Z = \frac{\sigma^m_{ZY} c_Z c_{hY}}{(1+\sigma^m_{ZY} c_Z) c_{hY} + c_Y} q_Z I_o \tag{3}$$

In these relationships c_Y and c_Z are the molar concentrations of Y and Z, respectively, c_{hY} is the half-value concentration for the monomer excimer Y system, q_{MY}, q_{DY} and q_Z are fluorescence quantum efficiencies, σ^m_{ZY} is the Stern-Volmer rate constant for transfer which is a measure of the transfer efficiency and is given by

$$\sigma^m_{ZY} = k^m_{ZY} \tau_{MY} \tag{4}$$

where τ_{MY} is the fluorescence decay time for the monomer emission when there is no acceptor molecules present. It is assumed that the samples are excited with light of intensity I_o (in Einstein sec^{-1}) and that the solutions do not contain oxygen or any other quenching agent.

For the system Pyrene (Y) + 9,10 diphenyl anthracene (Z) dissolved in benzene, which does not absorb the radiation used to excite the samples (mainly the 3130 Å Hg line), the intensities of pyrene monomer emission, pyrene excimer emission and DPA emission were obtained experimentally, and analysed using the equations written above. From the linear relationships $1/I_{DY}$ versus c_Z, it was possible to evaluate the values of σ^m_{ZY} (the Stern-Volmer rate constant) for a number of solutions with different pyrene concentrations (TABLE I).

It is seen that σ^m_{ZY} and so, from (4), k^m_{ZY} increases with increasing pyrene concentration Since the viscosity of the solutions remains

constant, and the relative amount of pyrene monomer and excimer has already been taken into account by the kinetic scheme, this variation can be taken as an indication that there is energy migration among pyrene molecules.

TABLE I

c_Y (mole l^{-1})	σ^m_{ZY} (l mole^{-1})
0.200	20264
0.180	18572
0.160	18837
0.140	17756
0.120	16958
0.100	14889
0.090	14527
0.080	10952
0.070	11727
0.060	11823
0.040	8391
0.020	5978
0.010	5327
0.008	5090
0.006	5163
0.004	4901

3 — DISCUSSION

As stated before, the theory of long range non radiative energy transfer proposed by FORSTER [3] [4] is unable to account for the magnitude of the experimentally obtained transfer rate constants. For these cases the theory of diffusion controlled reactions, [15] [16] has been invoked following KALLMANN and FURST's [6] suggestion.

Actually, two different approaches can be found in the literature. Some authors [17] [18] propose a modification of FORSTER's theory

whereby the variation of the distance between energy donor and energy acceptor is introduced. For the other group of theories it is the diffusion equation that is modified to include long-range energy transfer.

The work of YOKOTA and TANIMOTO [19] and of GOSELE et al [20] [21] deserve a special reference among the latter. For YOKOTA and TANIMOTO, the transfer rate constant is given by

$$k = \frac{4\pi N D}{1000} r_F \tag{5}$$

where D is the diffusion coefficient, N is Avogadro's number and r_F (FORSTER's radius) is

$$r_F = k' \left(\frac{\alpha}{D}\right)^{1/4} \tag{6}$$

k' being 0.676 or 0.910 according to the method used to solve the equations and α is

$$\alpha = \frac{R_o}{\tau_o} \tag{7}$$

where R_o is FORSTER's critical radius for transfer and τ_o the decay constant for monomer emission in the absence of acceptor.

In more recent work GOSELE has given the following expression for the energy transfer rate constant

$$k = \frac{4\pi N D}{1000} r_{eff} \tag{8}$$

with

$$r_{eff} = r_F + R_e f(Z_o) \tag{9}$$

where

$$Z_o = \frac{1}{2 R_e^2} \times \left(\frac{\alpha}{D}\right)^{1/2} \simeq \left(\frac{r_F}{R_e}\right)^2 \tag{10}$$

$f(Z_o)$ being a complex funcion which is given graphically by the authors in the original paper, and R_e is the encounter distance.

In neither of those papers energy migration is taken into account. For this process two different models have been proposed one invol-

ving a resonance transfer between neighbouring molecules [22], which follows FORSTER's early suggestion [3], the other involving successive monomer and excimer formation and dissociations [23] [24]. In this case it is possible to define an energy migration coefficient with the form

$$\Lambda = \frac{< a >^2}{6\,\bar{t}_{\text{mig}}} \tag{11}$$

$< a >$ being the r.m.s. of the distance between molecules, and

$$\bar{t}_{\text{mig}} = \frac{1}{k_{\text{DMY}}\, c_{\text{Y}}} + \frac{1}{k_{\text{MDY}}} \tag{12}$$

the «mean time» for the migration, i.e., the time taken for a monomer to interact with a ground state molecule and form an excimer plus the time taken for the excimer to dissociate, k_{DMY} and k_{MDY} being the rate constants for excimer formation and dissociation, according to the equation

$$\text{M}_{\text{Y}} + \text{M}_{\text{Y}}^{*} \underset{k_{\text{MDY}}}{\overset{k_{\text{DMY}}}{\rightleftharpoons}} \text{D}_{\text{Y}}^{*} \tag{13}$$

The effect of energy migration is then introduced adding Λ to the diffusion coefficient in the expression of the diffusion equation, the «theoretical» value of the rate constant being

$$k_{\text{theor.}} = \frac{4\pi \text{N}(\text{D} + \Lambda)}{1000}\, r_{\text{eff}} \tag{14}$$

Both models lead to similar analytical expressions [25]. However it was found that VOLTZ model did not fit the experimental results reported here. Accordingly the results were analysed in terms of (14) and (11).

Taking D (the sum of diffusion coefficients for Py and DPA) to be 2.5×10^{-5} cm^2s^{-1}, $\tau_{\text{MY}} = 320$ ns, $R_e = 6$ Å, $k' = 0.676$, one obtains, from (6) $r_{\text{F}} \simeq 7$ Å and taking from the curve given by GOSELE the value 0.08 for $f(Z_o)$, k given by (5) is 1.40×10^{10} l mole^{-1} sec^{-1}.

Now if we plot k_{ZY}^m calculated from the values in table I and extrapolate to $c_Y = 0$ it is possible to obtain $k_{ZY}^m \simeq 1.20 \times 10^{10}$ l mole^{-1} sec^{-1} which is in fair agreement with the calculated value (it is worth noting that no correction for radiative transfer was made here). Taking now $<a> = 4$ Å, $k_{DMY} = 3.9 \times 10^{11}$ mole. l sec^{-1}, $k_{MDY} = 9.8 \times 10^{10}$ sec^{-1} it is possible to calculated k_{theor} from (14). In the figure, the

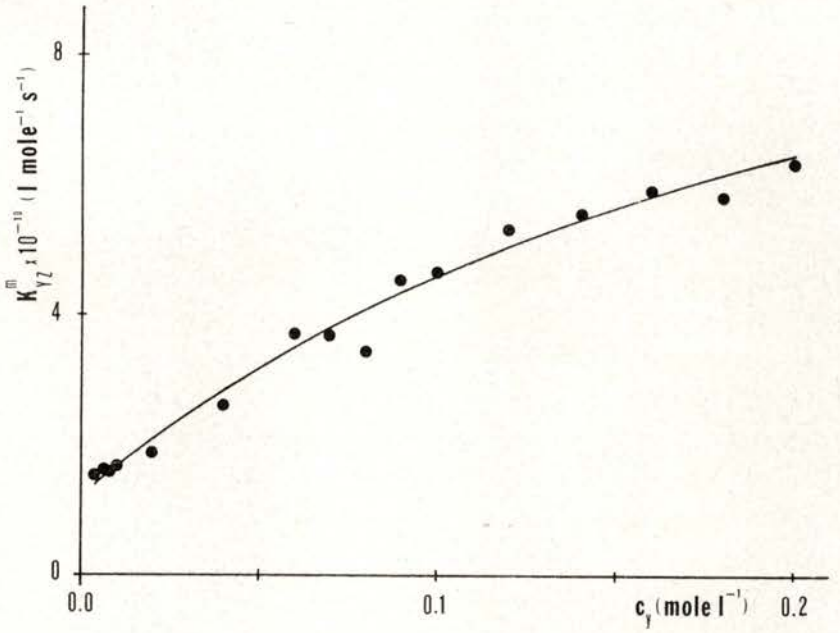

Fig. 1 — The rate constant for the energy transfer from Pyrene monomer to DPA as a function of Pyrene concentration for deoxygenated solutions. Circles: Experimental values. Full curve: calculated from (11) (12) and (14).

values of k_{ZY}^m obtained from the experimental values in Table I together with the calculated curve are indicated. The fitting is quite good. However the values of k_{DMY} and k_{MDY} neded are quite high when compared with published values ($k_{DMY} = 4.2 \times 10^9$ mole^{-1} l sec^{-1}, $k_{MDY} = 3.7 \times 10^6$ sec^{-1}). This discrepancy has already been verified in cases where this model for migration has been invoked [23]. This fact is taken as an indication that the model used needs to be modified although its form seems to be adequate. Work is in progress to elucidate this problem and the results will be published soon.

REFERENCES

[1] G. CARIO, J. FRANCK — *Z. Physik* **17**, 202 (1923).

[2] E. J. BOWEN — *J. Chem. Phys.* **13**, 306 (1945).

[3] TH. FORSTER — *Ann. Physik* **6**, 55 (1948).

[4] TH. FORSTER — *Z. Naturf.* **4a**, 321 (1949).

[5] L. J. BASILE — *Trans. Far. Soc.* **60**, 1702 (1964).

[6] W. KALLMANN, M. FURST — *Liquid Scintillation Counting*, ed. C. G. BELL, F. N. HAYES — *Pergamon Press* 1953, p. 3.

[7] S. F. KILIN, M. S. MIKHELASHVILI, I. M. ROZMAN — *Opt. Spect.* **16**, 576 (1964).

[8] A. WEINREB — *J. Chem. Phys.* **35**, 91 (1961).

[9] E. J. BOWEN, R. LIVINGSTON — *J. Am. Chem. Soc.* **76**, 6300 (1954).

[10] J. B. BIRKS, K. N. KUCHELA — *Proc. Phys. Soc.* **77**, 1083 (1961).

[11] A. M. SAMSON — *Opt. Spectr.* **16**, 378 (1964).

[12] M. V. FOK — *Opt. Spect.* **17**, 437 (1964).

[13] J. C. CONTE — *Memórias Acad. Ciências* (Lisboa) **13**, 199 (1969).

[14] J. C. CONTE — *Rev. Port. Quim.* **11**, 169 (1969).

[15] M. Von SMOLUCHOWSKI — *Z. Physik Chem.* **92**, 129 (1917).

[16] B. SVESHNIKOFF — *Ach Physicochem. USSR* **3**, 257 (1935).

[17] J. FEITELSON — *J. Chem. Phys.* **44**, 1500 (1966).

[18] Y. ELKANA, J. FEITELSON, E. KATCHALSKI — *J. Chem. Phys.* **48**, 2399 (1968).

[19] M. YOKOTA, O. TANIMOTO — *J. Phys. Soc. Japan* **22**, 779 (1967).

[20] U. GÖSELE, H. HAUSER, U. K. A. KLEIN, R. FREY — *Chem. Phys. Lett.* **34**, 519 (1975).

[21] U. K. A. KLEIN, R. FREY, H. HAUSER, U. GÖSELE — *Chem. Phys. Lett* **41**, 139 (1976).

[22] R. VOLTZ, G. LAUSTRIAT, A. COCHE — *J. Chem. Phys.* **63**, 1253 (1966).

[23] J. B. BIRKS, J. C. CONTE — *Proc. Roy Soc.* (London) **303 A**, 85 (1968).

[24] J. B. BIRKS — *Energetics and Mechanisms in radiation biology* ed. G. O. PHILLIPS, *Academic Press* 1968, p. 203.

[25] T. P. BELIKOVA, M. D. GALANIN — *Opt. Spektr.* **1**, 168 (1956).

[26] J. C. CONTE, T. R. SOUSA — *Int. Symp. on excited biological molecules*, Lisbon, April 1974.

NONRADIATIVE ENERGY TRANSFER. II - THE INFLUENCE OF THE CONCENTRATION OF THE ENERGY DONOR (*)

A. GONÇALVES DA SILVA, J. M. G. MARTINHO, J. C. CONTE
Centro de Química Física Molecular da Universidade Técnica de Lisboa,
Instituto Superior Técnico, Lisboa

ABSTRACT — The results obtained for fluorescence emission from solutions of pyrene (Py) and 9,10 diphenyl anthracene (DPA) in benzene containing oxygen at atmospheric pressure and excited under steady state conditions with u.v. light were analysed to get information about the quenching effect of oxygen on pyrene excited monomer. The influence of pyrene concentration is discussed.

1 — INTRODUCTION

In part I of this work the results obtained for the transfer rate constants from pyrene (Py) to 9,10 diphenylanthracene (DPA) dissolved in benzene and under conditions of steady state excitation with u.v. radiation were presented. The results refer to deoxygenated (by N_2 bubbling) solutions. However, during the experimental work fluorescence emission from air-equilibrated samples was also obtained which makes possible the study of the effect of oxygen which is known [1] to be a quenching agent for fluorescence, whereby fluorescence intensity is reduced relative to that observed when there is no oxygen present.

When the solutions contain dissolved oxygen, the equations that give the intensities of pyrene excited monomer emission (I'_{MY}), pyrene excimer emission (I'_{DY}) and DPA emission (I'_{Z}) have a simi-

(*) Results presented at the Conference of the Portuguese Physics Society (Lisbon, February 1978).

lar form to those that can be derived for deoxygenated samples in similar conditions [2], namely

$$I'_{MY} = \frac{c'_{hY}}{(1+\sigma'^{m}_{ZY}\, c_Z)\, c'_{hY} + c_Y}\, q'_{MY}\, I_o \tag{1}$$

$$I'_{DY} = \frac{c_Y}{(1+\sigma'^{m}_{ZY}\, c_Z)\, c'_{hY} + c_Y}\, q'_{DY}\, I_o \tag{2}$$

$$I'_{Z} = \frac{\sigma'^{m}_{ZY}\, c_Y\, c'_{hY}}{(1+\sigma'^{m}_{ZY}\, c_Z)\, c'_{hY} + c_Y}\, q'_{Z}\, I_o \tag{3}$$

where the quantum efficiencies q'_{MY} q'_{DY} and q'_{Z}, the half-value concentration c'_{hY} and the «Stern-Volmer constant» for transfer from the energy donor monomer σ'^{m}_{ZY} in the presence of oxygen are related whith the corresponding quantities for deoxygenated samples through the «Stern-Volmer constants» for oxygen quenching defined as

$$\chi'_{MY} = k'_{MY}\ \tau_{MY} \tag{4}$$

$$\chi'_{DY} = k'_{DY}\ \tau_{DY} \tag{5}$$

$$\chi'_{Z} = k'_{Z}\ \tau_{Z} \tag{6}$$

τ_{MY}, τ_{DY} and τ_Z being the decay constants for Py excited monomer and excimer emission and DPA emission, respectively and k'_{MY}, k'_{DY}, k'_Z the rate constants for oxygen quenching corresponding to the same entities.

As a matter of fact, in terms of the quantities defined in part I

$$q'_{MY} = \frac{q_{MY}}{1+\chi'_{MY}\,[O_2]} \tag{7}$$

$$q'_{DY} = \frac{q_{DY}}{1+\chi'_{DY}\,[O_2]} \tag{8}$$

$$q'_Z = \frac{q_Z}{1+\chi'_Z\,[O_2]} \tag{9}$$

$$\sigma'^{m}_{ZY} = \frac{\sigma^{m}_{ZY}}{1+\chi'_{MY}\,[O_2]} \tag{10}$$

$$c'_{hY} = c_{hY}\,\frac{1+\chi'_{MY}\,[O_2]}{1+\chi'_{DY}\,[O_2]}\,(1+\chi'_{MDY}\,[O_2]) \tag{11}$$

with

$$\chi'_{MDY} = \frac{k'_{DY}}{k_{DY}+k_{MDY}} \tag{12}$$

k_{MDY} being the rate parameter for excimer dissociation and k_{DY} the reciprocal of the excimer decay constant.

2 — EXPERIMENTAL RESULTS AND ANALYSIS

For solutions not containing DPA ($c_Z = 0$)

$$\frac{1}{I'_{MY}} = a'_M + b'_M\,c_Y \tag{13}$$

$$\frac{c_Y}{I'_{DY}} = a'_D + b'_D\,c_Y \tag{14}$$

$$\frac{I'_{DY}}{I'_{MY}} = b'_{DM}\,c_Y \tag{15}$$

with

$$a'_M = \frac{1}{q'_{MY}\,I_o} \qquad b'_M = \frac{1}{c'_{hY}\,q'_{MY}\,I_o} \tag{16}$$

$$a'_D = \frac{c'_{hY}}{q'_{DY}\,I_o} \qquad b'_D = \frac{1}{q'_{DY}\,I_o} \tag{17}$$

$$b'_{DM} = \frac{1}{c'_{hY}}\;\frac{a'_M}{b'_D} \tag{18}$$

Then

$$c'_{hY} = \frac{a'_M}{b'_M} = \frac{a'_D}{b'_D} = \frac{a'_M}{b'_D\, b'_{DM}} \tag{19}$$

The linear relationships (13) (14) and (15) are well verified, as it can be seen from figures 1, 2 and 3 and it is possible to obtain $c'_{hY} = 11 \times 10^{-3}$ mole l^{-1}, $a'_M = 23.63$, $b'_D = 12.63$, while from the corresponding straight lines for deoxygenated samples one gets $c_{hY} = 7 \times 10^{-4}$ mole 1^{-1}, $a_M = 1.40$, $b_D = 4.23$. Now from equations (7), (8), (9), (16), (17), and (18)

$$\chi'_{MY}[O_2] = \frac{I_o\, q_{MY}}{I_o\, q'_{MY}} - 1 = 15.9 \tag{20}$$

$$\chi'_{DY}[O_2] = \frac{I_o\, q_{DY}}{I_o\, q'_{DY}} - 1 = 1.99 \tag{21}$$

If we take the values [3] $k_{MDY} = 3.7 \times 10^6$ s^{-1}, $k_{DY} = 2.1 \times 10^7$ s^{-1} we further obtain

$$\chi'_{MDY}[O_2] = \frac{\chi'_{DY}[O_2]}{1 + k_{MDY}/k_{DY}} = 1.70 \tag{22}$$

With these values and the value $c_{hY} = 7 \times 10^{-4}$ mole. 1^{-1}, using [11] it is possible to evaluate $c'_{hY} = 10.7 \times 10^{-3}$ mole. 1^{-1}, in agreement with the value obtained experimentally.

Since the measurements were made at constant temperature, concentration of oxygen, may be assumed to be constant and equal to 1.6×10^{-3} mole. 1^{-1} [4]. This implies then that the quenching constant k'_{MY} does not depend on pyrene concentration in contrast to what happens with the rate transfer constant k^m_{YX} as it was shown in part I of this work. This being true, it is seen from (10) that σ'^m_{ZY} must vary with pyrene concentration, and be proportional to σ^m_{ZY}.

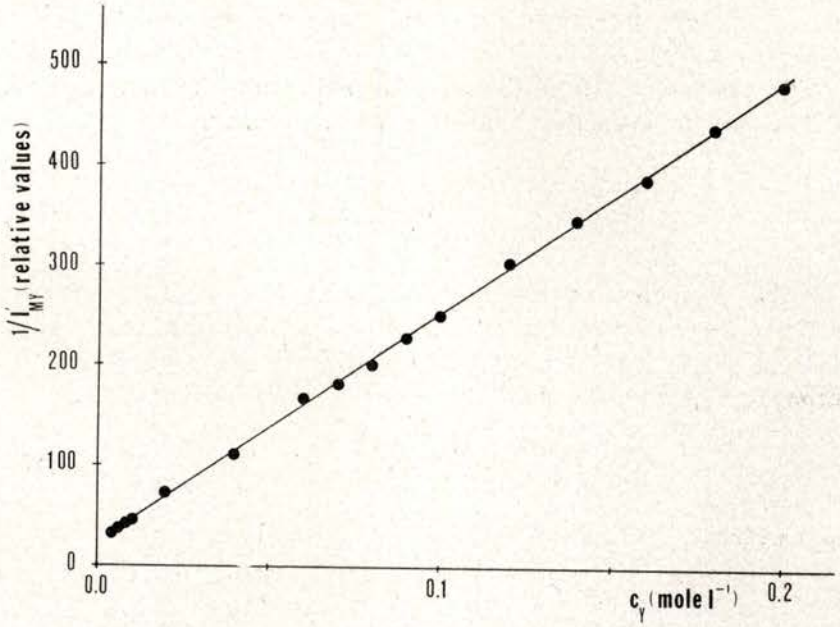

Fig. 1 — Reciprocal of Pyrene monomer fluorescence intensity as a function of Pyrene concentration for air equilibrated pyrene solutions in benzene not containing DPA.

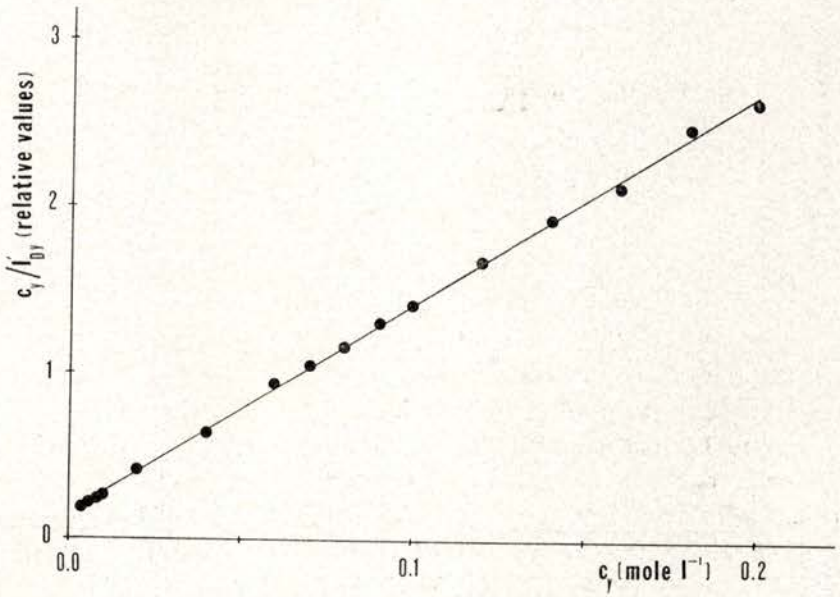

Fig. 2 — The ratio between Pyrene concentration and excimer fluorescence intensity as a function of Pyrene concentration for air equilibrated pyrene solutions in benzene not containing DPA.

To evaluate σ'^{m}_{ZY} from the experimental results the same process as that used to evaluate σ^{m}_{ZY} must be used. From (**2**)

$$\frac{1}{I'_{DY}} = A'_D + B'_D\, c_Z \tag{23}$$

with

$$A'_D = \frac{1}{I_o\, q'_{DY}} \left(\frac{c'_{hY}}{c_Y} + 1 \right) \tag{24}$$

$$B'_D = \frac{1}{I_o\, q'_{DY}} \frac{c'_{hY}}{c_Y}\, \sigma'^{m}_{ZY} \tag{25}$$

from which

$$\sigma'^{m}_{ZY} = \frac{B'_D}{A'_D} \left(1 + \frac{c_Y}{c'_{hY}} \right) \tag{26}$$

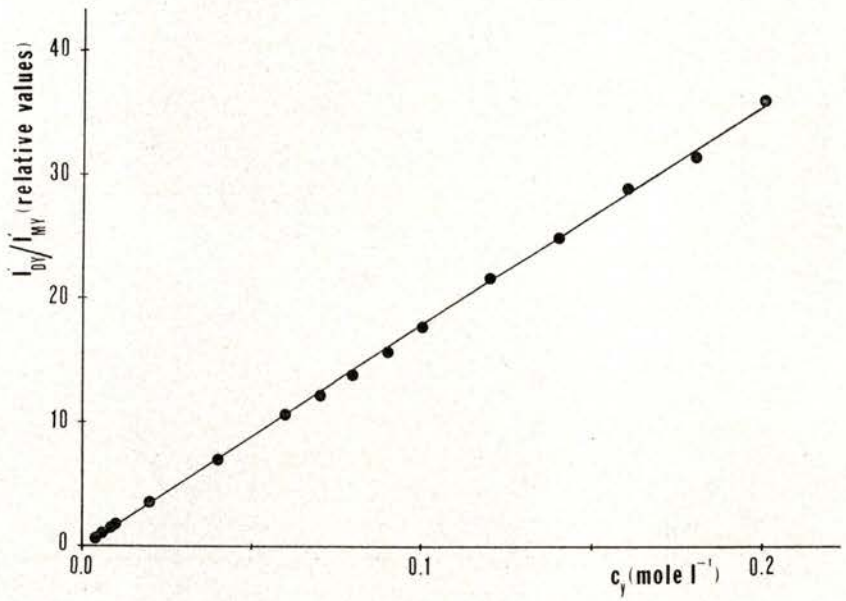

Fig. 3 — The ratio between the fluorescence intensities of Pyrene excimer and monomer as a function of Pyrene concentration for air equilibrated pyrene solutions in benzene not containing DPA.

If we take the values of I'_{DY} obtained for the same solutions as those used for the evaluation of the different values of σ^m_{ZY} and indicated in Tabel I of Part I of this work it is possible to get the values of σ'^m_{ZY}. These values are indicated in Table I.

TABLE I

c_Y (mole. l^{-1})	σ^m_{ZY} (l mole.$^{-1}$)
0.200	697.7
0.180	635.4
0.160	631.2
0.140	503.0
0.120	564.6
0.100	447.4
0.090	516.2
0.080	498.6
0.070	484.7
0.060	435.2
0.040	428.4
0.020	323.5
0.010	304.9
0.008	290.4
0.006	285.4
0.004	237.9

Although σ'^m_{ZY} varies with pyrene concentration as σ^m_{ZY} does, the fact is that the two quantities are not proportional. If now we consider equation (10) to be valid, this fact implies that k'_{MY} must vary with c_Y. In fact, using (10) we can obtain the curve in figure 4 which, in contrast with the conclusion reached before, would prove that the quenching effect of oxygen upon pyrene excited monomer would depend on an energy migration process among pyrene molecules, in a similar way as the nonradiative energy process discussed in Part I.

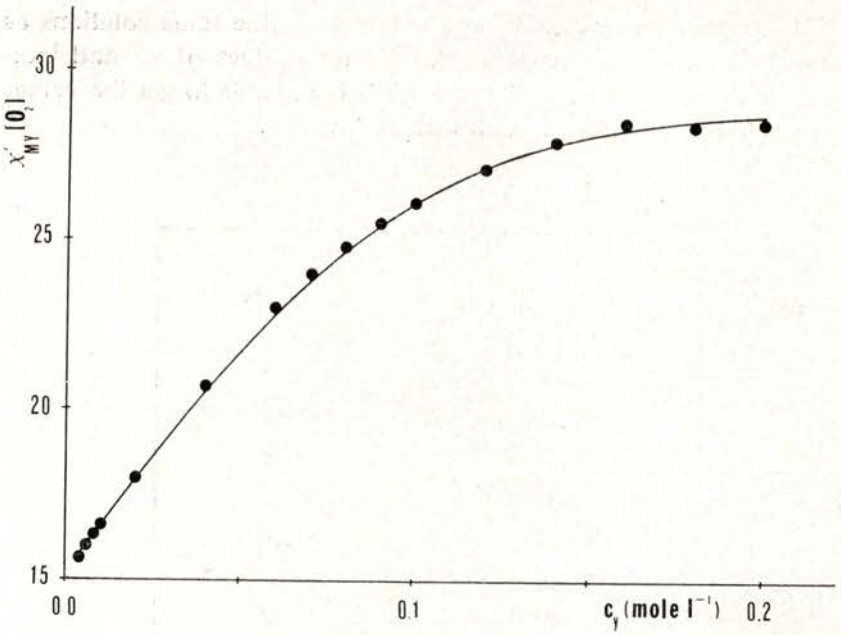

Fig. 4 — The Stern Volmer rate constant for oxygen quenching of Pyrene monomer times oxygen concentration as a function of Pyrene concentration.

3 — CONCLUSIONS

The possible analogy between quenching processes and non radiative energy processes in binary systems has already been stressed in a number of publications [5]. On this basis, it would be expected that if before it reaches an acceptor molecule the energy migrates among energy donor molecules the same would happen before a quenching process would take place.

However the problem as it is presented here lies deeper. It has to do with the consistency of the model. On one hand the results favour a model which does not give evidence for a variation of k'_{MY} with c_Y. But this same fact can be used to reach the conclusion that this variation must exist.

It is known [6] that oxygen quenching may be a complex process. But this alone does not explain the discrepancies reported here. As pointed out in Part I, no correction for any radiative energy

transfer (which would affect the Y → Z transfer but not the oxygen quenching effect) was made so far. Also, the results were analysed assuming that the transfer to DPA only takes place from the excited pyrene monomer. If this is reasonable for energetic reasons, it is a fact that an equilibrium does exist between pyrene monomer and excimer involving energies above and below the first excited singlet state of DPA. However, the assumption of a negligible transfer from the excimer is supported by the good linear correlations of the variations of $1/I_{DY}$ and $1/I'_{DY}$ with c_Z.

Furthermore, the fact that oxygen is present introduces another feature in the process. The quenching effect competes with the transfer for the dissipation of energy from the excited pyrene monomer, and it is known [7] that in this case the overall process is the sum of the individual effects. What is not known is what happens when these individual processes depend on migration and/or diffusion for which case difficulties in the mathematical analysis have already been stressed [8].

All these problems must be clarified. They are under study at this Laboratory and the results will be reported later.

The help given by Mr. V. R. Pereira and D. V. Louro to obtain the experimental quantities referred to both in Part I and Part II of this work is gratefully acknowledged.

REFERENCES

[1] H. TSUBOMURA; R. S. MULLIKEN — *J. Amer. Chem. Soc.* **82**, 5996 (1960).

[2] J. C. CONTE — *Rev. Port. Quim.* **11**, 169 (1969).

[3] T. R. SOUSA — *Unpublished results.*

[4] A. MCKEOWN; R. HIBBARD — *Anal. Chem.* **28**, 1490 (1956).

[5] J. B. BIRKS; J. C. CONTE — *Proc. Roy Soc.* **303A**, 85 (1968).

[6] B. STEVENS; R. R. WILLIAMS — *Chem. Phys. Lett.* **36**, 100 (1975).

[7] J. C. CONTE — *Trans. Far. Soc.* **65**, 2382 (1969).

[8] M. V. FOK — *Opt. Spect.* **17**, 437 (1964).

CRITICAL EXPONENTS OF THE NEMATIC-SMECTIC-A TRANSITION FROM TWIST VISCOSITY (*)

A. C. DIOGO and A. F. MARTINS
Centro de Física da Matéria Condensada (INIC), Lisboa

ABSTRACT — It has been predicted that the twist viscosity γ_1 behaves critically like

$$\gamma_1 = \gamma_1^0 + b \cdot \left(\frac{T - T_{NA}}{T_{NA}}\right)^{-x}$$

as the temperature approaches the nematic-smectic-A second-order transition point T_{NA}. Experimentally, a wide variety of values for the exponent x have been reported which range from 0.33 to 1.07.

We show that such discrepancy is mainly due to a wrong evaluation of the non-critical part γ_1^0 of the twist viscosity, for which various «a priori» expressions have been used so far. Using here a new theoretical expression for γ_1^0 recently deduced by us, which reads

$$\gamma_1^0 = c \cdot S.^2 \exp\left(\frac{\varepsilon S}{kT}\right)$$

and reanalysing the available data, we show that only one critical exponent $x \simeq 0.33$ is compatible with the experimental data. Our analysis also gives the parameters c and ε which have a molecular interpretation and can be independently checked.

1 — INTRODUCTION

Since the prediction that the nematic-smectic-A phase transition (N-A transition) may be continuous [1-3], the interest in evaluating the critical exponents characterizing this transition has been the

(*) Results presented at the Conference of the Portuguese Physics Society (Lisbon, February 1978).

source of a lot of experimental work. The theoretical description of this transition has been based on two main models: a Landau-type one due to McMillan [4], using the mean-field approximation, and, alternatively, De Gennes' model [2, 3] which predicts for this transition the critical exponents of the superfluid transition in Helium-4.

Concerning the twist viscosity, both theories predict a critical divergence of γ_1 like $(T/T_{NA}-1)^{-x}$ as the temperature T approaches the N-A transition temperature T_{NA}. This enhancement is due to fluctuations of the smectic-A order parameter $\Psi(r) = |\Psi(r)| e^{i\phi(r)}$ in the nematic phase. These fluctuations of $\Psi(r)$ (originating cybotactic groups) have a characteristic correlation length ξ, which grows like $(T/T_{NA}-1)^{-\nu}$ as $T \to T_{NA}$. Mean field theory predicts $x=\nu=0.5$ [4] and a calculation of Jähnig and Brochard [5–7] using the model of De Gennes leads to $x = \nu/2 \simeq 0.33$.

The precise determination of the critical exponent x requires an accurate knowledge of the temperature dependence of the regular part, γ_1^0, of the twist viscosity γ_1. Up to now the analysis of experimental data has always been performed by taking for γ_1^0 various «a priori» expressions without theoretical support, and this is one of the reasons for the wide variety of values of x reported in the literature, which range from 0.33 to 1.07.

We have recently derived theoretically an expression describing the temperature dependence of γ_1 in nematics not showing critical behaviour [8], which has the form

$$\gamma_1^0 = c.\ S^2 \exp\left(\frac{\varepsilon S}{kT}\right) \qquad (1)$$

where S is the usual nematic order parameter (as defined in [9]), k is the Boltzmann constant, T is the absolute temperature, ε is a constant related to the Maier-Saupe mean-field potential [10], and c is nearly constant over the temperature range of the nematic phase. Explicit expressions for c and ε are given in ref [8].

In this paper we shall apply expression (1) in order to get the critical exponent x of γ_1 in two nematic materials showing second-order N-A transitions. The total viscosity (experimentally measured) is given by

$$\gamma_1 = \gamma_1^0 + b.\left(\frac{T - T_{NA}}{T_{NA}}\right)^{-x} \qquad (2)$$

where γ_1^0 is given by (1) and the second term in the right-hand side represents the critical contribution. Expression (2) has been proposed in refs [4] and [6] but without explicitation of the form of γ_1^0 (T).

The nematic materials considered here are the following:

1) 40.8: N[4-n-butoxybenzilidene]-4′-octylaniline
2) HAB: 4,4′-di-n-hexylazoxybenzene

These two materials have monomolecular layers in the smectic-A phase.

In the next section we give the results of a least squares fit of expression (2) to the experimental data on γ_1 (T) quoted for 40.8 and HAB from the Bordeaux group [11].

In section 3 we shall discuss our results and compare them with the theoretical predictions [4, 7, 8] and with a similar analysis performed by us [12] for two other materials which have bimolecular layers in the smectic-A phase.

In section 4 we shall present the main conclusions of this work.

2 — RESULTS

In this section we present the results of a computation of the four parameters c, ε, b, x, needed to characterize the thermal dependence of γ_1, according to Eq. (1) and Eq. (2).

Our method of computation has been discussed elsewhere [12] and consists in an iterative linear regression over expression (2) minimizing the root mean square error (r.m.s. error) taken as a function of the parameters c, ε, b and x. It is also possible to vary slightly T_{NA} within the range of the experimental error in order to obtain a better fit.

For these computations it is necessary to have an analytical expression for the temperature dependence of the nematic order parameter S for each nematic. As we do not know at present the absolute values of S for the materials studied, we have used instead, the values of the anisotropy of the magnetic susceptibility $\Delta\chi$(T) from ref [13], which are proportional to S.

The two sets of data were fitted with an empirical expression of the form

$$\Delta\chi \times 10^7\,(\text{c.g.s.}) = [s_1 + s_2 . t^{1/2} + s_3 . t^{1/4} + s_4 . t^{1/6}]^{1/2} \qquad (3)$$

where $t = T_{NI} - T + \lambda$, T_{NI} is the nematic-isotropic transition temperature of the compound considered, T is the absolute temperature, and all the other symbols represent numerical constants to be computed by the least squares method.

Figure 1 shows the data on $\Delta\chi(T)$ for 40.8, from Ref. [13], fitted with expression (3). A similar fit has been obtained for HAB.

We also tried to fit the same data with a theoretical expression proposed by Hess [14], viz

$$S(T) = S(T_{NI}) . \left[\frac{3}{4} + \frac{1}{4} \left(1 + \Theta . \frac{T_{NI} - T}{T} \right)^{1/2} \right] \qquad (4)$$

but with poor results in the temperature range near T_{NI}, as shown in figure 2.

In Table I we present the computed values of c^*, ε^*, b, x, and the r.m.s. error for 40.8, HAB, and, for the sake of completeness,

TABLE I

Material	Origin of data	$T_{NI} - T_{NA}$ (K)	C^* (Poise)	ε^* (Kcal/mole)	b (Poise)	x	r.m.s. error
CBOOA	[21]	25.02	0.0199 [a)c)]	2.5230 [a)c)]	0.0268 [c)]	0.332 [c)]	0.0084 [c)]
CBOOA	[15]	24.75	0.0092 [a)]	3.1491 [a)c)]	0.0218 [c)]	0.330 [c)]	0.0089 [c)]
8OCB	[22]	12.347	0.0122 [b)]	4.0602 [b)c)]	0.0470 [c)]	0.352 [c)]	0.0518 [c)]
HAB	[11]	38.18	0.0998 [a)]	1.2273 [a)c)]	0.1673 [c)]	0.328 [c)]	0.0165 [c)]
40.8	[11]	15.33	0.0642 [a)]	0.8495 [a)]	0.0654	0.333	0.0129

a) Computed with $\Delta\chi \times 10^7$ instead of S.

b) Computed with the order parameter S' of a spin probe dissolved in the nematic phase (see [12]).

c) See ref. [12].

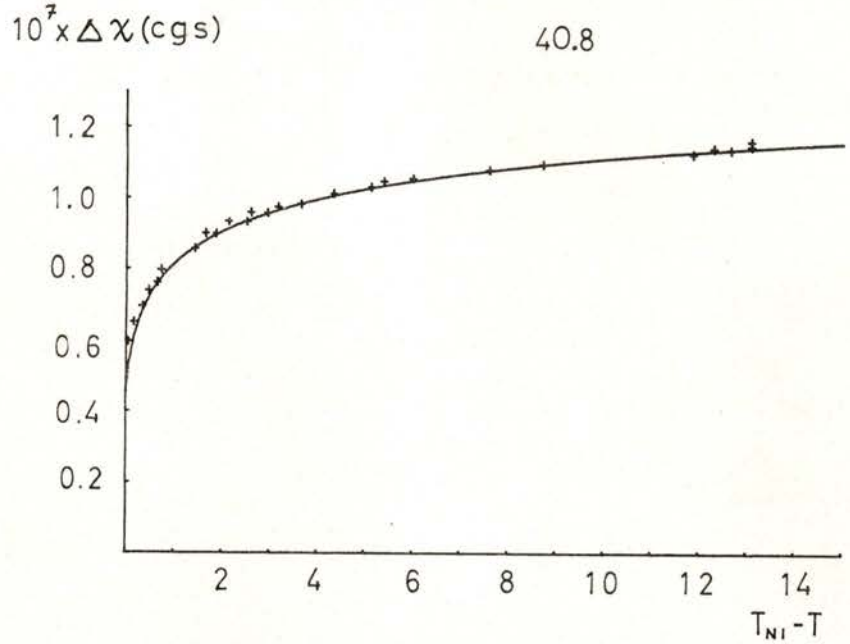

Fig. 1 — Anisotropy of the magnetic susceptibility $\Delta\chi.10^7$ (C.G.S.) for 40.8. Data points from [13], fitted with expression (3) with $s_1 = -0.45762$, $s_2 = -0.18941$, $s_3 = 1.29634$, $s_4 = 2.7035 \times 10^{-5}$, $\lambda = 0.1$.

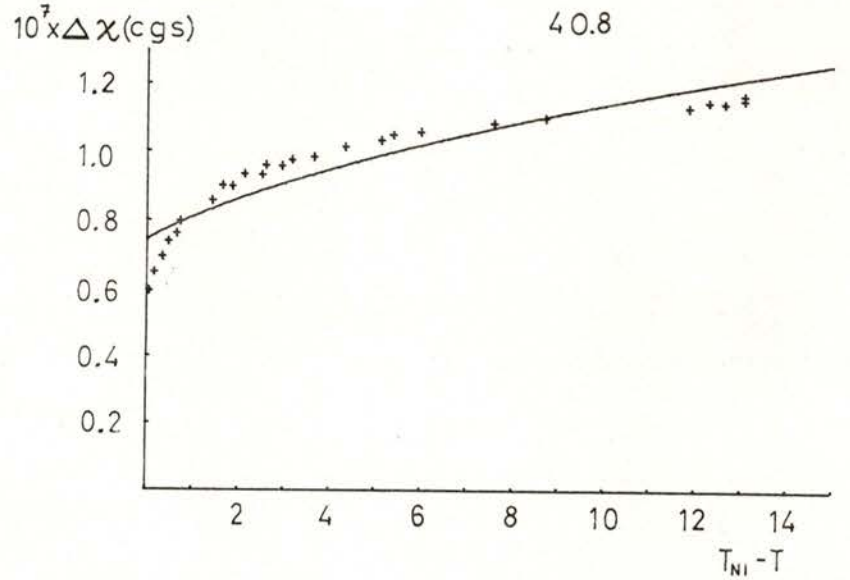

Fig. 2 — The same data of fig. 1, now fitted with expression (4). The best fit (full curve) is for $S(T_{NI}) = 0.75$ and $\Theta = 290$.

also for CBOOA [N-4-cyanobenzilidene-4′-octyloxi-aniline] and 80CB [4, octyloxy-4′, cyanobiphenyl] [12]. We denote by c^* and ε^* the values of c and ε computed with $\Delta\chi \times 10^7$ instead of S; they are related by:

$$c = c^* \cdot \frac{\Delta\chi \times 10^7}{S} \quad \text{and} \quad \varepsilon = \varepsilon^* \cdot \frac{\Delta\chi \times 10^7}{S} \tag{5}$$

The plots of $\gamma_1 (T_{NI} - T)$ for 40.8 and HAB are presented in figures 3 and 4 respectively, and show good agreement with the experimental data.

We may check our determination of γ_1° by plotting $ln(\gamma_1 - \gamma_1^\circ)$ as a function of $ln(T - T_{NA})$. If γ_1° is correctly evaluated, then the log-log plots must give a straight line *over the whole nematic range.* These plots are presented in figs. 5 and 6, which effectively show straight lines over the whole nematic range. We also note that the r. m. s. errors are nearly the same in each case.

3 — DISCUSSION

We have already remarked that the choice of different expressions for γ_1° leads to different values for x. It can be shown that even within a narrow region near T_{NA}, where the regular part γ_1° of the twist viscosity is nearly constant, the slope y found by plotting $\log \gamma_1$ vs. $\log(T - T_{NA})$ is a function of the ratio $\zeta = \gamma_1^\circ / \gamma_1$. This explains why the plots of $ln\,\gamma_1$ vs. $ln(T - T_{NA})$ give a curve that tends only asymptotically (as $ln(T - T_{NA}) \to \infty$) to a straight line with a slope equal to the critical exponent x. The result given by this type of fit depends on the temperature range $T - T_{NA}$ over which data are retained for the definition of the «straight line». The value of x found in this way is controled by the last points retained and not by the points close to T_{NA} as it should be. This explains the large dispersion of values for the critical exponent x reported so far.

Fundamental in our method of analysis is the original way of accounting for the regular part of the viscosity. In the analyses reported so far, the thermal dependence of the regular part of the viscosity had been assumed in all cases, and in various forms. By

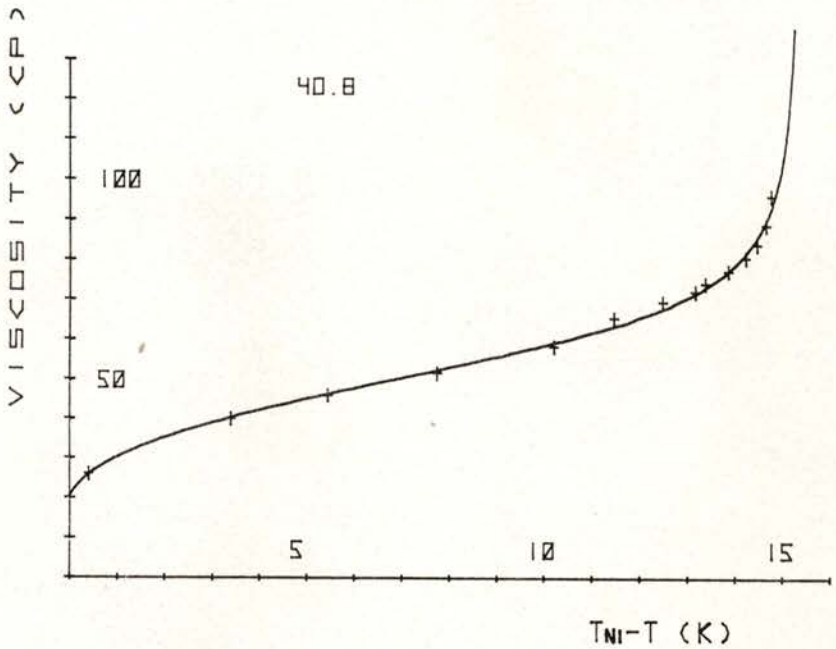

Fig. 3 — Twist viscosity γ_1 $(T_{NI} - T)$ for 40.8. Data from [11] fitted with expression (2) (see Table I).

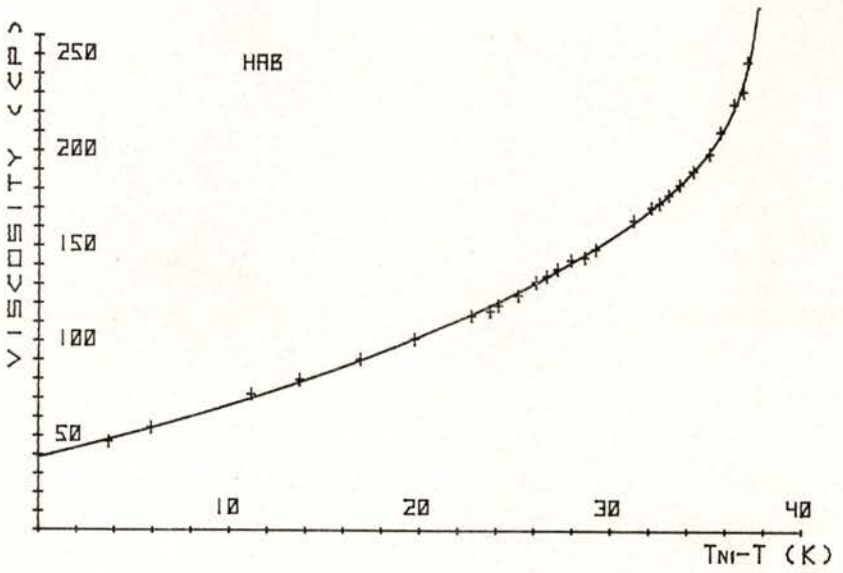

Fig. 4 — Twist viscosity for HAB. Data points from [11] fitted with expression (2) (see Table I).

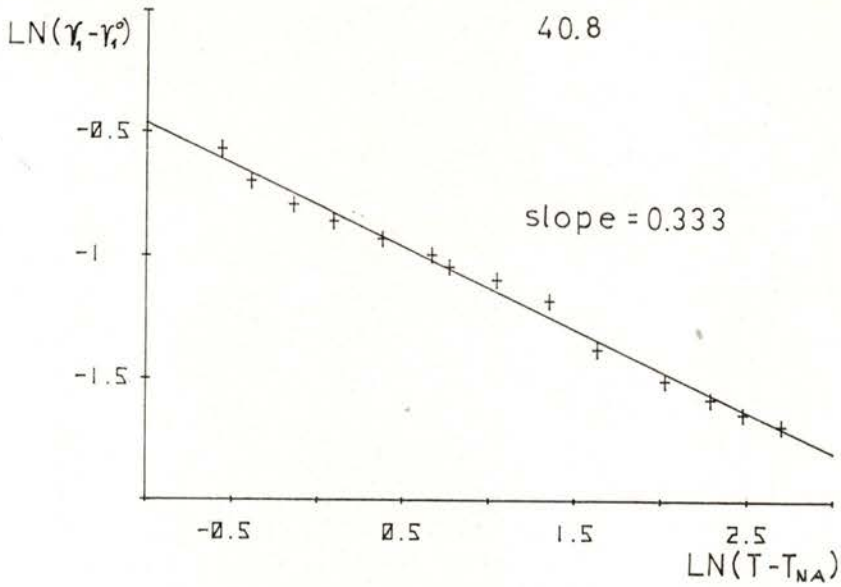

Fig. 5 — Plot of $ln(\gamma_1 - \gamma_1^0)$ vs $ln(T - T_{NA})$ for 40.8; γ_1^0 is given by (1) and the straight line is determined by a least squares fit.

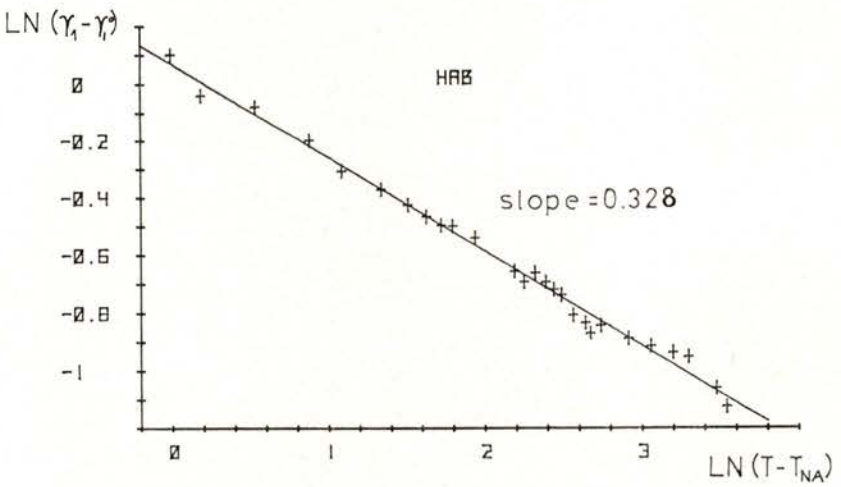

Fig. 6 — Plot of $ln(\gamma_1 - \gamma_1^0)$ vs $ln(T - T_{NA})$ for HAB; γ_1^0 is given by (1) and the straight line is determined by a least squares fit.

contrast, our analysis is based upon expression (1), which has been theoretically derived and experimentally tested in appropriate conditions [8]. The plots of $\log(\gamma_1 - \gamma_1^\circ)$ vs. $\log(T - T_{NA})$ shown in this paper give straight lines over the full nematic range and so give a meaningful result for the critical exponent.

After this methodological remark we shall discuss the values of the parameters b and x found from this analysis. The critical part of γ_1 is [4, 6] given by:

$$\tilde{\gamma}_1 = b\left(\frac{T - T_{NA}}{T_{NA}}\right)^{-x} = \frac{\pi}{4}\frac{kT}{d^2}\frac{\tau}{\xi_{11}} = \frac{3}{2}B_N^\circ\,\tau^\circ\left(\frac{T - T_{NA}}{T_{NA}}\right)^{-x} \qquad (6)$$

where d is the interlayer spacing of the smectic phase, ξ_{11} is the correlation length in a direction parallel to the nematic director and τ is a characteristic time of the cybotactic groups (mean lifetime). B_N may be considered as the rigidity modulus of the smectic layers of the cybotactic groups. Using de Gennes, model, Jähnig and Brochard [6, 7] found $\tau = \tau_o\ (T/T_{NA} - 1)^{-3\nu/2}$ and $\xi_{11} = \xi_{11}^\circ\ (T/T_{NA} - 1)^{-\nu}$, where $\nu \simeq 0.66$.

Taking $d \simeq 25$ Å for 40.8 [16] we find, using (6), $B_N^\circ \cdot \xi_{11}^\circ = 0.388$ erg. cm^{-2}, and $\tau_o / \xi_{11}^\circ = 0.124$ s cm^{-1}. From data [17] on the critical part of the bend elastic constant $\tilde{K}_3 = B_N^\circ\,(\xi_{11}^\circ)^2 \times (T/T_{NA} - 1)^{-0.66}$ we get $B_N^\circ\,(\xi_{11}^\circ)^2 \sim 1.6 \times 10^{-8}$ erg. cm^{-1}, so that we can find $\xi_{11}^\circ \sim 4$ Å and $\tau_o \sim 5 \times 10^{-9}$ s, in accordance with an order of magnitude evaluation by Brochard [5]. For HAB we take d 23 Å (~ molecular length) and find $B_N^\circ \cdot \xi_{11}^\circ = 0.396$ erg. cm^2 and $\tau_o / \xi_{11}^\circ = 0.282$ s cm^{-1}. Unfortunately we have not enough data to calculate ξ_{11}° but assuming $\xi_{11}^\circ \sim 10$ Å we find $\tau_o \sim 3 \times 10^{-8}$ s which compares well with the value obtained from acoustic attenuation measurements on a similar compound [18].

For the regular part of γ_1 we expect [8] that

$$\frac{\pi^2 V^*}{N_A k T} \cdot \gamma_1^\circ = \frac{1}{\nu_o} \qquad (7)$$

be comparable with τ_d^1 the dielectric relaxation time for the rotation of the nematic molecules around their short molecular axis. V^* is roughly the molar volume at the temperature T as extrapolated fom the isotropic phase, and N_A is Avogadro's number. For HAB, and with $T_{NI} - T \sim 13°$, we find $\gamma_1^\circ \sim 0.393$ P. In the lack of

data for V* in HAB we take $V^* \sim 322$ cm^3 mole^{-1} from data in ref. [19] about 4-4′ dipentyloxiazoxybenzene, a molecule of similar dimensions. We then find, from expression (7), $1/\nu_o \sim 4.8 \times 10^{-8}$ s, which is near the experimental value [20] $\tau_d^{(1)} \sim 10.8 \times 10^{-8}$ s.

From Maier-Saupe theory [9–10] we know that

$$\varepsilon = 1/m \times 1.355 \times 10^{-2} \times T_{NI} \text{ (Kcal mole}^{-1}\text{)} \qquad (8)$$

where m is a cluster parameter which accounts for steric short range order. Assuming $\Delta\chi \times 10^7/S \sim 1.5$ for 40.8 and $\Delta\chi \times 10^7/S \sim 1.4$ for HAB, using eq. (8) and Table I, we find $m = 3.7$ for the former, and $m = 2.6$ for the latter of these compounds. These values are rather satisfactory.

4 — CONCLUSION

The main conclusion of this work is that the use of expression (1) for the regular part of the twist viscosity γ_1 provides:

a) an unique value for the critical exponent of the twist viscosity divergence near a nematic-smectic-A phase transition ($x \simeq 0.33$) which agrees with De Gennes theory [2, 3] and the subsequent calculation of Jähnig and Brochard [6, 7], based on dynamical scaling;

b) the values of the parameters c and ε which are related to the intermolecular potential of Maier-Saupe [9, 10] and are characteristic of the nematic material;

c) a similar critical behaviour in nematic materials which give monomolecular smectic-A layers and in those which give bimolecular smectic-A layers [12];

d) a complete description of the temperature dependence of the twist viscosity over the whole nematic range.

REFERENCES

[1] MCMILLAN, W. L. — *Phys. Rev.* **A-4**, 1238 (1971).

[2] DE GENNES, P. G. — *Solid State Commun.* **10**, 753 (1972).

[3] DE GENNES, P. G. — *Mol. Cryst. Liq. Cryst.* **21**, 49 (1973).

[4] MCMILLAN, W. L. — *Phys. Rev.* **A-9**, 1720 (1974).

[5] BROCHARD, F. — *J. Physique* **34**, 411 (1973).

[6] JÄHNIG, F.; BROCHARD, F. — *J. Physique* **35**, 301 (1974).

[7] BROCHARD, F. — *J. Physique* **37, Coll C-3**, C3-85 (1976).

[8] MARTINS, A. F.; DIOGO, A. C. — *Portgal. Phys.* **9**, 129 (1975); MARTINS, A. F. — *Portgal. Phys.* **9**, 1 (1974).

[9] MAIER, W.; SAUPE, A. — *Z. Naturforschg.* **14-a**, 882 (1959).

[10] MAIER, W.; SAUPE, A. — *Z. Naturforschg.* **15-a**, 287 (1960)

[11] HARDOUIN, F.; ACHARD, M. F.; SIGAUD, G.; GASPAROUX, H. — *Physics Letters* **49-A**, 25 (1974).

[12] MARTINS, A. F.; DIOGO, A. C.; VAZ, N. P. — *Annales de Physique* **3**, 361 (1978).

[13] GASPAROUX, H.; HARDOUIN, F.; ACHARD, M. F.; SIGAUD, G. — *J. Physique* **36, Coll C-1**, C1-107 (1975).

[14] HESS, S. — *Z. Naturforschg.* **30-a**, 728 (1975).

[15] HARDOUIN, F.; ACHARD, M. F.; GASPAROUX, H. — *Solid State Commun.* **14**, 453 (1974).

[16] CHU, K.-S.; AILAWADI, N.; MOROI, D. — *Mol. Cryst. Liq. Cryst.* **38**, 45 (1977).

[17] D'HUMIÈRES, D.; LÉGER, L. — *J. Physique* **36, Coll C-1**, C1-113 (1975).

[18] KIRY, F.; MARTINOTY, P. — *J. Physique-Letters* **38**, L-389 (1977).

[19] PRASAD, J. S.; SUBRAMHANYAM, H. — *Mol. Cryst. Liq. Cryst.* **33**, 77 (1976).

[20] BATA, L.; BUKA A.; MOLNÁR, G. — *Mol. Cryst. Liq. Cryst.* **38**, 155 (1977).

[21] HUANG, C. C.; PINDAK, R. S.; FLANDERS, P. J.; HO, J. T. — *Phys. Rev. Lett.* **33**, 453 (1974).

[22] DELAYE, M. — *J. Physique* **37-Coll C-3**, C3-99 (1976).

MAGNETIZATION STUDIES ON Nb_3Sn MULTIFILAMENTARY WIRE (*)

C. S. FURTADO
Faculdade de Ciências e Tecnologia, Coimbra, Portugal

ABSTRACT — The results and interpretation of magnetization measurements made on superconducting multifilamentary Nb_3Sn, obtained by the bronze route, are presented. Curves of first magnetization and quasi-static loops were obtained by electronic integration, the explanation of which is given in terms of the critical state model taking also into account the existence of a surface current. The dependence of the hysteretic loss on the surface magnetic field is yet considered and explained on the same basis. Finally a method of determining the variation of the critical current density with the magnetic induction by means of small loops is described.

In recent years great interest has been shown in many dc and ac applications such as superconducting magnets, superconducting electrical machines and superconducting power transmission. One of the materials which has received some attention in view of its high transition temperature is Nb_3Sn. In the beginning, because of the high hysteretic losses, it was not regarded as a potential ac conductor. However, recently, new techniques of fabrication were developed which allowed the losses to be reduced. The results we present in this communication were obtained on Nb_3Sn multifilamentary wire prepared in the UKAEA Establishment of Harwell by the bronze route.

The explanation of the observed magnetic behaviour was based on Bean's critical model [1] applicable to hard superconductors. However, instead of considering, as Bean does, a constant critical current density, we suppose this density, J_c, dependent on the local magnetic induction, B, using Kim's relation $J_c = \alpha/(B + B_0)$.

(*) Results presented at the Conference of the Portuguese Physics Society (Lisbon, February 1978).

In this communication we begin by presenting briefly the related theory, after which the sample and experimental set-up are described. Then, we present and give explanation for the first magnetization curve and some of the symmetrical hysteretic loops we obtained. Finally we show a process by which one can get, easily, the relation $J_c = J_c(H)$ by means of small hysteretic loops recorded at different values of the applied magnetic field.

2 — THEORY

2.1 — *The Critical State*

The concept of the critical state was firstly introduced by Bean [1]. Its hypothesis are the following: *a*) there is a constant limit value for the critical current density, J_c, which is the maximum value that a supercondutor can carry without losses; *b*) this limit value J_c is locally induced by any e.m.f. no matter how small. Later it was admitted and proven experimentally that the critical current density depends on the local magnetic induction, $J_c = J_c(B)$. One of the functional relations which is frequently used is that proposed by Kim et al [2] $J_c = \alpha/(B+B_0)$, where J_c is the critical current density, B the magnetic induction and α and B_0 characteristic parameters of the material. The critical current density J_c has its origin in the existence of metallurgical defects which work as pinning centres of the fluxoids. Maxwell's equation $\nabla \times \vec{B} = k\vec{J}$ allows one to relate J_c with the fluxoid concentration, n, since we have $B = n\,\phi_0$, where $\phi_0 = 2.70 \times 10^{-15}$ Wb is the value of the magnetic flux associated with a fluxoid and $k = 4\pi/10$ with B in Gauss and J in A cm^{-2}.

In the case of a cylindrical sample Maxwell's law just referred can be written

$$\pm \int_{H_0}^{B(x)} \frac{dB}{J(B)} = kx \quad ,$$

x being measured in the relation to the surface and the sign $\pm$ appearing because the vector equation is written in a scalar form. The lower limit of the integral is the magnetic field seen by the bulk, which means

that the surface magnetization is subtracted to the applied magnetic field. In the case of Nb_3Sn, the hysteretic contribution of the surface was not considered. However, we have taken into account the Meissner magnetization Me. According to Fietz and Webb [3] we consider $H_0 = H_a + 4\pi Me$, where H_a is the applied magnetic field.

2.2 — *Expressions for the case of full penetration*

When in every point of the sample there is magnetic field, we say that full penetration has ocurred. In this situation, critical current takes place all over the sample. We did use expressions (a), (b), (c) and (e) as given by Fietz et al [4]. As their expressions (d), (f), and (g) led us to incongruous results, we attempted to deduce new ones for the corresponding situations (see Appendix 1), which we refer in table 1.

2.3 — *Expressions for the case of partial penetration*

We have also deduced the corresponding expressions for the case in which the magnetic field does not penetrate the sample fully (see Appendix 2). The results are as follows, where H_{om} is the peak field seen by the bulk.

H_a increasing, $0 \leq H_0 \leq H_{om}$:

$$4\pi\overline{M} = \frac{2}{3\alpha k\omega}\left(\frac{(H_{om}+B_0)^2+(H_0+B_0)^2}{2}\right)^{3/2} -$$

$$-\frac{1}{3\alpha k\omega}((H_0+B_0)^3+B_0^3) - \frac{B_0}{2\alpha k\omega}((H_{om}+B_0)^2 - B_0^2) - H_a\,.$$

H_a decreasing, $H_{om} \geq H_0 \geq 0$:

$$4\pi\overline{M} = \frac{1}{3\alpha k\omega}((H_0+B_0)^3+B_0^3) + \frac{B_0}{2\alpha k\omega}((H_{om}+B_0)^2 -$$

$$-2(H_0+B_0)^2+B_0^2) - \frac{2}{3\alpha k\omega}\left(\frac{(H_{om}+B_0)^2-(H_0+B_0)^2}{2}+B_0^2\right)^{3/2} - H_a\,.$$

TABLE I

Validity Region	Average magnetization $4\pi\overline{M}=\int_0^{\omega}(B(x)-H_a)\,dx$
H_a increasing $0<H_a<H_{c1}$, first magnetization	$4\pi\overline{M}=-H_a$ (a)
H_a increasing $H_{c1}<H_a<((B_0+H_{c1})^2+2\alpha k\omega)^{1/2}-B_0$ first magnetization	$4\pi\overline{M}=-H_a-\frac{(B_0+H_a)^2}{\alpha k\omega}\frac{B_0}{6}-\frac{H_a}{3}+$ $+\frac{(B_0+H_{c1})^2}{\alpha k\omega}\frac{B_0}{6}-\frac{H_{c1}}{3}$ (b)
H_a increasing $((B_0+H_{c1})^2+2\alpha k\omega)^{1/2}-B_0<H_a<H_p$	$4\pi\overline{M}=-(B_0+H_a)-\frac{1}{3\alpha k\omega}\{[(H_0+$ $+B_0)^2-2\alpha k\omega]^{3/2}-(H_0+B_0)^3\}$ (c)
H_a decreasing $H_{c1}<H_a<((H_p+B_0)^2-4\alpha k\omega)^{1/2}-B_0$	$4\pi\overline{M}=-(B_0+H_a)+\frac{1}{3\alpha k\omega}\{[(H_0+$ $+B_0)^2+2\alpha k\omega]^{3/2}-(H_0+B_0)^3\}$ (e)
H_a increasing $-H_{c1}<H_a<H_{c1}$	$4\pi\overline{M}=B_0+\frac{1}{3\alpha k\omega}B^3-\frac{1}{3\alpha k\omega}(2\alpha k\omega+$ $+B_0^2)^{3/2}-H_a$
$H_{c1}<H_a<((B_0-H_{c1})^2+2\alpha k\omega)^{1/2}-B_0$	$4\pi\overline{M}=-\frac{1}{3\alpha k\omega}[(2\alpha k\omega+2B_0^2-$ $-(H_0+B_0)^2)^{3/2}-(H_0+B_0)^3]-\frac{B_0}{\alpha k\omega}$ $((H_0+B_0)^2-B^2)+B_0-H_a$

Obs.: H_p is the peak value of the applied field H_a.

The value of the average remanent magnetization, i.e. the value of the average magnetization when the applied field is zero, is obtained by putting $H_0=0$ in any of the above expressions:

$$4\pi \bar{M}_{rem} = \frac{2}{3\alpha k \omega}\left(\frac{(H_{om}+B_0)^2+B_0^2}{2}\right)^{3/2} - \frac{B_0}{2\alpha k \omega}(H_{om}+B_0)^2 - \frac{1}{6\alpha k \omega}B_0^3.$$

3 — SAMPLES AND MEASUREMENT TECHNIQUE

The samples consisted of groups of 4 wires, approximately 4 cm long. These wires were cut from a stool produced by the bronze route, according to the technique initiated at A.E.R.E. Harwell in 1969 [5]. The basic building block of the composite is a 37 filament hexagon in a bronze matrix (Cu/7.5 a % Sn) which has been stacked in the configuration shown in the photomicrograph (Figure 1) with 37 of

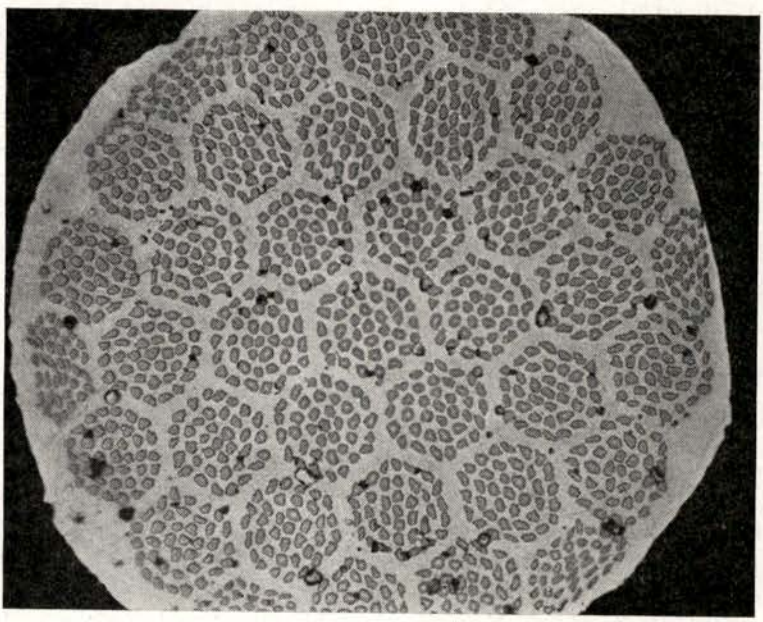

Fig. 1 — Wire of Nb_3Sn composite (37 × 37 filaments).

these blocks ($37 \times 37 = 1369$ filaments). The wire is drawn down to its final shape being simultaneously twisted: the diameter of each filament is about 8 μm, the external diamater equal to 0.43 mm and the twist pitch equal to 6.44 mm. This wire is then introduced in a large quartz tube (~ 3 cm in diameter) which is placed in a tube furnace and kept under a dynamic vacuum better than 10^{-5} torr during 24 hours at

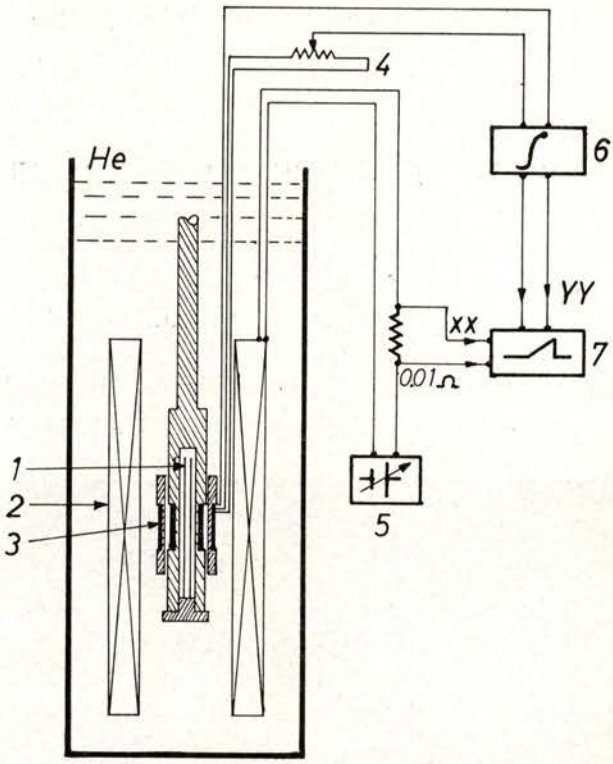

Fig. 2 — Circuit for electronic integration

1 — sample; 2 — superconducting magnet; 3 — pick-up coil; 4 — potential divider; 5 — sweeping d.c. power supply; 6 — integrator; 7 — x y recorder

750°C. The Sn diffuses from the matrix to the Nb filaments with the formation of a Nb_3Sn layer between the bronze and the Nb cores. After the heat treatment the sample cools down slowly under vacuum.

The experimental arrangement is shown in Figure 2. The magnetization is measured by electronic integration. The signal is obtained

from a pick-up coil which consists of two coils connected in series opposition, the inner one with 10000 turns and the outer with 527. The final compensation is obtained by means of a voltage divider connected between the ends of the last turn of the outer coil. The signal, after being integrated using an electronic integrator, was introduced in the Y-axis of a recorder. In the X-axis was introduced a signal taken from a resistor which was traversed by the current generating the magnetic field.

4 — RESULTS AND DISCUSSION

The curve of first magnetization and the loops for peak values of 1160, 1600, 2400 and 29680 Oe are presented in Figure 3 *a*, *b*, *c*, *d*, and *e*. They show the average magnetization, $-4\pi\bar{M}$, in terms of the applied field H_a. In full are the experimental curves and the dotted ones were evaluated with the above expressions deduced on the basis of the critical model using Kim's relation.

$\bar{M}$ varies linearly with H_a between -400 and 400 Oe, approximately, which can be interpreted as due to the Meissner current. Increasing H_a the magnetization reaches a maximum after which starts decreasing monotonically up to the peak field H_{am}. After this value has been reached and the external field starts to decrease it is not noticeable any hysteretic surface current: this behaviour is characteristic of high $\varkappa$ materials, as is the case of Nb_3Sn. In decreasing the magnetic field, the absolute value of the magnetization, after passing through zero, starts to increase, but with opposite sign, up to the remanent magnetization for $H_a = 0$.

Let us now look at the calculated curves. In their evaluation it was considered an average equilibrium magnetization, defined by the following pairs of values $\{H_a - 4\pi Me\} = \{(0,0);\ (400,\ 400);\ (500,\ 220);\ (800,\ 120);\ (>1200,\ 100)\}$. The best fitting for the loops whose peak values are 1200, 1600 and 2400 Oe was obtained by putting in Kim's relation $\alpha = 1{,}2 \times 10^{10}$ G-A/cm^2 and $B_0 = 1100$ Oe. The choice of these parameters gets further confirmation based on the variation of the remanent average magnetization, $4\pi\bar{M}_{rem}$, in terms of the applied magnetic field, as Figure 4 shows. The field of full penetration is, in this case, equal to 2200 Oe, approximately. For the curve of first magnetization and the loop of 29680 Oe peak field, the best fitting was with $\alpha = 5 \times 10^{10}$ G-A/cm^2 and $B_0 = 6300$ Oe.

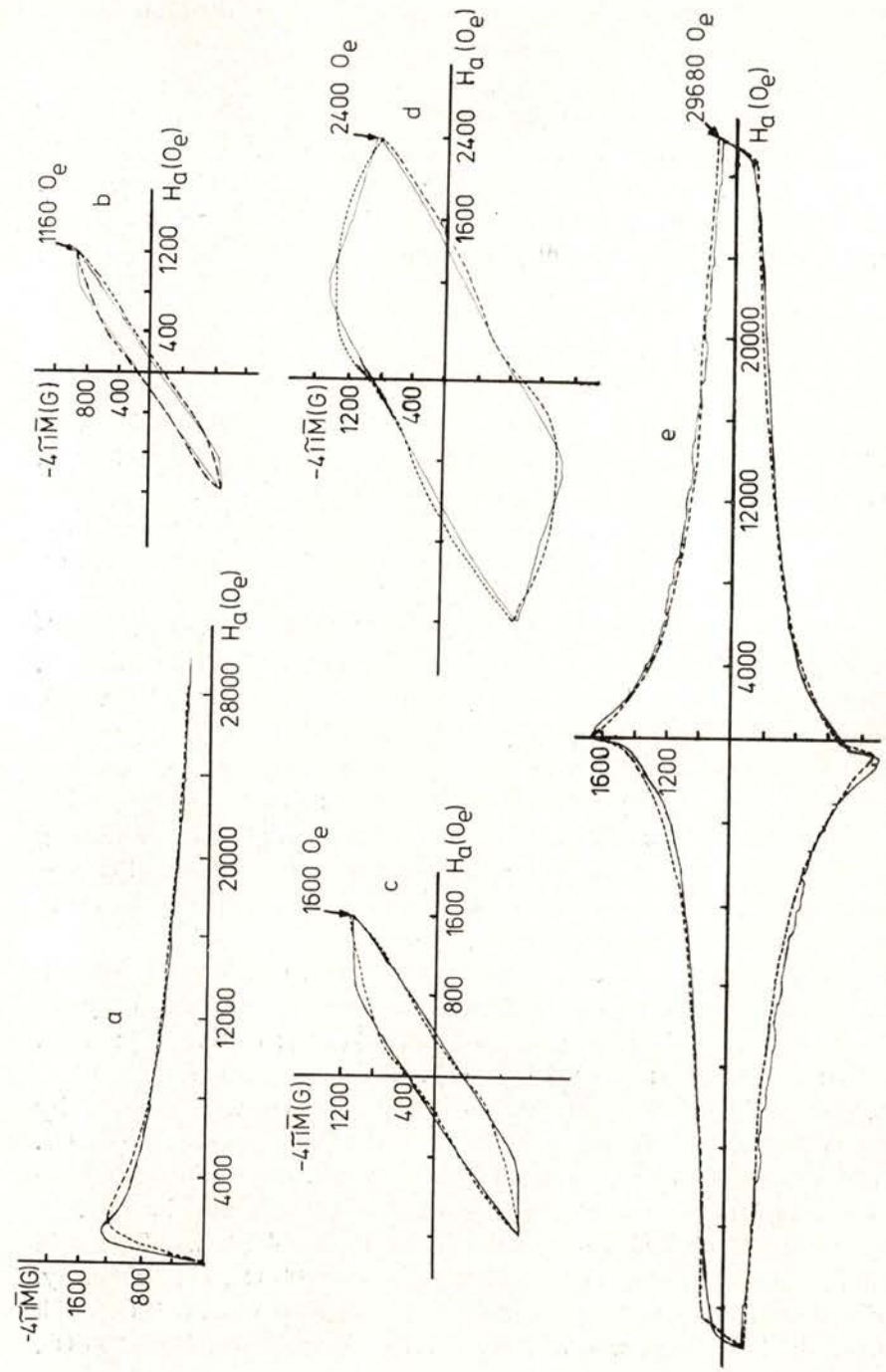

Fig. 3 — Curve of first magnetization and quasi-static loops.

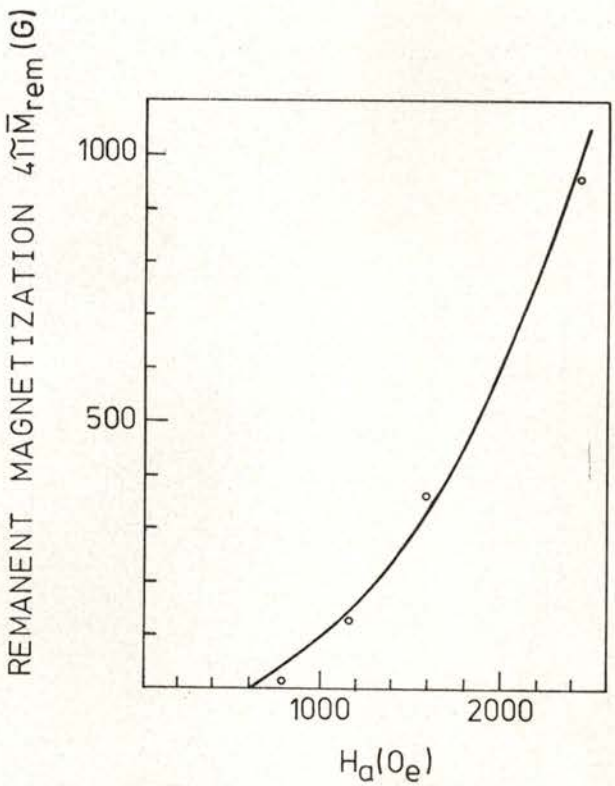

Fig. 4 — Dependence of the remanent magnetization on the applied magnetic field.

For these parameters the field of full penetration is equal to 2600 Oe approximately. Therefore, we are bound to consider the material well described magnetically by two Kim's relations: one for low fields (<3000 Oe) and the other for high fields. As Figure 5 shows these functions of critical current density vs. the applied magnetic field agree satisfactorily with the experimental one.

5 — DETERMINATION OF $J_c = J_c(H)$ BY MEANS OF SMALL LOOPS

The magnetization measurements brought the idea of using small loops traced at different values of the applied magnetic field to determine the relation $J_c = J_c(H)$. Let us imagine we reduce the value of the appied field from H_a to $H'_a < H_a$. If $\Delta H_a = H_a - H'_a$ is small

it is justifiable to consider in this interval, the critical current density J_c as constant. The variation of the average induction $\Delta \overline{B}$ is then

$$\Delta \overline{B} = \frac{(\Delta H_a)^2}{4\, k\, \omega\, J_c} \quad .$$

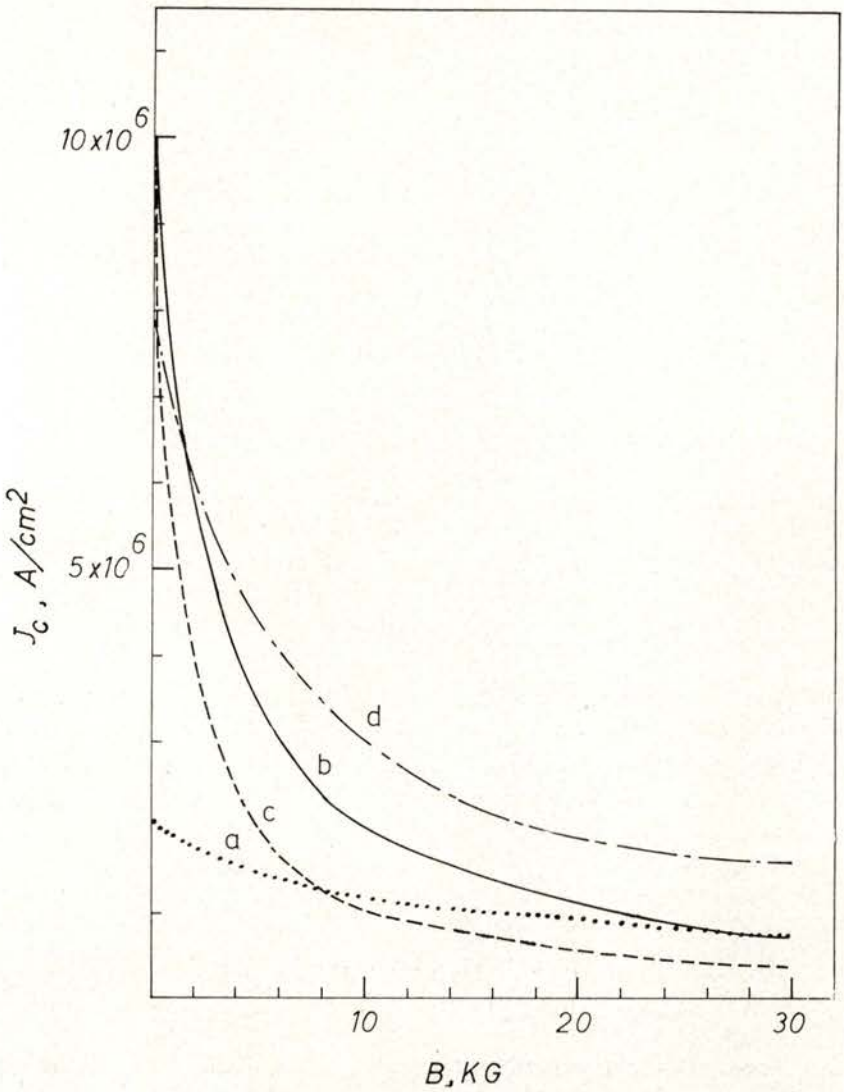

Fig. 5 — Dependence of the critical current density on the magnetic induction. *a* — experimental; *b* — Kim's relation $J_c = 2.5 \times 10^{10}/(B + 2300)$; *c* and *d* — obtained from quasi-static magnetization measurements.

Considering Kim's relation $J_c = \alpha/(B + B_0)$ and taking $B \simeq H_a$, which is reasonable, one gets

$$\frac{\Delta \bar{B}}{(\Delta H_a)^2} = \frac{H_a + B_0}{4\ \alpha k \omega} .$$

By the use of small loops, as those presented in Figure 6, we evaluate $\Delta \bar{B} = \Delta(4\pi \bar{M}) - \Delta H_a$. Then by choosing $\Delta \bar{B}/(\Delta H_a)^2$ as ordinate and H_a as abcissa we can easily obtain B_0 and $\alpha k \omega$. In our case, we get from Figure 7, $B_0 = 2\,300$ Oe and $\alpha k \omega = 1{,}0 \times 10^7$ which yields $J_c = 2.5 \times 10^{10}/(B + 2300)$, which is represented in *b* of Figure 5. This curve is compared with the experimental one and those obtained from the quasi-static magnetization measurements *c* and *d* (Figure 5).

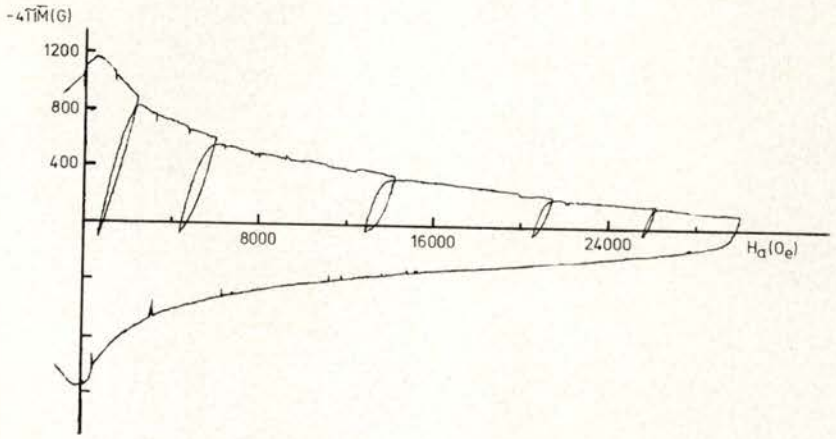

Fig. 6 — Example of experimental small loops.

This work was done as a member of the 'Projecto CF3' (INIC); the experiments took place during a stay in the UKAEA Establishme of Harwell, graciously financed by the Royal Society (London) and the Academia das Ciências de Lisboa to whom I express my gratitude. It is also an agreeable duty to thank Drs. J. A. Lee and J. P. Charlesworth, of Harwell, for the kindness of their hospitality.

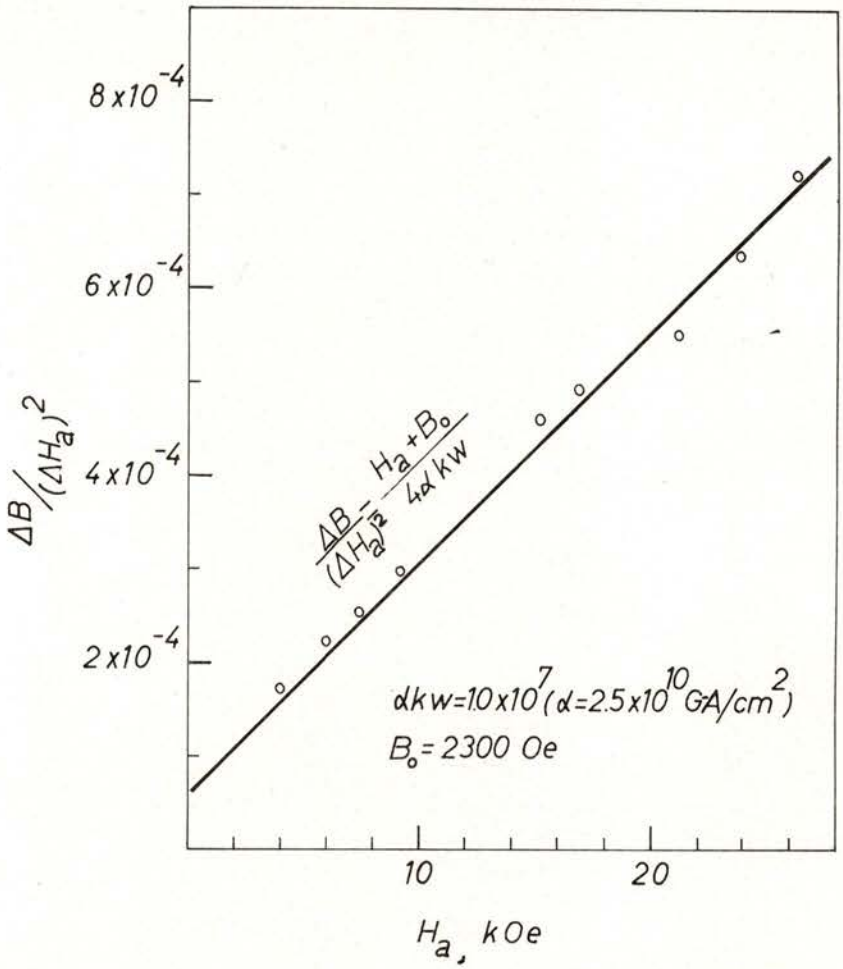

Fig. 7 — Dependence of $\Delta B/(\Delta H_a)^2$ on the applied magnetic field.

APPENDIX 1 — *Evaluation of the average magnetization for increasing H_a in case of full penetration and $0 < H_0 < (B_\theta^2 + 2\alpha k \omega)^{1/2} - B_0$.*

It is admitted in the following calculations that a superconducting slab, after being fully penetrated by the magnetic field in the negative direction, starts to be subjected to a positive applied magnetic field as Figure 8 shows.

From Maxwell's equation and supposing $J(B)=\alpha/(B+B_0)$ we have in $(0, d)$

$$-\int_{H_0}^{B(x)}(B+B_0)\,dB=\alpha k x$$

or

$$B(x)=((H_0+B_0)^2-2\alpha k x)^{1/2}-B_0.$$

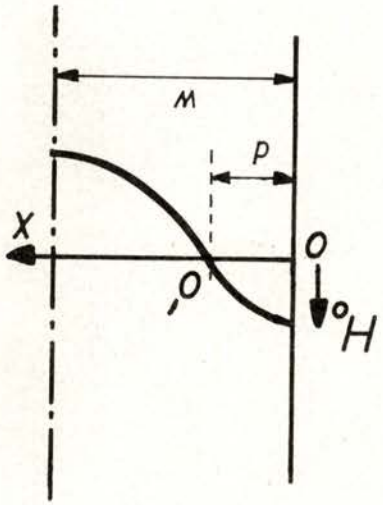

Fig. 8 — Profile of the magnetic induction for increasing H_a and $0 < H_0 < (B_0^2 + 2\,\alpha k \omega)^{1/2} - B_0$.

The value of d is determined by the condition $B(x)=0$:

$$d=\frac{(H_0+B_0)^2-B_0^2}{2\alpha k}$$

Choosing the origin in $0'$ we have

$$-\int_0^{B(x)}(B+B_0)\,dB=\alpha k x$$

or

$$B(x)=B_0-(2\alpha k x+B_0^2)^{1/2}.$$

The magnetic flux per unit length is then:

$$(0, d): \int_0^d B(x)\, dx = \int_0^d \{((H_0 + B_0)^2 - 2\alpha k x)^{1/2} - B_0\}\, dx;$$

$$(d, \omega): \int_0^{\omega - d} B(x)\, dx = \int_0^{\omega - d} (B_0 - (B_0^2 + 2\alpha k x)^{1/2})\, dx =$$

$$= B_0(\omega - d) + \frac{1}{3\alpha k} B_0^3 - \frac{1}{3\alpha k} (2\alpha k(\omega - d) + B_0^2)^{3/2};$$

$$\text{Total } (0, \omega): -\frac{1}{3\alpha k}\{(2\alpha k\omega + 2B_0^2 - (H_0 + B_0)^2)^{3/2} - (H_0 + B_0)^3\} -$$

$$- \frac{B_0}{\alpha k}((H_0 + B_0)^2 - B_0^2) + B_0\omega \quad .$$

Then the average magnetization is

$$4\pi \bar{M} = -\frac{1}{3\alpha k\omega}\{(2\alpha k\omega + 2B_0^2 - (H_0 + B_0)^2)^{3/2} - (H_0 + B_0)^3\} -$$

$$- \frac{B_0}{\alpha k\omega}((H_0 + B_0)^2 - B_0^2) + B_0 - H_a \quad .$$

When $-H_{c1} \leqslant H_a \leqslant H_{c1}$ the value of the magnetic field seen by the bulk, H_0, is zero and $d = 0$. Then the flux per unit length is

$$B_0\omega + \frac{1}{3\alpha k} B_0^3 - \frac{1}{3\alpha k} (2\alpha k\omega + B_0^2)^{3/2}$$

and the average magnetization

$$4\pi \bar{M} = B_0 + \frac{1}{3\alpha k\omega} B_0^3 - \frac{1}{3\alpha k\omega} (2\alpha k\omega + B_0^2)^{3/2} - H_a \quad .$$

APPENDIX 2 — *Evaluation of the expressions for the average magnetization in the case of partial penetration*

We are going to deduce the expressions for the average magnetization in the case the maximum value of the magnetic field at the surface, H_{om}, is not enough for all the sample to be penetrated by the magnetic flux.

Decreasing Branch

We begin with the decreasing branch of the loop: the magnetic field at the surface, after passing by its maximum H_{om}, starts to decrease until it becomes zero. Figure 9 represents schematically the profile of the magnetic induction B (x) for a given value H_0 of the surface magnetic field.

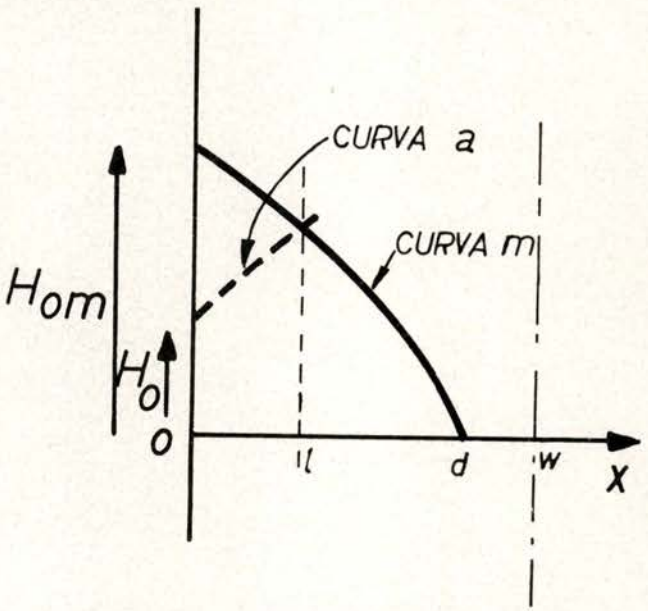

Fig. 9 — Profile of the magnetic induction for decreasing H_a in case of partial penetration.

By integrating

$$-\int_{H_{om}}^{B(x)} (B+B_0)\, dB = \alpha k x,$$

we get the expression of the curve m

$$B(x) = ((H_{om}+B_0)^2 - 2\alpha k x)^{1/2} - B_0.$$

Similarly, by integration of $\int_{H_0}^{B(x)} (B+B_0)\, dB = \alpha k x$, we obtain the expression of curve a

$$B(x) = ((H_0+B_0)^2 + 2\alpha k x)^{1/2} - B_0.$$

The value of the penetration depth of the magnetic field, d, is obtained considering $B(x)=0$ in the expression of the curve m

$$d=\frac{(H_{om}+B_0)^2-B_0^2}{2\alpha k}$$

Now we need to know the abcissae l of the point of intersection of the two curves. Its value is given by

$$l=\frac{(H_{om}+B_0)^2-(H_0+B_0)^2}{4\alpha k}$$

The flux can now be evaluated:

$$\int_0^l B(x)\,dx+\int_l^d B(x)\,dx=\int_0^l\{((2\alpha kx+(H_0+B_0)^2)^{1/2}-B_0\}\,dx+$$

$$+\int_l^d\{((H_{om}+B_0)^2-2\alpha kx)^{1/2}-B_0\}dx=\frac{2}{3\alpha k}\left(\frac{(H_{om}+B_0)^2+(H_0+B_0)^2}{2}\right)^{3/2}-$$

$$-\frac{B_0}{2\alpha k}((H_{om}+B_0)^2-B_0^2)-\frac{1}{3\alpha k}((H_0+B_0)^3+B_0^3)\,.$$

Then the average magnetization is

$$4\pi\overline{M}=\frac{2}{3\alpha k\omega}\left(\frac{(H_{om}+B_0)^2+(H_0+B_0)^2}{2}\right)^{3/2}-\frac{B_0}{2\alpha k}((H_{om}+B_0)^2-$$

$$-B_0^2)-\frac{1}{3\alpha k}((H_0+B_0)^3+B_0^3)-H_a$$

Increasing Branch

Now we consider the situation where the magnetic field after having assumed its minimum value $-H_{om}$ increases from 0 to $+H_{om}$. Figure 10 shows the profile of the magnetic induction for a given value H_0 of the field at the surface. To calculate the magnetic flux per unit length we can add the flux between 0 and l' with twice the flux between $(d+l')/2$ and d:

$$\int_0^d B(x)\,dx=\int_0^{l'}B(x)\,dx+2\int_{\frac{d+l'}{2}}^{d}B(x)\,dx$$

In the interval $(0, l')$ we have $B(x)=((H_0+B_0)^2-2\alpha k x)^{1/2}-B_0$ and in $((d+l')/2, d)$, $B(x)=B_0-((H_{om}+B_0)^2-2\alpha k x)^{1/2}$ since the curve m' is symmetrical to the curve m (see Figure 10). The value of l' is determined putting $B(x)=0$ in the curve b:

$$l'=\frac{(H_0+B_0)^2-B_0^2}{2\alpha k}$$

Immediately we evaluate

$$(d+l')/2=\frac{(H_{om}+B_0)^2+(H_0+B_0)^2-2B_0^2}{4\alpha k}\ .$$

Now we can do the integration

$$\int_0^d B(x)\,dx=\int_0^{l'}[((H_0+B_0)^2-2\alpha k x)^{1/2}-B_0)]\,dx$$

$$+2\int_{(d+l')/2}^{d}[B_0-((H_{om}+B_0)^2-2\alpha k x)^{1/2}]\,dx\,,$$

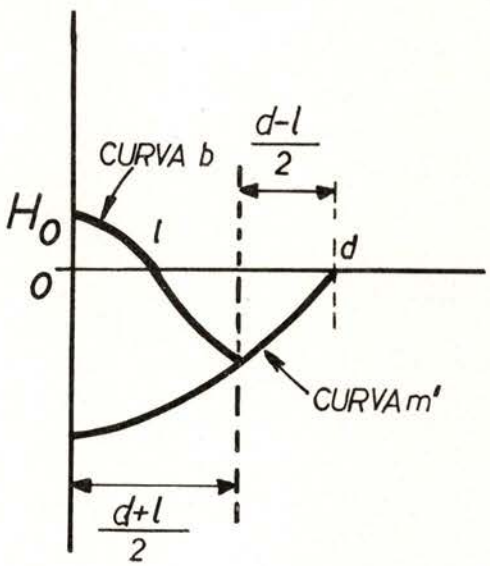

Fig. 10 — Profile of the magnetic induction for increasing H_a in case of partial penetration.

and finally obtain

$$4\pi\bar{M} = \frac{1}{3\alpha k\omega}[(H_0+B_0)^3+B_0^3] + \frac{B_0}{2\alpha k\omega}[(H_{om}+B_0)^2 - 2(H_0+B_0)^2 + B_0^2] - \frac{2}{3\alpha k\omega}\left[\frac{(H_{om}+B_0)^2-(H_0+B_0)^2}{2} + B_0^2\right]^{3/2} - H_a .$$

REFERENCES

[1] C. P. BEAN, *Phys. Rev. Lett.* **8**, 250 (1962).

[2] Y. B. KIM, C. F. HEMPSTEAD and A. R. STRNAD, *Phys Rev.* **129**, 528 (1963).

[3] W. A. FIETZ and W. W. WEBB, *Phys. Rev.* **178**, 657 (1969).

[4] W. A. FIETZ, M. R. BEASLEY, J. SILCOX and W. W. WEBB, *Phys. Rev.* **136**, A335 (1964).

[5] C. F. OLD and J. P. CHARLESWORTH, *Cryogenics* **16**, 469 (1976).

EXTREMUM PRINCIPLES IN THERMOSTATICS (*)

H. L. PINA

Centro de Termodinâmica Aplicada e Mecânica dos Fluidos
Instituto Superior Técnico, Lisboa

ABSTRACT —Thermostatics may be based on the following principle of equilibrium [1,5]:

Thermodynamic systems choose for equilibrium state that which minimizes the internal energy.

This minimum must be thought as subject to constraints, so the problem of finding the equilibrium state is one of minimization with constraints.

It is also said that this principle of minimum internal energy is equivalent to a principle of maximum entropy, the equivalence being shown by physical arguments. In this paper we present a rigorous demonstration of the equivalence of these two principles as well as the conditions for its validity, based on the theory of Lagrange multipliers.

1 — LAGRANGE MULTIPLIERS

Before going directly into Thermostatics we shall present the fundamental theorem of the theory of Lagrange multipliers [3, 4]. In what follows we assume all the functions to possess the required continuity and differentiability properties.

Theorem 1 Let $x \in R^n$, $f: R^n \to R$ and Ω the set defined by the constraints $g_\alpha : R^n \to R$

$$g_\alpha(x) = 0 \ , \ \alpha = 1, \ldots, m < n \qquad (1.1\ a)$$

(*) Results presented at the Conference of the Portuguese Physics Society (Lisbon, February 1978).

Suppose x_o affords a local minimum to $f(x)$ in Ω, and that x_o is normal, i.e., the matrix

$$\left(\frac{\partial g_\alpha}{\partial x^i}(x_o)\right) \quad (\alpha = 1, \ldots, m,\ i = 1, \ldots, n) \qquad (1.1\ \mathrm{b})$$

has rank m. Then there exist unique multipliers $\lambda_1, \ldots, \lambda_m$ such that the function

$$F(x) = f(x) + \sum_{\alpha=1}^{m} \lambda_\alpha\, g_\alpha\,(x) \qquad (1.1\ \mathrm{c})$$

is minimum at x_o, i.e.,

$$\nabla F(x_o) = \nabla f(x_o) + \sum_{\alpha=1}^{m} \lambda_\alpha \nabla g_\alpha(x_o) = 0 \qquad (1.1\ \mathrm{d})$$

Furthermore the inequality

$$F''(x_o, h) \geqslant 0 \qquad (1.1\ \mathrm{e})$$

holds for all solutions $h \neq 0$ of the equations

$$g'_\alpha(x_o, h) = <\nabla g_\alpha(x_o), h> = 0,\ \alpha = 1, \ldots, m \qquad (1.1\ \mathrm{f})$$

that is, for all h tangent to Ω.

(We are using the following notation:

$f'(x, h)$	denotes the differential of f at x in the direction of h
$\nabla f(x)$	is the gradient of f at x
$<.,.>$	represents the inner product and
$\lvert\ .\ \rvert$	is the associated norm).

The numbers $\lambda_1, \ldots, \lambda_\alpha$ are called Lagrange multipliers and the function $F(x)$ is known as the Lagrangean. The theorem presents only the necessary conditions for the existence of the multipliers. It is possible to show [3] that the condition

$$F''(x_o, h) > 0 \qquad (1.2)$$

for all solutions $h \neq 0$ of (1.1 f) is sufficient for the existence of a minimum.

We may now return to Thermostatics proper, which assumes that the state of perfect fluids [2,6] is determined by the values of the specific entropy s, the specific volume v and mole fractions $y_1, \ldots, y_r$ of the r chemical constituents of the fluid. The specific internal energy u is also a state function. When the states are homogeneous, the sole case treated in this paper, to minimize the global internal energy of a system is equivalent to minimize the specific internal energy at each of its points. Thus the equilibrium states are those which minimize

$$u = u\ (s,\ v,\ y_1, \ldots, y_r) \tag{1.3}$$

subject to appropriate constraints. Theorem 1 just presented yields a technique to obtain this minimum and therefore the states of equilibrium.

2 — PRINCIPLE OF RECIPROCITY

In this paragraph we show the following

Theorem 2. Let f, g, F, x_o and $\lambda_1, \ldots, \lambda_m$ be as in Theorem 1. Suppose that the $\lambda's$ are not all zero. Therefore there exists a $\lambda_\beta \neq 0$ such that x_o minimizes (if $\lambda_\beta > 0$) or maximizes (if $\lambda_\beta < 0$) $g_\beta\ (x)$ subject to the following set of constraints:

$$f\ (x) = f\ (x_o) \tag{2.1 a}$$

$$g_\alpha\ (x) = 0 \quad , \quad \alpha = 1, \ldots, \beta - 1,\ \beta + 1, \ldots, m \tag{2.1 b}$$

The proof is easy. According to Theorem 1, the point x_o minimizes the Lagrangean

$$\mathrm{F}\ (x) = f\ (x) + \sum_{\alpha=1}^{m} \lambda_\alpha\ g_\alpha\ (x) = \lambda_\beta\ g_\beta\ (x) + f(x) + \sum_{\alpha \neq \beta} \lambda_\alpha\ g_\alpha\ (x) \tag{2.2 a}$$

Since by hypothesis $\lambda_\beta \neq 0$ we may write

$$\frac{1}{\lambda_\beta}\ \mathrm{F}\ (x) = g_\beta\ (x) + \frac{1}{\lambda_\beta} f(x) + \sum_{\alpha \neq \beta} \frac{\lambda_\alpha}{\lambda_\beta}\ g_\alpha\ (x) \tag{2.2 b}$$

and because x_o yields a minimum to F (x), $\nabla \mathrm{F}\ (x_o) = 0$

Hence

$$0 = \frac{1}{\lambda_\beta} \nabla F(x_o) = \nabla g_\beta(x_o) + \frac{1}{\lambda_\beta} \nabla f(x_o) + \sum_{\alpha \neq \beta} \frac{\lambda_\alpha}{\lambda_\beta} \nabla g_\alpha(x_o) \quad (2.2\ c)$$

Put, for the sake of simplicity,

$$\bar{f}(x) = g_\beta(x) \quad (2.3\ a)$$

$$\bar{g}_\alpha(x) = g_\alpha(x) \text{ if } \alpha \neq \beta \quad (2.3\ b)$$

$$\bar{g}_\beta(x) = f(x) - f(x_o) \quad (2.3\ c)$$

and consequently

$$\bar{F}(x) = g_\beta(x) + \frac{1}{\lambda_\beta}[f(x) - f(x_o)] + \sum_{\alpha \neq \beta} \frac{\lambda_\alpha}{\lambda_\beta} g_\alpha(x) \quad (2.4\ c)$$

Expression (2.2 c) shows that $\bar{F}(x)$ is the Lagrangean and

$$\bar{\lambda}_\alpha = \frac{\lambda_\alpha}{\lambda_\beta} \text{ if } \alpha \neq \beta \quad (2.4\ d)$$

$$\bar{\lambda}_\beta = 1/\lambda_\beta \quad (2.4\ e)$$

the Lagrange multipliers of the extremization of $g_\beta(x)$ subject to constraints (2.1).

It remains to discuss the sign of the second differential $\bar{F}''(x_o, h)$. We must have now

$$\bar{F}''(x_o, h) = \frac{1}{\lambda_\beta} F''(x_o, h) \geqslant 0 \quad (2.5)$$

for all $h \neq 0$ which are solutions of the equations $f'(x_o, h) = 0$ and

$$g'_\alpha(x_o, h) = 0\ ,\ \alpha = 1, \ldots, \beta - 1, \beta + 1, \ldots, m \quad (2.6\ a,b)$$

We have to prove that the h's so obtained define the same set as in (1.1 f).

This can be done easily by noting that it x_o is a minimum of $f(x)$ subject to constraints (1.1 a) one must have

$$f'(x_o, h) = <\nabla f(x_o), h> = 0 \qquad (2.7\ a)$$

for all $h \neq 0$ satisfying (1.1 a) Similarly in the second case we have at x_o the equations

$$g'_\beta(x_o, h) = <\nabla g_\beta(x_o), h> = 0 \qquad (2.7\ b)$$

for all $h \neq 0$ satisfying (2.6 a, b). We see by inspection that the two sets of equations differ only in the order the equations are written and define thus the same h's. Therefore the sign of $\overline{F}''(x_o, h)$ is the same as $F''(x_o, h)$ if $\lambda\beta > 0$ and the contrary if $\lambda\beta < 0$, which completes the proof.

We are in condition to apply the reciprocity principle to Thermostatics. Consider the following problem: minimize

$$u = u(s, v, y_1, \ldots, y_r) \qquad (2.8\ a)$$

subject to

$$s = s_o \qquad (2.8\ b)$$

and eventually to other constraints which we omit now. According to theorem 1 we must have that at equilibrium (which we denote by the subscript o)

$$\frac{\partial u}{\partial s}(s_o, v_o, y_{1o}, \ldots, y_{ro}) + \lambda = 0 \qquad (2.9)$$

and recalling the definition of absolute temperature T

$$T \equiv \frac{\partial u}{\partial s}(s, v, y_1, \ldots y_r) \qquad (2.10)$$

we see that the minimum of internal energy is equivalent to the maximum of entropy if and only if

$$-\lambda = T > 0 \qquad (2.11)$$

The reciprocity principle in this case collapses at $T = 0$. For systems with a negative temperature the minimum principle of internal

energy is associated with a minimum principle of entropy, and a maximum principle of entropy with a maximum principle of internal energy.

3 — INEQUALITY CONSTRAINTS

In the preceding paragraph we have concentrated on the variables u and s to derive the reciprocity principle. When we observe other variables as v and y_i's we recognize that they are by definition non-negative. Thus we must take this fact in due account when setting the minimization or maximization problem. If constraints are given by inequalities the theorem of Kuhn-Tucker applies [3,4]. Before presenting this theorem some preliminary definitions are required.

Definition 3.1 Let the inequality constraints

$$g_\alpha(x) \leqslant 0 \quad , \quad \alpha = 1, \ldots, m \tag{3.1}$$

be given. If $g_\beta(x_o) = 0$ the βth constraint is said to be *active* at x_o. If $g_\beta(x_o) < 0$ the βth constraint is said to be *inactive* at x_o.

Definition 3.2 Let Ω be the set of points x satisfying

$$g_\alpha(x) \leqslant 0\,,\ \alpha = 1, \ldots, p\,;\ g_\beta(x) = 0\,,\ \beta = p+1, \ldots, m \tag{3.2 a, b}$$

A point x_o is *regular* if every outer normal w of Ω at x_o is expressible in the form

$$w = \sum_{\alpha=1}^{m} \lambda_\alpha \nabla g_\alpha(x_o) \tag{3.2 c}$$

where $\lambda_1, \ldots, \lambda_p$ are non-negative and $\lambda_\alpha = 0$ wherever $g_\alpha(x_o) < 0$, *i.e.*, the αth constraint is inactive.

We are in condition to give the following

Theorem 3. Suppose x_o yields a local minimum to $f(x)$ on the set Ω defined by the constraints

$$g_\alpha(x) \leqslant 0 \ , \ \alpha = 1, \ldots, p \ ; \ g_\beta(x) = 0 \ , \ \beta = p+1, \ldots, m \qquad (3.3\ a)$$

If x_o is a regular point of Ω then there exist multipliers $\lambda_1, \ldots, \lambda_m$ such that

$$\lambda_\alpha \geqslant 0 \ , \ \alpha = 1, \ldots, p \text{ with } \lambda_\alpha = 0 \text{ if } g_\alpha(x_o) < 0 \qquad (3.3\ b)$$

and such that the function

$$F(x) = f(x) + \sum_{\alpha=1}^{m} \lambda_\alpha g_\alpha(x) \qquad (3.3\ c)$$

is a minimum at x_o, i.e.,

$$\nabla F(x_o) = 0 \qquad (3.3\ d)$$

and

$$F''(x_o, h) > 0 \qquad (3.3\ e)$$

for all $h \neq 0$ satisfying the relations:

$$g'_\alpha(x_o, h) \leqslant 0 \text{ if } \alpha \text{ is active and } \lambda_\alpha = 0 \qquad (3.3\ f)$$
$$g'_\alpha(x_o, h) = 0 \text{ if } \alpha \text{ is active and } \lambda_\alpha > 0 \qquad (3.3\ g)$$
$$g'_\alpha(x_o, h) = 0 \text{ if } \alpha \text{ is inactive} \qquad (3.3\ h)$$

We are now in position to solve the following problem: minimize $u = u(s, v, y_1, \ldots, y_r)$ subject to the constraints:

$$s - s_o = 0 \qquad (3.4\ a)$$

$$-v \leqslant 0 \qquad (3.4\ b)$$

$$v - b \leqslant 0 \qquad (3.4\ c)$$

$$-y_i \leqslant 0 \ , \ i = 1, \ldots, r \qquad (3.4\ d)$$

$$\sum_{i=1}^{r} y_i - 1 = 0 \qquad (3.4\ e)$$

Constraint (3.4 a) specifies the value of the entropy and constraint (3.4 b) assures us that the solution of the above problem will not yield negative values for the volume. Constraint (3.4 c) is introduced here because for perfect fluids the volume is not specified in advance but only an upper bound is given. For instance, when dealing with

gases, the volume of the container is such an upper bound, but there is no a priori reason to suppose the gas will never assume a volume less than this. If in fact we do require that the gas occupies always the largest volume available to it then we must be aware we have introduced a constitutive assumption. Constraints (3.4 d, e) are mere consequences of the definitions of molar fractions.

Applying theorem 3 we obtain

$$\partial u/\partial s\ (\ldots)+\lambda_1=0 \tag{3.5 a}$$

$$\partial u/\partial v\ (\ldots)-\lambda_2=0\,,\lambda_2>0\,,\lambda_2=0 \text{ if } v>0 \tag{3.5 b}$$

$$\partial u/\partial v\ (\ldots)+\lambda_3=0\,,\lambda_3>0\,,\lambda_3=0 \text{ if } v<b \tag{3.5 c}$$

$$\partial u/\partial y_i\ (\ldots)-\lambda_{3+i}=0\,,\lambda_{3+i}>0\,,\lambda_{3+i}=0 \text{ if } y_i>0 \tag{3.5 d}$$

$$\partial u/\partial y_i\ (\ldots)-\lambda_{3+r+i}=0 \tag{3.5 e}$$

where the symbol $(\ldots)$ stands as an abbreviation to the list of variables $(s_o, v_o, y_{1o}, \ldots, y_{ro})$.

As we have seen, the temperature is assumed to be non-negative, therefore by (2.11) $-\lambda_1=\mathrm{T}\geqslant 0$. This implies that the entropy at the minimum is s_o. There is no loss of generality in this case to substitute the equality constraint (3.4 a) by an inequality constraint

$$s-s_o<0 \tag{3.6}$$

The pressure is given in Thermostatics by

$$\mathrm{P}=-\frac{\partial u}{\partial v}(s, v, y_1, \ldots, y_r) \tag{3.7}$$

If a perfect fluid is such that the constraint (3.5 c) is always active for all $b\geqslant 0$ then we can assert by (3.4 c) that the pressure P is a non-negative function or that the internal energy u is a non-increasing function of the volume v. It is easily seen that the converse is also true.

If we had set $v=b$ instead of (3.4 c), the conclusion we have just reached would not have been possible. In fact we would have introduced, in an implicit way, a constitutive hypothesis.

4 — LAGRANGEANS IN THERMOSTATICS

Let us return to the problem of minimising $u\ (s, v, y_1, \ldots, y_r)$ subject to $s - s_o \leqslant 0$. As we have shown in 3, the Lagrangean function for this case is

$$f = u\ (s, v, y_1, \ldots\ y_r) - T_o\ (s - s_o) \qquad (4.1\ a)$$

We can write also that, because f is minimum at equilibrium,

$$u\ (s_o, v_o, y_{1o}, \ldots, y_{ro}) \leqslant u\ (s, v, y_1, \ldots, y_r) - T_o\ (s - s_o) \qquad (4.1\ b)$$

or

$$u\ (s_o, v_o, y_{1o}, \ldots, y_{ro}) - T_o\ s_o \leqslant u\ (s, v, y_1, \ldots, y_r) - T_o\ s \qquad (4.2)$$

We recognize both members of this inequality to be the Helmholtz free energy at the temperature T_o, evaluated at equilibrium (the LHS) and at any state (the RHS). Therefore for a given temperatura T_o the equilibrium state minimizes the Helmholtz free energy.

It is now immediate that the corresponding principle for the constraint $v - v_o \leqslant 0$ is the minimization of the entalpy $h = u + Pv$, such that

$$u\ (s_o, v_o, y_{1o}, \ldots, y_{ro}) + P_o\ v_o \leqslant u\ (s, v, y_1, \ldots, y_r) + P_o\ v \qquad (4.3)$$

For the set of constraints $s - s_o \leqslant 0$, $v - v_o \leqslant 0$ the Gibbs free energy $g = u - Ts + Pv$ is the one to minimize and we have

$$u\ (s_o, v_o, y_{ko}) + P_o\ v_o - T_o\ s_o \leqslant u\ (s, v, y_k) + P_o\ v - T_o\ s \qquad (4.4)$$

This inequality is identical to that postulated by Coleman and Noll [2].

The author wishes to thank Professor A. G. Portela for several fruitful discussions on the subject of this paper.

REFERENCES

[1] A. B. CALLEN, *Thermodynamics,* Wiley, 1960.

[2] B. D. COLEMAN and W. NOLL, *Arch. Rat. Mech. Anal.,* **4**, 2, 1959.

[3] M. R. HESTENES, *Optimization Theory,* Wiley, 1975.

[4] D. G. LUENBERGER, *Optimization by Vector Space Methods,* Wiley, 1969.

[5] L. TISZA, *Generalized Thermodyamics,* MIT Press, 1966.

[6] C. TRUESDELL and W. NOLL, *The Non-Linear Field Theories of Mechanics,* Encyclopedia of Physics, Vol. III/3, Springer, 1965.

NEW FABRICATION TECHNIQUES FOR MULTIMODE INTEGRATED OPTICS (*)

G. H. CHARTIER **, A. D DE OLIVEIRA ***,
O. PARRIAUX ***, P. JAUSSAUD **

ABSTRACT — Ion exchange fabrication of low loss waveguides in glass has been demonstrated using $Li_2SO_4 - K_2SO_4$ eutectic. The process is extremely fast and the resulting distribution can be controlled by application of an electric field.

1 — INTRODUCTION

The present trend in optical communication systems towards multimode fibres has created a growing interest in the design of suitable deep integrated components. The thermal migration of ions in glass is one of the few fabrication techniques of low loss multimode waveguides. Ag/Na ion exchange from a silver salt melt [1] is a very widely used and convenient method, but it requires a very long immersion time and leads to a standard graded index profile which is difficult to modify. However the technique can be successfully extended to overcome these difficulties by using other melts, which are stable at higher temperatures and employing field assisted diffusion [2].

(*) Results presented at the Conference of the Portuguese Physics Society (Lisbon, February 1978).

(**) ENSEGP, Institut National Polytechnique, Domaine Universitaire 38 400 Grenoble, France.

(***) Department of Electronics and Electrical Engineering, University College London, Torrington Place, London, WC1, UK.

This paper reports the fabrication and the characteristics of highly multimode planar waveguides made by Li/Na ion exchange, and describes the improvements and possibilities offered by an electric field assisted Ag/Na ion exchange technique.

2 — Li/Na ION EXCHANGE WAVEGUIDE FABRICATION

Small monovalent lithium ions can easily diffuse in a glass matrix where an exchange with the sodium ions of different polarisability takes place. The stability of lithium salts allows higher diffusion temperatures to be used. Their high melting points, which are unsuitable for soda lime glass, suggest the use of an eutectic melt, 80% mol Li_2SO_4 – 20% K_2SO_4, which brings the melting point down to 524°C [3]. Soda lime microscope slides were preheated and immersed in the eutectic for different immersion times t and temperatures T. The refractive index profiles were then determined by the WKB evaluation from the angular position of the m-lines. Figure 1

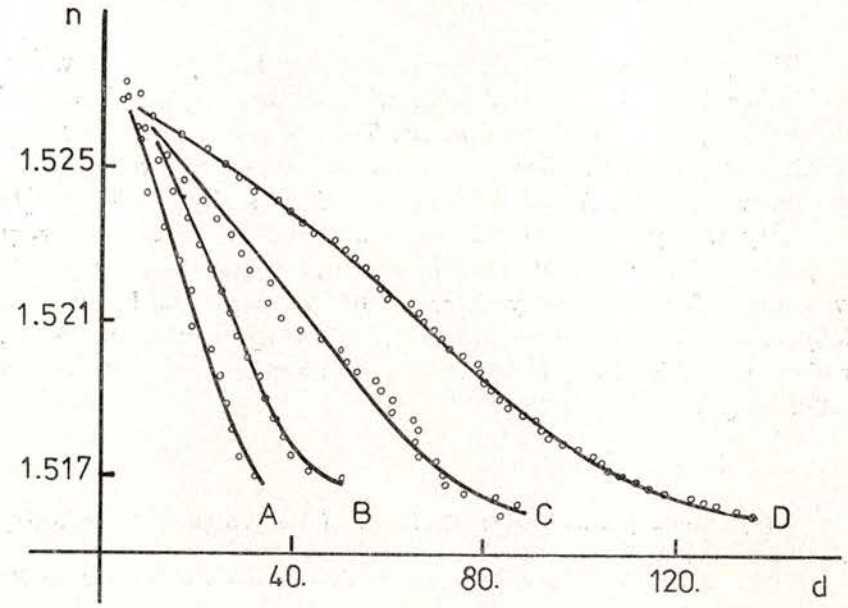

Fig. 1 — Index profiles n(d) obtained at T = 575°C for several immersion times t. The depth d is in microns. A: 1 min., B: 2 min., C: 5 min. D: 17 min.

shows the index profile of a number of waveguides with t as a parameter. By comparison with the Ag/Na technique, a 35 microns deep waveguide requires 50 hours at T=250°C, whereas the Li/Na technique requires only 1 min. at T=575°C, as shown by figure 1, curve B. The refractive index difference $\Delta n = 0.015$ between the surface index n_s and the substrate index is considerably smaller than in the Ag/Na case, but is even more compatible with the index characteristics of usual multimode fibers, as is the waveguide depth with the fibre core cross section.

The data were processed in order to find the function which best fits the experimental index profiles. Amongst the exponential, gaussian, error function, second order polynomial and linear profiles, the latter presents by far the smallest standard deviation, being the first order term of the solution of Fick's equation with a concentration dependent diffusion coefficient [4]:

$$n(x) = n_s - \Delta n \; x/d \tag{1}$$

Using the results of figure 1 it was shown that d depends linearly on $\sqrt{t}$, so that an effective diffusion constant D can be defined:

$$d = 2\sqrt{\mathrm{D}\,t} \tag{2}$$

D was determined by immersing several glass slides at different temperatures T for the same time. The linear dependence of the logarithm of D against inverse temperature shown by figure 2 suggests for D the standard expression:

$$\mathrm{D} = \mathrm{D}_0 \exp(-\mathrm{T}_0/\mathrm{T}) . \tag{3}$$

From our experimental data we found $\mathrm{D}_0 = 5.4 \times 10^{-3}$ $\mathrm{m^2 s^{-1}}$ and $\mathrm{T}_0 = 1.6 \times 10^4$ °C. It follows for instance that a waveguide made at temperature T_1 can be made p times deeper by using a melt at temperature T_2 such that

$$\mathrm{T}_2 = \mathrm{T}_1 \mathrm{T}_0/(\mathrm{T}_0 - 2\mathrm{T}_1 \, ln \, p) . \tag{4}$$

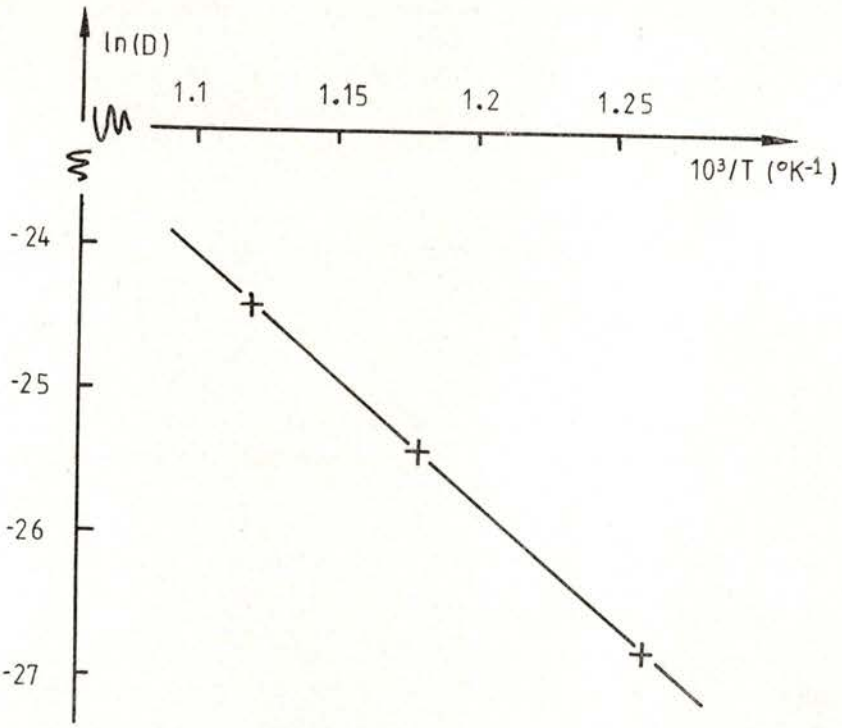

Fig. 2 — Temperature dependence of the diffusion constant D for 5 min. immersion time.

3 — FIELD ASSISTED Ag/Na ION EXCHANGE

An external electric field E may be used to enhance or modify the ion exchange rate and the penetration depth. Microscope slides were covered on one side by a negative aluminium electrode whereas the other side, which had been very carefully cleaned, was covered by a positive evaporated silver layer. An ionic current flows from the Ag anode to the Al cathode. The total charge is a direct measure of the waveguide depth. Waveguides were produced in the temperature and field ranges 170°C to 300°C and 0 to 2.10^5 V/m. Figure 3 shows the dramatic influence that can be achieved by varying the field. In the case of profile D, 13 well confined modes can propagate (only 2 without field). The dashed line H′ represents the guide profile

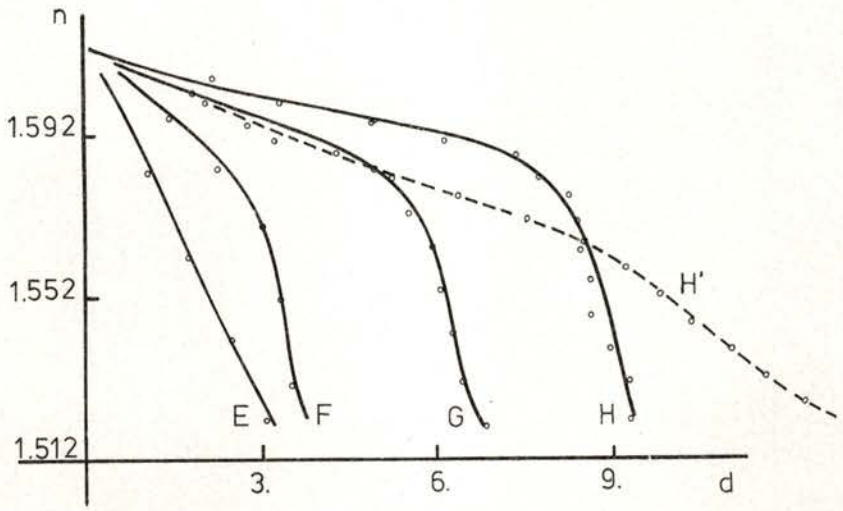

Fig. 3 — Influence of the applied field on the index profile n(d). The depth d is in microns. Immersion time t = 30 min. Temperature T = 250°C.

E: V = 10 V, F: V = 30V, G: V = 50V, H: V = 100V
H': t = 330 min., T = 250°C, V = 0 V

which, by passive diffusion during $5^1/_2$ hours, also propagates 13 modes.

The diffusion process can be described here by a Fick's equation with an extra term $-\mu E\, \partial c/\partial x$ involving the gradient of the concentration, $c(x, t)$, an effective mobility μ and E. Although its coefficients are concentration dependent, as is the electric field, the solution for constant coefficients was used to fit approximately the experimental profiles [5]:

$$n(x, t) = n_s - {}^1/_2\, \Delta n\, [\mathrm{erfc}\, ((x - \mu E t)/2\sqrt{D t}) + \\ + \exp(\mu E x/D)\, \mathrm{erfc}\, ((x + \mu E t)/2\sqrt{D t})] \qquad (5)$$

by adjusting D and μ. Despite some minor discrepancies, some values of the mobility were determined and confirmed by resistance measurements during the experiments. Figure 4 shows the linear dependence of the logarithm of the mobility against inverse temperature, which can be written [6]:

$$ln\ \mu = A + B/T \qquad (6)$$

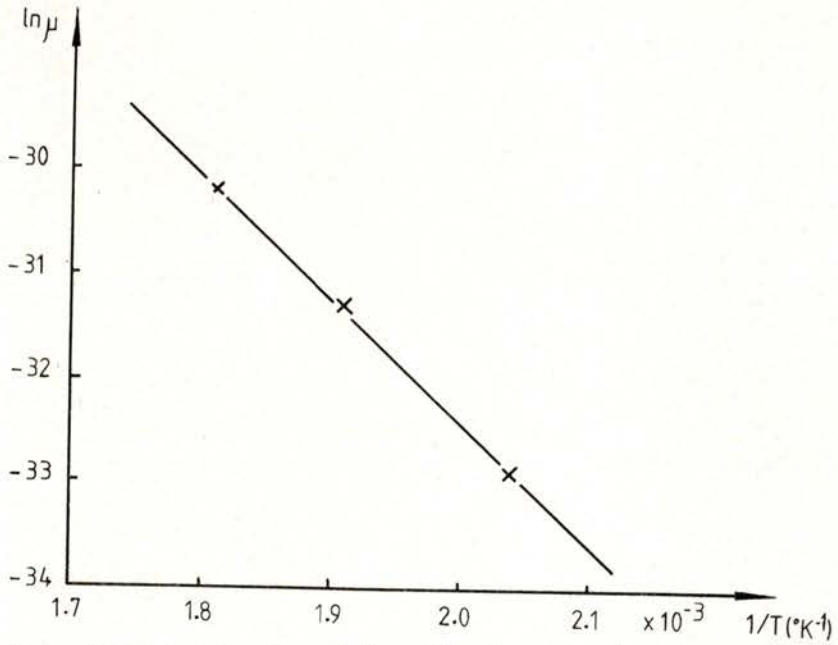

Fig. 4 — Temperature dependence of the mobility for t = 30 min., voltage 50 Volts, at various temperatures (217, 250, 280°C).

where the constants A and B are found to be -9 and -1.2×10^{-4} respectively.

4 — CONCLUSION

The present development of fibre optic systems ascribes an important role to multimode integrated optics. One major problem in this new field is to realise waveguides presenting a satisfactory geometrical and electromagnetic match to multimode fibres. These requirements are fulfilled by the waveguide fabrication techniques presented in this paper. Sufficient depth and an additional control of the index distribution by an electric field can be achieved in very short times.

The authors are grateful to C.W. Pitt for useful discussions and Professor E.A. Ash for his support to this work. A NATO Fellowship (ADdeO) and a Fellowship of the Fonds National Suisse de la Recherche Scientifique (OP) are gratefully acknowledged.

REFERENCES

[1] M. G. F. WILSON, C. W. PITT, R. MANKU, A. D. DE OLIVEIRA, O. PARRIAUX, «Optical power division in a multimode-waveguide intersection», Electronics Letters, Vol. **12**, N.º 17, Aug. 1976, pp. 434-435.

[2] T. ISAWA, H. NAKAGOME, T. KIMURA, «Optical waveguides formed by electrically induced migration of ions in glass plates», 1972 Quantum Electronic Conference, Montreal, 1972, pp. 545-546.

[3] LEVIN, M. C., «Phase diagrams for ceramists», ed. by 'The American Ceramic Society', 1969, fig. 2888.

[4] G. STEWART, C. A. MILLER, P. J. R. LAYBOURN, C. D. W. WILKINSON, R. M. De La Rue, «Planar optical waveguides formed by silver-ion migration in glass», IEEE J. of Quantum Electronics, Vol. **QE-13**, N.º 4, April 1977, pp. 192-200.

[5] T. KANEKO, H. YAMAMOTO, «On the ionic penetration of silver film into glasses under the electric field», 10th Int. Cong. on Glass, Kyoto, Japan, 1974, pp. 8-79—8-86.

[6] N. M. TALLAN, «Electrical Conductivity in Ceramics and Glasses», Dekker, 1974, p. 564.

SELF-IMAGING DEVICES FOR MULTIMODE OPTICS (*)

O. D. D. SOARES
Laboratório de Física da Faculdade de Ciências
Centro de Física da Universidade do Porto, Portugal

ABSTRACT — Planar optical waveguides, suitable for light-propagation can be used for self-imaging. The formation of one-dimensional self-images is demonstrated experimentally in solid waveguide slabs of homogenous refractive index. The position of the self-images along the guide are shown to be dependent on the optical path of the signal wave. Reflective means can shorten the device size, and provide focussing so that a two-dimensional imaging device could be fabricated. The integration of a dispersive element such as a grating is proposed to permit the design of angularly dispersive devices for multiplexing of several optical signals at different wavelengths. Possible applications in multimode optics include branching couplers and frequency multiplexers for multimode transmission systems.

1 — INTRODUCTION

The self-imaging propriety for optical waveguides was first suggested by Bryngdahl [1]. The formation of single and multiple self-images in thick dielectric homogenous slab has been described, and demonstrated experimentally by Ulrich [2] employing liquid waveguides. The use of a liquid held between two optical flats facilitates variations of the slab thickness in order to adjust to the imaging condition. The liquid is contained by capillary forces which also provide an easy mechanism to the implementation of a guide whose width is tapered. A magnified or demagnified image is then produced according to the direction of propagation of the radiation along the tapered waveguide [3].

(*) Results presented at the Conference of the Portuguese Physics Society (Lisbon, February 1978).

Practical applications in optical communications suggest the research for self-imaging devices on a sheet of homogenous transparent material in the form of solid planar dielectric waveguides.

The inherent mechanical simplicity of such a component would permit easy fabrication in quantity and therefore potential low cost.

To study the method application, we used glass slides, 60 μm to 230 μm thick to simulate the waveguiding structure, which proved to exhibit self-imaging performance.

Whilst a glass slide component has mechanical simplicity, the device design must embody means of adjustment so that tolerance demands in the direct realization of the device are practically tractable. Further, the overall device size should be kept small enough so that it can be incorporated as an integrated part of an optical fibre cable system if necessary. We have then considered the introduction of reflective means to provide miniaturization features. This is possible as reflective optics can be used to form a non-dispersive system of the propagable mode spectrum [4]. Reflective optics also provides a focussing mechanism so that a convenient device design can be achieved to offer simultaneously two-dimensional imaging. Furthermore, it also presents favourable performance with respect to aberrations [5] when compared with a refractive element.

A dispersive element such as a grating can be, in principle, properly integrated in the system so that different wavelength components of the optical signal are diffracted or reflected from the grating at slightly different angles. These angularly dispersed beams offer the possibility of separating several signals supported by different wavelengths, i.e. exhibiting means for multiplexing and demultiplexing [6].

2 — SELF-IMAGING PLANAR WAVEGUIDE

The planar optical waveguide with uniform refractive index can produce images of one-dimensional objects in which the information is arranged along a line normal to the direction of propagation along the guide [7].

However, we consider here a thick planar guide and a one-dimensional object in which the information is arranged in the direction of propagation along the waveguide — a narrow slit P, Fig. 1, at one end of the guide, illuminated from the left. It is an

inherent property of highly multimode, parallel or weakly tapered guides (adiabatic adaptation of all modes). that to any interior object point P there exists a number of real self-images S_1, S_2... S_j further down the guide. At intermediate positions multiple self-images of P are formed e.g. M_1, M_2... M_j [3]. The self-images result from the interference of a number of modes which propagate at different velocities, and whose phases all coincide in the self-image.

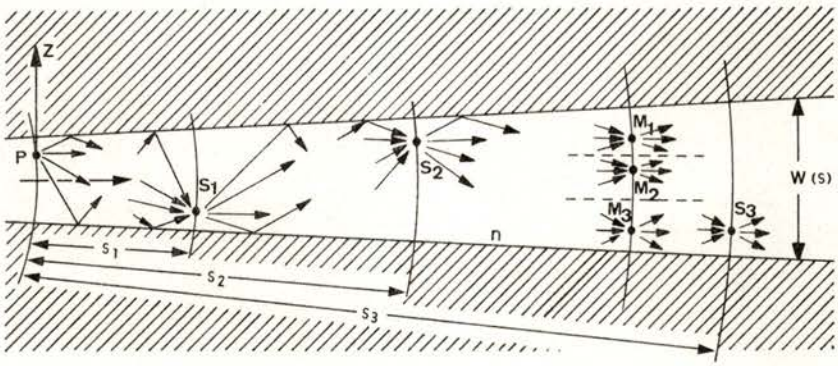

Fig. 1 — Cross-section of a planar optical guide.

The object P forms single self-images S_j and multiple self-images like M_j.

The positions of the self-images along the guide are characterized by an imaging parameter [3]:

$$h = s\ \lambda / 4\, n\ W_a(0)\ W_a(s) \qquad (1)$$

where s is the radial separation of object P and image, λ is the vacuum wavelength, and n is the refractive index of the guide material. W_a is the active thickness of the guide, equal to the local physical thickness corrected by the Goos-Hänchen penetration. On a surface characterized by $h = p/q$, where p and q are small integers with no common factor, q separated sub-images are formed. The self-image has a magnification factor equal to $W_a(s)/W_a(0)$. In a uniform guide ($W = \text{const}$), the single self-images have unit magnification and lie equidistant at:

$$S_h = 4\, h\, n\ W_a{}^2 / \lambda \qquad (2)$$

It should be noticed that the device is reciprocal, and can function with both coherent and incoherent illumination provided the source is sufficiently monochromatic or means for wavelength separation are taken into account.

To study some applications of the self-imaging property to multimode optics, we used a glass slab as the waveguide (Deckglas, D 236, Deutsche Spezialglas AG).

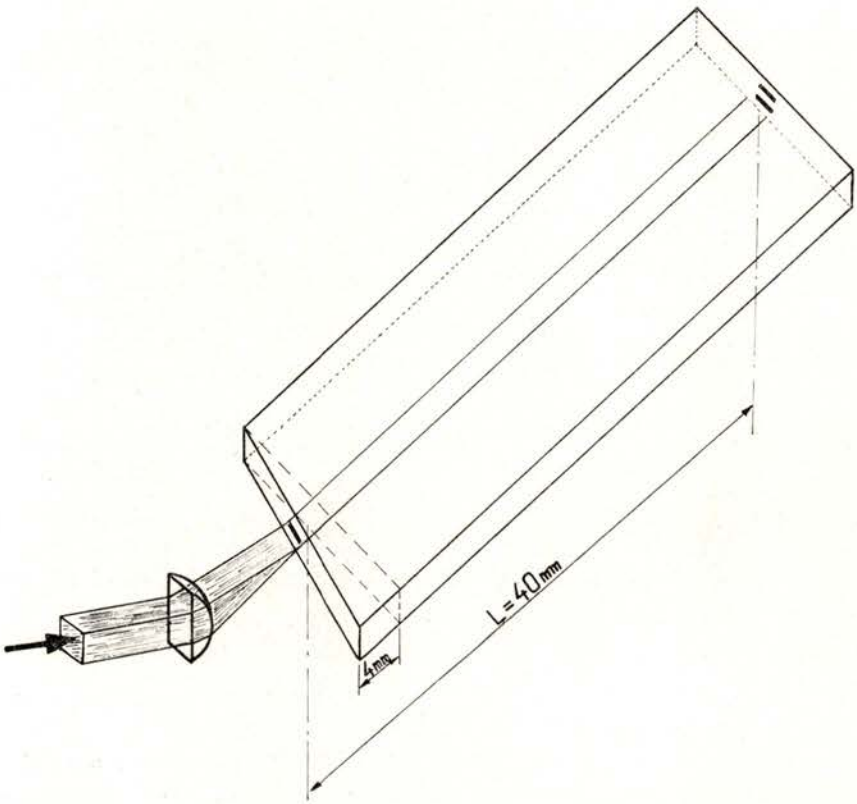

Fig. 2 — Waveguide geometry for self-imaging.

While there are several possible methods of fabrication which could be investigated we have chosen a polishing technique in view of simplicity. A stack of plates is formed by waxing together about ten glass sheets cut to size. It is obviously essential that all the plate edges are of good optical finish and this is checked by inspection.

In a typical experiment we used a sheet of glass, $n = 1.5217$ at $\lambda = 0.6328$ μm with a thickness of 185 ± 5 μm. To verify the self-imaging condition we carried out experiments using a tunable dye laser source ($0.56 \div 0.62$ μm). The waveguide endfaces were made oblique, Fig. 2, to provide an easy way for adjustement of the waveguide length. It has been possible to observe the formation of multiple self-images, Fig. 3 with a resolution better than 5 μm.

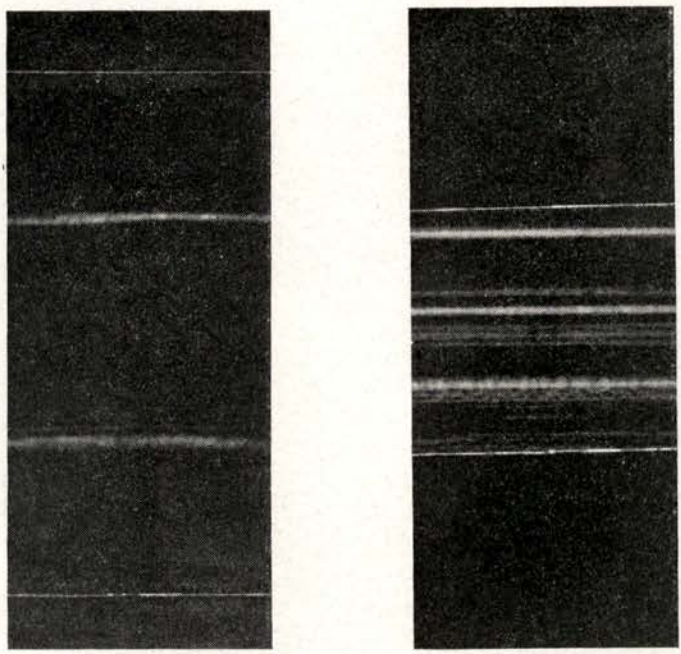

(a) *(b)*

Fig. 3 — Multiple self-images in glasse sheet planar waveguide.
(a) $h = 1/2$, $W_a = 185 \pm 5$ μm *(b)* $h = 1/3$, $W_a = 185 \pm 5$ μm

3 — MINIATURIZATION BY REFLECTIVE MEANS

Practical applications in multimode systems require that the overall device size should be kept small enough to be incorporated as an integral part of the system. Furthermore, the thickness of the plate must be at least twice the core diameter of the optical fibre. The optical path of the beam becomes then rather lengthy. A compro-

mise can be found by folding over the optical path by recourse to multiple reflections as reflective optics can be made non-dispersive of the propagating mode spectrum.

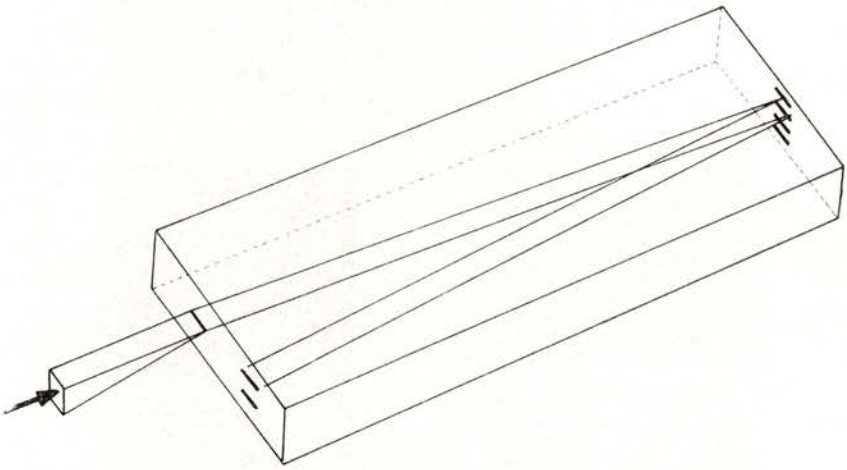

Fig. 4 — Reflective means to the miniaturization of self-imaging devices

We conducted experiments that show the formation of self-images following multiple reflections, Fig. 4.

In addition, it is expected to be possible to use total internal reflection for the sake of simplicity of design, Fig. 5.

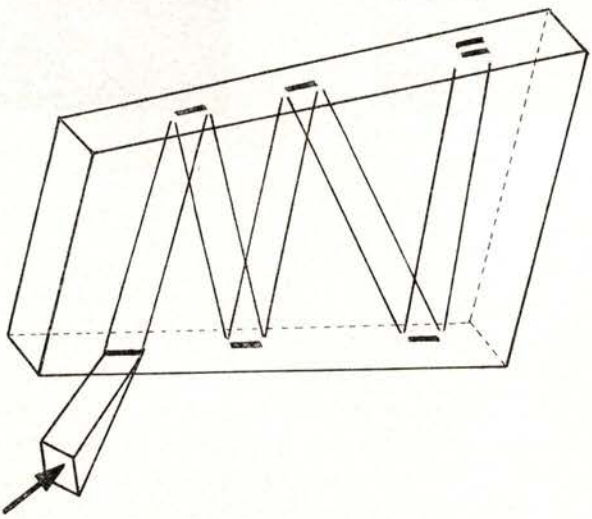

Fig. 5 — Miniaturization by recourse to the total internal reflection for self-imaging devices

4 — TWO-DIMENSIONAL IMAGING BY FOCUSSING

Self-imaging for a *planar* dielectric guide provides a mechanism for imaging the input beam into one or multiple real images in one--dimension. Correspondingly, in a *rectangular* waveguide, highly overmoded in both transverse dimensions real images can be formed when equation (2) is satisfied for both transverse dimensions [8]. A device based in this doubly self-imaging rectangular waveguide presents manufacturing tolerances that makes it unattractive. Alternatively, we sought a design using reflective means. A cylindrical mirror can realize the focussing in a transverse direction. A spherical cylinder offers a simple geometry and consequently an easy fabrication technique. However, an elliptical cylinder offers the following advantages:

i) The aberrations can be controlled as they vary inversely with a certain power of the radius of the osculating sphere [9], which can be made large.
ii) Total internal reflection is praticable.
iii) Input region is largely separated from the output area.
iv) The input aperture can be made different from the output aperture.
v) Manufacturing tolerances are relaxed, and adjustment of imaging condition is simplified.

The advantages of using an elliptical cylinder seem thus to outweight the inconvenience of going to aspheric surfaces.

5 — BRANCHING COUPLERS

To expand communications with optical fibres further developments in branching, coupling, multiplexing and demultiplexing devices are needed. In some application areas such as the data bus and the data link, there is a strong requirement for tapping a portion of the optical signal from a main transmission line fibre (branching) or inserting another optical signal into the fibre (coupling) [10].

One configuration of a representative application of self-imaging to a branching device is schematically shown in Fig. 6, where the

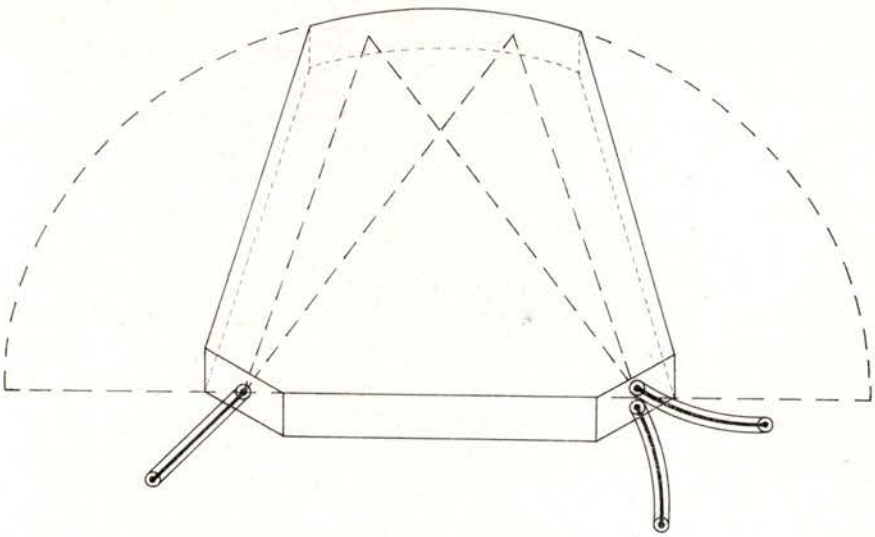

Fig. 6 — Configuration of a branching coupler.

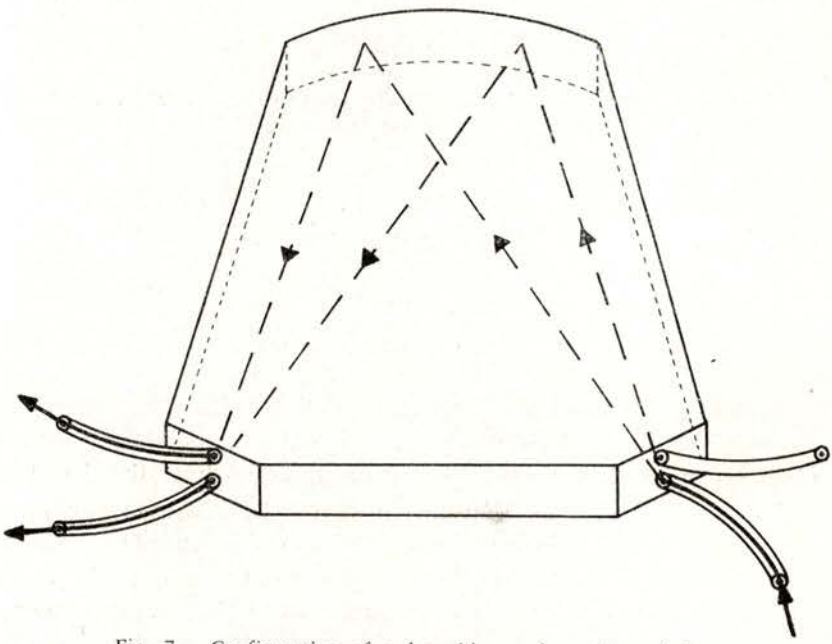

Fig. 7 — Configuration of a branching and coupling device.

signal from an optical fibre is branched into two optical fibres. Reciprocal operation of this device conducts to a 3 dB loss. However, the design can be modified to realize a bi-directional coupler as can be clearly seen from Fig. 7.

6 — OPTICAL MULTIPLEXER

One way to increase the information capacity of optical fibre transmission systems is by multiplexing signals at several different wavelengths on a single fibre [6].

The introduction into the device design of a dispersive element could be explored to make a multiplexer. The device is reciprocal, and could function either as a multiplexer or as a demultiplexer. Fig. 8 illustrates a type of multiplexer-demultiplexer design using a reflection grating.

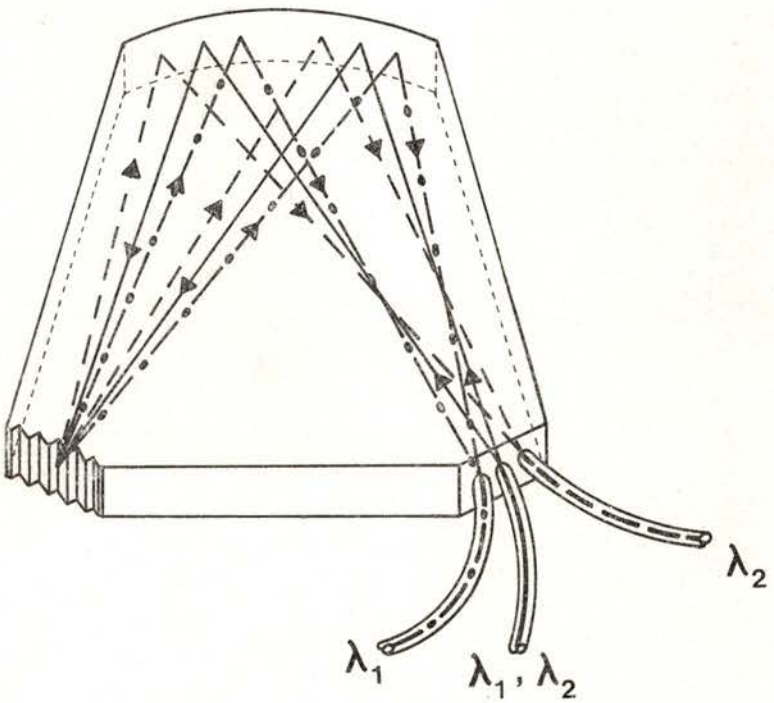

Fig. 8 — Basic design of a multiplexer using self-imaging and reflection grating.

7 — CONCLUSION

Self-imaging in solid planar waveguides has been demonstrated. Reflective means have been introduced for miniaturization.

An elliptical cylinder design has been briefly analysed to produce a two-dimensional imaging device.

A novel principle for the implementation of branching couplers and multiplexer devices for multimode fibre transmission systems has been described.

Further experimental and theoretical analysis is required to define the aberrations and imaging resolution, to assess the losses and undesirable cross-talk in the transmission, and to establish manufacturing tolerances.

Material studies should be considered to find an appropriate fabrication technology which could include the novel plastic optics area.

The author would like to thank the Deutscher Akademischer Austauschdienst for providing a research grant, and the Max-Planck--Institut für Festkörperforschung for their hospitality during a three months visit.

The original discussions and prelimary work took place during that time with Dr. R. Ulrich's group.

The author works with Centro de Física da Universidade do Porto, financed by the Instituto Nacional de Investigação Científica, Portugal.

REFERENCES

[1] O. BRYNGDAHL, *J. Opt. Soc. Am.* **63**, (1973) 416.
[2] R. ULRICH, *Opt. Commun.* **13**, (1975) 259.
[3] R. ULRICH, G. ANKELE, *Appl. Phys. Lett.* **27**, (1975) 337.
[4] L. BRILLOUIN, *Academic Press,* NY 1960.
[5] M. J. RIEDL, *Electro-Optical Systems Design* **6**, (1974) 58.
[6] W. J. TOMLINSON, *Appl. Opt.* **16**, (1977) 2180.
[7] E. A. ASH, E. SEAFORD, O. SOARES, K. S. PENNINGTON, *App. Phys. Lett.* **24**, (1974) 207.
[8] A. SIMON, R. ULRICH, *Appl. Phys. Lett.* **31**, (1977) 77.
[9] J. DYSON, *Proc. Phys. Soc.* **B62**, (1949) 565.
[10] W. K. BURNS, *Appl. Opt.* **15**, (1976) 1053.

CALCULATION OF THE IONIC TEMPERATURE OF AN ARGON PLASMA (*)

A. V. B. GASPAR, J. A. C. SERRA
Centro de Electrodinâmica das Universidades de Lisboa (CEUL-INIC)

ABSTRACT — Considering the experimental difficulty in determining the ion temperature of a plasma, namely at high pressures or high temperatures, this work aims at a theoretical determination of the ionic temperature (T_i) of an Argon plasma in a supposedly homogeneous region where the distribution functions of the electrons (e), ions (i) and neutrals (o) are assumed to be Maxwellian.

T_e (the electron temperature), T_o (the neutral temperature), n_o (the neutral density) and n_e (the electron density) are known. All temperatures are below 10 eV. It is also assumed that ions possess no specific heating mechanisms.

It is observed that for the same T_e, T_i approaches T_o for higher T_o. As a general rule, for higher T_e values, T_i values (at the same T_o) are found to be lower. Finally, a graphic representation of $\Delta_r = (T_i - T_o)/T_o$ as a function of T_o, for different T_e values, shows curves to intersect; this is due to the fact that the curve representing the ion heating rate at the same T_i is not a monotonous function of T_e, which shows that for a given T_i value there will always exist pairs of T_e values leading to the same heating rate value.

The results obtained can only be applied to large dimension plasmas with small applied fields. The validity conditions are close to those of a high pressure arc.

1 — INTRODUCTION

If it is relatively easy to obtain, experimentally, the electronic temperature of a plasma, the same cannot be said about the ionic temperature; in fact, there exists only one simple experimental technique which makes it possible to obtain it and wich consists in measuring the broadening due to the Doppler effect produced by

(*) Results presented at the Conference of the Portuguese Physics Society (Lisbon, February 1978).

thermal agitation, observable in certain particularly adequate lines. This technique meets with difficulties, both for high pressures, where the pressure broadening is generally dominant and for the high temperatures for which lines are to be found on the low wave lengths where it is rather difficult to obtain a sufficient resolution in the domain of wave lengths.

From this difficulty has arisen the necessity of a theoretical calculation of the ionic temperature.

Our purpose is, therefore, to calculate the ionic temperature of an Argon plasma in a supposedly homogeneous region where the distribution functions of the particles — electrons (e), ions (i) and neutrals — are assumed to be Maxwellian.

T_e (the electron temperature), and T_o (the neutral temperature) are known, as well as the neutral gas pressure and the plasma density (density of charged particles). This density varies between 10^{18} and 10^{20} m^{-3}. All temperatures are assumed to be below 10 eV.

It is also assumed that ions possess no specific heating mechanisms (magnetic field, ionic wave – instability).

To calculate the ionic temperature we shall start from the relation which expresses the stationary state characterized by the balance between the mean energy transmitted by electrons to ions through elastic collision, and the mean energy transmitted by ions to neutrals during their interaction processes.

2 — ENERGY BALANCE EQUATION REFERRED TO IONS

Ions are heated by collision with electrons and cooled by collision with neutrals. We shall use the same general approach for ion-electron and ion-neutral collisions even if there is a more exact method for the calculation of the former [2].

2.1 — *Ion heating rate by collision with electrons*

From Fokker — Planck term there results

$$\left[\frac{dE_i}{dt}\right]_{e-i} = n_e \bar{\nu}_{ei} f_{ei} E_e \qquad (1)$$

$\bar{\nu}_{ei}$ – mean frequency of electron-ion collisions
f_{ei} – electron energy fraction which is, on the average, transferred to the ion in an elastic collision
n_e – electron density
E_e – electron mean energy

Cravath [1] established that the energy fraction which is, on the average, transferred in an elastic collision between particles with Maxwellian distributions from the faster particle (j) to the slower (k) is given by

$$f_{jk} = \frac{8}{3} \frac{m_j \, m_k}{(m_j + m_k)^2} \left(1 - \frac{T_k}{T_j}\right) \tag{2}$$

m_j – mass of particle j
m_k – mass of particle k

In the present case, particle j is the electron and particle k the ion. On the other hand, since $m_e << m_i$, $m_e + m_i \simeq m_i$.
Substituting in (2) we have

$$f_{ei} = \frac{8}{3} \frac{m_e}{m_i} \left(1 - \frac{T_i}{T_e}\right) \tag{3}$$

The collision mean frequency is given by

$$\bar{\nu}_{jk} = n_k \, \bar{\sigma}_{jk} \, \bar{g}_{jk} \tag{4}$$

$\bar{\sigma}_{jk}$ – mean cross section of kinetic energy transference
$\bar{g}_{jk}$ – mean relative velocity for Maxwellian distributions [1]

$$\bar{g}_{jk} = \left(\frac{8k \, T_j}{\pi m_j}\right)^{1/2} \left(\frac{m_j}{m_k} \frac{T_k}{T_j} + 1\right)^{1/2} \tag{5}$$

Introducing the simplification due to mass relations (for the Argon case $m_e / m_i = 1{,}36 \times 10^{-5}$), we have

$$\bar{g}_{ei} = \left(\frac{8k \, T_e}{\pi m_e}\right)^{1/2} \tag{6}$$

The mean cross section of an electron-ion elastic collision is approximately [2]

$$\bar{\sigma}_{ei} = \frac{q_e^2 \, q_i^2 \, ln\Lambda}{4\pi\varepsilon_o^2 (3kT_e)^2} \tag{7}$$

where $ln\Lambda$ is the so-called «Coulombian Logarithm».

$$\Lambda = 12\pi n_e^{-1/2} (\varepsilon_o kT_e / q_e^2)^{3/2} \tag{7'}$$

As the first ionization potentials of the Argon atom are 15,75 eV and 43,37 eV, and since in our case all temperatures are below 10 eV, pratically all ions are simply ionized. Should it not be so, we would have to define the ionic mean charge:

$$\bar{q}_i = \frac{\Sigma_j \, n_{ij} \, q_{ij}}{\Sigma_j \, n_{ij}} \tag{8}$$

In our case, as previously seen, $q_i \simeq q_e$ and therefore (7) becomes

$$\bar{\sigma}_{ei} = \frac{q_e^4 \, ln\Lambda}{36\pi\varepsilon_o^2 (k\,T_e)^2} \tag{9}$$

Substituting in (1) expressions (3), (4), (6), and (7), the following equation is obtained (*)

$$\left[\frac{dE_i}{dt}\right]_{e-i} = \frac{4 \, q_e^4 \, n_e \, n_i \, m_e \, ln\Lambda \, (1 - T_i/T_e)}{9\pi\varepsilon_o^2 \, (2\pi m_e \, kT_e)^{1/2} \, m_i} \tag{10}$$

2.2 — *Ion cooling rate by collision with neutrals*

$$\left[\frac{dE_i}{dt}\right]_{i-o} = -\, n_i \, \bar{\nu}_{io} \, f_{io} \, E_i \tag{11}$$

$\bar{\nu}_{io}$ — ion-neutral collision mean frequency
f_{io} — fraction of ion kinetic energy transferred, on the average, to neutrals, during collision
E_i — ion mean kinetic energy.

(*) A more exact description gives a factor $^1/_2$ (instead of $^4/_9$), which we shall use in the numerical calculations.

To calculate this term it is necessary to take into account the charge transfer collision phenomenon which consists in the capture, by the ion, of the peripheric electron of the neutral, and which results in the identity transfer of the particles.

A priori, the following cases may be considered as possible:

a) Purely elastic dominant collisions (because less frequent, charge transfer inelastic collisions are negligible)

$$A(W_A) + B^+(W_B) \rightarrow A(W'_A) + B^+(W'_B)$$

b) If charge transfer inelastic collisions are not negligible, two hypotheses have to be considered:

b.1) During the charge transfer collision there is no energy transference between particles beyond the one resulting from this change

$$A(W_A) + B^+(W_B) \rightarrow A^+(W_A) + B(W_B)$$

b.2) Besides the charge transfer there exists kinetic energy transference between particles

$$A(W_A) + B^+(W_B) \rightarrow A^+(W'_A) + B(W'_B)$$

Let us analyse the more general case b.2).

E will represent the energy before the collision and E′ the energy after the collision. $f_{io_{t.c.}}$ will be the kinetic energy mean fraction elastically transferred during the charge transfer collision.

Ion:

$$E'_i = E_o + f_{io_{t.c.}} E_i \tag{12}$$

Neutral:

$$E'_o = E_i - f_{io_{t.c.}} E_i \tag{13}$$

The kinetic energy lost, on an average, by the ion through collision with a neutral is given by:

$$\Delta E_i = E_i - E'_i = E_i - E_o - f_{io_{t.c.}} E_i \tag{14}$$

Let $f_{io_{eq}}$ represent the ion energy fraction which is, on an average, transferred to the neutral during a charge transfer collision. Then,

$$f_{io_{eq}} = \frac{\Delta E_i}{E_i} = 1 - \frac{E_o}{E_i} - f_{io_{t.c.}} = \left(1 - \frac{T_o}{T_i}\right) - f_{io_{t.c.}} \qquad (15)$$

Let us now find the value of $f_{io_{eq}}$ for the other cases.

a) In this limit, since the charge transfer is negligible, $f_{io_{eq}} = f_{io}$ (kinetic energy fraction transferred on an average in an *i-o* purely elastic collision); f_{io} is determined by expression (2) where $m_o \simeq m_i$

$$f_{io} = 2/3\ (1 - T_o / T_i) \qquad (16)$$

b) In the limit b.1), $f_{io_{t.c}} = 0$

Then $$\Delta E_i = E_i - E_o$$

$$f_{io_{eq}} = (1 - T_o / T_i) \qquad (17)$$

Assuming that in expression (15) $f_{io_{t.c}} \leqslant f_{io}$, we can have for any of the cases considered

$$f_{io_{eq}} = \alpha\,(1 - T_o / T_i) \qquad (18)$$

where α varies from 1/3 (case b.2, with $f_{io_{t.c}} = f_{io}$) to the unit (case b.1):

$$1/3 \leqslant \alpha \leqslant 1 \qquad (19)$$

The values of the elastic collision cross sections and of the charge transfer for the case of Ar at low energy being of the same order of magnitude [3], it seems correct to take an average value $\bar{\alpha} = 2/3$ and the total cross section (elastic + charge transfer). In the absence of experimental results on the energy band lower than 1 eV, the value of the total cross section should be obtained by extrapola-

tion of the values available. It should be pointed out that, for extremely low collision energies this extrapolation is not valid, as in this case a polar binary complex may be formed, there arising then a situation which, for such energies, leads to a theoretically higher cross section [4].

Let us now determine $\bar{\nu}_{io}$

$$\bar{\nu}_{io} = n_o \, \bar{\sigma}_{io} \, \bar{g}_{io} \tag{20}$$

The experimental curve of $(\bar{\sigma}_{io})_{\text{t.c.}}$ as a function of E_i [5] is very approximately described by the expression

$$(\bar{\sigma}_{io})_{\text{t.c.}} = (6{,}9 - 0{,}25 \; ln \; E_i)^2 \times 10^{-20} \; \text{m}^2 \tag{21}$$

with E_i in eV.

$\bar{g}_{io}$ is obtained from expression (5) with $m_o \simeq m_i$,

$$\bar{g}_{io} = \left(\frac{8k\,T_i}{\pi m_i}\right)^{1/2} \left(1 + \frac{T_o}{T_i}\right)^{1/2} \tag{22}$$

Substituting in (11), and with $E_i = 3/2 \; k \; T_i$, we have

$$\left[\frac{dE_i}{dt}\right]_{i-o} = - n_i \, n_o \, \bar{\sigma}_{io} \left(\frac{8k\,T_i}{\pi m_i}\right)^{1/2} \left(1 + \frac{T_o}{T_i}\right)^{1/2} \left(1 - \frac{T_o}{T_i}\right) k \, T_i \tag{23}$$

3 — FINAL EQUATION

From equations (10) and (23) we get

$$\frac{T_e^{3/2} \, (T_i + T_o)^{1/2} \, (T_i - T_o)}{(T_e - T_i)} = \frac{n_e}{n_o} \, \frac{q_e^4 \quad ln \, \Lambda}{8 \pi \, \varepsilon_o^2 \, (m_i/m_e)^{1/2} \, \bar{\sigma}_{io} \, k^2} \tag{24}$$

The solution of equation (24) to determine T_i is very complex since $\bar{\sigma}_{io} = f \, (T_i)$. On the other hand $ln \, \Lambda = f \, (n_e, \, T_e)$. However, from the observation of the dependence of $\bar{\sigma}_{io}$ on E_i and of the

values of $ln\,\Lambda$ the following simplifying hypothesis may be considered:

Equation (21) was determined for E_i values between 1 eV and 100 eV (1 eV $\simeq$ 10.000 K). Since $T_e > T_i > T_o$, and considering the range of values used for T_e, for T_o and for n_e/n_o, it can be concluded that T_i will take values between the approximate limits of 300 K (0,03 eV) and 10000 K (1 eV). Thus, and since $(\bar{\sigma}_{io})_{t.c.}$ varies very little with E_i, the curve for $E_i < 1$ eV can be extrapolated and its mean value taken in the above mentioned range:

$$\begin{aligned} (\bar{\sigma}_{io})_{tc} &= 51 \times 10^{-20}\ m^2 \\ (\bar{\sigma}_{io}) &= 102 \times 10^{-20}\ m^2 \end{aligned} \qquad (25)$$

Substituting in equation (24) the values of constants and the value of $\bar{\sigma}_{io}$ given by (25), we have

$$\frac{T_e^{3/2}\,(T_i + T_o)^{1/2}\,(T_i - T_o)}{(T_e - T_i)} = \delta \qquad (26)$$

and

$$T_e^3\,T_i^3 - (\delta^2 + T_e^3\,T_o)\,T_i^2 + (2\delta^2 - T_e^3\,T_o^2)\,T_i + (T_e^3\,T_o^3 - \delta^2\,T_e^2) = 0 \qquad (27)$$

where $$\delta = 6.36 \times 10^6\,(n_e/n_o)^2\,ln\,\Lambda$$

and $ln\,\Lambda$ is given in (7′).

Solution was worked out by a numerical method, results having been obtained for several electronic temperatures and n_e/n_o ratios. Two groups of typical curves are presented (Figs. 1 and 2).

4 — DISCUSSION OF RESULTS

It can be seen from Figs. 1 and 2 that for constant T_e, T_i approaches T_o for higher T_o. This result is to be expected since

when T_o approaches T_e, the equilibrium temperature T_i which results from the energy balance equation

$$\left[\frac{dE_i}{dt}\right]_{e-i} = -\left[\frac{dE_i}{dt}\right]_{i-o}$$

tends to approach T_o and T_e.

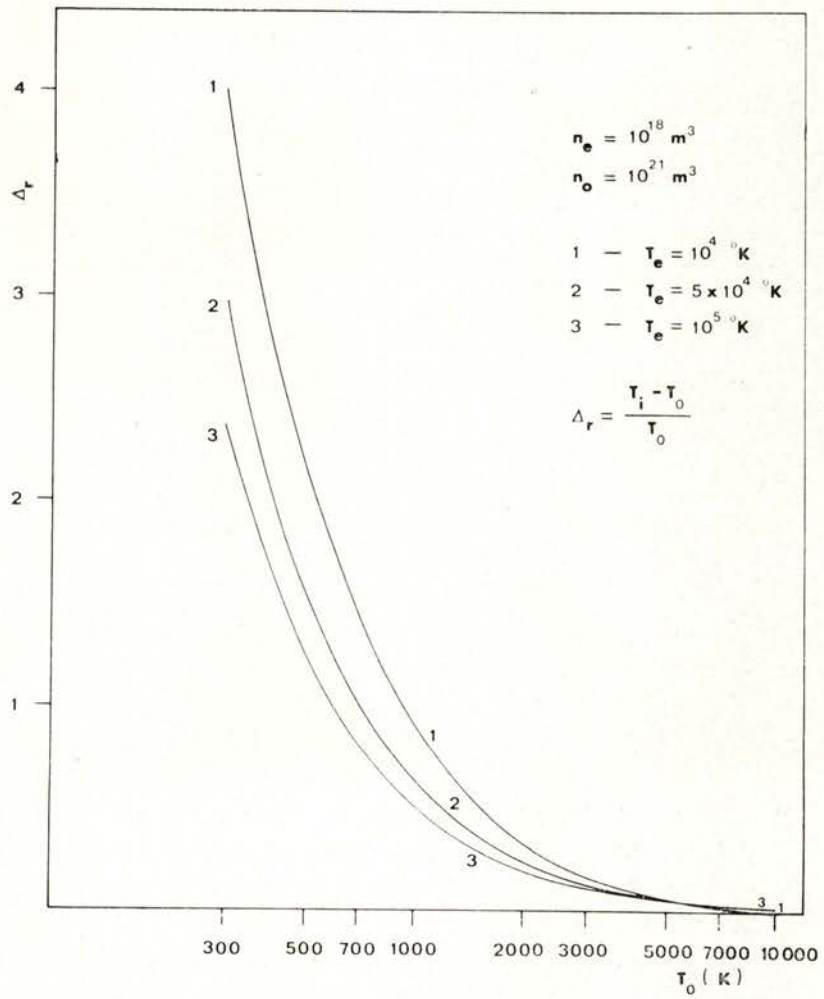

Fig. 1 — Ionic temperature of an argon plasma as a function of the neutral temperature (T_0) for several values of the electron temperature (T_e).

On the other hand and as a general rule, for higher T_e values we get lower T_i values (for the same T_o). However curves of Fig. 1 and 2 are found to intersect. This is due to the fact that the curve representing the ion heating rate for a given T_i is not a monotonous function of T_e. Thus there will always exist for a given T_i value, pairs of T_e values which lead to the same heating rate value.

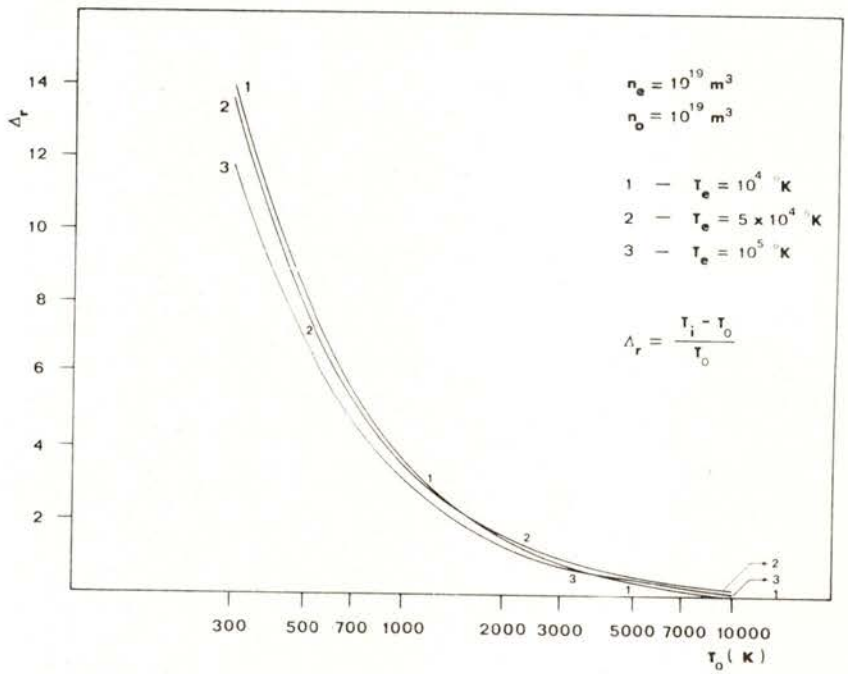

Fig. 2 — Ionic temperature of an argon plasma as a function of the neutral temperature (T_0) for several values of the electron temperature (T_e).

The results obtained have a limited field of validity since they can only be applied to regions of homogeneous plasma where the ion heating and cooling mechanisms are exclusively due to elastic collisions, respectively with electrons and neutrals. Now this can only occur for large dimension plasmas with small applied fields, whether electric or magnetic.

The validity conditions required are acceptable for a high pressure arc, the present results being then applicable.

On the other hand the parameters used in the equations can hardly be regarded as independent in a real plasma. A possible development of this work would be the inclusion of a balance condition for the neutrals with a view to a more consistent theory.

REFERENCES

[1] AUSTIN M. CRAVATH, «The rate at which ions lose energy in elastic collisions» — *Phys. Rev.*, **36**, 248 (1930).

[2] DAVID J. ROSE & MELVILLE CLARK Jr, *Plasma and Controlled Fusion*, M.I.T. Press 1961, p. 163 and 169.

[3] EARL W. MCDANIEL, *Collision Phenomena in ionized gases*, John Wiley, 1964, p. 164.

[4] E. E. NIKITIN, *Theory of elementary Atomic and Molecular Processes in Gases*, Clarendon Press, 1974.

[5] P. MAHADEVAN & G. D. MAGNUSON, «Low Energy (1-to 100 eV) Charge-Transfer Cross-Section Measurements for Noble-Gas-Ion Collisions with Gases», *Phys. Rev.*, **171**, 103 (1968).

Imprensa Portuguesa • Rua Formosa, 108-116 • 4000 Porto

SOCIEDADE PORTUGUESA DE FÍSICA
AV. REPÚBLICA 37-4.°, 1000 LISBOA, PORTUGAL

PORTUGALIAE PHYSICA publishes articles or research notes with original results in theoretical, experimental or applied physics; invited review articles may also be included.

Manuscripts, with an abstract, may be written in English or French; they should be typewritten with two spaces and in duplicate. Figures or photographs must be presented in separate sheets and be suitable for reproduction with eventual reduction in size; captions should make the figures intelligible without reference to the text. Authors are requested to comply with the accepted codes concerning references.

There is no page charge. Author(s) will get 50 free reprints (without covers); these are to be shared among all the authors of the article. Authors interested in more reprints should say so when sending their manuscripts; quotations shall be sent with the proofs.

Subscription rates for volume 10:

1,000 Escudos (US$20) — individuals
2,500 Escudos (US$50) — libraries

PORTUGALIAE PHYSICA may also be sent on an exchange basis; we wellcome all suggestions to such effect.

All mail to be addressed to

PORTUGALIAE PHYSICA

C/O LABORATÓRIO DE FÍSICA, FACULDADE DE CIÊNCIAS
PRAÇA GOMES TEIXEIRA
4000 PORTO PORTUGAL

CONTENTS